Dynamics of Slender Cantilevered Cylinders Subjected to Internal and External Axial Flows

Mahdi Chehreghani

Doctor of Philosophy

Department of Mechanical Engineering

McGill University

Montreal, Québec

April 2024

A thesis submitted to McGill University in partial fulfillment of the requirements of the degree of Doctor of Philosophy

TABLE OF CONTENTS

ABSTRACT viii

ABRÉGÉ x

ACKNOWLEDGEMENTS xii

ORIGINAL CONTRIBUTIONS TO KNOWLEDGE xiv

CONTRIBUTION OF AUTHORS xvi

LIST OF TABLES xviii

LIST OF FIGURES xx

1 Introduction 1

1.1 Introduction, motivation and general remarks 1

1.2 Literature review 9

1.2.1 Pipes conveying fluid 9

1.2.2 Cylinders in axial flow 15

1.2.3 Tubular beams subjected to both internal and external flows . 18

1.3 Limitations of the studies in the literature 21

1.4 Thesis scope and objectives 22

1.5 Thesis structure . . . 24

2 Dynamics of Slightly Curved Cantilevered Pipes Conveying Fluid: An Experimental Investigation **26**

Preface . . . 26

2.1 Introduction . . . 28

2.2 Apparatus and methodology . . . 31

2.3 Results . . . 37

2.3.1 Dimensionless terms . . . 37

2.3.2 Results for fluid-discharging pipes . . . 37

2.3.3 Results for fluid-aspirating pipes . . . 43

2.3.4 Comparing the dynamics of discharging and aspirating curved pipes . . . 49

2.4 Concluding remarks . . . 50

References . . . 51

Complementary discussion on system I . . . 58

3 Dynamics of Free-Clamped Cylinders in Axial Flow: An Experimental Investigation **59**

Preface . . . 59

3.1 Introduction . . . 61

3.2 Experimental set-up, data acquisition and methodology . . . 65

3.3 General observations and results . . . 68

3.3.1 Dynamics of inverted cylinders with an embedded metal strip 68

3.3.2 Dynamics of inverted cylinders able to move in 3D . . . 74

3.3.3 Critical flow velocities and frequencies . . . 77

3.4 The mechanisms of flutter and static divergence 78
3.5 Concluding remarks 81
Appendix A. Material damping of the elastomer cylinders 83
Appendix B. Energy transfer considerations for flutter 83
References 84

4 Dynamics of a Cantilevered Pipe Conveying Fluid and Counter-currently Subjected to Partially Confined External Axial Flows: Experimental Investigation I 89

Preface 89
4.1 Introduction 92
4.2 Experimental apparatus and procedure 96
4.2.1 Test section 96
4.2.2 Data acquisition 97
4.2.3 Experimental methodology 98
4.2.4 Data analysis 98
4.3 Results 98
4.3.1 Experimental results for $\boldsymbol{r_{ann} \simeq 1/4}$ 98
4.3.2 Experimental results for $\boldsymbol{r_{ann} \simeq 1/2}$ 102
4.3.3 Experimental results for $\boldsymbol{r_{ann} \simeq 3/4}$ 110
4.4 Summary and conclusion 114
Appendix. Dimensionless parameters 118
References 119

5 Dynamics of a Cantilevered Pipe Conveying Fluid and Counter-currently Subjected to Partially Confined External Axial Flows: Experimental Investigation II **123**

Preface . . . 123

5.1 Introduction . . . 124

5.2 Apparatus and methodology . . . 129

5.2.1 Experimental setup . . . 129

5.2.2 Data acquisition and processing . . . 131

5.3 Dimensionless parameters . . . 132

5.4 Results on the effect of external flow confinement . . . 134

5.4.1 Interdependent internal and external flow . . . 135

5.4.2 Independent internal and external flows . . . 138

5.5 The effect of annulus-to-pipe length ratio . . . 141

5.6 The effect of pipe slenderness . . . 142

5.7 The effect of flow constriction at the upstream or downstream end of the annular region . . . 144

5.7.1 Obstruction at the annular region inlet . . . 144

5.7.2 Obstruction at the annular region outlet . . . 146

5.8 The effect of pipe material . . . 147

5.9 The effect of eccentricity . . . 149

5.9.1 Interdependent internal and external flow . . . 149

5.9.2 Independent internal and external flow . . . 149

5.10 Conclusion . . . 151

Appendix A. The linear equation of motion of the basic system . . . 152

Appendix B. The expressions for mass, damping and stiffness matrices . . . 154

References . . . 154

Complementary discussion on system III - experimental investigation . . . 160

6 Dynamics of a Cantilevered Pipe Conveying Fluid and Partially Subjected to a Confined Counter-current External Axial Flow of a Different Fluid: A Theoretical Investigation 161

Preface . . . 161

6.1 Introduction . . . 162

6.2 Model development . . . 169

6.2.1 Derivation of the equation of motion . . . 169

6.2.2 The equation of motion . . . 178

6.2.3 The non-dimensional equation of the motion . . . 179

6.2.4 Solution procedure . . . 180

6.3 Numerical results and discussion . . . 182

6.3.1 Validation . . . 182

6.3.2 Results of the present model for system parameters associated with typical full-scale systems . . . 184

6.4 Parametric study . . . 189

6.4.1 The effect of well-head pressure . . . 190

6.4.2 The effect of brine-to-product density ratio . . . 190

6.4.3 The effect of external flow confinement . . . 191

6.4.4 The effect of confinement length ratio . . . 192

6.4.5 The effect of pipe slenderness . . . 193

6.5 Conclusion . . . 194

References . . . 197

Complementary discussion on system III - theoretical investigation . . . 204

7 Conclusions and Suggested Future Work . . . **205**
7.1 Summary of findings . . . 206
7.1.1 System I . . . 206
7.1.2 System II . . . 207
7.1.3 System III . . . 207
7.2 Future work . . . 209
References . . . 211

ABSTRACT

The main objective of this thesis is to study the dynamics of slender cantilevered cylinders subjected to internal, external, or simultaneous internal and external axial flows. The motivation for further research on the dynamics of slender structures in contact with fluid stems not only from their presence in some engineering and biological systems, but also because of the rich dynamics they display. In particular, the dynamics of three closely related systems of slender tubular beams subjected to internal and external axial flows are investigated experimentally and/or by developing an analytical fluid-structure interaction model.

System I is a slightly curved cantilevered pipe conveying fluid. A bench-top-size apparatus consisting of a reservoir and a hanging straight or curved cantilevered pipe conveying fluid was utilized. It was observed that for initially curved discharging pipes, due to the exaggeration of the initial curvature of the pipe, increasing flow velocity gives rise to a large flow-induced static deformation prior to the abrupt onset of a vigorous flutter. On the other hand, aspirating curved pipes develop an anaemic (weak) flutter with increasing flow velocity, overlaid on a relatively large static deformation.

System II is an inverted cantilevered cylinder in axial flow, that is a cylinder with the upstream end free and the downstream end clamped. Water-tunnel experiments were conducted to investigate fluid-elastic instabilities. It was observed that, at relatively low flow velocities the inverted cylinder undergoes small amplitude motion due to turbulent buffeting before the onset of an unsteady flutter in the first mode. The amplitude of flutter increased with flow, eventually resulting in an abrupt static divergence at sufficiently high flow rates. The influence of various system parameters was examined. Results indicate that the dynamics is only slightly affected by the shape of the free end, which contrasts sharply with its effect on the dynamics of conventional cylinders where flow is directed from the clamped end towards the free end.

System III involves a hanging fluid-discharging pipe subjected to a reverse external flow over its upper portion through the annulus formed by a co-axial shorter outer rigid tube. Using a bench-top-size apparatus, numerous experiments were conducted to investigate the dynamical behaviour of the system, including post-instability dynamics. Specifically, for various external-to-internal flow velocity ratios, the influence of the following system parameters on the dynamics was examined experimentally: (i) confined length of the pipe, (ii) degree of confinement, (iii) pipe slenderness, (iv) pipe material, (v) placement of a constraint at the annular flow inlet/outlet, (vi) eccentric positioning of the outer rigid tube relative to the pipe. Varying the system parameters in some cases led to significantly different qualitative and/or quantitative dynamical behaviour. Increasing the external-to-internal flow velocity ratio resulted in a lower critical flow velocity in all cases. Additionally, employing the Newtonian approach and considering the presence of two different fluids in the container, an analytical model for system III was derived. This idealized model can serve as a useful tool for prediction of fluid-elastic instabilities of brine-strings during product retrieval in salt-mined caverns, which are utilized for storage and subsequent retrieval of hydrocarbons and hydrogen gas. The results obtained suggest that, depending on the system parameters, the brine-string system may become unstable via static divergence or flutter. The results demonstrate that simplifying the system by considering a single fluid in the cavern, and thus for the flows within and around the brine-string, results in overestimating the critical flow velocity. Extensive computations were conducted using parameters relevant to full-scale brine-strings to explore the effect of the main system parameters on the dynamics.

ABRÉGÉ

Cette thèse explore la dynamique des cylindres en porte-à-faux soumis à des écoulements axiaux internes, externes ou combinés. La motivation découle de leur présence dans divers systèmes et de leur riche dynamique. Trois systèmes de poutres tubulaires minces soumis à des écoulements sont étudiés expérimentalement ou via des modèles analytiques d'interaction fluide-structure.

Le système I est un tuyau en porte-à-faux légèrement incurvé transportant du fluide dans un réservoir. Il a été observé expérimentalement que pour les tuyaux de décharge initialement courbées, en raison de l'exagération de la courbure initiale, l'augmentation de la vitesse d'écoulement donne lieu à une déformation statique importante avant l'apparition brusque d'un battement vigoureux. Par coutre, les tuyaux courbes aspirants développent un flottement anémique avec une vitesse d'écoulement croissante, superposé à une déformation statique relativement importante.

Le système II est un cylindre en porte-à-faux inversé soumis à flux axial, c'est-à-dire un cylindre dont l'extrémité amont est libre et l'extrémité aval est serrée. Des expériences en tunnel d'eau ont été menées pour étudier les instabilités fluide-élastiques. Il a été observé qu'à des vitesses d'écoulement relativement faibles, le cylindre subit un mouvement de faible amplitude induit par la turbulence avant l'apparition d'un flottement dans le premier mode. L'amplitude du flottement augmente avec le débit, entraînant finalement une divergence statique abrupte à des débits suffisamment élevés. L'influence de divers paramètres du système a été examinée. Les résultats indiquent que la dynamique n'est que légèrement affectée par la forme de l'extrémité libre, ce qui contraste fortement avec son effet sur la dynamique des cylindres conventionnels où le flux est dirigé de l'extrémité serrée vers l'extrémité libre.

Le système III implique un tuyau suspendu parcouru d'un fluide et soumis à un écoulement externe inverse sur sa partie supérieure à travers l'anneau formé par un tube rigide externe coaxial plus court. À l'aide d'un appareil de laboratoire, de nombreuses expériences ont été menées pour étudier le comportement dynamique du système, y compris la dynamique post-instabilité. Pour divers rapports de vitesse d'écoulement externe/interne, l'influence des paramètres suivants sur la dynamique a été examinée expérimentalement: (i) la longueur confinée du tuyau, (ii) le degré de confinement, (iii) l'élancement du tuyau, (iv) matériau du tuyau, (v) placement d'une contrainte à l'entrée/sortie du flux annulaire, (vi) positionnement excentré du tube rigide extérieur par rapport au tuyau. La variation des paramètres du système a conduit dans certains cas à un comportement dynamique significativement différent. L'augmentation du rapport de vitesses d'écoulement externe/interne a entraîné une vitesse d'écoulement critique plus faible dans tous les cas. De plus, en utilisant l'approche newtonienne et en considérant la présence de deux fluides différents dans le réservoir, un modèle analytique idéalisé pour ce système a été dérivé qui peut servir d'outil pour prédire les instabilités fluide-élastiques du tuyau lors de la récupération des produits dans les cavernes d'extraction de sel, qui sont utilisées pour le stockage et la récupération ultérieure des hydrocarbures et de l'hydrogène gazeux. Les résultats obtenus suggèrent que, en fonction des paramètres du système, le tuyau peut devenir instable par divergence statique ou flottement. Les résultats démontrent que simplifier le système en considérant un seul fluide dans la caverne conduit à surestimer la vitesse critique d'écoulement. Des calculs approfondis ont été effectués en utilisant des paramètres pertinents pour les chaînes de saumure à grande échelle afin d'explorer l'effet des principaux paramètres du système sur la dynamique.

ACKNOWLEDGEMENTS

Foremost, I want to extend my heartfelt gratitude and appreciation to my supervisors, Professor Michael Païdoussis and Professor Arun Misra, for their guidance and supervision throughout this research endeavor. Words cannot adequately express my deep appreciation for their role not only as academic guides but also as mentors and inspirational figures in my life journey. I am deeply thankful to Professor Païdoussis for granting me the opportunity to pursue my Ph.D. under his mentorship. It is a profound honour to learn about Fluid-Structure Interactions from such a distinguished scientist in the field. I am truly grateful for his kindness and continuous support. I express my gratitude to Professor Arun Misra for his kindness and continuous support, insightful discussions, valuable feedback, and constructive comments. I am deeply honoured that I have had the chance of working with him.

I would like to express my gratitude to my thesis advisory committee members, Professors Mathias Legrand and Jovan Nedić for their valuable comments which helped me to progress in my work. Also, I would like to express my appreciation to Professor Meyer Nahon of McGill University and Yahya Modarres-Sadeghi of University of Massachusetts Amherst for accepting to read this thesis and to act as examiners of my thesis.

I would like to thank Mary Fiorilli for her assistance with administrative matters. I am appreciative of Professor Farhang Daneshmand of Pennsylvania State University-Scranton for sharing useful results from his computational analysis. Thanks also go to Professor Mojtaba Kheiri of Concordia University for all the interesting discussions and brilliant thoughts we have had.

During my academic journey, I was fortunate to be surrounded by exceptional friends and lab-mates. I am particularly thankful to Ahmed Shaaban for our shared experiences, fruitful discussions, and collaborative planning for research. My heartfelt appreciation also goes to Iman Gholami, my fellow researcher in the fluid-structure interaction group, and my roommate, whose friendship has been a constant source of inspiration. I extend my gratitude to all my friends and colleagues in the department: Ahmed Abdelbaki, Aram Bahmani, Mohammad Faisal Butt, and Mohammad Tavallaeinejad.

I would like to express my deepest love and gratitude to my parents, to whom I owe my life and success. I am forever grateful for their faith in me. Also, I thank my beloved sister and brother for their support and encouragement. Despite the physical distance that separates me and my family in Iran, their unwavering presence in my life has consistently provided love, encouragement, and strength.

Words cannot describe my gratitude to my wonderful fiancée, Nava, whose loving support has been my strength through every challenge and success. Her presence during this journey has been a blessing beyond words.

ORIGINAL CONTRIBUTIONS TO KNOWLEDGE

Several advancements have been achieved in enhancing the understanding of fluid-structure interactions in slender cylinders subjected to axial flow. The main contributions of the present thesis can be listed as follows.

1. Determining experimentally the effect of a slight initial curvature on the dynamical behaviour of cantilevered pipes discharging/aspirating fluid.

2. Discovering experimentally the dynamics of a free-clamped cylinder in water flow, as well as determining the effect of the main system parameters such as cylinder free-end shape, slenderness, flexural rigidity, and planar or 3D motions.

3. Characterizing experimentally the dynamics of a hanging fluid-discharging pipe subjected to partially confined counter-current external axial flow through an annular region contained by a shorter rigid tube at the upper portion of the pipe.

4. For the system of item 3, characterizing the effect of the following system parameters on the dynamical behaviour:

   (a) annulus-to-pipe length ratio (confined length ratio)

   (b) degree of confinement (size of the annular gap)

   (c) pipe slenderness (pipe length-to-diameter ratio)

   (d) pipe material properties

   (e) placement of a constraint at the annular flow inlet/outlet (flow constriction at the upstream or downstream end of the annular region)

   (f) eccentric positioning of the outer rigid tube relative to the pipe

5. For the the system of item 3, determining the influence of post-instability impacting of the pipe on the outer rigid tube.
6. Developing an analytical model for the dynamics of a cantilevered pipe conveying fluid and partially subjected to a confined reverse external axial flow of a different fluid, serving as an idealized model for the dynamics of brine-strings in salt-mined caverns.
7. Discovering the influence of the main system parameters on the dynamics of the system of item 6. In particular, using parameters relevant to full-scale brine-strings in salt-mined caverns, discovering the influence of (i) brine-product interface level, (ii) the ratio between brine and product densities and viscosities, (iii) the well-head pressure, (iv) degree of confinement of the external flow, (v) confinement length ratio and (vi) brine-string slenderness on the stability of the system.

CONTRIBUTION OF AUTHORS

For the manuscripts in which I am the first author and are included in this manuscript based thesis, the contributions of co-authors are listed as follows.

1. Experimental investigation of the dynamics of slightly curved cantilevered pipes conveying fluid by M. Chehreghani, A. Shaaban, A. K. Misra, M. P. Païdoussis [1]:
   My contribution involved conceptualization, investigation, developing appropriate methodology, conducting experiments, data curation, conducting formal analysis of the results, data visualization, and writing the original draft of the paper. A. Shaaban assisted with conducting experiments and contributed to reviewing and editing the paper. This work was enriched by pertinent comments and input from my supervisors, namely Profs. Misra and Païdoussis. They provided essential input for the conceptualization of the work, supervised the project, acquired funding, managed project administration, and contributed to reviewing and editing the paper.

2. Fluid-elastic instability of inverted cantilevered cylinders in axial flow by M. Chehreghani, I. Gholami, A. K. Misra, M. P. Païdoussis [2]:
   My role throughout the project involved conceptualization, conducting investigations, developing the appropriate methodology, carrying out experiments, curating data, conducting formal analysis of the results, visualizing data, and drafting the original paper. I. Gholami provided assistance in conducting experiments and contributed to the review and editing of the manuscripts. Professors Misra and Païdoussis offered crucial guidance during the project, provided funding, managed project administration, and contributed to the review and editing of the paper.

3. Experiments on the dynamics of a cantilevered pipe conveying fluid and subjected to reverse annular flow by M. Chehreghani, A. R. Abdelbaki, A. K. Misra, M. P. Paï-

doussis [3]:

I contributed to various aspects of this study, including conceptualization, investigation, methodology development, experimentation, data acquisition, data analysis, data visualization, and drafting the original manuscript. A. R. Abdelbaki assisted with specific parts of the experiments, particularly the results for $_{rann} \simeq 1/2$, and contributed to the review and editing of the paper. My supervisors enhanced the quality of this paper with valuable comments and input; they provided essential guidance in conceptualizing the study, overseeing its progress, securing funding, managing project administration, and contributing to the review and editing of the paper.

4. Dynamics of a hanging fluid-discharging pipe subjected to reverse external flow: An experimental investigation by M. Chehreghani, A. Shaaban, A. K. Misra, M. P. Païdoussis [4]:

   I played a primary role in various aspects of the project, including conceptualization, investigation, method development, experiment execution, data acquisition, analysis, visualization, and initial paper drafting. A. Shaaban assisted in conducting experiments and contributed to the review and editing process. The quality of the work was enriched by valuable feedback from my supervisors, who provided essential comments, oversaw project management, provided funding, and contributed to the review and editing of the paper.

5. Dynamics of a cantilevered pipe conveying fluid and partially subjected to a confined counter-current external axial flow of a different fluid by M. Chehreghani, A. K. Misra, M. P. Païdoussis [5]:

   All the work conducted in this paper (currently under review), including conceptualization, derivations, validation, calculations, analysis, investigation, and writing the original draft, was done by myself. The work was enriched by pertinent comments and input from my supervisors, Professors Misra and Païdoussis.

LIST OF TABLES

2.1 Mechanical properties and dimensions of the pipes used in the experiments. . 33

2.2 Multiplicative conversion factors from dimensionless flow velocity and frequency to dimensional terms, and the dimensionless parameters for the pipes used in the experiments. 35

3.1 Dimensions and material properties of the flexible cylinders used in the experiments. 64

3.2 Conversion factors between dimensional and dimensionless flow velocity and frequency. 67

3.3 Dimensionless critical flow velocities and frequencies. 78

3.4 Qualitative dynamical characteristics of conventional and inverted cantilevered cylinders in axial flow. 81

4.1 Material properties and dimensions of the flexible pipe used in the experiments. 97

4.2 Summary of the results showing the critical internal flow velocities in m/s for instability. 116

4.3 The dynamical behaviour of the system right after the initiation of impacting. 117

5.1 Properties of the flexible pipes used in the experiments. 130

5.2 Multiplicative factors to convert the dimensionless to dimensional terms. . . 133

5.3 The effect of r_{ann} on the dimensionless critical internal flow velocities of pipe A with $\alpha_{ch} = 1.97$. 142

5.4 Critical flow velocities of the instability of pipe A (ε = 27.56) and pipe B (ε =13.81). 144

5.5 Comparing $u_{cr,1}$ for pipe A with different values of dimensionless eccentricity with respect to the outer tube. 151

6.1 Dimensionless critical flow velocity, $u_{i,cr}$ and the mode of instability for the bench-scale-system parameters. F2: flutter in the second mode 182

6.2 Dimensionless critical flow velocity, $u_{i,cr}$ and the mode of instability for the system introduced in Section 6.3.1.2 with $L = 200$ m and various α_{ch}. Di: static divergence in the ith mode, Fi: flutter in the ith mode 185

6.3 Dimensions of some typical brine-string systems. 187

6.4 Dimensionless parameters associated with the systems of Table 6.3. In these calculations, the two fluids in the brine-string and storage cavern are brine and propane. 188

6.5 Multiplicative factors to convert the dimensionless to dimensional terms and the relationship between internal and/or external flow velocities associated with the systems of Table 6.3. In these calculations, the two fluids in the brine-string and storage cavern are brine and propane. 188

6.6 Critical flow velocity, $u_{i,cr}$, and the mode of instability for the systems of Table 6.3. Di: static divergence in the ith mode, Fi: flutter in the ith mode. The dimensional values of $U_{i,cr}$ (m/s) are given in parentheses. 189

6.7 Dimensionless critical flow velocity, $u_{i,cr}$ and the mode of instability for B-brine-propane system with different values of well-head-pressure. Di: static divergence in the ith mode, Fi: flutter in the ith mode 191

6.8 Dimensionless critical flow velocity, $u_{i,cr}$ and the mode of instability for system B with three different brine-to-product density and viscosity ratios. Di: static divergence in the ith mode, Fi: flutter in the ith mode 191

LIST OF FIGURES

1.1 A long aspirating pipe utilized in ocean mining operations to extract manganese nodules or diamonds from the seabed, after Ref. [18] 3

1.2 A 500 m^3 Dracone, air-inflated after discharging fresh-water cargo, leaving the island of Santorini, Greece (Dunlop Dracones 1965), after Ref. [27]. 4

1.3 A schematic view of a typical seismic array survey, after Ref. [28]. 4

1.4 (a) Schematic view of a typical drill-string with its internal flow-powered rotating drill bit, from [30]; (b) An idealized drill string, with the drill bit entirely disregarded. The system can be modelled as a hanging fluid-discharging cantilevered pipe, in which the fluid upon exiting the pipe flows upwards as a confined axial flow [31]. 5

1.5 Schematic view of the formation of salt-mined caverns formed by pumping fresh water downwards: (a) through a vertical pipe, the "brine-string", and brine flowing upwards through a shorter concentric annular region formed by a rigid "casing" surrounding the pipe at its upper portion, a flow configuration that favours expansion of the lower part of the cavern; (b) through the outer casing, with brine flowing upwards through the aspirating brine-string, a flow configuration that favours the expansion of the upper part of the cavern; from Ref. [33]. 6

1.6 Various utilizations of salt-mined caverns, after [35]. 7

1.7 (a) Schematic view of a salt-mined cavern in hydrocarbon storage applications, after [36]; (b) An idealized brine-string in retrieval mode modelled as a hanging fluid-discharging cantilevered pipe subjected to a partially confined external axial flow. 8

1.8 Schematic view of the three systems of slender cantilevered cylinders subjected to internal, external, or simultaneous internal and external axial flows; (a) system I: a slightly curved cantilevered pipe discharging/aspirating fluid; (b) system II: an inverted cantilevered cylinder in axial flow, i.e. a cylinder with the upstream end free and the downstream end clamped; (c) system III: a hanging fluid-discharging pipe subjected to a reverse external flow over its upper portion through the annulus formed by a co-axial shorter outer rigid tube. 22

2.1 Schematic view of the pressure vessel of the SMRI-PRCI apparatus used in the experiments and the dual-camera system. (a) The hanging cantilevered pipe discharges water down into the pressure vessel that is filled with air, with the discharged water from the pipe exiting from the bottom of the pressure vessel; (b) zoomed view of the discharging pipe configuration. (c) The pressure vessel is filled with water and the pipe aspirates the fluid (the fluid introduced into the vessel from its top end flows upwards in the pipe); (d) zoomed view of the aspirating pipe configuration. 32

2.2 Photographs of the two pipes used in the experiments: (a) the straight pipe; (b) the pipe with a semi-circular initial curvature. 34

2.3 Characterization of the pipe curvature with a combination of a cantilevered beam mode shapes. 34

2.4 Bifurcation diagrams showing the rms of total displacement, mean deflection and the oscillatory displacement as a function of flow velocity for: (a, c) fluid-discharging straight pipe; (b, d) fluid-discharging curved pipe. Rms amplitude: (●) pre-instability, (■) post-instability; (×) mean deflection. . . . 38

2.5 Continuous wavelet transform scalogram with the vertical bands corresponding to the flow velocity steps for (a) fluid-discharging straight pipe; (b) fluid-discharging curved pipe. 39

2.6 Dynamics of the fluid-discharging *straight* pipe at $u = 6.25$ ($U = 6.85$ m/s). (a) Displacement time traces; (b) polar trajectory of the motion; (c) phase plane contour plot of the front displacement; (d) autocorrelation of oscillatory part of the front displacement; (e) PDF of oscillatory part of the front displacement; (f) Poincaré map. 40
2.7 Dynamics of the fluid-discharging *curved* pipe at $u = 6.34$ ($U = 6.95$ m/s). (a) Displacement time traces; (b) polar trajectory of the motion; (c) phase plane contour plot of the front displacement; (d) autocorrelation of the oscillatory front displacement; (e) PDF of the oscillatory front displacement; (f) Poincaré map. 41
2.8 The largest Lyapunov exponent of the displacement time series for fluid-discharging pipes: (●) straight pipe front, (■) straight pipe side, (▲) curved pipe front, (♦) curved pipe side. 43
2.9 Bifurcation diagram showing the rms of total displacement and the difference between the rms of the total displacement and the mean deflection for: (a, c) fluid-aspirating straight pipe; (b, d) fluid-aspirating curved pipe. Rms amplitude: (●) pre-instability, (■) post-instability; (×) mean deflection. . . 44
2.10 Continuous wavelet transform scalogram in which the vertical bands correspond to the value of the flow velocity for (a) fluid-aspirating straight pipe; (b) fluid-aspirating curved pipe. 45
2.11 Dynamics of the fluid-aspirating *straight* pipe at $u = 5.18$ ($U = 5.68$ m/s). (a) Displacement time traces; (b) polar trajectory of the motion; (c) phase plane contour plot of the front displacement; (d) autocorrelation of oscillatory part of the front displacement; (e) PDF of oscillatory part of the front displacement; (f) Poincaré map. 47
2.12 Dynamics of the fluid-aspirating *curved* pipe at $u = 5.18$ ($U = 5.68$ m/s). (a) Displacement time traces; (b) polar trajectory of the motion; (c) phase plane contour plot of the front displacement; (d) autocorrelation of oscillatory part of the front displacement; (e) PDF of oscillatory part of the front displacement; (f) Poincaré map. 48

2.13 Variation of the largest Lyapunov exponent of the displacement time series by increasing u for fluid-aspirating pipes. (●) Straight pipe front displacement, (■) straight pipe side displacement, (▲) curved pipe front displacement, (♦) curved pipe side displacement. 49

3.1 Schematic view of (a) the water tunnel; (b) the test-section with the data acquisition systems. 63

3.2 The water tunnel with a synchronized dual-camera system used to track the motion of the cylinder. 65

3.3 Dynamics of cylinder I-C (cylinder I with a conical end-piece) illustrated by means of (a) bifurcation diagram showing the rms amplitude of motions versus increasing flow velocity, (●) pre-instability, (■) flutter, (▲) static divergence, and (×) with decreasing flow velocity; (b) Morse wavelet scalogram in which the vertical strips correspond to discrete values of the flow velocity. 67

3.4 Dynamics of cylinder I-C right after the threshold of flutter at $u = 0.64$ ($U = 0.98$ m/s), represented through (a) time traces of the front and top displacements, (b) PSD of motions, (c) phase portraits of the top displacement, and (d) PDF of top displacement. 69

3.5 Comparing the dynamics of cylinder I with (●) an ogival end-shape, I-O, (▶) conical end-shape, I-C, and (■) blunt end-shape, I-B, by means of (a) bifurcation diagrams showing the rms amplitude of motions versus flow velocity; (b) dominant dimensionless frequency of oscillations, ω, at each flow velocity step. 70

3.6 Comparing the dynamics of cylinders with various lengths: (a) bifurcation diagram for (▲) cylinder I-C, (●) cylinder II-C and (■) cylinder III-C, all with a conical end-shape; (b) critical flow velocities for flutter (♦) and static divergence (◀). 71

3.7 Morse wavelet scalograms representing the distribution of frequencies at each flow velocity (a) for cylinder II-C and (b) for cylinder III-C. 72

3.8 The post-divergence dynamics of cylinder III-C at $u = 0.82$ ($U = 0.63$ m/s) illustrated by means of (a) polar plot, (b) 3D trajectory of motion, (c) time traces of the front and top displacements, (d) PSD of top displacements, (e,f) phase portraits of the top and front displacements, respectively. 73

3.9 Strouhal numbers calculated based on the frequency associated with vortex shedding, f_{vs}, versus flow velocity for post-divergence of cylinder III-C. . . . 74

3.10 (a,b) Bifurcation diagrams showing the rms amplitude versus flow velocity for a silicone-rubber cylinder and a santoprene cylinder, respectively, both with a conical end-piece. With increasing flow velocity: (●) pre-instability; (■) flutter; (▲) static divergence; and (×) with decreasing flow velocity. (c,d) The corresponding Morse wavelet scalograms for the frequency of oscillation. 75

3.11 Dynamics of cylinder IV-C just after the onset of flutter at $u = 0.65$ ($U = 0.7$ m/s) illustrated by means of (a) polar plot, (b) position-triggered Poincaré map, (c) time traces of the front and top displacements, (d) PSD of motions, (e,f) phase portraits of the top and front displacements, respectively. 76

3.12 Summary of the results showing the critical flow velocities for instabilities. Blue (the shorter) and red (the taller) columns at each case, correspond to the onset of flutter and static divergence, respectively. 77

3.13 Graphical illustration of the qualitative dynamics observed with increasing flow velocity: the cylinder is subjected to flutter, followed by an abrupt static divergence. 81

4.1 (a) Schematic view of the system under consideration; Q_a denotes the additional volume of the fluid into the tank to modify the U_o/U_i ratio; (b) the SMRI/PRCI apparatus with a dual-camera system used to track the motion of the pipe tip. 95

4.2 Bifurcation diagrams showing the static and rms amplitude of oscillations versus the internal flow velocity, U_i, for $r_{ann} \simeq 1/4$ and (a) $U_o/U_i = 0.055$; (b) $U_o/U_i = 0.1$; (c) $U_o/U_i = 0.2$; (d) $U_o/U_i = 0.4$; (e) $U_o/U_i = 0.6$; (f) $U_o/U_i = 0.8$. 99

4.3 PSD plots for $U_o/U_i = 0.055$ and $r_{ann} \simeq 1/4$ at (a) $U_i = 5.68$ m/s; (b) $U_i = 6.16$ m/s; (c) $U_i = 6.63$ m/s; (d) $U_i = 7.10$ m/s. 101

4.4 (a) Time series for $U_o/U_i = 0.055$ and $r_{ann} \simeq 1/4$ at $U_i = 6.63$ m/s; (b) polar plot; (c)-(e) phase portraits of the front, side and combined displacements, respectively; (f) Poincaré map of the oscillation. 103

4.5 Impacting behaviour for $U_o/U_i = 0.2$ and $r_{ann} \simeq 1/4$, illustrated by means of polar plots and PSDs, at (a) and (b) $U_i = 4.42$ m/s; (c) and (d) $U_i = 6.32$ m/s; (e) and (f) $U_i = 7.26$ m/s. 104

4.6 (a) Time series at $U_i = 1.74$ m/s for $U_o/U_i = 0.6$ and $r_{ann} \simeq 1/4$; (b) PSD; (c) polar plot; (d) Poincaré map; (e) PDF of front displacement; (f) PDF of side displacement. 105

4.7 Bifurcation diagrams showing the static and rms amplitude of oscillations versus the internal flow velocity, U_i, for $r_{ann} \simeq 1/2$ and (a) $U_o/U_i = 0.055$; (b) $U_o/U_i = 0.1$; (c) $U_o/U_i = 0.2$; (d) $U_o/U_i = 0.4$; (e) $U_o/U_i = 0.6$; (f) $U_o/U_i = 0.8$.107

4.8 PSD plots for $U_o/U_i = 0.055$ and $r_{ann} \simeq 1/2$ at (a) $U_i = 5.21$ m/s; (b) $U_i = 6.16$ m/s; (c) $U_i = 6.63$ m/s; (d) $U_i = 7.10$ m/s; (e) $U_i = 7.58$ m/s; (f) $U_i = 8.05$ m/s. 108

4.9 High frequency oscillations for $U_o/U_i = 0.4$ and $r_{ann} \simeq 1/2$ shown by means of polar plots and PSDs at high flow velocities: (a) and (b) $U_i = 2.08$ m/s; (c) and (d) $U_i = 2.34$ m/s; (e) and (f) $U_i = 2.59$ m/s. 109

4.10 Bifurcation diagrams showing the static and rms amplitude of oscillations versus the internal flow velocity, U_i, for $r_{ann} \simeq 3/4$ and (a) $U_o/U_i = 0.055$; (b) $U_o/U_i = 0.1$; (c) $U_o/U_i = 0.2$; (d) $U_o/U_i = 0.4$; (e) $U_o/U_i = 0.6$; (f) $U_o/U_i = 0.8$.111

4.11 PSD plots for $U_o/U_i = 0.055$ and $r_{ann} \simeq 3/4$ at (a) $U_i = 4.47$ m/s; (b) $U_i = 5.21$ m/s; (c) $U_i = 5.68$ m/s; (d) $U_i = 6.16$ m/s; (e) $U_i = 6.63$ m/s; (f) $U_i = 7.10$ m/s. 112

4.12 (a) Polar plot of the system at $U_i = 9.95$ m/s for $U_o/U_i = 0.055$ and $r_{ann} \simeq 3/4$; (b) PSD; (c) PDF of front displacement; (d) PDF of side displacement. 113

4.13 Dynamical behaviour of the system for $U_o/U_i = 0.2$ and $r_{ann} \simeq 3/4$ illustrated by means of polar plots and PSDs, at (a) and (b) $U_i = 1.58$ m/s; (c) and (d) $U_i = 1.89$ m/s; (e) and (f) $U_i = 2.84$ m/s. 115
4.14 Dynamical behaviour of the system for $U_o/U_i = 0.6$ and $r_{ann} \simeq 3/4$ right after the pipe started lightly touching the annulus, at $U_i = 0.47$ m/s, (a) polar plot; (b) PSD. 116

5.1 Schematic view of the SMRI-PRCI apparatus and the synchronized dual-camera system. Internal flow with velocity U_i, and the flow in the surrounding annular region with velocity U_o, as well as parameters related to the geometry are shown in the zoomed view. Q_a denotes the additional fluid entering the pressure vessel to achieve higher values of U_o/U_i. Approximate size of the pressure vessel: 0.5 m in diameter; 1 m in height. 129
5.2 Schematic plot depicting (a) the placement of a flow-constricting rigid ring of inner diameter D_{ir} at the inlet (lower end) of the outer rigid tube and the cross-sectional view showing the pipe, the rigid ring and the outer rigid tube; (b) the placement of the rigid ring at the outlet (top end) of the outer rigid tube; (c) elevation and cross-sectional views of the off-centre placement of the outer rigid tube with respect to the central pipe; e denotes the eccentricity. 131
5.3 Bifurcation diagrams showing the rms amplitude of total displacement and the mean deflection versus u_i for interdependent internal and external flows (Q_a =0) and (a) $\alpha_{ch} = 3.37$ (D_{ch}=54 mm and U_o/U_i =0.015); (b) $\alpha_{ch} = 1.97$ (D_{ch} =31.5 mm and U_o/U_i=0.055). Rms amplitude: (●) pre-instability, (■) instability, (▲) impact; (×) mean deflection; (∗) critical flow for instability. . 134
5.4 (a) Morse wavelet scalogram in which the vertical strips indicate values of the internal flow velocity; (b) variation of the largest Lyapunov exponent of the front (●) and side (■) displacement time series as a function of internal flow velocity. 136

5.5 Dynamics of the system at $u_i = 5.63$ ($U_i = 6.16$ m/s) for the wider outer rigid tube ($\alpha_{ch} = 3.37$), with interdependent internal and external flows ($U_o/U_i = 0.015$) and the parameters given in Section 5.4.1 by means of (a) time traces; (b) front versus side displacement; (c) pseudo-phase space of the combined displacement; (d) PDF of the combined displacement; (e) Poincaré map; (f) autocorrelation of the combined displacement. 137
5.6 Bifurcation diagrams showing the rms amplitude of total displacement and the mean deflection as a function of u_i for independent internal and external flows ($Q_a \neq 0$). For the wider annulus, $\alpha_{ch} = 3.37$ (D_{ch}=54 mm): (a) $U_o/U_i = 0.2$; (c) 0.4; (e) 0.8. For the narrower annulus, $\alpha_{ch} = 1.97$ (D_{ch} =31.5 mm): (b) $U_o/U_i = 0.2$; (d) 0.4; (f) 0.8. Rms amplitude: (●) pre-instability, (■) instability, (▲) impact; (×) mean deflection; (∗) critical flow for instability. . 139
5.7 Morse wavelet scalogram in which the vertical strips indicate values of the internal flow velocity for $\alpha_{ch} = 3.37$ and U_o/U_i = (a) 0.2, (b) 0.4, and (c) 0.8. (d) Variation of the largest Lyapunov exponent of the front and side displacement time series versus u_i for $\alpha_{ch} = 3.37$ and $U_o/U_i = 0.2$: front (■) and side (+); $U_o/U_i = 0.4$: front (●) and side (×); $U_o/U_i = 0.8$: front (♦) and side (∗). 140
5.8 Bifurcation diagrams showing the rms amplitude of total displacements as a function of (a) u_i; (b) u_o; for pipe B ($\varepsilon = 13.81$) and U_o/U_i= 0.015: (●); 0.2: (■); 0.4: (▲); 0.8: ♦; (∗) critical flow for instability. 143
5.9 Bifurcation diagrams showing the rms amplitude of total displacement and the mean deflection versus u_i for investigating the effect of placement of an obstruction at the inlet of the outer rigid tube for pipe A with α_{ch} = 3.37 (D_{ch}=54 mm). (a) Interdependent internal and external flows (Q_a =0, U_o/U_i =0.015); (b) U_o/U_i=0.4. Filled markers show the rms amplitude and hollow markers show the mean static deflection: $\bar{g}_r$ =1 (no ring): (●), $\bar{g}_r$ =0.66: (■), $\bar{g}_r$ =0.42: (▲), $\bar{g}_r$ =0.24: (♦). 145

5.10 Bifurcation diagrams showing the rms amplitude of total displacement and the mean deflection versus u_i for investigating the effect of placement of an obstruction at the outlet of the outer rigid tube for pipe A with α_{ch} = 3.37 (D_{ch}=54 mm) and (a) interdependent internal and external flows (Q_a =0, U_o/U_i =0.015); (b) U_o/U_i=0.4. Rms amplitude: (●) pre-instability and no ring, (◆) pre-instability and $\bar{g}_r$ =0.05, (■) instability and no ring, (▶) instability and $\bar{g}_r$ =0.05, (▲) impact and no ring, (◊) data points for $\bar{g}_r$ = 0.10; (×) mean deflection and no ring, (+) mean deflection for the cases with a ring; (∗) critical flow for instability. 146
5.11 Bifurcation diagrams showing the rms amplitude of total displacements and the mean deflection versus u_i for the pipe C and, (a) interdependent internal and external flows (U_o/U_i=0.033); (b) independent internal and external flows (U_o/U_i =0.4). Rms amplitude: (●) pre-instability, (■) instability, (▲) impact; (×) mean deflection; (∗) critical flow for instability. 147
5.12 Bifurcation diagram presenting the rms amplitude of total displacements and the mean deflection as a function of u_i showing the effect of eccentricity for pipe A, U_o/U_i= 0.015. (●) Rms amplitude and (○) mean deflection for concentric system. (■) Rms amplitude and (□) mean deflection for $\bar{e}$ = 0.208. (▲) Rms amplitude and (△) mean deflection for $\bar{e}$ = 0.416. (◆) Rms amplitude and (◊) mean deflection for $\bar{e}$ = 0.727. 150
5.13 Bifurcation diagrams showing the rms amplitude of total displacements as a function of u_i for the eccentrically located pipe A, $\bar{e}$ = 0.416 and (a) U_o/U_i =0.2; (b) U_o/U_i =0.8. Rms amplitude: (●) pre-instability, (■) instability, (▲) impact; (×) mean deflection; (∗) critical flow for instability. . . 150

6.1 Formation of salt caverns: site selection, leaching salt deposit through fresh water injection, forming a cavern filled with brine, brine removal through gas or liquid injection in order to store hydrocarbons therein (after Liu et al. [3]). For a clearer viewing, please refer to the coloured online version. 164

6.2 Schematic view of the system under consideration: (a) a brine-string in a typical solution-mined cavern; (b) an idealized model of the product retrieval operation. For a clearer viewing, please refer to the coloured online version. . 165

6.3 Brine string damage (after Ratigan [1]): (a) in a gas storage well; (b) in a liquid storage cavern. 165

6.4 Schematic views showing (a) forces acting on an element δx of the deformed pipe; (b) forces acting on an element δx of the internally flowing fluid; (c) forces acting on an element δx of the externally flowing fluid; (d) forces acting on an annular fluid element of length δx. 171

6.5 A typical Argand diagram for the system parameters associated with the bench-top-scale system with $r_{ann} \simeq 1/2$, given in Section 6.3.1.1 undergoing second mode flutter at $u_i = 6.44$. Mode 1 (○), Mode 2 (□), Mode 3 (△), Mode 4 (◇). 183

6.6 Variation of $u_{i,cr}/\varepsilon$ with increasing ε for the system parameters as in Section 6.3.1.2 with $r_{ann} = 0.85$ and $\alpha_{ch} = 1.676$. 186

6.7 Argand diagram for system B, defined in Section 6.3.2, in which the two fluids in the cavern are: (a) brine-propane (greatest r_{if}); (b) brine-brine. The first one undergoes static divergence in the second mode at $u_i = 44.10$, and the second static divergence in the first mode at $u_i = 60.07$. Mode 1 (○), Mode 2 (□), Mode 3 (△), Mode 4 (◇). 187

6.8 Argand diagram for (a) Case I with $C_N = 0.5C_T = 0.0125$ and the greatest r_{if} subject to static divergence in the first mode at $u_i = 11.91$; (b) Case IV with $C_N = 0.5C_T = 0.0125$ and the moderate r_{if} subject to flutter in the fourth mode at $u_i = 15.12$. Mode 1 (○), Mode 2 (□), Mode 3 (△), Mode 4 (◇). . . . 190

6.9 Variation of $u_{i,cr}$ with the annular gap confinement, $\alpha_{ch} = D_{ch}/D_o$. To achieve various values of α_{ch}, the parameter that is varied is the diameter of the outer casing, D_{ch}, while the remaining parameters are as in B-brine-propane system defined in Section 6.3.2 192

6.10 Variation of $u_{i,cr}$ with the annular confinement length, $r_{ann} = L'/L$. To achieve various values of r_{ann}, the parameter that is varied is the length of the outer casing, L', while the remaining parameters are as in the B-brine-propane system defined in Section 6.3.2. 193

6.11 Variation of $u_{i,cr}/\varepsilon$ with the brine-string slenderness, $\varepsilon = L/D_o$. To achieve various values of ε, the parameter that is varied is the brine-string length, L, while the remaining parameters are as in B-brine-propane system introduced in Section 6.3.2 194

CHAPTER 1

Introduction

1.1 Introduction, motivation and general remarks

When the leaves of trees reconfigure and flutter in the wind, a heart beats, airplane wings oscillate, or a fish swims, the motions of a structure and the surrounding fluid are coupled; this is known as Fluid-Structure Interaction (FSI). FSI involves the deformation of a structure caused by fluid forces, which, in turn, influences the fluid forces. The dynamics of slender structures in contact with fluid, mainly cylindrical ones, namely cylinders subjected to internal flow (pipes conveying fluid), external axial flow, and simultaneous internal and external axial flows, have been studied quite extensively.

Not only do slender structures in contact with fluids arise in nature, but they also have numerous practical applications. Industrial examples include pipelines, heat-exchangers, nuclear reactor fuel elements, towed slender ships, and renewable energy harvesters. Physiological instances of slender structures interacting with axial flow can be observed in blood vessels and urinary tracts. Apart from many practical applications, studies on the dynamics of these systems are often curiosity driven and fundamental [6, 7]. The rich dynamical behaviour that slender cantilevered cylinders subjected to internal and/or external axial flows display, as well as their presence in many engineering systems, serves as the driving force behind this manuscript-based thesis [1–5].

While certain flow-induced vibrations (FIV), such as those utilized in creating music with woodwind instruments, propulsion of watercraft [8, 9], or energy harvesters [10], are desirable, many others are undesirable and potentially dangerous [11]. This necessitates the study of FIV in slender structures because beyond a critical flow velocity, these structures undergo instability, which may lead to catastrophic failure. These instabilities are associated with Movement-Induced Vibrations (MIV), where the excitation arises from movements of the structure [12]. Flutter, a dynamic instability, and divergence, a static instability, are examples of MIV.

Pipes conveying fluid is a canonical FSI problem that has been studied extensively, with research dating as far back as 1939 [13]. Applications of this system include Ocean Thermal Energy Conversion (OTEC) [14], soft robots [15], renewable energy systems [16], ultra-sensitive nanosensors [17], and long pipes used in ocean mining operations [18] as shown in Fig. 1.1. The dynamical behaviour of the system of a pipe conveying fluid is very rich and it provides a simple experimental and theoretical framework for better understanding and explaining known dynamic behaviours and exploring new dynamical characteristics, thus becoming a paradigm in the field of dynamics [6, 19]. The primary reason for the extensive attention paid by researchers to the dynamics of this system is its capacity to exhibit a diverse range of dynamic behaviuors, despite being relatively simple to analyze and easy to realize physically. For instance, a pipe with both ends supported becomes unstable via static divergence (buckling) at high-enough flow rates; since it is a gyroscopic conservative system, it cannot flutter [20]. A cantilevered pipe, on the other hand, is a nonconservative system and is subject to an oscillatory instability, i.e. flutter, at sufficiently high flow velocities [21–23]. The complexity of the dynamics of fluid-conveying cantilevered pipes increases when a mass is attached to its free end [24], or when its motion is restricted by motion-restraining constraints [25]; in these cases, the existence of chaotic regions has been demonstrated.

Another canonical FSI problem involves the dynamics and stability of slender flexible cylindrical structures under external axial flow, although have been extensively investigated since the 1960s. Fluid-elastic instability in this system often occurs at flow velocities higher than those typically encountered in usual engineering applications. Consequently, research on flow-induced vibrations of cylinders in axial flow, similar to studies on fluid-conveying pipes, has been primarily driven by curiosity, while some studies have been application-oriented [26]. Examples of industrial applications of this system include heat-exchanger and nuclear reactor internals, often configured as clusters of cylinders. In such arrangements, the critical flow velocity for instability can be significantly lower than that for an isolated cylinder, potentially leading to undesirable FIV at flow velocities that are common under normal

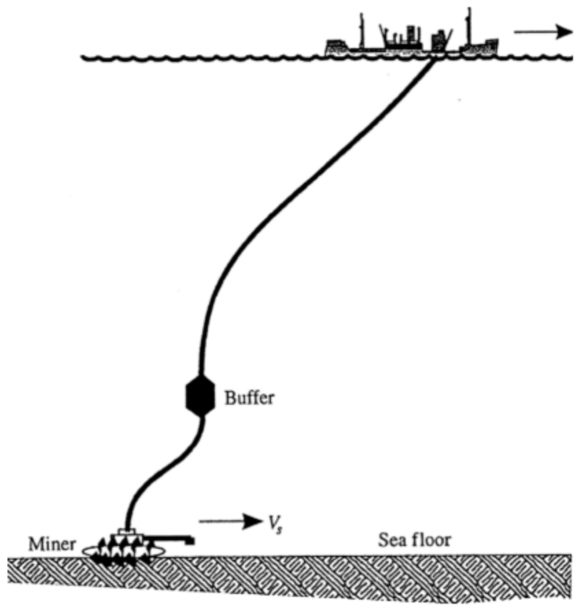

Figure 1.1: A long aspirating pipe utilized in ocean mining operations to extract manganese nodules or diamonds from the seabed, after Ref. [18].

operating conditions. Slender cylindrical structures in axial flow may also be found in the transportation industry, particularly trains, as well as quasi-cylindrical containers towed by ships, e.g. the "Dracone", and towed seismic arrays.

The "Dracone", shown in Fig. 1.2, is a flexible sausage-shaped container that is towed, mostly submerged, behind a small watercraft and is used for transporting lighter-than-seawater fluids, including fresh water, by sea. The towed seismic arrays, shown in Fig. 1.3, consist of very long cylindrical structures aligned in parallel, partially or fully immersed in seawater, and pulled by a watercraft across the sea-surface. These arrays are used in sonar applications, in order to detect submarines, schools of fish, and underwater mineral resources [27]. Equipped with sonar sensors, these arrays capture acoustic signals reflected from the seabed layers. Analysis of these sonar signals enables the identification of resources such as oil or gas deposits within the seabed.

The scope of the present thesis primarily involves investigating the dynamics of slender cantilevered cylinders subjected to counter-current internal and external axial flows. This may be considered as curiosity-driven research; yet a strong motivation for this study stems from its industrial applications. A cantilevered pipe simultaneously subjected to counter-

Figure 1.2: A 500 m^3 Dracone, air-inflated after discharging fresh-water cargo, leaving the island of Santorini, Greece (Dunlop Dracones 1965), after Ref. [27].

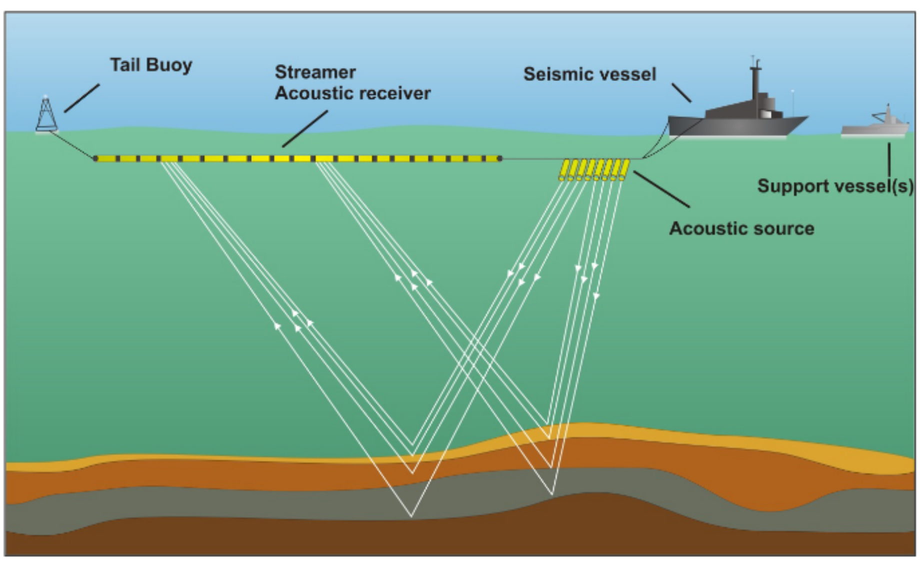

Figure 1.3: A schematic view of a typical seismic array survey, after Ref. [28].

(a) (b)

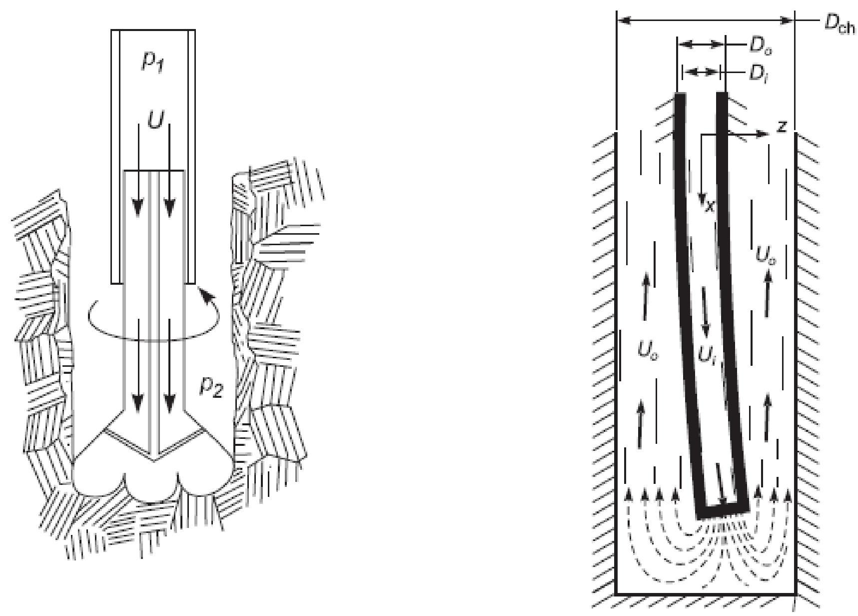

Figure 1.4: (a) Schematic view of a typical drill-string with its internal flow-powered rotating drill bit, from [30]; (b) An idealized drill string, with the drill bit entirely disregarded. The system can be modelled as a hanging fluid-discharging cantilevered pipe, in which the fluid upon exiting the pipe flows upwards as a confined axial flow [31].

current internal and external axial flows is an idealized model for engineering systems, such as tubes in parallel-flow tubular heat-exchangers [29], the drill-string with a floating fluid-powered drill-bit [30, 31] (neglecting the drill-bit, as shown in Fig. 1.4(b)), and brine-strings in salt-mined caverns.

Salt-mined caverns are formed through the process of drilling a well into underground salt deposits, followed by leaching the salt using fresh water pumped down through a very long vertical cantilevered pipe, known as the "brine-string", which is typically 1-2 km in length and extends from the surface to near the base of the cavern. The injected fresh water dissolves the minerals, resulting in brine. Then, by injecting additional fresh water, the brine is brought to the surface through a shorter concentric annular region contained by a rigid outer "casing". The outer casing is cemented onto the overburden and caprock, with a small portion of it extending into the cavern; thus, a significant portion of the brine-string extends beyond the casing enclosure [32]. Hence, the brine-string (hanging cantilevered pipe) is sub-

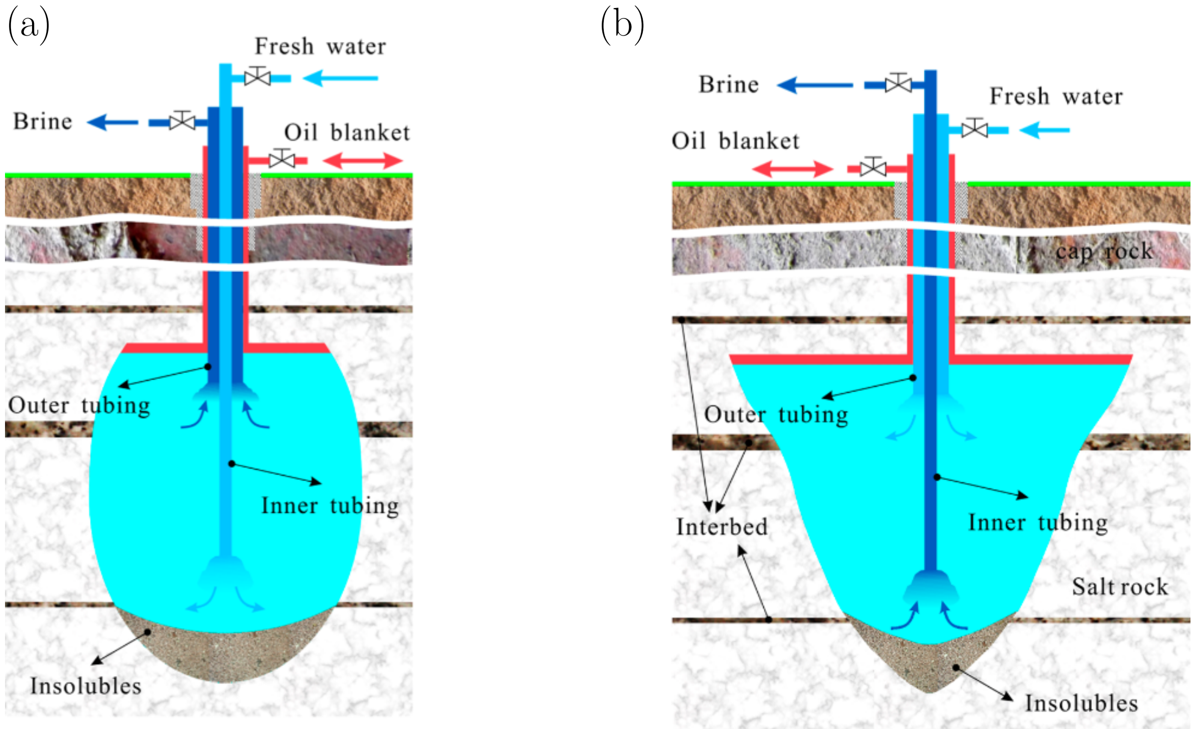

Figure 1.5: Schematic view of the formation of salt-mined caverns formed by pumping fresh water downwards: (a) through a vertical pipe, the "brine-string", and brine flowing upwards through a shorter concentric annular region formed by a rigid "casing" surrounding the pipe at its upper portion, a flow configuration that favours expansion of the lower part of the cavern; (b) through the outer casing, with brine flowing upwards through the aspirating brine-string, a flow configuration that favours the expansion of the upper part of the cavern; from Ref. [33]

jected to counter-current internal and external axial flows, with the external flow partially confined over the upper portion of the pipe, as shown in Fig. 1.5(a). This process leaves behind a huge underground cavern filled with brine. It is also possible to form the caverns via the opposite flow configuration: the outer casing discharges the fresh water downwards, and the brine flows upwards through the brine-string, as shown in Fig. 1.5(b). The selection of which flow configuration to implement is generally determined by the desired cavern shape [33], as detailed in the caption of Fig. 1.5.

Salt-mined caverns, as shown in Figs. 1.6 and 1.7(a), can be utilized for storage and subsequent retrieval of lighter-than-brine liquid and gaseous "products" [32, 34], including hydrocarbons, such as crude oil, propane, natural gas and ethylene. Additionally, salt-mined

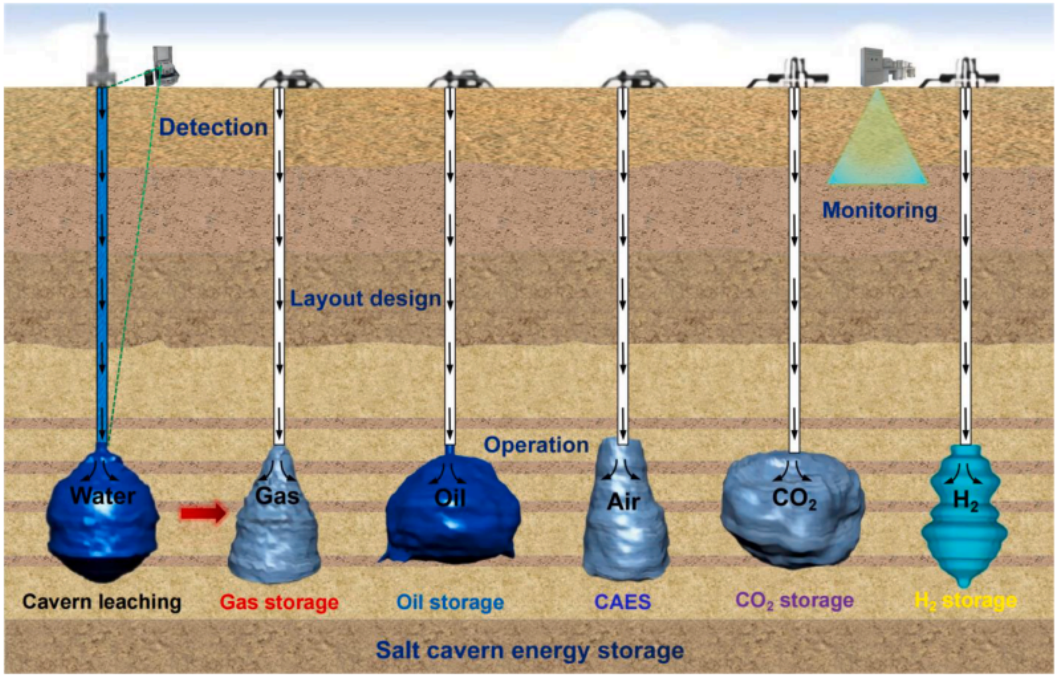

Figure 1.6: Various utilizations of salt-mined caverns, after [35].

caverns can serve as storage facilities for hydrogen gas, carbon-dioxide or compressed air in Compressed Air Energy Storage (CAES) plants [35]. In particular, CAESs assist in managing and regulating energy consumption for peak shaving and valley filling in renewable energy facilities, helping to cope with the intermittency and fluctuations in energy generated from such sources [35].

Solution-mined caverns can be utilized in two different operational modes: the "storage" and the "production" or "retrieval" modes, which involves two different flow configurations [34, 36], the same configurations as those illustrated in Fig. 1.5. The retrieval *modus operandi*, which is shown schematically in Fig. 1.7(b) is the primary focus of this thesis. In the retrieval mode, brine is injected into the brine-string, while the lighter-than-brine (hydrocarbon) product is extracted through the outer casing for sale during commercially propitious times. Therefore, a fluid-discharging cantilevered flexible pipe subjected to a partially-confined reverse annular flow through the upper portion of the pipe, with the whole system within a container, serves as an idealized model for this mode of operation. In this retrieval mode, achieving the highest possible extraction flow rate is advantageous. How-

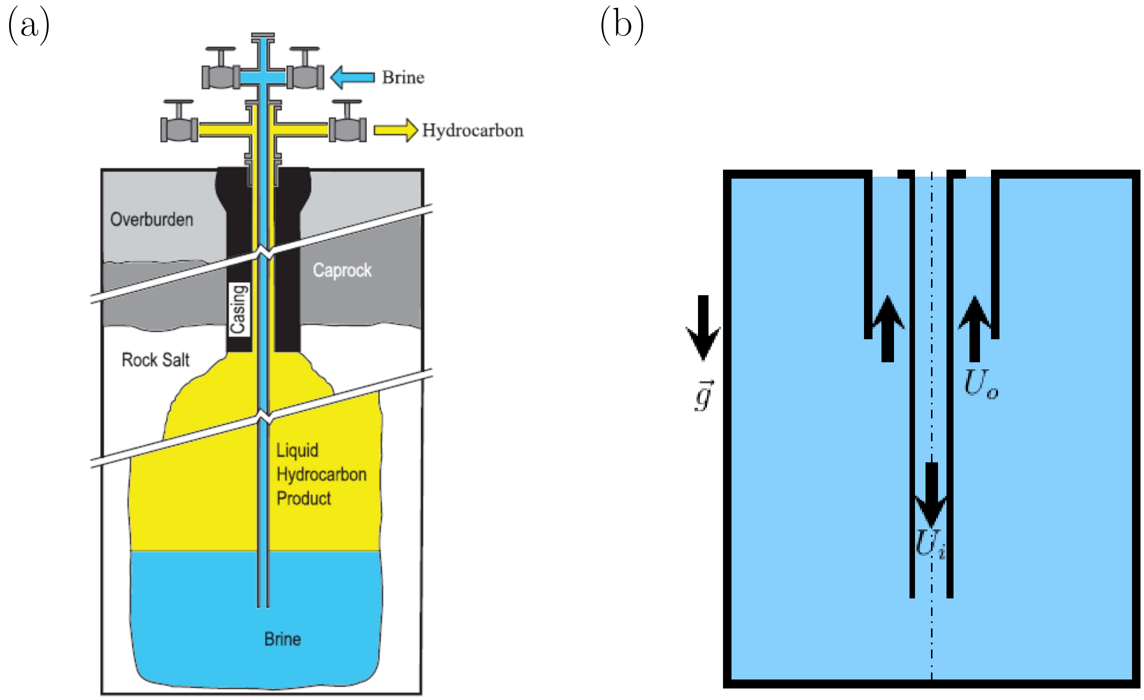

Figure 1.7: (a) Schematic view of a salt-mined cavern in hydrocarbon storage applications, after [36]; (b) an idealized brine-string in retrieval mode modelled as a hanging fluid-discharging cantilevered pipe subjected to a partially confined external axial flow.

ever, operating at high extraction rates poses a challenge: the potential for the brine-string to undergo fluid-elastic instability at high flow velocities.

The repercussions of operating solution-mined caverns at flow velocities beyond the critical for fluid-elastic instabilities are severe, potentially resulting in impacting of the brine-string on the rigid casing. In extreme circumstances, the brine-string could suffer damage or even fracture from repeated impacts. Engineers have struggled with the challenge of mitigating flow-induced vibrations and suppressing fluid-elastic instabilities in brine-strings for many years, as these phenomena have been identified as likely causes of breakages or permanent deformations of brine-strings. In particular, once flutter is initiated, the amplitude of the oscillation of the brine-string results in repeated impacts on the outer casing. This can cause fretting wear and potential breakage of the brine-string, with parts of the brine-string falling to the bottom of the cavern. If the brine-string develops static divergence (buckling) rather than flutter, similar consequences may result. The brine-string intermittently contacts the outer casing, shifting from one side to the other. Alternatively, in cases of "sticking", the buckled brine-string "chatters" against the outer casing, leading to fretting wear and potential damage. These incidents result in significant financial and environmental damages. Consequently, research efforts are aimed at understanding the dynamics of brine-strings, so as to prevent catastrophic accidents and determine safe ranges of flow velocities in the brine-string, ensuring stability of the system [4, 9].

1.2 Literature review

The literature on the dynamics of cylinders subjected to internal, external, and simultaneous internal and external axial flows is very extensive. In this section, a selective, rather than all-inclusive review is provided. Therefore, this review targets highlighting the fundamental and the most important theoretical and experimental studies addressing the dynamics of pipes conveying fluid, cylinders in axial flow, and pipes subjected to simultaneous internal and external axial flows. The interested reader is referred to Refs. [6, 9, 26, 27] for a comprehensive discussion of studies on the dynamics of slender structures in axial flow.

1.2.1 Pipes conveying fluid

The dynamics of a pipe conveying fluid has extensively attracted scholars' attention and is referred to as a paradigm in dynamics [6, 19], as most of the so-called fluid-elastic instabilities can be illustrated with this system. This system, despite being relatively simple to analyse and easy to realize physically, displays a rich dynamical behaviour. Understanding the FSI in pipes conveying fluids is essential, not only to avoid catastrophic accidents in piping systems [11], but also to enable understanding of the dynamical behaviour of more complex systems.

The first study on the dynamics of pipes conveying fluid is attributed to Bourrières [13], who derived a general nonlinear equation of motion of a cantilevered pipe and conducted experiments regarding the stability of the system. Studies on the dynamics of pipes conveying fluid were continued by Ashley and Haviland [37], Housner [38], Feodos'ev [39] and Niordson [40] for simply-supported pipes. Also, different boundary conditions were considered in Refs. [41, 42].

Almost ten years later, the dynamics of a cantilevered articulated pipe made of N rigid and flexibly interconnected pipes was studied both theoretically and experimentally by Benjamin [21, 43]; for N tending to infinity, the case of a continuous system would be approached. Among its many achievements, formulating the appropriate form of the Lagrange equation was the most significant for the aforementioned system, involving an energy transfer from the fluid to the pipe. It was shown that, at sufficiently high flow velocities, the system undergoes oscillatory instability. In addition, in the case of a vertically hung articulated pipe conveying water, buckling was observed; for air-conveying pipes the static instability never materialized. Benjamin's work was followed by Gregory and Païdoussis [22]; the linear equation of motion was derived via a Newtonian approach. Using an exact method as well as an approximate one, the stability of a continuous tubular cantilever was examined. In Ref. [44] the flutter of a cantilevered pipe conveying fluid was observed for the first time, verifying the theoretical results in [22] and the flutter discussed by Benjamin [43].

Afterward, the dynamical behaviour of the articulated system of a cantilevered pipe conveying fluid was investigated by Païdoussis and Deksnis [45]; for an increasing number of articulations, N, it was demonstrated that, for the continuous system ($N \to \infty$) buckling never takes place, in contrast to the findings by Benjamin [21, 43] for the articulated system. Considering gravity forces, it was found by Païdoussis [46] that, in contrast to hanging tubular cantilevers, "standing" ones may buckle under their own weight; however, the flow directed from clamped to free end could stabilize the system within a range of flow velocities, prior to the occurrence of flutter at high enough flow.

Following the pioneering research carried out between 1950 and 1970 on the dynamics of fluid-conveying pipes, numerous researchers have explored several variations of this system, both theoretically and experimentally. This includes investigating the effect of added supports, masses, springs, as well as other modifications [47–53]. For the sake of brevity, these studies are not discussed here.

Stability of pipes subjected to either constant or harmonically time-varying flow velocity was studied theoretically by by Païdoussis and Issid [54]. In the former case, they concluded that, for pipes with supported ends, beyond a certain critical flow velocity, not only does buckling occur, but also at higher flow velocities flutter arises. This constitutes a paradox because, being a conservative system, pipes with supported ends are not expected to flutter.

Indeed, as shown by Holmes [20], the predicted coupled-mode flutter is associated with a an unstable, non-physical solution. In Ref. [54] the equation of motion was modified to model a harmonically perturbed flow velocity, obtaining a rich array of parametric resonance oscillations.

In the area of fluid-structure interaction, nonlinearity is important, and in many circumstances fundamental in the proper characterization of the phenomena. Extending some prior studies, e.g., that of Bourrières [13], a nonlinear theoretical model for simply supported pipes discharging fluid was obtained by Thurman and Mote Jr. [55]. In their work, it was demonstrated that the linear study of the problem is totally insufficient. New research was initiated on the dynamics of pipes conveying fluid, employing the modern nonlinear dynamics methods. The two-dimensional motion of a two-segment articulated pipe was investigated by Rousselet and Herrmann [56]. Krylov-Bogoliubov's method was used in order to solve the nonlinear equations of motion and the results highlighted the importance of taking nonlinearities into account.

Taking advantage of the center manifold theory, the onset of buckling and oscillatory instability of a pipe conveying flow was investigated by Holmes [57]. The nonlinear equation of motion was obtained, extending the linear one of Païdoussis and Issid [54] by including the terms due to the deflection-induced axial tensile forces. Thereafter, Holmes and Marsden [58] applied center manifold reduction to the problem of flow-induced vibrations. Hence, the governing PDE was locally replaced by a vector field. Moreover, Holmes and co-workers [20, 57, 58] demonstrated that a Hopf bifurcation is responsible for instability of cantilevered pipes conveying fluid at sufficiently high flow velocities. They also proved that the Païdoussis-type coupled-mode flutter in simply-supported pipes does not take place, contrary to the linear theory predictions of Païdoussis and Issid [54]. Bajaj et al. [23] proved that, depending on the system parameters, a sub- or supercritical Hopf bifurcation into a periodic motion arises in the case of a cantilevered pipe conveying fluid.

Extending the work in Ref. [56], a nonlinear equation of motion of a continuous cantilevered tubular beam was derived by Rousselet and Herrmann [59], using both energy and Newtonian approaches. The equation of motion of the fluid takes into account the pressure loss caused by the fluid flow in the pipe.

Considering nonlinear motion-restraining spring constraints, the fluid-elastic oscillation of a constrained cantilevered pipe was examined both theoretically and experimentally by Païdoussis and Moon [25], as first model to deal with a fluttering pipe impacting on surrounding walls. By means of analytical and numerical methods, the existence of chaotic regions was demonstrated. Research on the planar nonlinear dynamics and chaos of a pipe conveying fluid was conducted by Semler [60]. The core of his work was to derive the nonlinear equations of motion associated with either simply-supported or cantilevered pipes. Then, the PDEs were compared to existing derivations. Results indicated that chaotic motions may occur due to perturbations, or motion-limiting constraints.

The dynamics of a hanging pipe with a rigid end-mass was studied experimentally by Copeland and Moon [61]. It was found that the system generally follows a quasi-periodic route to chaos. Nonlinear dynamics and chaos of constrained cantilevers were investigated further by Païdoussis and Semler [62]. In Semler et al. [63] it was demonstrated that their proposed PDEs for pipes with both ends fixed are the most accurate and complete. In Semler and Païdoussis [64] the nonlinear dynamics of a pipe with a mass defect at the free end was investigated, showing that, for this system, chaos may arise via the intermittency route.

Making use of the proper orthogonal decomposition method, a reduced-order model was established in Sarkar and Païdoussis [65] to investigate the 2-D nonlinear dynamics of a cantilevered pipe conveying fluid.

In a three-part study, the 3-D nonlinear dynamics of cantilevered pipes conveying fluid was examined by Païdoussis and co-workers. Firstly, modifying the nonlinear equation of motion of Semler et al. [63], the three-dimensional nonlinear dynamics of unrestrained and restrained cantilevered tubular beams was studied by Wadham-Gagnon et al. [66]. This study was then extended by Païdoussis et al. [67] to investigate the dynamics of the same system modified by arrays of two or four springs or one spring located at a specific distance from the clamped end. Finally, Modarres-Sadeghi et al. [24] studied the 3-D nonlinear dynamics of a cantilevered pipe with a lumped mass mounted at the free end of the pipe.

Later on, research on the two- and three-dimensional dynamics of cantilevered pipes was undertaken by Modarres-Sadeghi et al. [68] to investigate the post-flutter dynamics of both horizontal and vertical pipes by increasing the flow velocity beyond the Hopf bifurcation. It was found that the post-flutter dynamics of the system depends on the mass parameter. See also Wang et al. [69] and Duan et al. [70].

Pipes commonly used in real-world applications often suffer geometric imperfections, including a curved shape. As discussed by Païdoussis [6], many experimental studies have unintentionally employed slightly curved pipes, particularly in earlier research. For example, in the study by Bishop and Fawzy [71], surgical-grade silicone rubber pipes with slight initial bending were utilized. Prior to the onset of instability, a static deformation of the pipe was observed. This led to the conclusion that the reason for the inconsistency between the onset of instability observed in the experiments and that predicted by theoretical models for a perfectly straight pipe is the absence of straightness and the residual internal stress in the imperfect pipes. Using extensible and inextensible centreline theoretical models, Misra et al. [72, 73] examined the dynamics of curved pipes with supported ends. It was shown that inextensible centreline theory leads to the wrong conclusion that semi-circular pipes conveying fluid develop buckling. This wrong conclusion is due to neglecting the effect of steady-state forces; however, this effect was taken into account in the extensible theory of Misra et al. [73]. The dynamics of cantilevered pipes conveying fluid subjected to different slightly curved shapes was studied by Zhou et al. [74]. The conclusion drawn was that as the flow velocity increases, the initial curvature of the pipe undergoes a significant amplification. Ultimately, as flow rates reach a sufficiently high level, the pipe undergoes an oscillatory instability. The onset of this instability depends on the static equilibrium position of the pipe just before reaching the threshold of fluid-elastic instability. Zhou et al. [75] investigated the free and forced vibration of L-shaped pipes. The findings revealed that this system experiences significant static deformation before the initiation of self-excited limit-cycle oscillations. Moreover, under forced vibrations, period-n, quasi-periodic, and chaotic motions were obtained, with variations depending on the flow velocity as well as the amplitude and frequency of the excitation force.

Flow-induced oscillation of a cantilevered pipe conveying fluid with an inclined end-nozzle was studied both theoretically and experimentally by Lundgren et al. [76]. They obtained a group of integro-differential equations for the system, and an oscillatory instability was predicted beyond a critical flow rate, either in the plane of static deformation or normal to it, depending on the system parameters. The bifurcations of fluid-conveying cantilevered tubular beams with an end-nozzle were also examined by Jian and Yuying [77].

Later on, the dynamics of cantilevered pipes conveying fluid was studied by Rinaldi and Païdoussis [78], both experimentally and theoretically for pipes fitted with a "stabilizing end-piece". For a straight-through axial discharge, the system was found to lose stability via a Hopf bifurcation, but for radial discharge the system remains stable over the entire range of the considered flow rates.

Modifying the centrifugal force term in the equation of motion in Païdoussis and Issid [54], the effect of laminar and turbulent flow profiles was considered in Guo et al. [79]. For different so-called profile-modification factors, the critical flow velocity for the onset of divergence was found to be higher in the laminar flow regime.

Nonlinear interactions between unstable oscillatory modes in a cantilevered pipe conveying fluid was investigated by Yamashita et al. [80]. It was concluded that the instability of a cantilevered pipe in one mode can trigger instability in another mode, leading to a complex double Hopf bifurcation interaction. Zhou et al. [81] explored the planar and non-planar oscillations of a cantilevered pipe subjected to axial base excitation, concluding that, at supercritical flow rates, applying axial base excitation can mitigate instability for certain specific system parameters. The dynamics of pipes conveying fluid has been studied by many others. See for example Ni et al. [82], Dehrouyeh-Semnani et al.[83], Zhang et al. [84] and Gu et al. [85].

The dynamics of fluid-aspirating cantilevered pipes, in which fluid flows in the opposite direction to that of fluid-discharging cantilevered pipes (i.e., from the free end towards the clamped one), has been a subject of controversy in FSI [6]. Over the past years, since the 1960s, some theoretical studies have suggested that a pipe aspirating fluid does not undergo flutter, and some experimental studies have reported that this is so, at least within the range of examined flow velocities. This includes experiments conducted at the Chalk River Nuclear Laboratories and documented in [27], the study by Païdoussis [86], and more recently, by Hisamatsu and Utsunomiya [87]. Conversely, Païdoussis and Luu [88] have concluded that aspirating pipes are intrinsically unstable, suggesting that flutter occurs at relatively low, rather than vanishing, flow velocities, and the difference might be attributed to dissipation caused by friction with the surrounding fluid medium. Some studies, including those conducted by Kuiper and Metrikine [89, 90] and Païdoussis et al. [91], conclude that self-excited flutter does occur, but not at vanishing flow rates, but rather at sufficiently high flow rates. Upon reviewing the literature, one might conclude that perhaps pipes aspirating fluid do indeed flutter at sufficiently high flow rates, but in the experiments flutter tends to be of a weak and anaemic nature [9, 92–95].

While conducting experiments with very thin elastomer vertical cantilevered pipes, which would normally expected to lose stability by flexural, beam-like dynamical instability, shell-mode flutter was observed by Païdoussis and Denise [96]. This finding revealed another aspect of the problem. Employing shell models, stability of the thin pipes conveying fluid was studied by Païdoussis and Denise [97]. They found that both clamped-clamped and cantilevered finite-length circular cylindrical shells, lose stability by flutter in their second circumferential mode provided that the flow velocity, surpasses a certain critical value. Applying Galerkin-type solutions, a so-called "standing wave analysis" was conducted by Weaver and Unny [98] and Weaver and Myklatun [99] for simply supported and clamped-clamped shells, respectively. Beam and shell mode instabilities were also investigated in Shayo and Ellen [100]. However, shell-mode instabilities are not the of interest in the present study. For more details, the interested reader is referred to Refs. [6, 101].

1.2.2 Cylinders in axial flow

Although the dynamics of cylinders in axial flow is of interest for its industrial applications, e.g., in heat-exchangers, nuclear reactor fuel element bundles and steam generators, some studies on this topic have also been "curiosity driven" [7]. From a historical point of view, Hawthorne [102] was the first to study the stability of a "Dracone", or generally towed cylinders in axial flow. Païdoussis [103, 104] extended and generalized that work for different boundary conditions and did experiments to validate the analysis. Later on, in Païdoussis [105], the dynamics of towed totally submerged cylinders was examined. However, the most accurate linear model for a slender cylinder in axial flow was established by Païdoussis [106] in which an error caused by incorrect incorporation of the viscous forces into the equation of motion in Païdoussis [103] was corrected. Moreover, the stability of a cluster of identical cylinders was also investigated. Unfortunately, use of the incorrect version of the model by other researchers resulted in erroneous conclusions, as discussed by de Langre et al. [107].

The critical flow velocity for the onset of divergence of pinned-free cylinders in axial flow was determined analytically by Triantafyllou and Chryssostomidis [108]. Modelling the cylinder as a string, rather than a beam, stability analysis of a very long cylinder was examined by Triantafyllou and Chryssostomidis [109].

Further studies were conducted by Chen [110], Païdoussis [111], Gagnon and Païdoussis [112, 113], and more recently by Wang et al. [114], on the dynamics of clustered cylinders in axial flow. Additionally, to study the case of a cylinder in highly confined annular flow, some modifications in the modelling have been made by Païdoussis et al. [115] and Mateescu et al. [116–118].

Because of applications in oil exploration, a number of studies on the dynamics of very long arrays of several towed cylinders have been conducted, by Païdoussis [46], Païdoussis and Yu [119], Dowling [120, 121], and Triantafyllou and Chryssostomidis [122]. More recently, using a modified linear theory, the stability of towed cylinders was revisited by Kheiri and Païdoussis [123]. Later on, Kheiri et al. [124] derived the first nonlinear model for the dynamics of a towed flexible cylinder, and Kheiri et al. [125] conducted an experimental study on this system. It was concluded that, increasing the flow velocity, for a towed cylinder with more or less streamlined ends, rigid-body instability occurs first, followed by flexural instabilities at higher towing speeds. However, a blunt tail end-piece can eliminate all instabilities.

Post-divergence coupled-mode flutter has been observed in experiments by Païdoussis [104] for cylinders in axial flow. In contrast, as mentioned in the previous section, nonlinear theory proves that coupled-mode flutter never occurs in pipes conveying fluid with supported ends [20]. This is one of the most important differences when comparing the internal and external flow problems. From a nonlinear point of view, the dynamics of a cantilevered cylinder in axial flow was investigated by Païdoussis and co-workers. In Païdoussis et al. [126], the physical dynamics of the system was studied. It was concluded that the stability of cantilevered cylinders is greatly dependent on the shape of the free end. Generally, cantilevered cylinders lose stability by divergence at sufficiently high flow velocities and, at higher flow velocities, single-mode flutter occurs, provided that the free end is well-streamlined; but, if the free end is blunt, neither buckling nor flutter materializes. The second part of that study [127] is devoted to the derivation of the nonlinear equation of the motion and solution methods. Finally, Semler et al. [128] obtain solutions of the nonlinear problem and discuss the theoretical and experimental results.

Nonlinear dynamics of a cylinder with an extensible centerline subjected to axial flow was investigated by Modarres-Sadeghi [129]. For cylinders with both ends supported, the weakly nonlinear equations of motion were derived by Modarres-Sadeghi et al. [130]. The dynamics of the system was predicted to be as follows: as the flow velocity increased, a supercritical pitchfork bifurcation occurs, leading to divergence. Then, a secondary Hopf bifurcation which leads to flutter was predicted. At still higher flow velocities, the limit cycle was found to evolve into chaos. In Païdoussis et al. [131] it was demonstrated that, for a pinned-pinned cylinder in axial flow, post-divergence flutter does exist, as a Hopf bifurcation arising from the divergence solution. For the nonlinear dynamics of cylinders with both ends pinned or clamped, see also Refs. [132, 133]. More recently, using a linear model, for a pinned-free cylinder in axial flow, the critical flow velocity for the onset of divergence and also conditions for rigid body oscillations were determined by Kheiri and Païdoussis [134].

The first study on the dynamics of an inverted cantilevered cylinder in axial flow was carried out by Rinaldi and Païdoussis [135], i.e., with the flow directed from the free end toward the clamped one. At relatively low flow velocities, small-amplitude first-mode oscillations, which could be interpreted as flutter, were observed in the experiments with air flow. Increasing the flow velocity further, the oscillatory motion was diminished and a static divergence developed. In this experiment, the free end of the cylinder was fitted with end-pieces of different shapes. However, the only instability predicted by linear theory was buckling at sufficiently high flow velocities; also the onset of instability was overestimated as compared to the observations. Using the same parameters as in Ref. [135] and a nonlinear static analysis, the stability of inverted cylinders was examined by Sader et al. [136]. It was found that slender inverted cylinders are never globally unstable; a saddle-node bifurcation, which is then followed by another statically stable solution at higher velocities, was predicted. As compared to Rinaldi and Païdoussis [135], a lower critical velocity was obtained, in closer agreement with experiment. Subsequently, Abdelbaki et al. [137] developed a nonlinear model for the dynamics of inverted cylinders with ogival end-pieces, predicting a saddle-node bifurcation at relatively low flow rates, and loss of stability for enough perturbations. At higher flow velocities, static divergence in the first mode via a supercritical pitchfork bifurcation was obtained. Moreover, by further increasing the flow velocity, post-divergence flutter via a Hopf bifurcation was predicted. Recently, an improved linear model for the this system was presented by Rinaldi and Païdoussis [138]. This model predicts the dynamics of the system as follows: flutter at relatively low flow velocities and then buckling at higher flow rates. The critical flow velocities obtained are in fairly good agreement with the experimental results.

In this case also, the dynamics of cylindrical shells subjected to external axial flow has been extensively studied; refer to Païdoussis [27].

1.2.3 Tubular beams subjected to both internal and external flows

For decades, studies on the dynamics of pipes simultaneously subjected to internal and external axial flows have been conducted. Cesari and Curioni [139] predicted buckling instability of pipes with different boundary conditions and subject to internal and external axial flow, perhaps for the first time. Thereafter, the dynamics of vertical pipes conveying fluid and concurrently subjected to an independent external axial flow was investigated by Hannoyer and Païdoussis [29]. Taking into account the boundary-layer thickness of the external flow, internal dissipation and gravity, the equation of small motions was derived for both clamped-clamped and cantilevered pipes. For clamped-clamped pipes, the effect of the internal and external flows on the stability of the system was found to be additive, i.e., if either internal or external flow velocity is just less than its critical value for instability, an increase in the value of the velocity of the other flow would trigger instability. In contrast, if because of either internal or external flow, a cantilevered tubular beam is right below the threshold of instability , by further increasing the other flow, instability could be eliminated. Generally, in the aforementioned case, the dynamics of the system greatly depends on the shape of the free-end. For a blunt end, internal flow was found to be dominant and, although flutter arises at sufficiently high flow velocities, increasing the external flow velocity re-stabilizes the system. For a more or less streamlined end-piece, the dynamical behaviour is more complex, i.e., both static and dynamic instabilities occur. Experimental observations and theoretical predictions were found to be in good agreement. Also, the stability of a nonuniform slender beam subjected to internal and/or external flow was investigated both theoretically and experimentally in Hannoyer and Païdoussis [140, 141].

Motivated by some applications, such as modelling the internals of heat-exchangers and boilers, the dynamics of clusters of cylinders subjected to concurrent internal and external flows was examined in Païdoussis and Besançon [142].

Numerous studies have been conducted on the dynamics of a drill-string, e.g., by Bailey and Finnie [143], Finnie and Bailey [144], Den Hartog [30] and Grigoriev [145]. Also, one of the studies in Luu [146] is concerned with the stability of a long hanging cantilevered tubular beam conveying fluid which is also subjected to an external flow over its outer surface through an annulus formed by an outer rigid channel.

The equation of motion of an inclined pipe conveying fluid which is partially subjected to axial flow through a coaxial tubular beam was derived by Wang and Bloom [147]. In this model, for small lateral deflections, gravity, fluid viscous forces, as well as the turbulent boundary layer thickness of the external flow were taken into account. Using spatial finite-difference schemes, discretized equations were obtained through which the critical parameters regarding stability of the system could be found.

Thereafter, aiming at modelling the dynamics of a drill-string with a floating fluid-powered drill-bit, Païdoussis et al. [31] derived a mathematical formulation for of a hanging cantilevered pipe discharging fluid downwards, which, after exiting from the free end, flows upwards over an annular region confined by a rigid concentric cylindrical channel; i.e., for two counter-current interdependent axial flows. For system parameters associated with a drill-string system, as well as a bench-top-size experiment, computations were carried out. For relatively low degrees of confinement by the outer rigid channel, the internal flow was found to be dominant; at low flow rates, an increase in the damping caused by the existence of the annular flow was found to stabilize the system. On the other hand, for more or less high degrees of confinement, the annular flow was found to be dominant, which leads to destabilization of the system and precipitating flutter at relatively low internal flow velocities. The dynamics of a system with reverse flow directions to those in Ref. [31] was investigated by Qian et al. [148]; for a drill-string-like system, theoretical results demonstrated that divergence may take place in the case of relatively high degree of confinement. Also, Fujita and Moriasa [149] studied the same system for both flow configurations, i.e., as in Païdoussis et al. [31] and Qian et al. [148]. The stability of the system was examined by implementing a separate analysis for internal and annular flow.

Later on, Moditis [150] investigated the dynamics of a hanging flexible cantilevered pipe, coaxial with a shorter rigid outer tube, modelling a salt-cavern hydrocarbon storage system. Two different flow configurations were considered: (i) the cantilevered pipe discharges fluid downwards which, upon exiting the cantilever, flows upwards through the annular region around the pipe [36]; (ii) with the flow directions reversed. Based on the formulation of Ref. [31], a linear model was obtained. The Heaviside step function was used to model the discontinuity in the external flow velocity. Moreover, a series of experiments were conducted in a bench-top-sized system to validate the analytical results. It was found that the full-scale system undergoes divergence rather than flutter. Also, an asymptotic behaviour was obtained by increasing the length of the pipe. Subsequently, a numerical study on the same system was carried out by Kontzialis et al. [151]. Results were in good agreement with existing experimental data. A linear model was also derived by Minas et al. [152] to investigate the dynamics of a system in which the flow discharges radially at the end of the pipe through a special end-piece. See also Païdoussis et al. [153].

Dynamics of a cantilevered pipe subjected to concurrent internal and inverted external flow was further investigated by Abdelbaki. First of all, a linear analysis was carried out to examine the dynamics of a cantilevered pipe conveying fluid and subjected to a reverse partially-confined external axial flow over its upper part [154]. Instead of a Heaviside step function as in Ref. [150], a logistic function was used to model the discontinuity in the external flow velocity. It was concluded that the proposed model could better predict the onset of instability and the frequency of oscillations in comparison to Ref. [150]. Thereafter, a weakly nonlinear model was derived by Abdelbaki et al. [155] to study the dynamics of a hanging discharging cantilevered pipe simultaneously subjected to a fully confined external axial flow in the reverse direction. For a slender elastomer pipe, bifurcation diagrams were presented and the existence of limit-cycle oscillations, i.e., flutter in the first mode, was demonstrated. In Abdelbaki et al. [156], the previous study was extended to the case of a cantilevered pipe discharging fluid and subjected to a partially-confined external axial flow. For different dimensions and material properties, the stability of the system was investigated for increasing internal flow velocity, which also means an increase in the external flow velocity, by virtue of continuity. An oscillatory instability, i.e., flutter in the second mode, was predicted at sufficiently high flow velocities. Also, it was predicted that increasing flow velocity results in increased amplitude and frequency of oscillations. Moreover, generally, a longer or a tighter annulus destabilizes the system.

1.3 Limitations of the studies in the literature

The literature review in the foregoing allowed an assessment of the limitations, scarcity or absence of pertinent studies, which motivated the research reported in this thesis. Based on this literature review, to the best of the author's knowledge, no experimental work had been undertaken thus far to systematically investigate the dynamics of curved cantilevered pipes conveying fluid. Experimental results would be valuable for validating theoretical models of the problem and they can offer insights into the sensitivity of the dynamics of cantilevered pipes conveying fluid to an initial curvature.

The foregoing review also made it evident that there has been no systematic experimental study and characterization of the instability of free-clamped cylinders subjected to unconfined axial water flow. Conducting water tunnel experiments on flexible cantilevered cylinders in reverse axial flow provides the opportunity to investigate the onset of instability and the post-instability behaviour of the system, including the large-amplitude post-critical dynamics of the system. The experimental results would be useful for validating and developing analytical and numerical models. Also, the experimental results would shed some light on the physical dynamics and the mechanisms of instabilities for the system of inverted cantilevered cylinders.

The literature review in the previous section also highlights a noticeable scarcity of studies focusing on pipes simultaneously subjected to both internal and external axial flows, especially as compared to research on pipes conveying fluid and cylinders in axial flow. In particular, few studies have addressed cases where the internal and external flows are interdependent with the two flows in opposite directions. Furthermore, experimental studies for this specific system are very limited. Therefore, a systematic experimental investigation of

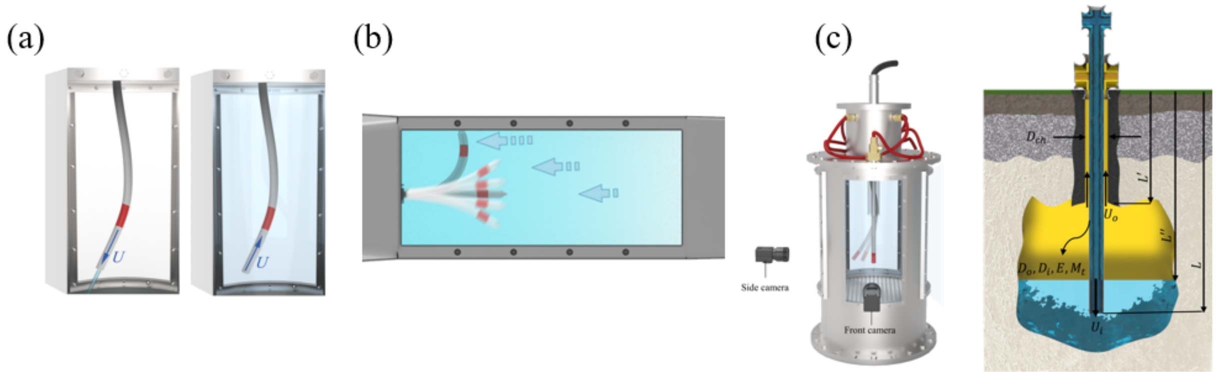

Figure 1.8: Schematic view of the three systems of slender cantilevered cylinders subjected to internal, external, or simultaneous internal and external axial flows; (a) system I: a slightly curved cantilevered pipe discharging/aspirating fluid; (b) system II: an inverted cantilevered cylinder in axial flow, i.e. a cylinder with the upstream end free and the downstream end clamped; (c) system III: a hanging fluid-discharging pipe subjected to a reverse external flow over its upper portion through the annulus formed by a co-axial shorter outer rigid tube.

the dynamics of a fluid-discharging cantilevered pipe simultaneously subjected to a reverse annular axial flow over its upper portion is needed. The literature shows that, no experimental investigation has been conducted to explore the dynamical behaviour of this system with impacting. Experiments can be useful in characterizing the effect of some of the main system parameters on its dynamics, including external flow confinement, confinement length, pipe slenderness and material, eccentricity between the pipe and the outer rigid tube, and external flow constriction at the inlet or outlet of the annulus. Moreover, the analytical models found in the literature have struggled to accurately predict critical flow velocities in real full-scale brine-string systems in salt-mined caverns as they do not account for the presence of two different fluids in the cavern. To achieve more realistic predictions of critical flow velocities for full-scale systems, it is imperative to eliminate these simplifications.

1.4 Thesis scope and objectives

The main objective of this thesis is to study the dynamics of slender cylindrical cantilevers subjected to internal, external, or simultaneous counter-current internal and external axial flows. In particular, the dynamics of three closely related systems of slender cylindrical structures subjected to internal and/or external axial flows are examined experimentally and/or by developing analytical FSI models. These three systems are schematically shown in Fig. 1.8. System I involves a slightly curved cantilevered pipe conveying fluid, system II is a free-clamped cylinder in axial flow, and system III involves a hanging cantilevered pipe discharging fluid and subjected to a reverse external flow over its upper portion through the annulus formed by a co-axial shorter outer rigid tube. The motivation for this study stems not only from curiosity and the lacunae mentioned in the previous section, but also from the industrial applications of these systems. Especially, for system III, which is the main part of this study, the most important motivation behind this investigation is to characterize the dynamics of brine-strings in salt-mined caverns during the retrieval mode of operation. Therefore, exploring the fluid-elastic instabilities and the dynamical behaviour of this system as the internal and external flow velocities are varied and the effect of the main system parameters is the primary concern of this thesis.

The aims and objectives of this thesis can be outlined as follows.

- Exploring experimentally the influence of a slight initial curvature on the dynamics of cantilevered pipes discharging/aspirating fluid.

- Determining experimentally the dynamics of an inverted cantilevered cylinder in water flow (system II), as well as investigating the influence of the main system parameters including the free-end shape of the cylinder, its slenderness, flexural rigidity and planar or 3D motions.

- Exploring experimentally the dynamics of system III, and investigating the effect of post-instability impacting of the pipe on the outer rigid tube, as well the effect of the main system parameters. These parameters include the (i) confined length ratio, (ii) size of the annular gap, (iii) pipe slenderness, (iv) pipe material properties and shape, (v) flow constriction at the upstream or downstream end of the annular region, and (vi) eccentric positioning of the outer rigid tube relative to the central pipe.

- Developing an analytical model for an idealized brine-string in salt-mined caverns during the retrieval mode of operation. This model represents the brine-string as a fluid-discharging cantilevered pipe conveying fluid and subjected to a partially confined reverse external axial flow of a different fluid.

1.5 Thesis structure

The papers in this manuscript-based thesis, consisting of five manuscripts [1–5], have been assembled in a logical rather than a chronological order. This thesis comprises seven chapters, with this chapter serving as the introduction (Chapter 1). The remaining six chapters are summarized as follows.

The first publication [1], presented in Chapter 2, discusses and analyzes experiments on the dynamics of a slightly curved cantilevered pipe discharging/aspirating fluid (system I). In this work, making use of a bench-top-size apparatus consisting of a hanging straight or curved cantilevered pipe conveying fluid, four different cases were explored: (i) a straight pipe discharging water in a reservoir filled with air, (ii) a curved pipe discharging water in a reservoir filled with air, (iii) a straight pipe aspirating water in a reservoir filled with water, and (iv) a curved pipe aspirating water in a reservoir filled with water.

In the second publication [2], presented in Chapter 3, the experimental results on the dynamics of an inverted cantilevered cylinder in axial water flow (system II) are presented and discussed. The effect of the main system parameters including the flexural rigidity of the cylinder, its length-to-diameter ratio and free-end shape are explored and the mechanisms underlying the onset of flutter and static divergence are discussed.

In the third and fourth publications [3, 4], presented in Chapters 4 and 5, a bench-top-size apparatus was utilized to explore the dynamics of system III. This apparatus consists of a pressure vessel filled with water, a hanging flexible cantilevered pipe conveying fluid downwards, and a shorter outer rigid tube surrounding the upper portion of the pipe, which contains an upwards flow. The primary focus of Chapter 4 (Ref. [3]) is to investigate the influence of the confinement length on the dynamics of the system for various ratios of external to internal flow velocity. Additionally, this study examines the post-instability dynamics and the effect of impacting of the pipe on the coaxial shorter outer rigid tube. Chapter 5 (Reference [4]) discusses the experimental findings regarding the effect of external flow confinement, pipe slenderness, pipe material, the positioning of a constraint at the external annular flow inlet/outlet, and the eccentric positioning of the outer rigid tube relative to the central pipe.

Chapter 6 is dedicated to the analytical model developed for the dynamics of system

III, serving as an idealized model for brine-strings during product retrieval in full-scale salt-mined caverns, presented in Ref. [5]. This paper, currently under review, utilizes a Newtonian approach to derive the equation of motion for system III. It considers the presence of two different fluids (brine and product) in the cavern and a variable brine-product interface level.

Chapter 7 provides a summary of the key findings from Chapters 2 to 6 and explores potential avenues for future research.

CHAPTER 2

Dynamics of Slightly Curved Cantilevered Pipes Conveying Fluid: An Experimental Investigation

Preface

In this chapter the dynamics of system I is investigated, in the first manuscript presented in this thesis [1]. This system involves a slender cantilevered cylinder subjected to internal flow, specifically a slightly curved clamped-free tubular beam conveying fluid. The fluid-elastic system of a pipe conveying fluid exhibits a rich variety of dynamical behaviours, including static divergence, Hopf bifurcation, and chaotic behaviour. A slight initial curvature introduces another layer of complexity to this system.

As mentioned in the introduction, despite the fact that pipes in real-world applications are often subject to imperfections, including initially curved shapes, research on pipes with initial curvature, particularly experimental studies, remains relatively scarce. Addressing this gap has led to the current investigation. This study was aimed at providing insights into the sensitivity of the dynamics of discharging/aspirating cantilevered pipes to geometric imperfections, in alignment with one of the objectives of the thesis stated in the Introduction.

In this work, four different cases were examined experimentally. Cases (i) and (ii) involved fluid-discharging straight or curved pipes; while cases (iii) and (iv) fluid-aspirating straight or curved pipes.

This study has revealed that, as the flow rate increases, discharging cantilevered curved pipes undergo substantial static deformation due to the exaggeration of the initial curvature. This static deformation is succeeded by a strong, abruptly occurring second-mode flutter at sufficiently high flows. Depending on the static equilibrium position of the pipe just before instability occurs, the onset of this flutter could be higher or lower than that for a straight discharging pipe. The oscillations were predominantly periodic and they occurred only in the plane of the initial curvature.

Aspirating curved pipes, with increasing flow rate, exhibited a sequence of dynamical states as follows. Initially, the pipe underwent a static deformation; subsequently, at sufficiently high flows, a weak first-mode flutter was superimposed on the mean deflection. As the flow rate was increased further, both the static deformation and the oscillations continued to amplify. Since aspirating pipes were submerged in water, the oscillations were influenced by the damping induced by the surrounding fluid, leading to relatively smaller amplitudes of oscillations, as compared to discharging pipes (in air). Unlike the two-dimensional motions observed in the case of discharging curved pipes, the motions of aspirating curved pipes were not confined to the plane of initial curvature. The observed flutter was characterized by its unsteady, near-intermittent, and weak nature, with a greater chaotic content, as compared to straight aspirating pipes.

Experimental investigation of the dynamics of slightly curved cantilevered pipes conveying fluid

M. Chehreghani, A. Shaaban, A.K. Misra, M.P. Païdoussis*

Department of Mechanical Engineering, McGill University,

817 Sherbrooke Street West, Montreal, QC, Canada H3A 0C3.

Abstract: The dynamics of slightly curved cantilevered tubular beams conveying fluid was investigated experimentally. Apart from exhibiting a rich dynamical behaviour, interest in the matter arises mostly because in real-world applications pipes conveying fluid are often subject to geometric imperfections, rendering a straight pipe curved. A bench-top-size apparatus consisting of a reservoir and a hanging straight or curved clamped-free pipe conveying fluid was utilized. Four different cases were explored: (i) a water-discharging straight pipe in air (in the reservoir filled with air), (ii) a water-discharging curved pipe in air, (iii) an aspirating straight pipe submerged in quiescent water (in the reservoir filled with water), and (iv) an aspirating curved pipe submerged in quiescent water. Making use of a contactless optical technique, the displacement time-series signal was obtained and analyzed to characterize the nature of the motions. It was found that curved cantilevered pipes conveying fluid display quite interesting nonlinear fluid-structure interaction dynamics. For initially curved discharging pipes, a large flow-induced static deformation materialized prior to the onset of an oscillatory instability. Aspirating curved pipes, on the other hand, are subjected to weak flutter superimposed on a static deformation.

Keywords:Fluid-structure interaction, Flow-induced instability, Hopf bifurcation, Flutter, Static deformation.

2.1 Introduction

The dynamics of the fluid-elastic system of a pipe conveying fluid has been studied quite extensively, since at least 1939 [1]. The main reason that the dynamics of this system has attracted so much attention since then is perhaps its ability to display a rich dynamical behaviour, despite being relatively simple to analyze and easy to realize physically [2].

*Corresponding author.

E-mail addresses: mahdi.chehreghani@mail.mcgill.ca, ahmed.shaaban@mail.mcgill.ca, arun.misra@mcgill.ca, michael.paidoussis@mcgill.ca

In addition to interest in the dynamics of pipes conveying fluid from a fundamental research point of view, studies on the subject are also motivated by applications; for instance, propulsion of watercraft [3, 4], submarine pipelines and risers [5, 6], Ocean Thermal Energy Conversion (OTEC) [7], and pipes in solution-mined caverns [8, 9].

After the pioneering work conducted in 1950-1970 on the dynamics of pipes conveying fluid [10–19], many researchers have examined numerous variations of this system, such as pipes with added supports, masses, linear and nonlinear springs and dashpots, end-nozzles, as well as pipes made of functionally graded materials, composite and soft active materials, just to name a few [20–30].

Pipes discharging fluid offer a simple experimental and theoretical tool to explain known dynamical behaviour and to explore new dynamical characteristics, thereby becoming a *paradigm* in dynamics [31]. For instance, it has been demonstrated via a nonlinear model that a pipe with supported ends is only subject to static divergence; being a gyroscopic conservative system, it cannot flutter [32, 33]. This invalidates the prediction of coupled-mode flutter via an earlier linear model [34]. A cantilevered fluid-discharging pipe, on the other hand, is a nonconservative system and develops an oscillatory instability via either a sub- or supercritical Hopf bifurcation at high enough flow rates [35–37]. For a cantilevered pipe with nonlinear motion-restraining constraints, beyond the Hopf bifurcation, the existence of a period-doubling route to chaos was demonstrated [23, 38, 39]. Another interesting finding is that the instability of a cantilevered pipe in a certain mode can give rise to instability of another mode, resulting in a complicated double Hopf bifurcation interaction [40]. Also, for a cantilevered pipe at a supercritical flow rate, an axial base excitation is able to eliminate instability for some particular system parameters [41].

The dynamics of cantilevered pipes aspirating fluid, i.e. with fluid flowing from the free end towards the clamped one (in the reverse direction to that of a discharging cantilever), has been controversial [42] and perhaps is still not a fully resolved issue in Fluid-Structure Interactions (FSI). Over the past 50 years, since the 1960s, some experimental and theoretical work has concluded that an aspirating pipe cannot flutter (at least over the range of flow velocities tested in the experimental investigations), namely, experiments described in [42] conducted at the Chalk River Nuclear Laboratories, and Ref. [43, 44]. In contrast, some studies have postulated that aspirating pipes are inherently unstable, and that the reason they flutter at relatively small, rather than vanishing, flow velocities is due to dissipation related to friction with the external fluid medium [45]. Some studies predict that self-excited oscillations do indeed occur, but at relatively high, rather than vanishing, flow rates [46–48]. Perhaps, the conclusion is that pipes aspirating fluid *do* flutter at high enough flows, but the flutter is of a rather weak and near-intermittent nature [2, 49–52].

Tubular slender structures used in real-world applications, as in soft robots [53], ocean mining [54], deep-water risers used for oil or on-board Liquefied Natural Gas (LNG) production [55] and renewable energy systems [56], are commonly subject to imperfections, often resulting in a curved pipe shape. However, compared to straight pipes, research on initially curved pipes is relatively scarce, usually only theoretical, often only considering pipes with supported ends. As discussed by [42], in many studies and particularly in early work, experiments were conducted using slightly curved pipes unintentionally. On this note, the important study by [57] is recalled where surgical quality silicone rubber pipes were used, which suffer a slight bend. A static "distortion" of the pipe prior to instability was reported and it was postulated that the reason for the prediction of lower instability boundaries using a theoretical model for the perfectly straight pipe is due to the lack of straightness and residual internal stress of the pipes.

The seminal work of Misra et al. [58, 59] investigates the dynamics of curved pipes with supported extremities and compares the results obtained via extensible and inextensible centreline theoretical models, concluding that semi-circular pipes conveying fluid do not buckle. Czerwiński and Łuczko [60] have studied the dynamics of curved pipes with fixed ends conveying steady or pulsating flows, both theoretically and experimentally. A nonlinear model for a clamped-clamped pipe discharging fluid with several initial curvature shapes was derived by Yun-dong and Ze-gang [61]. It was found that imperfect clamped-clamped pipes, with increasing flow velocity, are subjected to static deflection, but they do not lose stability.

Nonlinear dynamics of cantilevered fluid-discharging pipes with different slightly curved shapes was explored by Zhou et al. [62]. It was found that, with increasing flow velocity, the initial curvature of the pipe is dramatically magnified. Eventually, at high enough flows, the pipe is subjected to an oscillatory instability, the onset of which mainly depends on the static equilibrium position of the system just before the threshold of the hydro-elastic instability. Chen et al. [63] derived a geometrically exact nonlinear model for large-deformations of a vertical cantilevered pipe; in this work, the dynamics of a pipe with semi-circular initial shape was examined, focusing on the effect of the mass ratio and a gravity parameter.

Free and forced vibration of a discharging L-shaped pipe was studied theoretically by Zhou et al. [64]. It was found that the pipe develops a large static deformation prior to the onset of limit-cycle oscillations. In the case of forced vibrations, depending on the flow rate, the amplitude and frequency of the external force, period-n, quasi-periodic and chaotic regimes were detected.

A fuller review of the extensive work on pipes conveying fluid is provided in the monograph by Païdoussis [42] and in a recent review [2]. Nevertheless, the foregoing literature survey shows that, to the authors' best knowledge, there has been no experimental work to-date exploring systematically the dynamics of *curved cantilevered* pipes conveying fluid. This lacuna has motivated the present study, aiming to examine experimentally the dynamics of cantilevered pipes with an initial curvature. The evolution with increasing flow of the initially curved static equilibrium, as well as the onset of oscillatory instability of this hydro-elastic system, is investigated. Specifically, the dynamics of curved fluid-discharging and aspirating cantilevered pipes are compared to those of their straight counterparts. The experimental results provided in this paper could be useful in validating analytical and numerical models of the problem and they provide some insight on the sensitivity of the dynamics of cantilevered pipes conveying fluid to a slight initial curvature.

The rest of this paper is structured as follows. The experimental apparatus and methodology are described in Sect. 2.2. In Sect. 2.3, the experimental results are presented and discussed. Finally, Sect. 2.4 presents some concluding remarks.

2.2 Apparatus and methodology

The experiments were conducted in the SMRI-PRCI [Solution Mining Research Institute-Pipeline Research Council International] apparatus, schematically shown in Fig. 2.1, located in the FSI laboratory of McGill University. The experimental setup comprises a stainless steel cylindrical pressure vessel of approximately 0.5 m inner diameter with four symmetrically located glass windows, allowing viewing and access to the test-section, a flexible pipe hung

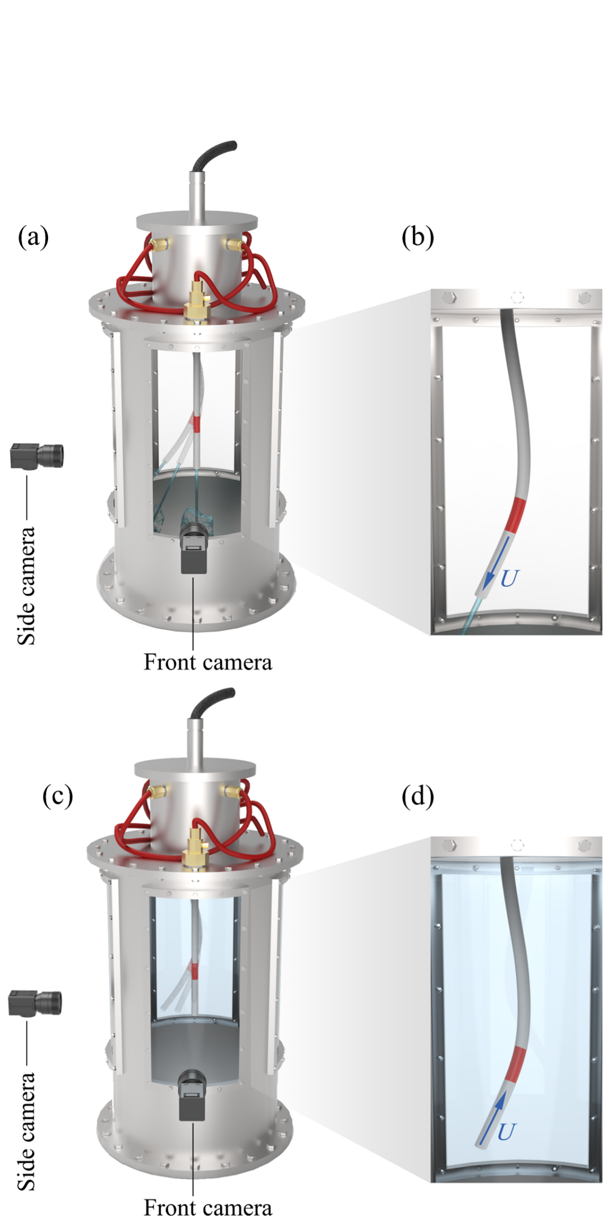

Figure 2.1: Schematic view of the pressure vessel of the SMRI-PRCI apparatus used in the experiments and the dual-camera system. (a) The hanging cantilevered pipe discharges water down into the pressure vessel that is filled with air, with the discharged water from the pipe exiting from the bottom of the pressure vessel; (b) zoomed view of the discharging pipe configuration. (c) The pressure vessel is filled with water and the pipe aspirates the fluid (the fluid introduced into the vessel from its top end flows upwards in the pipe); (d) zoomed view of the aspirating pipe configuration.

Table 2.1: Mechanical properties and dimensions of the pipes used in the experiments.

EI [Nm^2]	m[kg m^{-1}]	L [mm]	d_o [mm]	d_i [mm]
7.37 $\times 10^{-3}$	0.191	441	16.0	6.35

from its top end, a water storage tank, centrifugal pumps with digital controllers, a Bourdon tube pressure gauge, and a synchronized dual-camera system.

Two flexible pipes utilized in these experiments are shown in Fig. 2.2, the first straight and the second initially curved. Both pipes were made of RTV (Room-Temperature-Vulcanizing) silicone-rubber, and they were cast straight in-house from a two-component silicone-rubber liquid mixture in the manner described in Appendix D of Ref. [42]. They were both then mounted in an oven for 24 hours at a temperature of 180°C, the first one totally straight and the second one deformed using a semi-circular fixture, so that, when taken out from the oven, the curved pipe shape depicted in Fig. 2.2(b) was obtained. The two pipes had the same material properties and dimensions, given in Table 2.1, allowing us to compare the effect of curvature on the dynamics. In Table 2.1, EI stands for the flexural rigidity, L length, d_o outer diameter, d_i inner diameter and m mass per unit length of the pipe. The modal logarithmic decrement of the pipe in the r^{th} beam-eigenmode, based on a linear interpolation of the measured first three mode decrements, can be expressed by $\delta_r = 0.0521r - 0.0151$.

The initial curvature of the pipe when hung in air can be modelled with a linear combination of cantilever beam eigenfunctions:

$$\eta_0(\xi) = a\phi_1(\xi) + b\phi_2(\xi) + c\phi_3(\xi) + ..., \tag{2.1}$$

in which a, b, c,... are constants, $\xi = x/L$ is the dimensionless axial coordinate along the undeformed (straight) pipe axis, with origin located at the fixed end, $\eta = w/L$ is the dimensionless lateral pipe deflection, and

$$\begin{aligned}\phi_r(\xi) = {} & \cosh\lambda_r\xi - \cos\lambda_r\xi \\ & - \sigma_r\left(\sinh\lambda_r\xi - \sin\lambda_r\xi\right),\end{aligned} \tag{2.2}$$

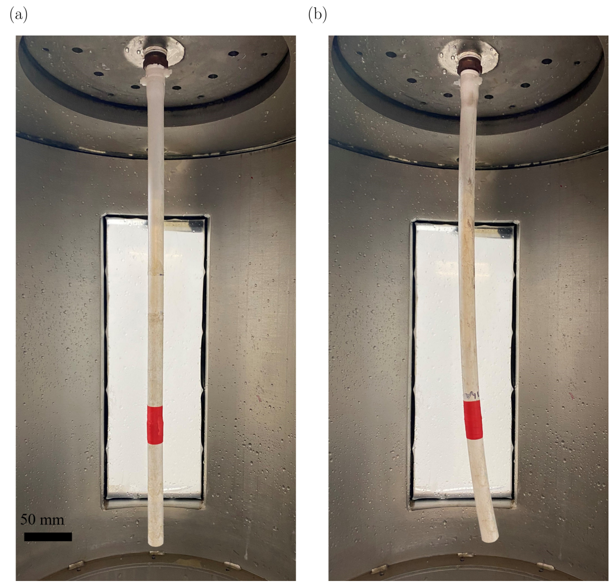

Figure 2.2: Photographs of the two pipes used in the experiments: (a) the straight pipe; (b) the pipe with a semi-circular initial curvature.

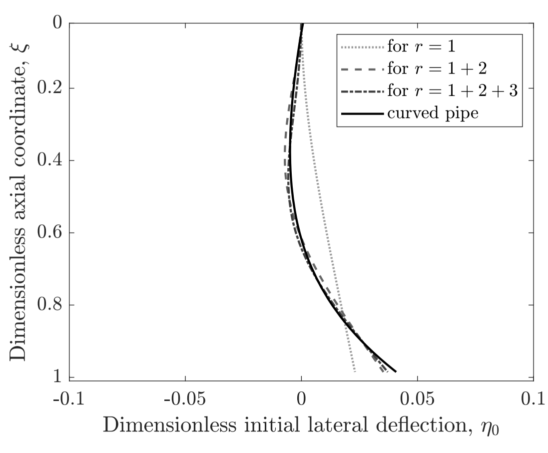

Figure 2.3: Characterization of the pipe curvature with a combination of a cantilevered beam mode shapes.

Table 2.2: Multiplicative conversion factors from dimensionless flow velocity and frequency to dimensional terms, and the dimensionless parameters for the pipes used in the experiments.

Flow configuration	$u \rightarrow U$ [m/s]	$\omega \rightarrow f$ [Hz]	ε	β	γ
Discharging pipe	1.095	0.1488	27.56	0.1417	25.38
Aspirating pipe	1.095	0.1080	27.56	0.07464	2.525

where

$$\sigma_r = \frac{\sinh \lambda_r L - \sin \lambda_r L}{\cosh \lambda_r L + \cos \lambda_r L}, \tag{2.3}$$

in which λ_r is the r^{th} eigenvalue of the dimensionless cantilever beam characteristic equation. Fig. 2.3 shows the characterization of the curved pipe with a linear combination of the first three cantilevered beam-modes, resulting in the following constant values: $a = 0.967 \times 10^{-2}$, $b = -0.838 \times 10^{-2}$ and $c = 0.150 \times 10^{-2}$. For the curved pipe used in this experiments, combination of the first three modes can approximate the pipe curvature sufficiently well.

In this experimental study, four cases were examined: (i) a water-discharging straight pipe in air, (ii) a water-discharging curved pipe in air, (iii) a water-aspirating straight pipe submerged in water, and (iv) a water-aspirating curved pipe submerged in water. In what follows, we shall simply refer to these cases as "discharging straight pipe", "discharging curved pipe", "aspirating straight pipe" and "aspirating curved pipe", respectively. For the experiments with discharging pipes, a centrifugal pump supplied water from a storage tank to the pipe and the pipe discharged water downwards. Water, upon exiting the pipe, was taken out from the bottom of the pressure vessel. In this case, the pressure vessel was filled with air, refer to Figs. 2.1(a, b). For the experiments with aspirating pipes, on the other hand, the pressure vessel was filled with water. In particular, in cases (iii) and (iv), a centrifugal pump supplied water from the storage tank to the pressure vessel top. The water was then aspirated by the pipe, as shown in Figs. 2.1(c, d).

In both discharging and aspirating flow configurations, the flow velocity inside the pipe, U, could be determined from the measured volumetric flow rate and the known value of d_i. Note that for the aspirating flow configuration, by continuity, the volumetric flow rate entering the pressure vessel outside the pipe, Q_o, equals the flow rate inside the aspirating pipe, Q_i; hence $U_o/U = d_i^2/(d_{ch}^2 - d_o^2)$, where U_o is the external flow velocity, and $d_{ch} \simeq$ 0.5 m is the pressure vessel inner diameter. Given the dimensions of the pipe used in the experiments, $U_o \simeq 1.6 \times 10^{-4} U$; therefore, considering that the fluid outside the pipe is quiescent is quite reasonable. For the aspirating flow configuration, the static pressure inside the pressure vessel was also measured (useful for eventual comparison with theory) via a conventional Bourdon tube pressure gauge.

In each experiment, the flow velocity was gradually increased to instability, using a digital controller. At each flow velocity step, the apparatus was kept running sufficiently long to ensure reaching a steady state. Then, making use of a non-contacting optical displacement follower, via two FLIR® Machine Vision synchronized colour cameras, the motion of the pipe was tracked and recorded at a frame rate of 64 FPS for a duration of one minute at each flow velocity step. More specifically, using a Grasshopper 3 USB 3.0 Vision perpendicular dual-camera system with an external trigger via a function generator, the motion of the centroid of a "red-spot" on the pipe, refer to Figs. 2.1 and 2.2, was recorded. The red-spot was 38 mm long and its centroid was located at $2L/3$ from the pipe clamped end. The "front" and "side" cameras were focused on the red-spot and were identically levelled and equidistant (with a distance of 1 m) from the front and side windows of the pressure vessel. The optical errors due to changes in object distance and observation angle were neglected.

Subsequently, making use of a video processing Matlab (Mathworks, Inc.) script, each recorded frame was converted into a binary image and once the red-spot was detected, the centroid of the area in pixel units could be determined. Next, the centroid location in pixel units was converted into millimeters using the known dimensions of the red-spot to obtain the front and side displacement time-series from the recorded videos at each flow velocity. The displacement time-series were then smoothed using a polynomial spline and further processed to yield qualitative and quantitative measurements of the motion Power Spectral Densities (PSDs), Probability Density Functions (PDFs), Lyapunov exponents, autocorrelation functions, Poincaré maps and bifurcation diagrams, in order to determine the nature of the pipe motions and its dynamics. In the displacement time-series analysis, the initial undeformed state of the pipe at zero flow velocity served as a reference relative to which the motions were measured.

2.3 Results

2.3.1 Dimensionless terms

It is convenient to use the dimensionless parameters, habitually used in the FSI community, to facilitate comparing the results obtained here with future analytical or subsequent experimental work. The conventional dimensionless flow velocity and frequency [42] are as follows:

$$
\begin{aligned}
u &= \left(\frac{M}{EI}\right)^{1/2} LU, \\
\omega &= \left(\frac{m+M+M_a}{EI}\right)^{1/2} L^2 \left(2\pi f\right),
\end{aligned}
\tag{2.4}
$$

in which $M = \rho_{if} A_i$ denotes the mass of the fluid inside the pipe per unit length flowing with a steady velocity U, and $M_a = \rho_{ef} A_o$ is the virtual (added) mass associated with the surrounding fluid medium per unit length, where ρ_{if} is the density of the internal fluid (water in this case), ρ_{ef} is the density of the surrounding fluid (air for discharging pipes and water for aspirating pipes); and $A_i = (\pi/4)d_i^2$ and $A_o = (\pi/4)d_o^2$ are the inner and outer cross-sectional area of the pipe, respectively. For the pipe used in the experiments, for both discharging and aspirating flow configurations, the conversion factors from dimensionless to dimensional terms are presented in Table 2.2, which could provide a "feel" of the experimental results. Also, shown in the table are:

$$
\begin{aligned}
\varepsilon &= \frac{L}{D}, \quad \beta = \frac{M}{m+M+M_a}, \\
\gamma &= \frac{(m+M-M_a)}{EI} gL^3,
\end{aligned}
\tag{2.5}
$$

where ε is the pipe slenderness, β is a mass parameter and γ is a gravity parameter.

2.3.2 Results for fluid-discharging pipes

In this section, the dynamics of a fluid-discharging curved cantilevered pipe is compared to that of a straight one. The experimental bifurcation diagrams showing the variation of displacement rms amplitude versus flow velocity for the fluid-discharging straight and curved pipes are presented in Fig. 2.4. In these bifurcation diagrams, the rms of the total displacement and the mean pipe deflection are plotted against u in Fig. 2.4(a, b), whereas in Fig.

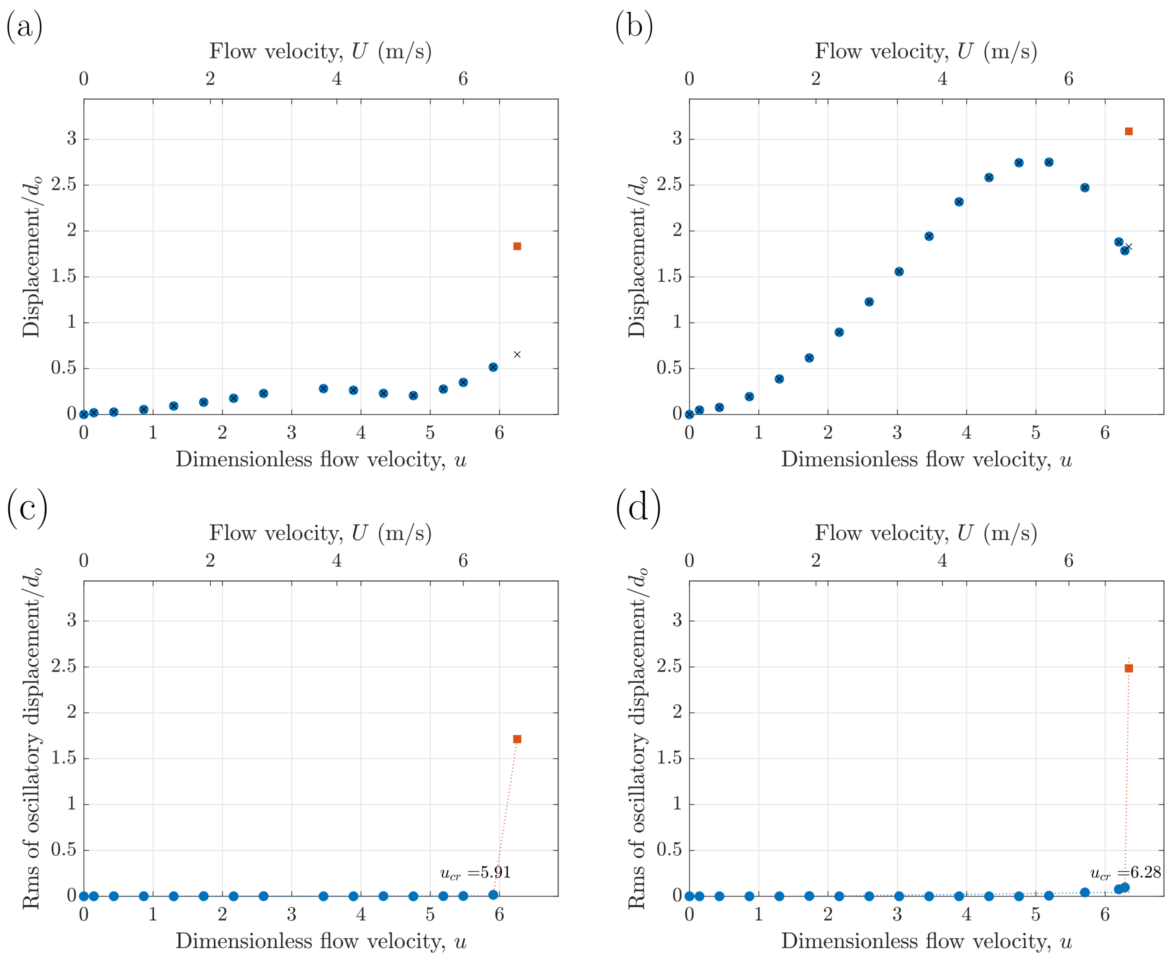

Figure 2.4: Bifurcation diagrams showing the rms of total displacement, mean deflection and the oscillatory displacement as a function of flow velocity for: (a, c) fluid-discharging straight pipe; (b, d) fluid-discharging curved pipe. Rms amplitude: (●) pre-instability, (■) post-instability; (×) mean deflection.

2.4(c, d) the variation of the oscillatory part of the displacement signal versus u is depicted. Additionally, wavelet transform scalograms showing the frequency content of the discharging straight and curved pipes at each flow step are shown in Fig. 2.5.

The bifurcation diagrams of Fig. 2.4 and scalograms of Fig. 2.5 indicate that both the straight and curved pipes are subjected to a self-excited oscillatory instability, namely second-mode flutter, at sufficiently high flow velocities; in Fig. 2.4(a, c) at $u = 5.91$, and in Fig. 2.4(b, d) at $u = 6.28$. This self-excited flutter is a movement-induced instability in Naudascher and Rockwell's classification [65]. The main difference between the dynamics

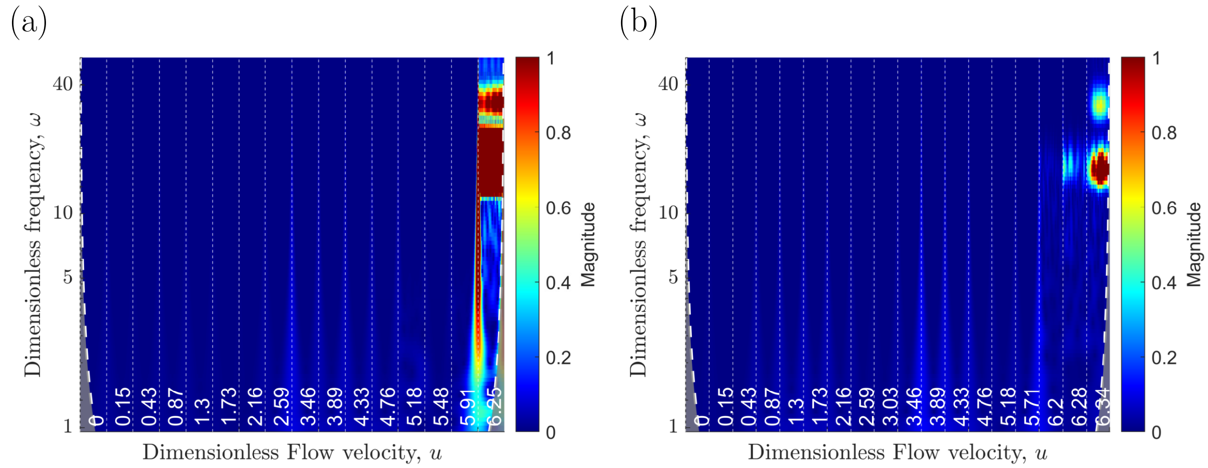

Figure 2.5: Continuous wavelet transform scalogram with the vertical bands corresponding to the flow velocity steps for (a) fluid-discharging straight pipe; (b) fluid-discharging curved pipe.

of the curved and straight pipes, however, is that the curved pipe developed a relatively large amplitude static deformation prior to the threshold of flutter. More specifically, at quite small flow velocities, $u < 0.83$, the curved pipe remained more or less stationary at its initial curved shape. Increasing the flow velocity resulted in a gradual exaggeration of the initial curvature towards one side, with the pipe deforming in a first-mode shape; and then in the opposite side, with the pipe now deforming in a second-mode shape. In this range of flow velocities, in addition to the large gradually increasing static deformation, very weak random superimposed oscillations with a small amplitude were observed, most likely due to turbulence buffeting. Eventually, increasing the flow velocity further to $u = 6.28$, resulted in large amplitude flutter.

It should be stressed that the deformation of the curved pipe took place in the plane of initial curvature and therefore both static deflection and oscillatory motions were 2D. The onset of the oscillatory instability for the curved pipe was higher than that for a straight pipe.

It is worth mentioning that another set of experiments was conducted making use of a pipe with a relatively larger initial curvature than the pipe shown in Fig. 2.2(b). The pre-instability static deformation of this pipe was so large that the middle portion of the pipe became almost horizontal and the red spot used for tracking was no longer visible from

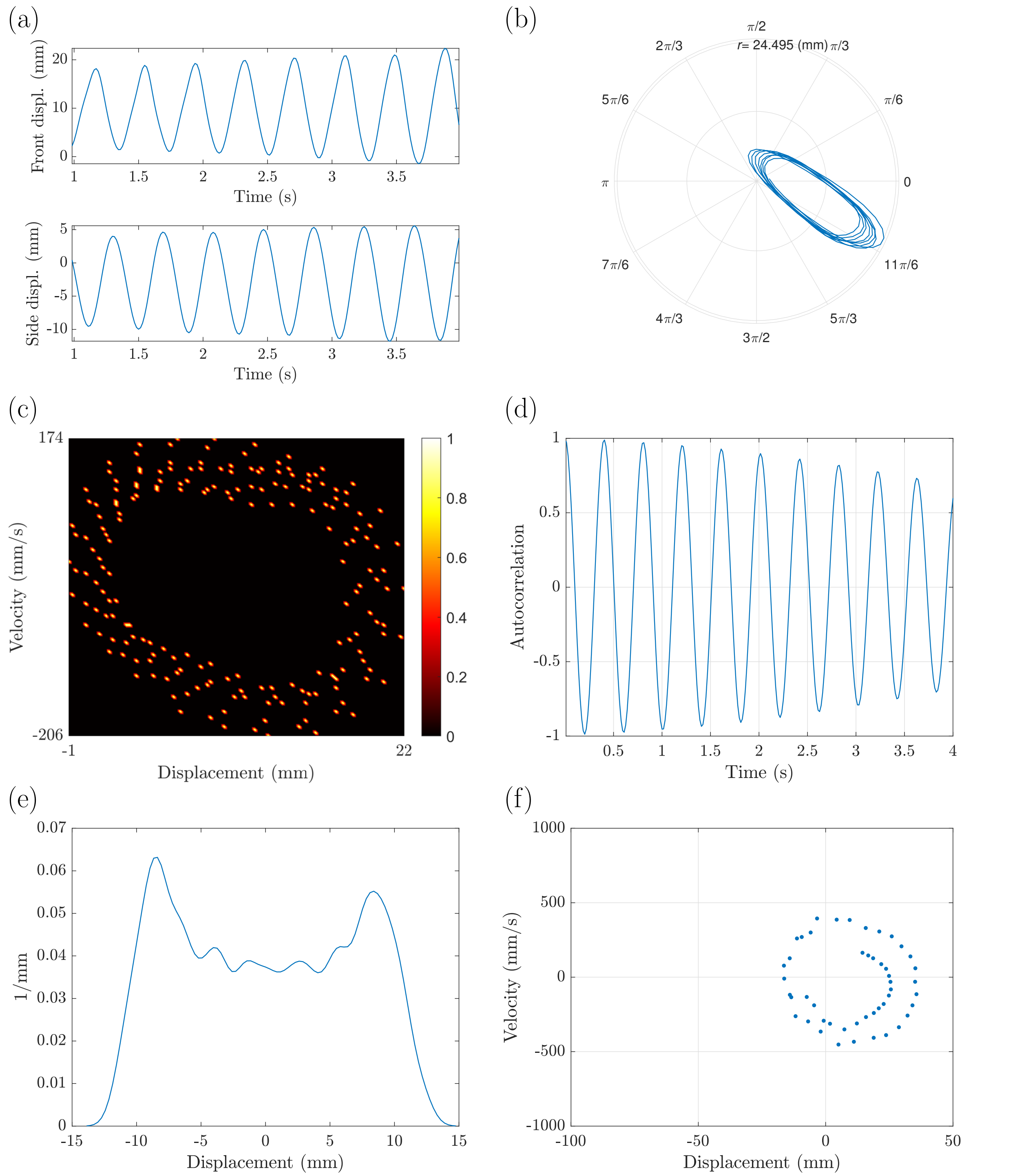

Figure 2.6: Dynamics of the fluid-discharging *straight* pipe at $u = 6.25$ ($U = 6.85$ m/s). (a) Displacement time traces; (b) polar trajectory of the motion; (c) phase plane contour plot of the front displacement; (d) autocorrelation of oscillatory part of the front displacement; (e) PDF of oscillatory part of the front displacement; (f) Poincaré map.

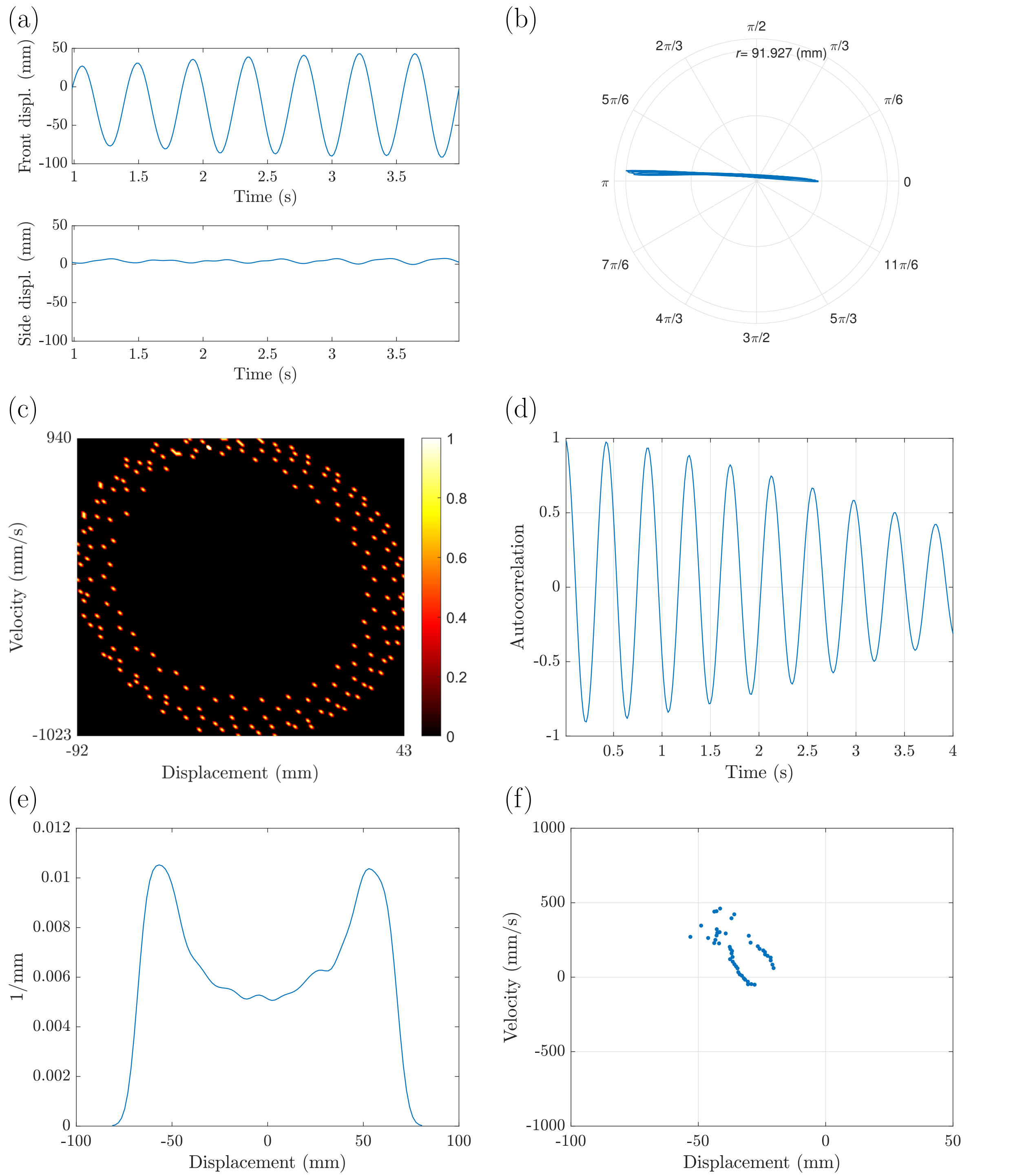

Figure 2.7: Dynamics of the fluid-discharging *curved* pipe at $u = 6.34$ ($U = 6.95$ m/s). (a) Displacement time traces; (b) polar trajectory of the motion; (c) phase plane contour plot of the front displacement; (d) autocorrelation of the oscillatory front displacement; (e) PDF of the oscillatory front displacement; (f) Poincaré map.

the windows of the pressure vessel; this pipe became unstable by flutter at relatively lower flow velocity than the straight pipe, namely at $u \simeq 4.90$ ($U \simeq 5.37$ m/s), as compared to $u = 5.91$ for the straight pipe. Therefore, the onset of flutter for a curved pipe may or may not be higher than that of a straight one, depending on the static equilibrium configuration of the pipe just prior to the threshold of instability.

The nature of the oscillation of the fluttering pipe can be compared by means of the analysis presented in Figs. 2.6 and 2.7 for the straight and curved pipe, respectively.

The time series of the displacement signals presented in Fig. 2.6(a) show a periodic 3D oscillation, whereas those of Fig. 2.7(a) a 2D periodic oscillation of larger amplitude. Nevertheless, both sets of time traces show that the oscillation is predominantly periodic. Also, the scalograms shown in Fig. 2.5 indicate a clear dominant frequency of $\omega \simeq 16.5$ ($f \simeq 2.45$ Hz), associated with the second-mode frequency of the pipe and its harmonic, $2\omega \simeq 33.0$ ($2f \simeq 4.90$ Hz). In the case of the straight pipe, as shown in Fig. 2.5(a), we see a rather diffuse second mode, whereas for the curved pipe it is more focused, as seen in Fig. 2.5(b); also, the frequency of 2ω is weaker for the curved pipe, probably due to the fact that the curved pipe has fewer degrees of freedom because of its initial curvature, resulting in 2D motions. Additionally, the polar visualization of the pipe motion in Fig. 2.6(b) and Fig. 2.7(b), confirm that the flutter observed for the curved pipe was a 2D periodic oscillation about the static equilibrium position of the pipe. Comparing the phase plane plots of Fig. 2.6(c) and Fig. 2.7(c) provides additional evidence of the periodic nature of the flutter observed for both curved and straight discharging pipes. Taking the different scales of the two figures into account, the phase portrait for the curved pipe displays relatively greater scatter; this may reflect a stronger chaotic component in the flutter of the curved pipe.

The autocorrelations of the oscillatory part of the front displacement for both pipes are characteristic of periodic motion, as they are both periodic and the autocorrelation of the signal does not rapidly approach zero [39]. The stronger decay of the autocorrelation in the case of the curved pipe, however, suggests that the weak chaotic component of the oscillation is relatively stronger for the curved pipe.

The double-hump shape of the PDFs of the oscillatory part of the front displacement shown in Fig. 2.6(e) and Fig. 2.7(e) is also characteristic of a periodic oscillation. Finally,

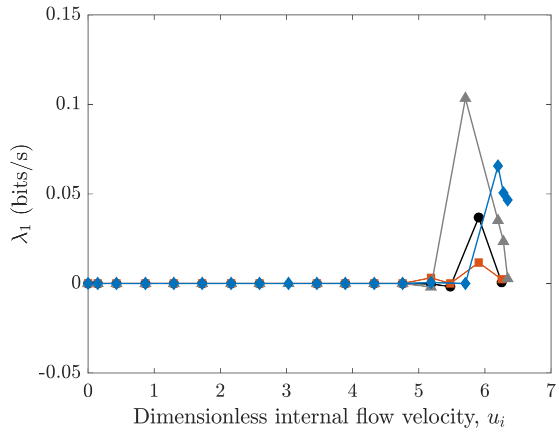

Figure 2.8: The largest Lyapunov exponent of the displacement time series for fluid-discharging pipes: (●) straight pipe front, (■) straight pipe side, (▲) curved pipe front, (◆) curved pipe side.

the Poincaré maps of Fig. 2.6(f) and Fig. 2.7(f) confirm the previous conclusion: the flow-induced instability results in a predominantly periodic oscillatory motion for both straight and curved discharging cantilevered pipes. Nevertheless, there exists a weak chaotic component, stronger in the curved pipe than in the straight one.

An effective version of the algorithm by Wolf et al. [66] was utilized to calculate the the largest Lyapunov exponent, λ_1, from the experimental time series. As seen in Fig. 2.8, $\lambda_1 \simeq 0$ in the range prior to the onset of flutter, as well as for $u \simeq 6.3$ where flutter occurs. Nevertheless, just prior to the onset of flutter, namely for u =5 to 6, there are positive, albeit small, values of λ_1, indicating enhanced chaotic content of the oscillation. This behaviour can be explained by the fact that the pipe undergoes a kind of "hesitation" just prior to flutter. This hesitation behaviour has previously been observed in experiments in some other FSI systems involving an oscillatory instability [42]. However, when flutter takes place, the chaotic component becomes very weak and the periodic content is dominant.

2.3.3 Results for fluid-aspirating pipes

In this section, the dynamics of aspirating curved and straight cantilevered pipes are compared. It is recalled that in this case the pipe is immersed in water. The experimental bifurcation diagrams of the pipe displacement as a function of the flow velocity are plotted in Fig. 2.9. The frequency content of the displacement signal for the straight and curved pipe is presented in Fig. 2.10(a, b), respectively. Note that Fig. 2.9(a, b), shows the rms of

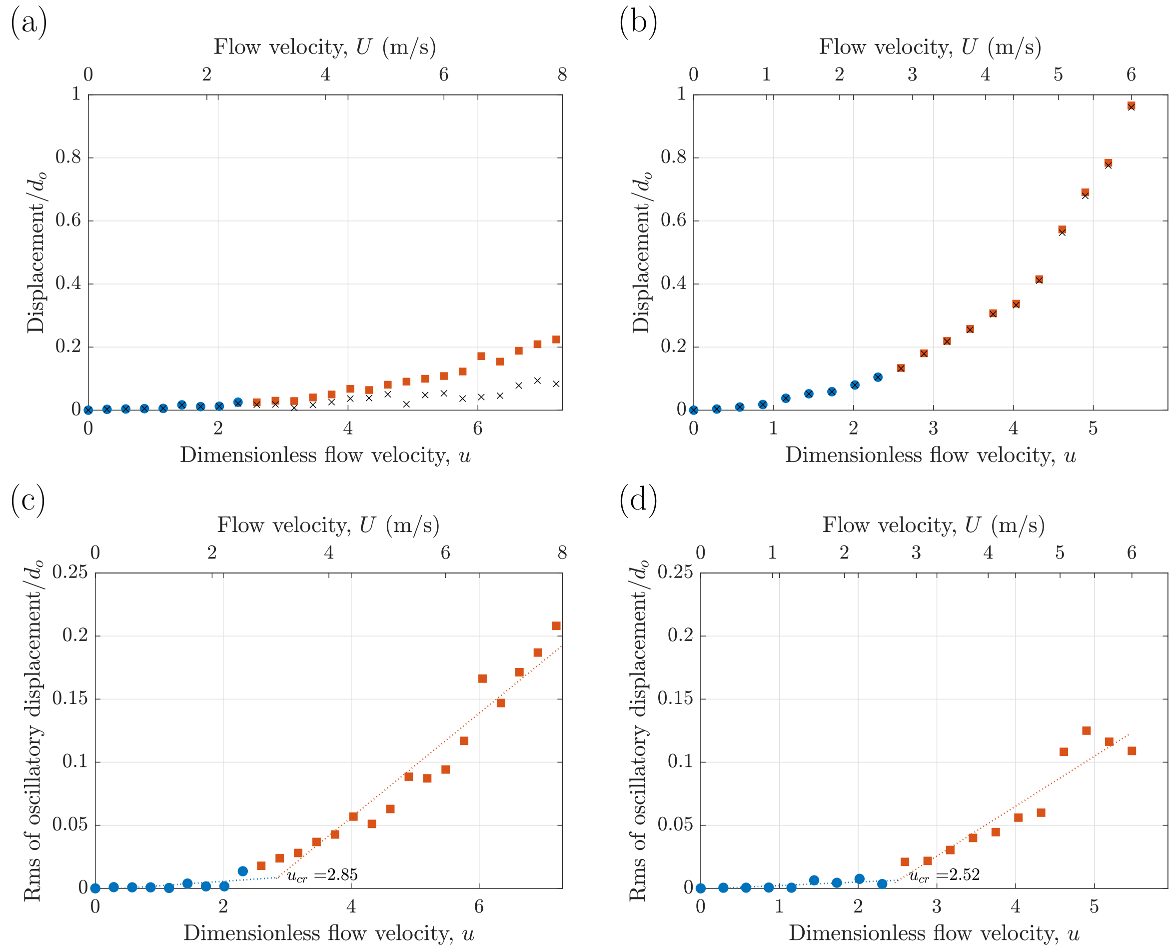

Figure 2.9: Bifurcation diagram showing the rms of total displacement and the difference between the rms of the total displacement and the mean deflection for: (a, c) fluid-aspirating straight pipe; (b, d) fluid-aspirating curved pipe. Rms amplitude: (●) pre-instability, (■) post-instability; (×) mean deflection.

the total displacement versus u, as well as the pipe mean deflection at each flow step; the oscillatory part of the displacement signal as a function of flow velocity is presented Fig. 2.9 (c, d).

We first discuss the dynamics of the straight aspirating pipe. The bifurcation diagrams of Fig. 2.9(a, c) and scalogram of Fig. 2.10(a), indicate that at relatively small flow rates, namely $u < 2.59$, the straight pipe remained stationary with only very small random motions, most likely due to turbulence in the flow. Increasing the flow velocity further resulted in stronger oscillations involving an increase in the slope in the bifurcation

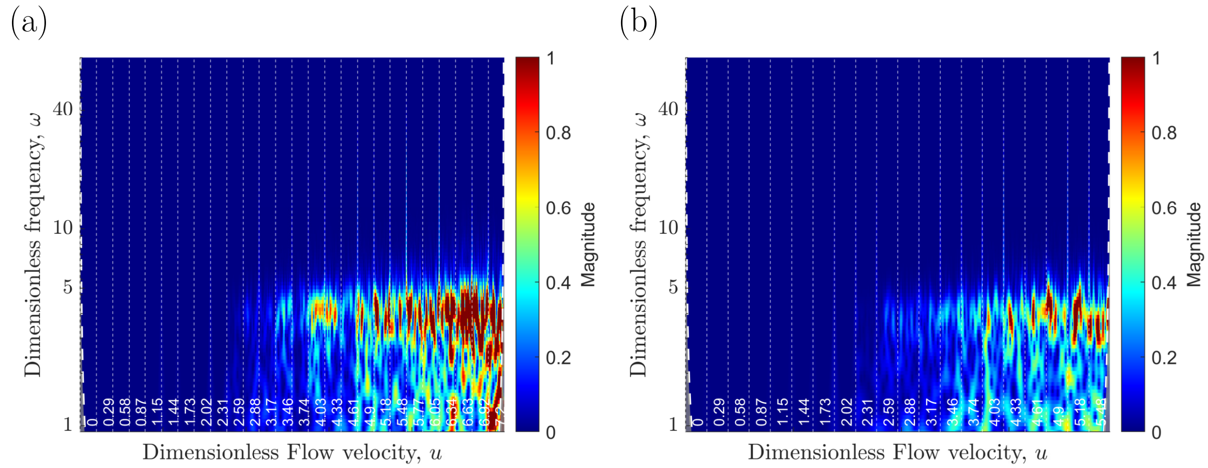

Figure 2.10: Continuous wavelet transform scalogram in which the vertical bands correspond to the value of the flow velocity for (a) fluid-aspirating straight pipe; (b) fluid-aspirating curved pipe.

diagrams of Fig. 2.9(a, c) at $u \simeq 2.85$ and the appearance of a first-mode-like frequency in the scalogram of Fig. 2.10(a), indicating the onset of an oscillatory instability via first-mode flutter. Increasing the flow velocity further gave rise to oscillations of larger amplitude and stronger first-mode frequency content. It should be remarked that, as compared to its fluid-discharging counterpart, transition from the static equilibrium position to instability for the aspirating straight pipe was rather gradual. Also, the instability observed was a rather anaemic first-mode flutter, likely as a result of the damping from the surrounding quiescent fluid (water) and influenced by the cross-flow component at the inclined pipe entrance.

The nature of this flutter is investigated further by means of the analysis shown in Fig. 2.11 for the post-instability oscillations of the straight aspirating pipe at a typical flow velocity of $u = 5.18$. The time traces of Fig. 2.11(a) illustrate the unsteadiness and near-intermittent nature of the flutter observed; however, one can still detect a strong periodic component. The polar trajectory of the pipe shown in Fig. 2.11(b) depicts how the direction and amplitude of the pipe oscillations varies. The phase plane plot of the front displacement, the autocorrelation, and the PDF of the front oscillatory displacement, as well as the Poincaré map presented in Fig. 2.11(c-f) provide further evidence of the unsteadiness and near-intermittent nature of the flutter, suggesting that, eventually, at higher flows, this system may follow the intermittency route to chaos.

Now we turn our attention to the curved aspirating pipe. In this case, the system became unstable via first-mode flutter at $u \simeq 2.52$, as shown in Fig. 2.9(b), i.e. at slightly lower critical flow velocity than that for the straight pipe (u=2.85); however, prior and after the onset of flutter, a relatively large gradual static deformation was observed as the flow velocity was increased. More specifically, the oscillations due to the instability were superimposed on the pipe mean deflection, as shown in Fig. 2.9(b, d). The bifurcation diagrams demonstrate that, even though the amplitudes of the static divergence for the curved pipe was relatively large, compared to the straight pipe, the amplitudes of the oscillatory part of the displacements were more or less similar. Fig. 2.10(b) shows the frequency of the motion at each flow velocity step: the first-mode oscillations superimposed on the mean deflection initiated at $u \simeq 2.59$ and developed to more powerful oscillations at higher flows. The bifurcation diagrams and the frequency scalograms suggest that, apart from the relatively large static deformation of the curved aspirating pipe, the oscillatory part of the displacement for both the curved and straight pipe, up to the maximum flow velocity investigated, were similar in terms of amplitude and frequency. The oscillations for the curved pipe took place about the mean deflected state, whereas for the straight pipe about the undeformed position. Similar to the straight pipe, the oscillatory instability developed was an unsteady weak first-mode flutter, influenced by the flow-induced damping due to the surrounding quiescent fluid and perhaps by the unbalanced impacting of the surrounding fluid at the tip of the pipe due to the cross-flow component of the fluid in the vicinity of the pipe inlet. As a result, the curved pipe is subjected to flutter of a more unsteady nature than the straight one.

The post-flutter oscillations of the curved aspirating pipe are explored further, at $u = 5.18$, in Fig. 2.12. The time traces of Fig. 2.12(a) exhibit an unsteady flutter of a fitful nature; yet, with substantial periodicity. The polar trajectory of the curved pipe presented in Fig. 2.12(b) confirms the near-intermittent nature of the oscillations. The phase-plane plot of Fig. 2.12(c) shows that the oscillations took place about the evolving static equilibrium position of the pipe. Comparing the autocorrelation, the PDF, and the Poincaré map of Fig. 2.12(d-f) for the curved aspirating pipe to those of Fig. 2.11(d-f) for the straight aspirating pipe demonstrates that the intermittency and unsteadiness of the motion is more pronounced in the case of the curved pipe. Similar to the straight aspirating pipe, the analysis presented

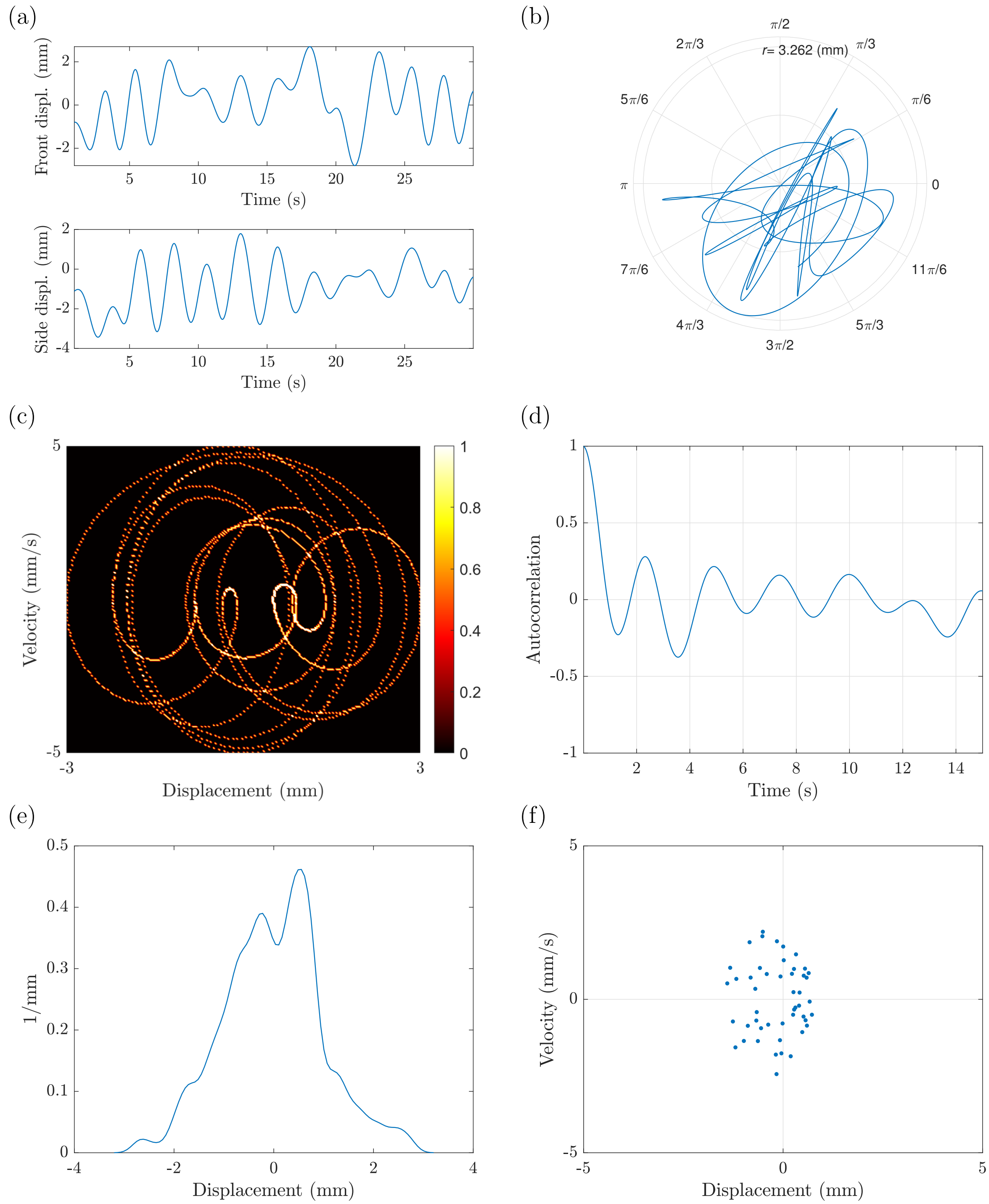

Figure 2.11: Dynamics of the fluid-aspirating *straight* pipe at $u = 5.18$ ($U = 5.68$ m/s). (a) Displacement time traces; (b) polar trajectory of the motion; (c) phase plane contour plot of the front displacement; (d) autocorrelation of oscillatory part of the front displacement; (e) PDF of oscillatory part of the front displacement; (f) Poincaré map.

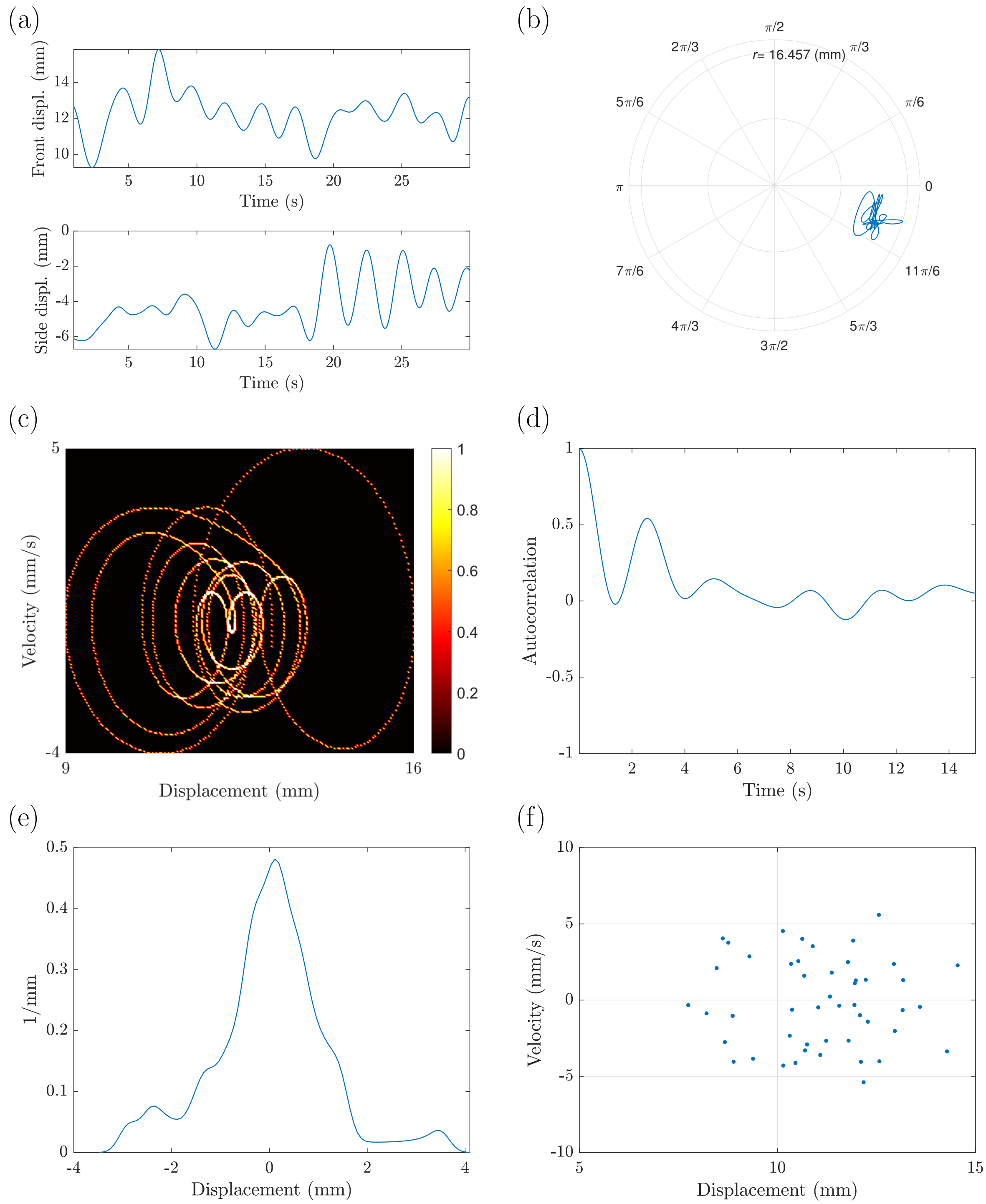

Figure 2.12: Dynamics of the fluid-aspirating *curved* pipe at $u = 5.18$ ($U = 5.68$ m/s). (a) Displacement time traces; (b) polar trajectory of the motion; (c) phase plane contour plot of the front displacement; (d) autocorrelation of oscillatory part of the front displacement; (e) PDF of oscillatory part of the front displacement; (f) Poincaré map.

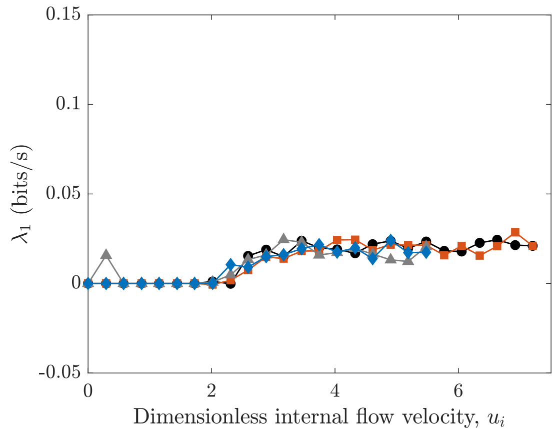

Figure 2.13: Variation of the largest Lyapunov exponent of the displacement time series by increasing u for fluid-aspirating pipes. (●) Straight pipe front displacement, (■) straight pipe side displacement, (▲) curved pipe front displacement, (♦) curved pipe side displacement.

in Fig. 2.12 suggests that, eventually, at higher flows, the system may become chaotic via the intermittency route to chaos.

Estimation of the largest Lyapunov exponent, λ_1, for the aspirating pipe is shown in Fig. 2.13. We see that $\lambda_1 \simeq 0$ up to $u \simeq 2$. Recalling that flutter occurs between $u = 2$ and $u = 3$ for both straight and curved pipes, the non-zero λ_1 in this flow range may be attributed to the fact that the oscillation, though predominantly periodic, inherently includes a relatively small chaotic component — which nevertheless appears not to grow with u, up to the maximum flow velocity attainable in the experiments.

2.3.4 Comparing the dynamics of discharging and aspirating curved pipes

One can compare the bifurcation diagrams and scalograms of Figs. 2.4(b, d) and 2.5(b), as well as the analysis provided in Fig. 2.7 for the discharging pipe to those of its aspirating counterpart presented in Figs. 2.9(b, d), 2.10(b) and 2.12. The curved discharging pipe is subjected to progressively growing large 2D static deformation and, at sufficiently high flows, abruptly to second-mode flutter in the plane of the initial curvature. The curved aspirating pipe, on the other hand, is subjected to gradual static deformation, and at high-enough flows to weak first-mode oscillations superimposed on the pipe mean deflection. For the aspirating curved pipe, the oscillations did not take place just in the plane of initial curvature, and they were of an anaemic intermittent nature.

It should be pointed out that the discharging and aspirating pipes had significantly different mass and gravity parameters (refer to Eq. (2.5)) because of the difference in the surrounding fluid medium (air in one, water in the other), which could have impacted the dynamics quite significantly.

2.4 Concluding remarks

The dynamics of fluid-conveying slightly curved cantilevered pipes was investigated experimentally and compared to that of straight pipes. Making use of a table-top-size apparatus, four different cases were explored: (i) a fluid-discharging straight cantilever, (ii) a fluid-discharging cantilever with an initial curvature, (iii) a fluid-aspirating straight cantilever submerged in water, and (iv) a fluid-aspirating curved cantilevered submerged in water.

For the discharging curved pipe, it was found that increasing the flow velocity gives rise to an exaggeration of the initial curvature of the pipe, resulting in a large static deformation prior to the threshold of instability at sufficiently high flows. The instability observed was a strong abruptly occurring flutter in the second mode, and it was predominantly periodic. Depending on the static equilibrium position of the pipe just before the instability threshold, the onset of flutter could be higher or lower than for the straight discharging pipe. Also, the oscillations took place only in the plane of the pipe curvature.

For the aspirating curved pipe, on the other hand, it was found that, with increasing flow velocity, the pipe first undergoes a relatively large static deformation; then, at high enough flows, a weak first-mode flutter was superimposed on the mean deflection. At still higher flow, the static deformation and the oscillations continued to grow. The pipe motions were not limited to the plane of initial curvature, in contrast to the 2D motions observed in the case of the discharging curved pipe. The observed flutter was rather unsteady, near-intermittent and weak, with a larger chaotic content than for the straight aspirating pipe. Being submerged in water, the oscillations of the aspirating pipes were influenced by the damping induced by the surrounding fluid, which contributes to making the amplitude of oscillations relatively small. Also, the oscillations were affected by the unbalanced impacting of the cross-flow component of the fluid at the tip of the pipe just below the pipe inlet.

Acknowledgments

The first author gratefully acknowledges McGill University for a McGill Engineering International Tuition Award (MEITA). Thanks also go to Mr. Aram Bahmani for helping with graphic designs.

Funding

This research was financially supported by Natural Sciences and Engineering Research Council of Canada (A.K.M., grant number 04957-2018), (M.P.P., grant number 06465-2018), the Solution Mining Research Institute (M.P.P., grant number U2017-3) and Pipeline Research Council International (M.P.P., grant number PR593-18700).

Data Availability

The data generated are available from the corresponding author upon reasonable request.

Declarations

Conflict of interest

The authors declare no financial, non-financial or personal interests that could have possibly influenced the work presented in the paper.

References

[1] F. J. Bourrières, Sur un phénomène d'oscillation auto-entretenue en mécanique des fluides réels, in: Publications Scientifiques et Techniques du Ministère de l'Air. France, No. 147., 1939.

[2] M. P. Païdoussis, Pipes conveying fluid: A fertile dynamics problem, J. Fluids Struct. 114 (2022) 103664.

[3] M. S. Triantafyllou, G. S. Triantafyllou, D. K. P. Yue, Hydrodynamics of fishlike swimming, Annu. Rev. Fluid Mech. 32 (1) (2000) 33–53.

[4] K. Zhou, H. L. Dai, L. Wang, Q. Ni, P. Hagedorn, Modeling and nonlinear dynamics of cantilevered pipe with tapered free end concurrently subjected to axial internal and external flows, Mech. Syst. Signal Process. 169 (2022) 108794.

[5] F. P. Gao, X. Y. Gu, D. S. Jeng, Physical modeling of untrenched submarine pipeline instability, Ocean Eng. 30 (10) (2003) 1283–1304.

[6] S. T. Santillan, L. N. Virgin, R. H. Plaut, Static and dynamic behavior of highly deformed risers and pipelines, J. Offshore Mech. Arct. Eng. 132 (2) (2010).

[7] L. A. Vega, Oceanocean thermal energy conversion, in: Meyers, R.A. (Ed.), Encyclopedia of Sustainability Science and Technology, Vol. 6, Springer, New York, NY, 2012, pp. 7296–7328.

[8] M. P. Païdoussis, Dynamics of a cantilevered pipe subjected to internal and reverse external axial flow: A review, J. Fluids Struct. 106 (2021) 103349.

[9] M. Chehreghani, A. R. Abdelbaki, A. K. Misra, M. P. Païdoussis, Experiments on the dynamics of a cantilevered pipe conveying fluid and subjected to reverse annular flow, J. Sound Vib. 515 (2021) 116480.

[10] H. Ashley, G. Haviland, Bending vibrations of a pipe line containing flowing fluid, J. Appl. Mech. ASME 17 (3) (1950) 229–232.

[11] G. W. Housner, Bending vibration of a pipeline containing flowing fluid, J. Appl. Mech. 19 (2) (1952) 205–208.

[12] F. Niordson, Vibrations of a cylindrical tube containing flowing fluid, in: Kungliga Tekniska Hogskolans Handlingar (Stockholm), No. 73, 1953.

[13] V. P. Feodos'ev, Vibrations and stability of a pipe when liquid flows through it, Inzhenernyi Sb. 10 (1) (1951) 69–70.

[14] T. B. Benjamin, Dynamics of a system of articulated pipes conveying fluid. I. Theory, Proc. R. Soc. London, Ser. A 261 (1307) (1961) 457–486.

[15] T. B. Benjamin, Dynamics of a system of articulated pipes conveying fluid. II. Experiments, Proc. R. Soc. London, Ser. A 261 (1961) 487–499.

[16] R. W. Gregory, M. P. Païdoussis, Unstable oscillation of tubular cantilevers conveying fluid. I. Theory, Proc. R. Soc. London, Ser. A 293 (1435) (1966) 512–527.

[17] R. W. Gregory, M. P. Païdoussis, Unstable oscillation of tubular cantilevers conveying fluid. II. Experiments, Proc. R. Soc. London, Ser. A (1435) (1966) 528–542.

[18] M. P. Païdoussis, E. B. Deksnis, Articulated models of cantilevers conveying fluid: the study of a paradox, J. Mech. Eng. Sci. 12 (4) (1970) 288–300.

[19] M. P. Païdoussis, Dynamics of tubular cantilevers conveying fluid, J. Mech. Eng. Sci. 12 (2) (1970) 85–103.

[20] J. L. Hill, C. P. Swanson, Effects of lumped masses on the stability of fluid conveying tubes, J. Appl. Mech. 37 (2) (1970) 494–497.

[21] S. S. Chen, Flow-induced instability of an elastic tube, in: Mech. Eng. ASME paper No. 71-Vibr-39, Vol. 93, New York, NY, 1971.

[22] S. S. Chen, J. A. Jendrzejczyk, General characteristics, transition, and control of instability of tubes conveying fluid, J. Acoust. Soc. Am. 77 (3) (1985) 887–895.

[23] M. P. Païdoussis, F. C. Moon, Nonlinear and chaotic fluidelastic vibrations of a flexible pipe conveying fluid, J. Fluids Struct. 2 (6) (1988) 567–591.

[24] Y. Modarres-Sadeghi, C. Semler, M. Wadham-Gagnon, M. P. Païdoussis, Dynamics of cantilevered pipes conveying fluid. Part 3: Three-dimensional dynamics in the presence of an end-mass, J. Fluids Struct. 23 (4) (2007) 589–603.

[25] T. S. Lundgren, P. R. Sethna, A. K. Bajaj, Stability boundaries for flow induced motions of tubes with an inclined terminal nozzle, J. Sound Vib. 64 (4) (1979) 553–571.

[26] X. Jian, H. Yuying, Bifurcations of a cantilevered pipe conveying steady fluid with a terminal nozzle, Acta Mech. Sin. 16 (3) (2000) 264–272.

[27] R. D. Firouz-Abadi, A. R. Askarian, M. Kheiri, Bending–torsional flutter of a cantilevered pipe conveying fluid with an inclined terminal nozzle, J. Sound Vib. 332 (12) (2013) 3002–3014.

[28] R. S. Reddy, S. Panda, G. Natarajan, Nonlinear dynamics of functionally graded pipes conveying hot fluid, Nonlinear Dyn. 99 (3) (2020) 1989–2010.

[29] Y. Guo, B. Zhu, Y. Li, Nonlinear dynamics of fluid-conveying composite pipes subjected to time-varying axial tension in sub-and super-critical regimes, Appl. Math. Model. 101 (2022) 632–653.

[30] W. Chen, L. Wang, Z. Peng, A magnetic control method for large-deformation vibration of cantilevered pipe conveying fluid, Nonlinear Dyn. 105 (2) (2021) 1459–1481.

[31] M. P. Païdoussis, G. X. Li, Pipes conveying fluid: a model dynamical problem, J. Fluids Struct. 7 (2) (1993) 137–204.

[32] P. J. Holmes, Bifurcations to divergence and flutter in flow-induced oscillations: a finite dimensional analysis, J. Sound Vib. 53 (4) (1977) 471–503.

[33] P. J. Holmes, Pipes supported at both ends cannot flutter, J. Appl. Mech. 45 (3) (1978) 619–622.

[34] M. P. Païdoussis, N. T. Issid, Dynamic stability of pipes conveying fluid, J. Sound Vib. 33 (3) (1974) 267–294.

[35] A. K. Bajaj, P. R. Sethna, T. S. Lundgren, Hopf bifurcation phenomena in tubes carrying a fluid, SIAM J. Appl. Math. 39 (2) (1980) 213–230.

[36] J. Rousselet, G. Herrmann, Dynamic behavior of continuous cantilevered pipes conveying fluid near critical velocities, J. Appl. Mech. 48 (4) (1981) 943–947.

[37] A. K. Bajaj, P. R. Sethna, Effect of symmetry-breaking perturbations on flow-induced oscillations in tubes, J. Fluids Struct. 5 (6) (1991) 651–679.

[38] M. P. Païdoussis, C. Semler, Nonlinear and chaotic oscillations of a constrained cantilevered pipe conveying fluid: a full nonlinear analysis, Nonlinear Dyn. 4 (6) (1993) 655–670.

[39] F. C. Moon, Chaotic and Fractal Dynamics: Introduction for Applied Scientists and Engineers, John Wiley & Sons, New York, 2008.

[40] K. Yamashita, T. Yagyu, H. Yabuno, Nonlinear interactions between unstable oscillatory modes in a cantilevered pipe conveying fluid, Nonlinear Dyn. 98 (4) (2019) 2927–2938.

[41] K. Zhou, Q. Ni, L. Wang, H. L. Dai, Planar and non-planar vibrations of a fluid-conveying cantilevered pipe subjected to axial base excitation, Nonlinear Dyn. 99 (4) (2020) 2527–2549.

[42] M. P. Païdoussis, Fluid-Structure Interactions: Slender Structures and Axial Flow, Vol. 1, 2nd edition, Academic Press, Oxford, 2014.

[43] M. P. Païdoussis, Aspirating pipes do not flutter at infinitesimally small flow, J. Fluids Struct. 13 (3) (1999) 419–425.

[44] R. Hisamatsu, T. Utsunomiya, Free vibration and stability of a fully submerged pipe aspirating water: An experiment and new physical insights, J. Fluids Struct. 116 (2023) 103789.

[45] M. P. Païdoussis, T. P. Luu, Dynamics of a Pipe Aspirating Fluid Such as Might be Used in Ocean Mining, J. Energy Resour. Technol. 107 (2) (1985) 250–255.

[46] G. L. Kuiper, A. V. Metrikine, Dynamic stability of a submerged, free-hanging riser conveying fluid, J. Sound Vib. 280 (3-5) (2005) 1051–1065.

[47] M. P. Païdoussis, C. Semler, M. Wadham-Gagnon, A reappraisal of why aspirating pipes do not flutter at infinitesimal flow, J. Fluids Struct. 20 (1) (2005) 147–156.

[48] G. L. Kuiper, A. V. Metrikine, Experimental investigation of dynamic stability of a cantilever pipe aspirating fluid, J. Fluids Struct. 24 (4) (2008) 541–558.

[49] S. Rinaldi, Experiments on the dynamics of cantilevered pipes subjected to internal and/or external axial flow, Master's thesis, Department of Mechanical Engineering, McGill University, Montreal, QC, Canada (2009).

[50] D. B. Giacobbi, The Dynamics of Aspirating Cantilevered Pipes and Pipes Conveying Variable Density Fluid, Master's thesis, Department of Mechanical Engineering, McGill University, Montreal, QC, Canada (2010).

[51] M. F. J. Butt, The dynamics of hanging tubular cantilevers simultaneously subjected to internal and external axial flows, Ph.D. thesis, Department of Mechanical Engineering, McGill University (2021).

[52] Y. Ma, Y. You, A. Feng, K. Chen, Experimental and analytical investigation of dynamic stability of a cantilevered pipe aspirating fluid, in: OnePetro, 32nd Int. Ocean Polar Eng. Conf., 2022.

[53] C. Zhou, Y. Yang, J. Wang, Q. Wu, Z. Gu, Y. Zhou, X. Liu, Y. Yang, H. Tang, Q. Ling, L. Wang, J. Zang, Ferromagnetic soft catheter robots for minimally invasive bioprinting, Nat. Commun. 12 (1) (2021) 1–12.

[54] J. S. Chung, A. K. Whitney, Axial stretching oscillation of an 18,000-ft vertical pipe in the ocean, J. Energy Resour. Technol. 105 (2) (1983) 195–200.

[55] S. Kaewunruen, J. Chiravatchradej, S. Chucheepsakul, Nonlinear free vibrations of marine risers/pipes transporting fluid, Ocean Eng. 32 (3-4) (2005) 417–440.

[56] L. A. Vega, Ocean Thermal Energy Conversion, Springer New York, New York, NY, 2013, pp. 1273–1305.

[57] R. Bishop, I. Fawzy, Free and forced oscillation of a vertical tube containing a flowing fluid, Philosophical Transactions of the Royal Society of London. Ser. A, Mathematical and Physical Sciences 284 (1316) (1976) 1–47.

[58] A. K. Misra, M. P. Païdoussis, K. S. Van, On the dynamics of curved pipes transporting fluid. Part I: Inextensible theory, J. Fluids Struct. 2 (3) (1988) 221–244.

[59] A. K. Misra, M. P. Païdoussis, K. S. Van, On the dynamics of curved pipes transporting fluid Part II: Extensible theory, J. Fluids Struct. 2 (3) (1988) 245–261.

[60] A. Czerwiński, J. Łuczko, Nonlinear vibrations of planar curved pipes conveying fluid, J. Sound Vib. 501 (2021) 116054.

[61] L. Yun-dong, S. Ze-gang, Analysis of planar motion for curved pipe conveying fluid with different types of initial configuration, J. Vib. Eng. Technol. (2021) 1–16.

[62] K. Zhou, Q. Ni, W. Chen, H. L. Dai, P. Hagedorn, L. Wang, Static equilibrium configuration and nonlinear dynamics of slightly curved cantilevered pipe conveying fluid, J. Sound Vib. 490 (2021) 115711.

[63] W. Chen, K. Zhou, L. Wang, Z. Yin, Geometrically exact model and dynamics of cantilevered curved pipe conveying fluid, J. Sound Vib. (2022) 117074.

[64] K. Zhou, H. R. Yi, H. L. Dai, H. Yan, Z. L. Guo, F. R. Xiong, Q. Ni, P. Hagedorn, L. Wang, Nonlinear analysis of L-shaped pipe conveying fluid with the aid of absolute nodal coordinate formulation, Nonlinear Dyn. 107 (1) (2022) 391–412.

[65] E. Naudascher, D. Rockwell, Flow-Induced Vibrations: An Engineering Guide, Courier Corporation, North Chelmsford, MA, 2012.

[66] A. Wolf, J. B. Swift, H. L. Swinney, J. A. Vastano, Determining Lyapunov exponents from a time series, Phys. D Nonlinear Phenom. 16 (3) (1985) 285–317.

Complementary discussion on system I

Further discussion is presented here to clarify and expand on some points, in addition to what is included in the first manuscript presented in this thesis [1].

- The term "semi-circular" used in the caption of Fig. 2.2 to describe the curvature of the pipe used in the experiments can be misleading and is a poor choice of word. It is a generic term and does not mean that the pipe is exactly a part of a circle, nor does it imply that the curvature can be described with a radius of curvature. As discussed, the initial curvature of the pipe when hung in the air can be modeled with a linear combination of cantilever beam eigenfunctions, as described in Eqs. (2.1)-(2.3).

- As discussed in the manuscript [1], additional experiments were conducted using a pipe with a greater initial curvature than the one shown in Fig. 2.2(b), primarily in the second mode. With increasing flow velocity, the pre-instability static deformation of this pipe became so large that the middle section became nearly horizontal, causing the red tracking spot to be obscured from view through the pressure vessel windows. Consequently, it was impossible to monitor the pipe motion with the camera system, making the measurement infeasible. Despite this, it was observed that this pipe became unstable via flutter at a lower flow velocity as compared to the straight pipe, specifically at $u \simeq 4.90$ ($U \simeq 5.37$ m/s), whereas the straight pipe experienced flutter at $u = 5.91$. Therefore, the onset of flutter for a curved pipe may or may not be higher than that for a straight pipe, depending on the static equilibrium configuration just prior to instability. To explore this further, additional experiments using pipes with different curvature shapes (modes) and varying degrees of curvature are needed.

CHAPTER 3

Dynamics of Free-Clamped Cylinders in Axial Flow: An Experimental Investigation

Preface

This chapter is devoted to the dynamics of system II, studied in the second manuscript presented in this thesis. System II involves an inverted cantilevered cylinder in external axial flow, with the flow directed from the free end towards the fixed one, as opposed to the conventional flow direction in early studies on cantilevered systems in axial flow, where the flow was directed from the clamped end towards the free one. This "reverse flow" configuration has recently attracted attention due to its interesting dynamical behaviour (academic interest) and its potential applications, such as control rods in nuclear reactors and energy harvesting.

In alignment with the second objective of the present thesis stated in the Introduction and aiming at conducting a systematic experimental investigation and characterization of the instability of inverted cylinders in unconfined axial water flow, a series of water tunnel experiments on system II were preformed. In this study, the onset of instability and the post-instability behaviour of the system were explored and the mechanisms underlying the instability was briefly discussed. The results revealed that, generally, the reverse flow direction in the inverted cylinder system reverses all the essential features of the dynamics, as compared to the conventional flow configuration. In particular, with increasing flow velocity, the inverted cylinder exhibited: turbulence buffeting, weak unsteady flutter-like first-mode oscillations, and eventually, at high enough flow velocities, an abruptly occurring static divergence of large amplitude.

Additionally, utilizing flexible cylinders of various lengths and end shapes with an embedded thin metal strip, as well as neutrally buoyant hollow cylinders of various materials, the influence of the main system parameters were examined. Through these investigations, it was found that the free-end shape plays almost no role in the dynamics of the inverted cylinder, which sharply contrasts with the effect of this parameter for cylinders in the conventional flow direction.

Fluid-elastic instability of inverted cantilevered cylinders in axial flow

M. Chehreghani, I. Gholami, A.K. Misra, M.P. Païdoussis*

Department of Mechanical Engineering, McGill University,

817 Sherbrooke Street West, Montreal, QC, Canada H3A 0C3.

Abstract: This paper describes and analyzes water-tunnel experiments involving flexible cantilevered cylinders in reverse axial flow, i.e. flow directed from the free towards the fixed end of the cylinder. It was found that the cylinder is subjected to small amplitude motion due to turbulent buffeting prior to first-mode flutter at relatively low flow velocities, followed eventually by an abrupt static divergence at higher flows. The observed flutter was quite unsteady and sometimes near-intermittent. The flutter amplitude increased with flow, prior to the onset of static divergence. The onset of static divergence displayed strong hysteresis, suggesting a subcritical bifurcation. The static divergence amplitude for very flexible cylinders could be very large, such that the free end of the cylinder would face downstream. The influence of some system parameters was investigated, such as cylinder flexural rigidity, slenderness and free-end shape. The dynamics was found to be only marginally affected by the free-end shape, in sharp contrast to the dynamics of cylinders subjected to flow directed from the clamped towards the free end. Finally, the mechanisms underlying the onset of flutter and static divergence are discussed briefly.

Keywords: Flutter; Static divergence; Saddle-node bifurcation; Free-clamped cylinders; Axial flow.

3.1 Introduction

Stability of slender flexible cylindrical bodies subjected to axial flow has been studied for many years, not only because of applications, e.g. in heat-exchanger and nuclear reactor internals, but also in view of the interesting dynamical features displayed [1, 2]. Hawthorne [3] was the first to study the stability of a "Dracone", a quasi-cylindrical container towed by a ship. Païdoussis [4, 5] extended and generalized that work for cylinders in axial flow with different boundary conditions and conducted experiments to validate the analysis.

*Corresponding author.

E-mail addresses: mahdi.chehreghani@mail.mcgill.ca, iman.gholami@mail.mcgill.ca, arun.misra@mcgill.ca, michael.paidoussis@mcgill.ca

A more accurate linear model for pinned-pinned and cantilevered isolated/clustered slender cylinders in axial flow was established a little later [6]. The dynamical behaviour for isolated cylinders is as follows. For a sufficiently high flow velocity the cylinder becomes unstable by static divergence ("buckling") of moderate amplitude. At higher flow velocities the cylinder develops flutter — single-mode flutter for cantilevered cylinders and coupled-mode flutter for cylinders with supported ends. The existence of coupled-mode flutter for cylinders with supported ends is associated with the peculiar viscous forces of the external fluid flow, and it has been observed experimentally [1]. In the closely related problem of pipes conveying fluid, although linear theory predicts coupled-mode flutter, it was shown by Holmes [7] that it cannot occur; and, indeed, it has never been observed.

Focusing on the physical dynamics and the mechanism of instability, Païdoussis et al. [8] further explored the stability of cantilevered cylinders subjected to axial flow in the conventional direction, i.e. flow directed from the clamped towards the free end. It was found that stability is greatly dependent on the shape of the free end. Generally, cantilevered cylinders with a well-streamlined end-shape lose stability by divergence at sufficiently high flow velocities, followed by a single-mode flutter at still higher flow rates, whereas cylinders with a blunt free end remain stable. Further important work has been done more recently by Kheiri and Païdoussis [9], Perets et al. [10] and Tabatabaei et al. [11].

Important related work on towed cylinders has been conducted by Païdoussis [12], Triantafyllou and Chryssostomidis [13, 14] and Dowling [15, 16], on locomotion of slender fish by Taylor [17], Lighthill [18, 19] and Triantafyllou et al. [20], on energy harvesting from fluttering cylinders in axial flow by Singh et al. [21] — citing only some of the papers in these areas.

We next consider the dynamics of cantilevered cylinders in reverse flow, i.e. with the flow directed from the free towards the clamped end, often referred to as *inverted* cylinders, or free-clamped cylinders, in axial flow. The stability of an inverted cantilevered vertical cylinder in confined axial air-flow was investigated for the first time by Rinaldi and Païdoussis [22]. In the experiments, at relatively low flow velocities, small-amplitude first-mode unsteady flutter-like oscillations were observed. At higher flow velocities, the oscillatory motion decreased and a static divergence (buckling) developed. However, the only instability

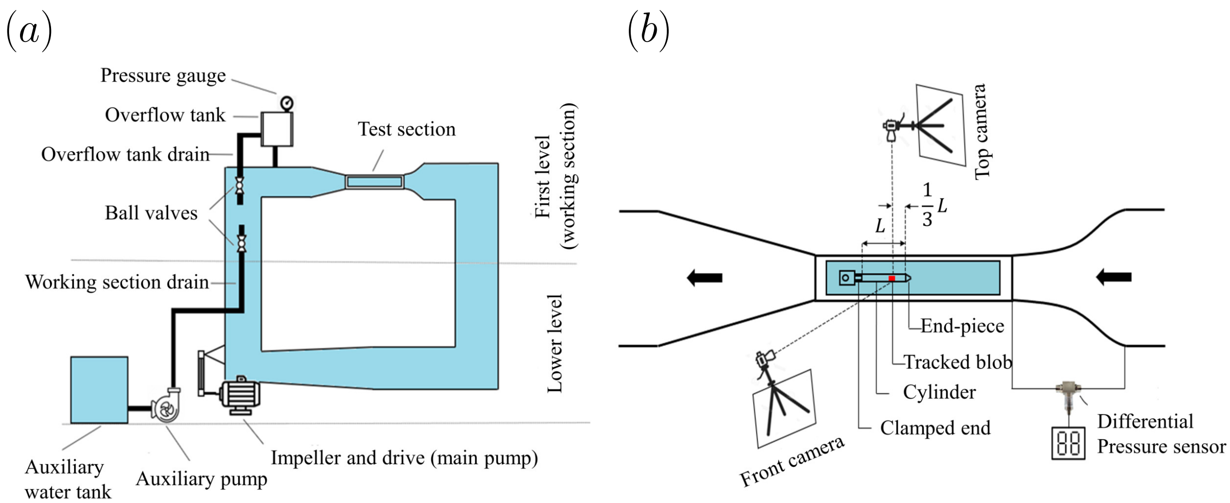

Figure 3.1: Schematic view of (a) the water tunnel; (b) the test-section with the data acquisition systems.

predicted by linear theory was static divergence at sufficiently high flow velocities.

Using the same parameters as in Rinaldi and Païdoussis [22] and a nonlinear static analysis, the stability of inverted cylinders was examined by Sader et al. [23]. It was found that slender inverted cylinders are never globally unstable; a saddle-node bifurcation, which is followed by a statically stable solution at higher velocities, was predicted. As compared to Rinaldi and Païdoussis [22], a critical velocity in closer agreement with experiment was obtained. More recently, an improved linear model for this system was presented by Rinaldi and Païdoussis [24]. This model predicts the dynamics of the system as follows: flutter at relatively low flow velocities and then static divergence at higher flow rates. The critical flow velocities obtained for both flutter and static divergence are in fairly good agreement with the experimental results.

This "reverse flow" configuration has recently attracted attention, not only because it displays interesting dynamical behaviour, but also because of potential applications in green-energy harvesting [25]. Also, many studies have investigated the flapping dynamics of inverted thin flexible plates or "flags" [23, 26–30]. Another significant engineering application is related to reverse axial flow in "solution-mined caverns" utilized to store hydrocarbons therein. In this application, a cantilevered pipe with an internal flow is subjected to an external annular flow in the reverse direction [31–33]. Additionally, some studies deal with the

Table 3.1: Dimensions and material properties of the flexible cylinders used in the experiments.

Cylinder	Material	EI [N m^2]	m [kg m^{-1}]	D [mm]	L [mm]
I	Silicone–rubber with metal strip	9.29 $\times 10^{-3}$	0.185	16	140
II	Silicone–rubber with metal strip	9.29 $\times 10^{-3}$	0.185	16	210
III	Silicone–rubber with metal strip	9.29 $\times 10^{-3}$	0.185	16	280
IV	Silicone–rubber without metal strip	4.54 $\times 10^{-3}$	0.134	16	140
V	Santoprene without metal strip	4.04 $\times 10^{-3}$	0.068	13	140

dynamics of cantilevered rods in reverse flow in nuclear reactor applications [34–38].

A fuller literature review is provided by Païdoussis [2]. However, it is evident from the foregoing literature survey that, up to now, to the best of authors' knowledge, apart from the Rinaldi and Païdoussis [22] rather limited set of experiments with cylinders in confined air-flow, there has been no other experimental work on the dynamics of the inverted system. Motivated by this lacuna, the main purpose of the present work is the systematic experimental study and characterization of the instability of free-clamped cylinders subjected to essentially unconfined axial water flow, in the facility shown in the schematics of Fig. 3.1 and in the photograph of Fig. 3.2. Conducting the experiments in a water tunnel with essentially no confinement provides us with the opportunity to investigate the large-amplitude post-instability dynamics of the system.

In this paper, the onset of instability as well as the post-critical behaviour of the system is investigated for planar or three-dimensional motions of cylinders of various lengths, end-piece shapes and material properties. The qualitative and quantitative effects of system parameters on the threshold, amplitude and frequency of instabilities are examined. The experimental results presented are helpful for validating and developing 2D and 3D analytical, as well as numerical models. Also, some insights explaining the physical dynamics and the mechanisms of instability are provided.

The rest of the paper is structured as follows. In Section 3.2, the experimental set-up and methodology are described. The experimental results are presented in Section 3.3. The mechanisms underlying the onset of flutter and static divergence is discussed in Section 3.4. Finally, Section 3.5 is devoted to concluding remarks.

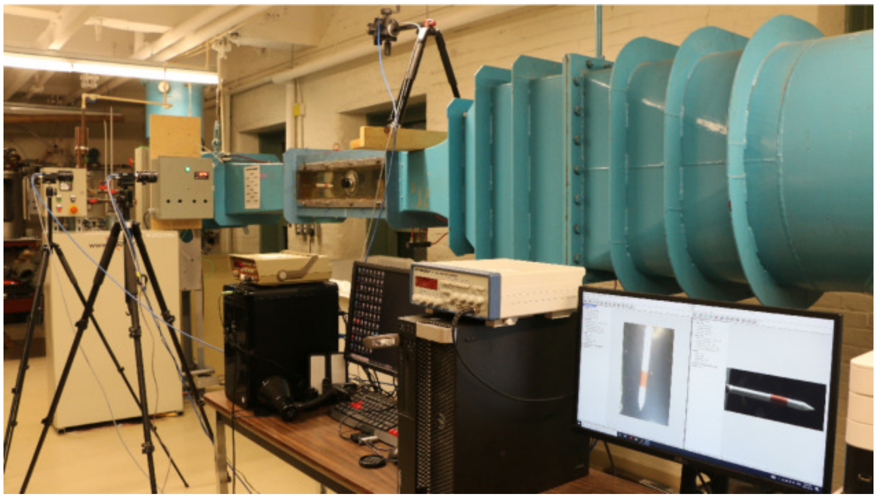

Figure 3.2: The water tunnel with a synchronized dual-camera system used to track the motion of the cylinder.

3.2 Experimental set-up, data acquisition and methodology

The Kempf & Remmers water tunnel with a fairly large horizontal test-section, shown in Fig. 3.2, was used in this experimental investigation. This tunnel spans two floors, with the test-section and control units located in the upper level; refer to Fig. 3.1. The test-section is about 1 m long with a 260 mm $\times$ 260 mm square cross-section. Rectangular plexiglas windows on the four sides of the test-section allow access and viewing.

The test specimens were flexible cylinders with material properties and dimensions as listed in Table 3.1. EI denotes the flexural rigidity of the cylinder, m its mass per unit length, D its diameter and L its length. The silicone-rubber (silastic RTV) cylinders were manufactured by casting a liquid silicone-rubber mixture in the manner described in Appendix D of Païdoussis [39]. Some of them integrally contained a thin metal strip, embedded in them during casting; when mounting these cylinders in the test-section the blade was in a vertical plane, ensuring that the cylinder is horizontal at equilibrium and forcing the oscillation to occur in 2D — also facilitating eventual comparison with a simple 2D analytical model. Otherwise, the cylinder was made hollow, in a way that when submerged in water it would be neutrally buoyant. Cylinder V was a commercial santoprene cylinder.

Three shapes of rigid 'end-pieces' of length l = 17.5 mm and almost the same density as the cylinder were used to examine their effect on stability; the first had a sharp conical shape and the second one was of a well-streamlined ogival shape; the third was a blunt end. The internal damping of the elastomer cylinders used in these experiments is considerable. A two-parameter visco-hysteretic dissipative model was found to best describe the damping characteristics of the elastomer cylinders. A description of this model and typical values of the coefficients involved for cylinders with and without an embedded metal strip are given in Rinaldi [40] and in Appendix D of Païdoussis [39]. An outline of the model and some typical values of the two parameters involved are given in the Appendix A. However, it should be remarked that damping of the cylinder in axial flow is overwhelmingly determined by frictional flow effects, rather than material damping [41].

To guarantee a uniform axial flow stream in the test-section, screens and a large flow-area contraction are utilized in the water tunnel upstream of the test-section. At flow velocities for which fluid-elastic instabilities took place, the Reynolds number was high enough to be in the turbulent flow regime, thereby allowing us to assume a flat velocity profile in the central part of the test-section. The maximum flow velocity attained in the test section of the water tunnel is 15 m/s, and the turbulence intensity does not exceed 0.5%.

Two different methods were used to measure the flow velocity in the test-section. For very low flow velocities, i.e. $U < 0.5$ m/s, a high-speed camera system (80-200 frames per second) was utilized to follow a small particle suspended in the water as it travelled a predetermined distance, measuring the travel time. For higher flow velocities, a differential pressure transducer was employed, determining the static pressure difference between the contraction area and a point just upstream of the test-section; refer to Fig. 3.1(b).

Non-contacting techniques have been used to capture cylinder motions. More specifically, through two transparent windows of the water tunnel perpendicular to each other, the motion of the centroid of a 'red-marked' 36 mm long region was tracked and recorded, using two synchronized identical FLIR® Grasshopper3 2.3 MP high-speed cameras. The centroid of this red-marked region, referred to as the "tracked blob" in Fig. 3.1(b), was located at $L/3$ from the free-end of the cylinder. The two cameras were triggered via a function generator to ensure synchronization.

In every experiment the flow velocity was increased step-wise to the first instability, and beyond that to static divergence. At each increment, the water tunnel was kept running

Table 3.2: Conversion factors between dimensional and dimensionless flow velocity and frequency.

Cylinder	I	II	III	IV	V
U(m/s)/u	1.54	1.02	0.768	1.07	1.25
f(Hz)/ω	1.26	0.560	0.315	0.945	1.15

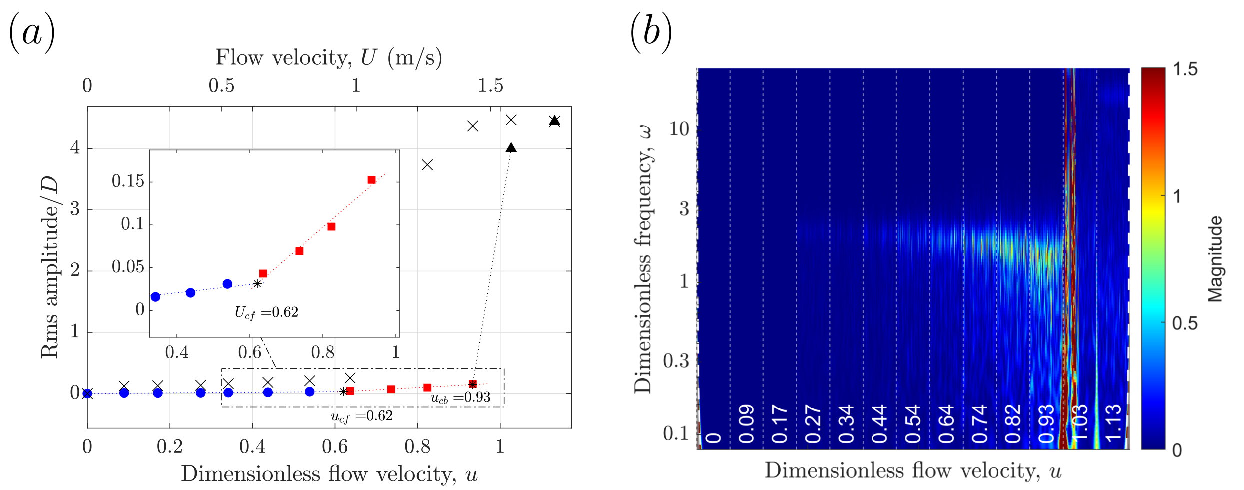

Figure 3.3: Dynamics of cylinder I-C (cylinder I with a conical end-piece) illustrated by means of (a) bifurcation diagram showing the rms amplitude of motions versus increasing flow velocity, (●) pre-instability, (■) flutter, (▲) static divergence, and (×) with decreasing flow velocity; (b) Morse wavelet scalogram in which the vertical strips correspond to discrete values of the flow velocity.

for a while to approach steady state. Then, using a dual-camera system, the motion of the cylinder was tracked and recorded for a duration of 3 minutes. To guarantee validity and consistency of the results, each experiment was repeated at least once.

Subsequently, an image-processing Matlab (Mathworks, Inc.) script was utilized to extract the displacement-time series from the recorded videos from both top and side cameras. The initial undeformed location of the cylinder at zero flow velocity served as a reference. More details on the image processing may be found in Chehreghani et al. [33]. The obtained time series data were further processed. Specifically, the nature of the motions could be determined by means of bifurcation diagrams, time traces, phase portraits, PSDs, PDFs and position-triggered Poincaré maps.

3.3 General observations and results

This being an experimental paper, it is considered important to give at least some of the results in dimensional terms. However, to facilitate comparison with results to be obtained in future by other researchers, most results are also given in dimensionless form. To this end, we employ the dimensionless flow velocity, u, and frequency, ω, extensively utilized in the past [1, 4], as follows:

$$u = \left(\frac{\rho_f A}{EI}\right)^{1/2} LU, \qquad \omega = \left(\frac{\rho_f A + m}{EI}\right)^{1/2} L^2\Omega, \tag{3.1}$$

where EI is the flexural rigidity of the cylinder and m its mass per length, U is the mean flow velocity, ρ_f is the fluid density, $A = \frac{1}{4}\pi D^2$, D being cylinder diameter and $\Omega = 2\pi f$ is the radian frequency, with f in Hz. The conversion factors from dimensionless to dimensional terms for the five cylinders of Table 3.1 are given in Table 3.2.

3.3.1 Dynamics of inverted cylinders with an embedded metal strip

Fig. 3.3(a) presents the experimental bifurcation diagram for cylinder I (refer to Table 3.1) with a conical end-piece, displaying the rms of displacement amplitude as a function of the flow velocity. At very low flow rates, i.e., $u < 0.27$ ($U < 0.42$ m/s), the cylinder stayed more or less stationary at its initial undeformed position. At $u = 0.27$ m/s, however, very weak small amplitude motions initiated. These weak motions were likely excited by turbulence in the flow (turbulent buffeting). At $u > 0.62$ ($U > 0.95$ m/s), considerably stronger oscillations were observed, distinguishable by a change in the slope in the bifurcation diagram and with a distinct dominant frequency of oscillations $\omega \simeq 1.87$ ($\simeq 2.36$ Hz), refer to Fig. 3.3(b), demonstrating the onset of self-excited flutter in the first mode – a "movement-induced instability" in the Naudascher and Rockwell [42] classification. It should be remarked that the graphical determination of the onset of instability is in practice the best approach. Increasing the flow velocity further gave rise to oscillations of higher amplitude with almost the same dominant frequency. During these oscillations, the cylinder tended to slightly move towards one side, which is attributed to imperfections in the clamping of the fixed end. Alternatively, this could be a flow-induced biased oscillatory motion, as observed in numerical simulations for inverted flags by Ryu et al. [43].

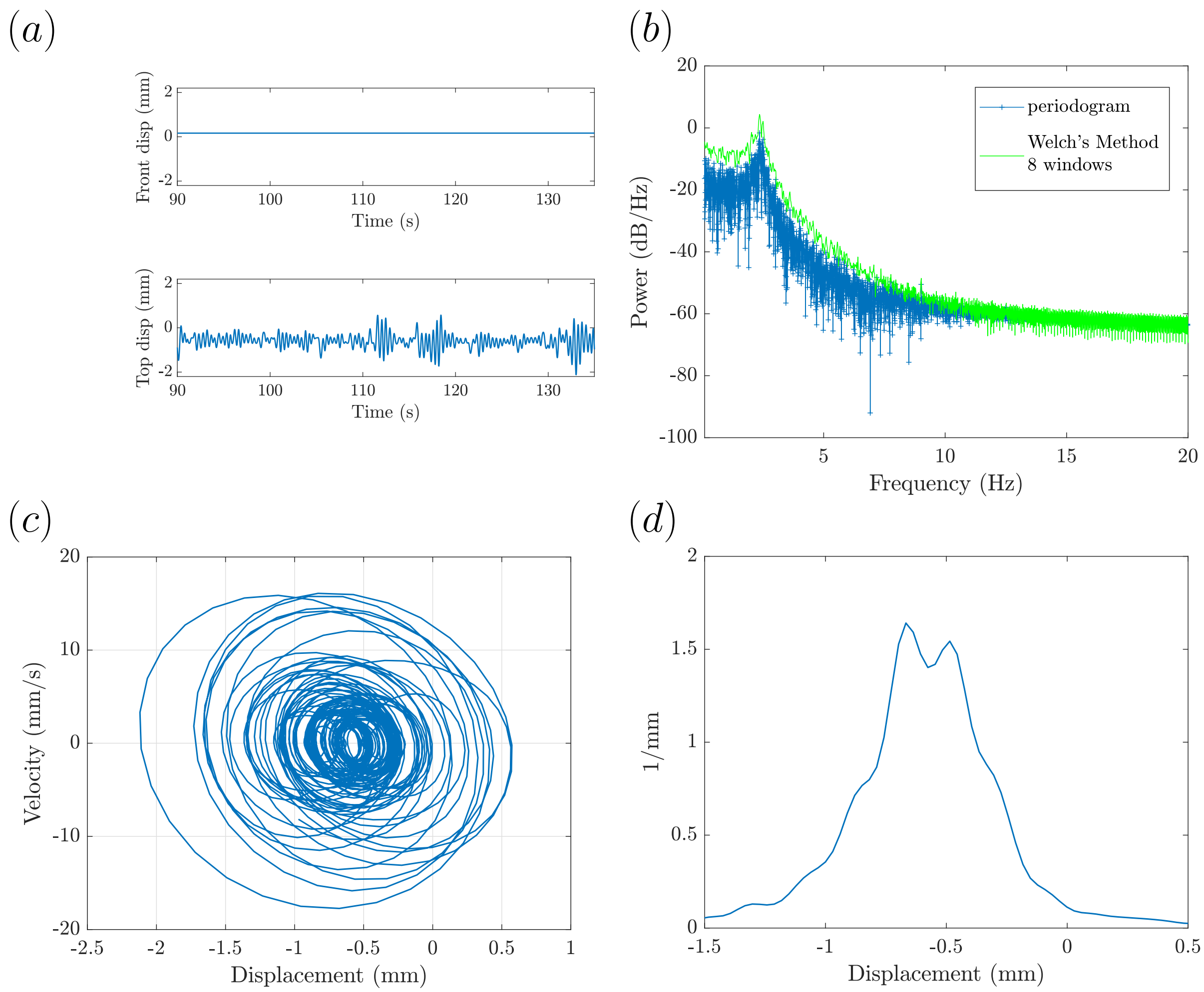

Figure 3.4: Dynamics of cylinder I-C right after the threshold of flutter at $u = 0.64$ ($U = 0.98$ m/s), represented through (a) time traces of the front and top displacements, (b) PSD of motions, (c) phase portraits of the top displacement, and (d) PDF of top displacement.

At still higher flow velocities, the cylinder suffered an abrupt static divergence in its first mode at $u = 0.93$ ($U > 1.43$ m/s), and eventually it started impacting on the walls of the water tunnel. As shown in Fig. 3.3, while decreasing the flow velocity down to $u = 0.62$ ($U = 0.95$ m/s), the cylinder remained in its buckled position, displaying a strong hysteresis; thus the onset of static divergence is associated with a subcritical bifurcation. Static divergence is usually associated with a pitchfork bifurcation, implying that the system was previously at equilibrium. This is not the case here, however, as there is no restabilization between flutter and static divergence; the cylinder switches abruptly from large-amplitude flutter to static divergence. Therefore, the alternative view of the observed behaviour by

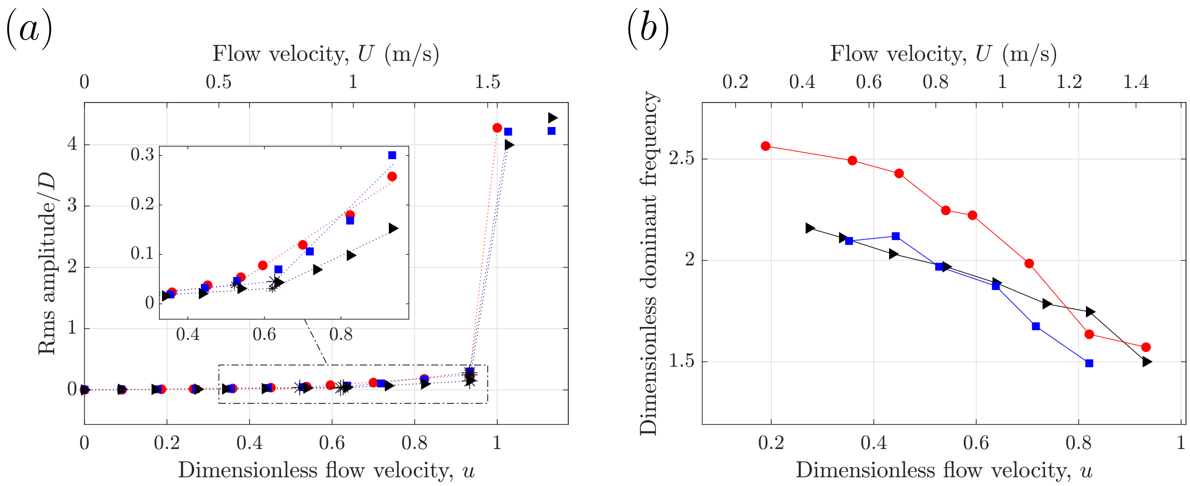

Figure 3.5: Comparing the dynamics of cylinder I with (●) an ogival end-shape, I-O, (▶) conical end-shape, I-C, and (■) blunt end-shape, I-B, by means of (a) bifurcation diagrams showing the rms amplitude of motions versus flow velocity; (b) dominant dimensionless frequency of oscillations, ω, at each flow velocity step.

Sader et al. [23] may be more appropriate: that the observed static divergence is generated via a saddle-node bifurcation. This is discussed further in Section 3.4. In what follows we shall simply refer to the phenomenon as static divergence.

Dynamics of the system at $u = 0.64$ ($U = 0.98$ m/s), right after the threshold of flutter, is explored further by means of the sample results in Fig. 3.4. The time traces captured by the front and top cameras in Fig. 3.4(a) display unsteady, near-intermittent planar oscillations and suggest the existence of a chaotic component in the dynamics of the system. Fig. 3.4(b) shows the power spectral density of the time series captured by the top camera. This PSD indicates a dominant frequency of $f = 2.36$ Hz, which corresponds to first-mode oscillations. Furthermore, the phase portrait and probability density function plots of the side displacement presented in Fig. 3.4(c,d) indicate a periodic motion; but, given the unsteadiness and chaotic component of the oscillations, intermittency may well be a possible route to chaos.

3.3.1.1 The effect of end-piece shape

As observed by [5] and discussed by [8] for the case of a clamped-free cylinder in axial flow, with the flow directed from the clamped end towards the free end, the end-shape plays

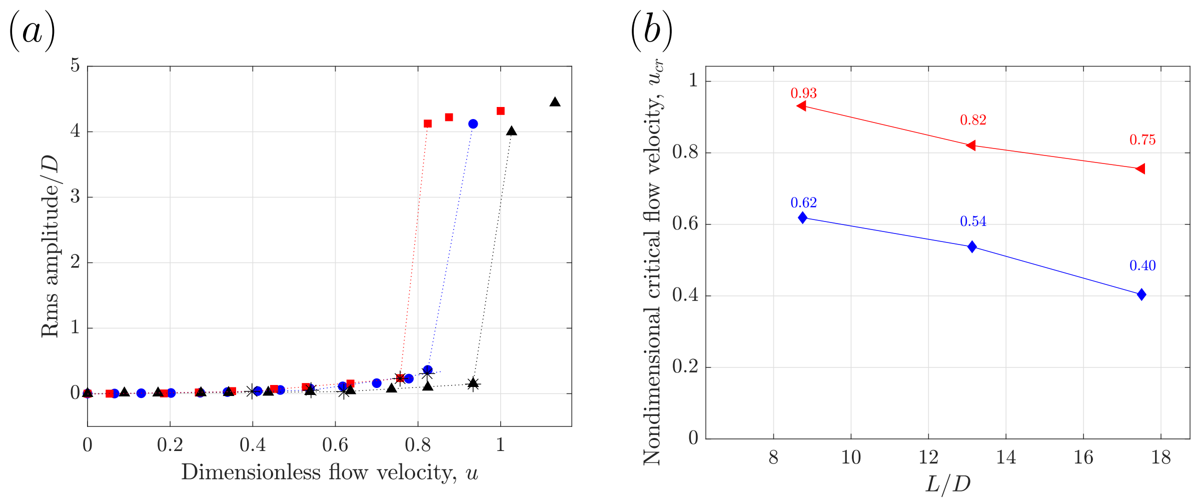

Figure 3.6: Comparing the dynamics of cylinders with various lengths: (a) bifurcation diagram for (▲) cylinder I-C, (●) cylinder II-C and (■) cylinder III-C, all with a conical end-shape; (b) critical flow velocities for flutter (♦) and static divergence (◀).

a very significant role in the stability of the system. It was demonstrated that clamped-free cylinders in axial flow lose stability by divergence at sufficiently high flow velocities and, at still higher flow rates, single-mode flutter occurs, provided that the free end is well-streamlined; but, if the free end is blunt, neither static divergence nor flutter materialize.

Fig. 3.5(a) compares the bifurcation diagrams for inverted (free-clamped) cylinder I with an ogival end-shape, I-O, a conical end-shape, I-C, and a blunt end-shape, I-B. It is seen that the effect of end-shape is marginal for inverted cantilevered cylinders, in contrast to the system with the opposite flow direction; the qualitative behaviour displayed in Fig. 3.5(a) is similar. Quantitatively, however, the onset of flutter changed to some extent from $u = 0.52$ ($U = 0.80$ m/s) for the ogival one and to $u = 0.62$ (0.96 m/s) for the conical one, and to $u = 0.62$ ($U = 0.96$ m/s) for the blunt one; yet, the onset of static divergence was unaffected. Fig. 3.5(b) compares the dominant frequency of motions, displaying a monotonically decreasing trend with increasing flow velocity in all cases. Note that the lowest of the dominant dimensionless frequencies, $\omega \simeq 1.5$, correspond to $f \simeq 1.89$ Hz, which is not very small, again suggesting that the observed static divergence does not develop via a pitchfork bifurcation, the classical static-divergence route.

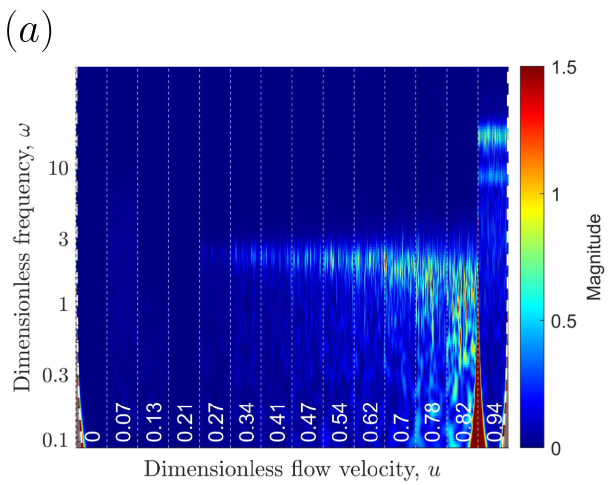

Figure 3.7: Morse wavelet scalograms representing the distribution of frequencies at each flow velocity (a) for cylinder II-C and (b) for cylinder III-C.

3.3.1.2 The effect of slenderness

The influence of length-to-diameter ratio was examined by conducting experiments with cylinders II and III. They both have the same characteristics as cylinder I, but different L/D. In all cases, a conical end-piece was utilized. The rms amplitude of motions plotted against the flow velocity for cylinders I-C, II-C and III-C is shown in Fig. 3.6(a). The qualitative behaviour is similar: first flutter in the first mode at relatively low flow velocities, and static divergence at higher flow velocities. Quantitatively, however, varying the L/D affects the onset of both oscillatory and static fluid-elastic instabilities, especially the latter one, as shown in Fig. 3.6(b). Thus, u is not a sufficient dimensionless parameter to collapse the dynamical behaviour to constant values of $u = u_{cr}$. This is discussed in Section 3.3.3.

The variation of frequency spectrum with flow velocity for cylinders II-C and III-C is shown in Fig. 3.7. In the case of cylinder III-C, the longer one, strong high frequencies are noticeable. These high frequencies vary approximately linearly with increasing flow velocity and they could be attributed to vortex shedding. The post-divergence behaviour can be further investigated, as there are enough post-divergence velocity steps in this case. The dynamics of the system just after the initiation of static divergence, at $u = 0.82$ ($U = 0.63$ m/s), is illustrated in Fig. 3.8. The dominant frequencies in the PSD plot of Fig. 3.8(d) are harmonics: $f_1 \simeq 2.8$ Hz, $f_2 = 2f_1 \simeq 5.6$ Hz, $f_3 = 3f_1 \simeq 8.4$ Hz and $f_4 = 4f_1 \simeq 11.2$ Hz,

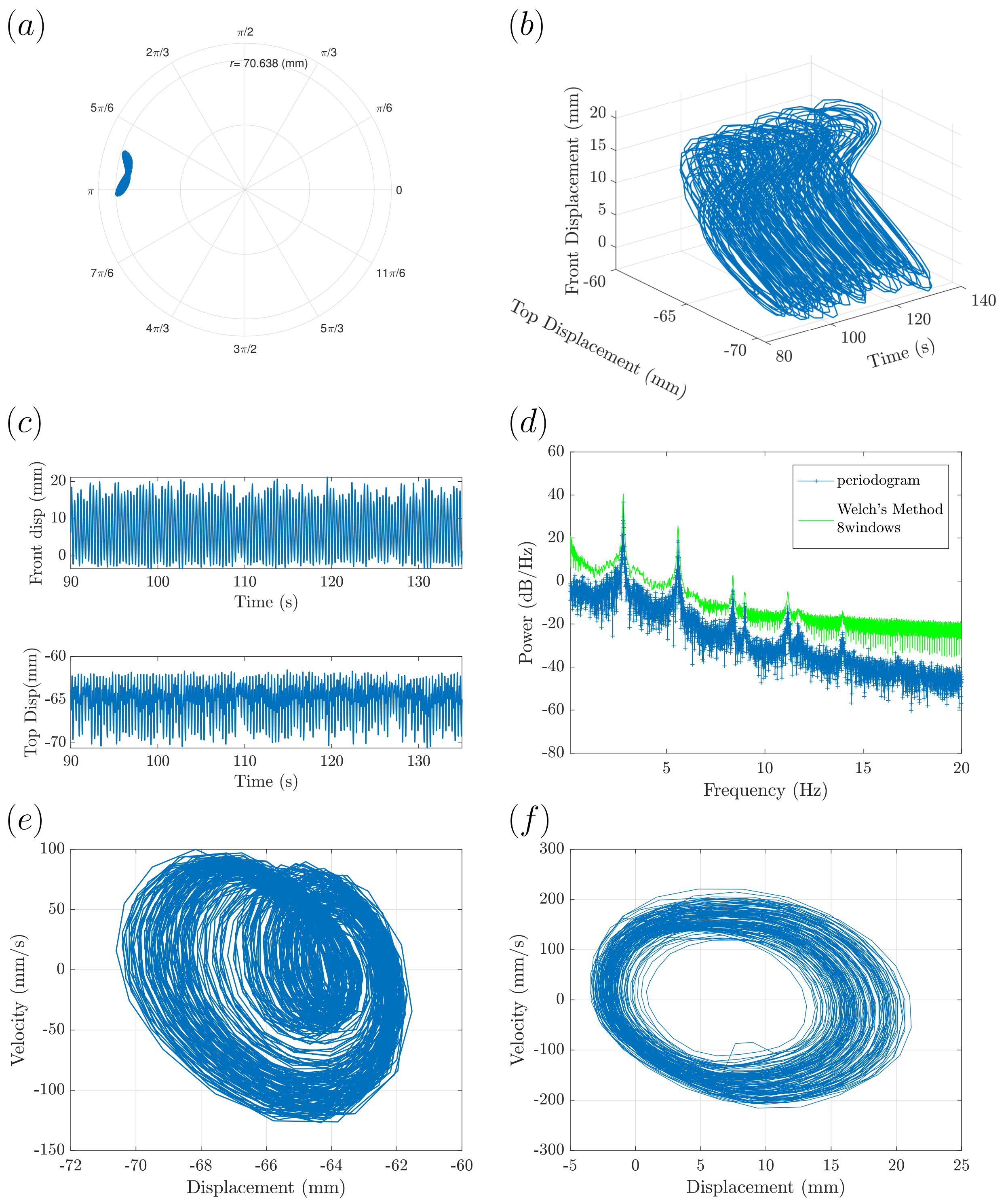

Figure 3.8: The post-divergence dynamics of cylinder III-C at $u = 0.82$ ($U = 0.63$ m/s) illustrated by means of (a) polar plot, (b) 3D trajectory of motion, (c) time traces of the front and top displacements, (d) PSD of top displacements, (e,f) phase portraits of the top and front displacements, respectively.

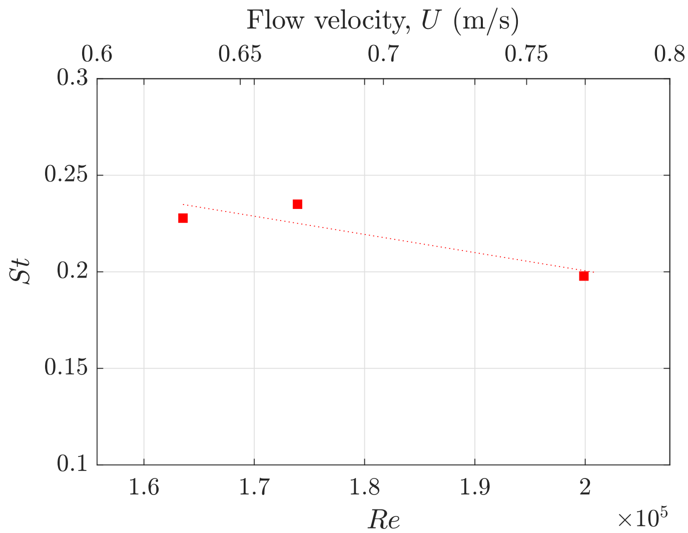

Figure 3.9: Strouhal numbers calculated based on the frequency associated with vortex shedding, f_{vs}, versus flow velocity for post-divergence of cylinder III-C.

except for the odd one, $f_o = 8.97$ Hz, which gives a Strouhal number $St = 0.23$, suggesting the frequency in this case is associated with vortex shedding; thus, $f_o = f_{vs}$. It should be highlighted that in the post-divergence state of the cylinder there is a considerable amount of cross-flow. Therefore, the existence of vortex shedding is possible. However, having not conducted flow visualization, it cannot be claimed that regular vortex shedding does in fact occur. Comparing Fig. 3.8(e) to Fig. 3.8(f), the double loop in the former suggests a figure-of-eight oscillation pattern. This pattern is visualized in the polar plot and 3D trajectories of Fig. 3.8(a,b). Fig. 3.9 presents the Strouhal numbers calculated based on f_{vs} at post-divergence flow velocities. The values of St are not too far from 0.2, which is the Strouhal number associated with vortex shedding for the ideal case of a long straight and immobile cylinder in cross-flow.

3.3.2 Dynamics of inverted cylinders able to move in 3D

The 3D dynamics of the system with cylinders made of different materials was investigated using cylinders IV-C and V-C, namely a silicone-rubber and a santoprene cylinder, both with the conical end-shape and no embedded metal blade. The bifurcation diagrams of rms amplitude versus flow velocity are shown in Fig. 3.10 for the two cylinders. Qualitatively, the same behaviour is displayed: the cylinder undergoes flutter at a relatively low

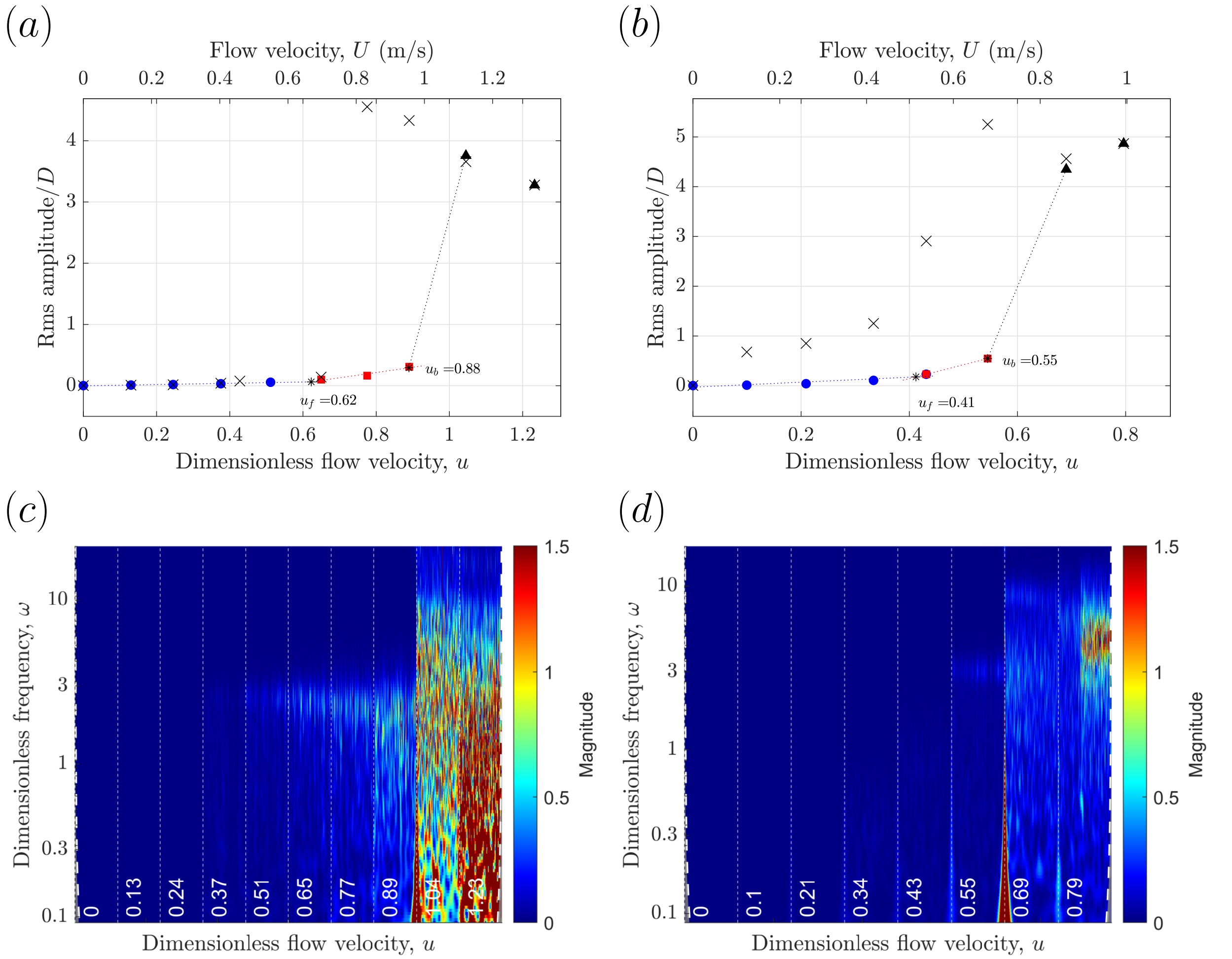

Figure 3.10: (a,b) Bifurcation diagrams showing the rms amplitude versus flow velocity for a silicone-rubber cylinder and a santoprene cylinder, respectively, both with a conical end-piece. With increasing flow velocity: (●) pre-instability; (■) flutter; (▲) static divergence; and (×) with decreasing flow velocity. (c,d) The corresponding Morse wavelet scalograms for the frequency of oscillation.

flow velocity, and then static divergence at higher flow rates. The flutter-like oscillations in the case of the santoprene cylinder are much weaker than those of the silicone-rubber one, as can be seen in Fig. 3.10(b,d). Also, the santoprene cylinder displayed a stronger subcritical behaviour compared to silicone-rubber cylinder.

Compared to cylinders I, II and III which had a metal strip embedded in them, cylinders IV and V exhibited similar behaviour, with two differences. First, the pre-divergence motions for cylinders IV and V were not planar anymore. Second, with the onset of static

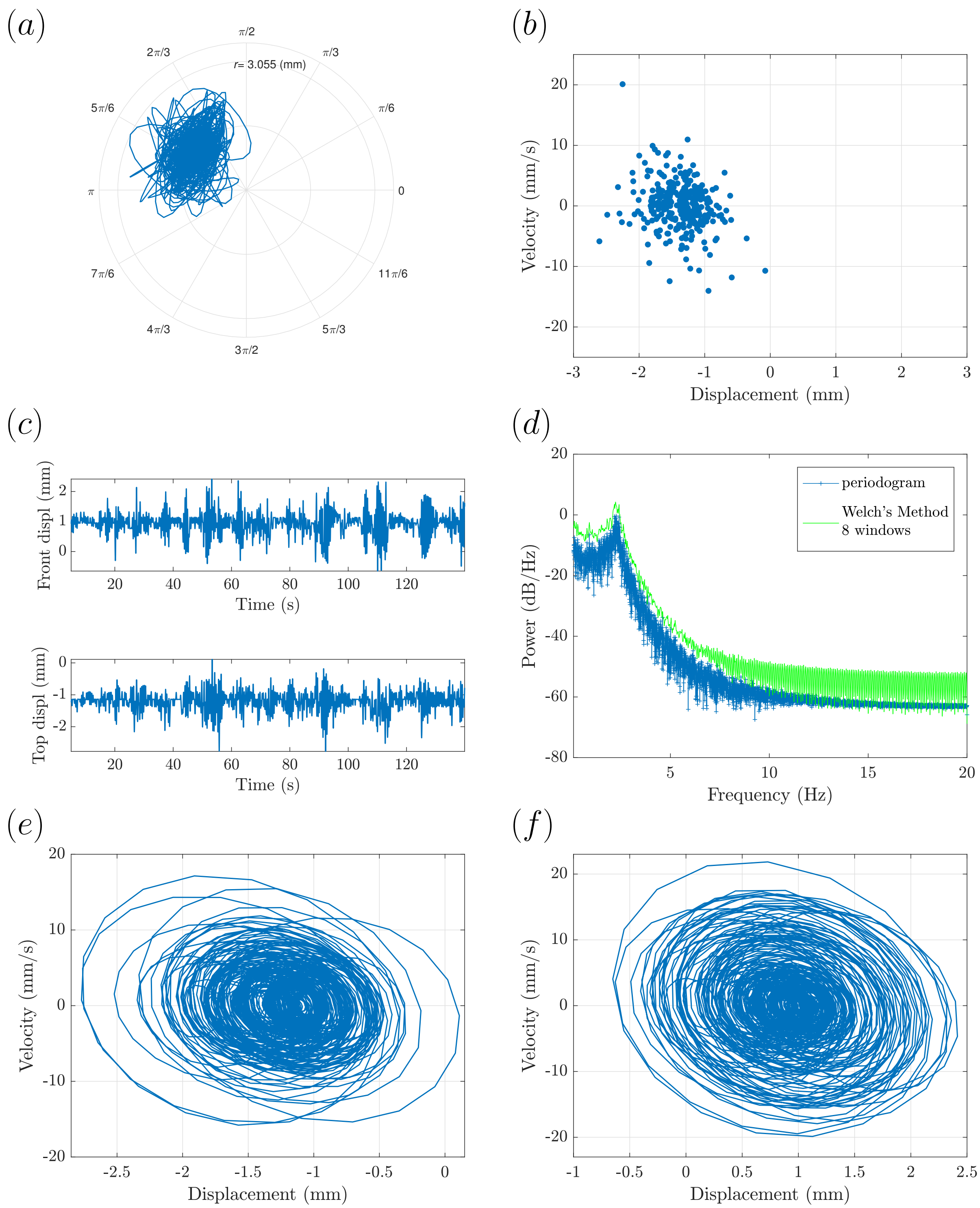

Figure 3.11: Dynamics of cylinder IV-C just after the onset of flutter at $u = 0.65$ ($U = 0.7$ m/s) illustrated by means of (a) polar plot, (b) position-triggered Poincaré map, (c) time traces of the front and top displacements, (d) PSD of motions, (e,f) phase portraits of the top and front displacements, respectively.

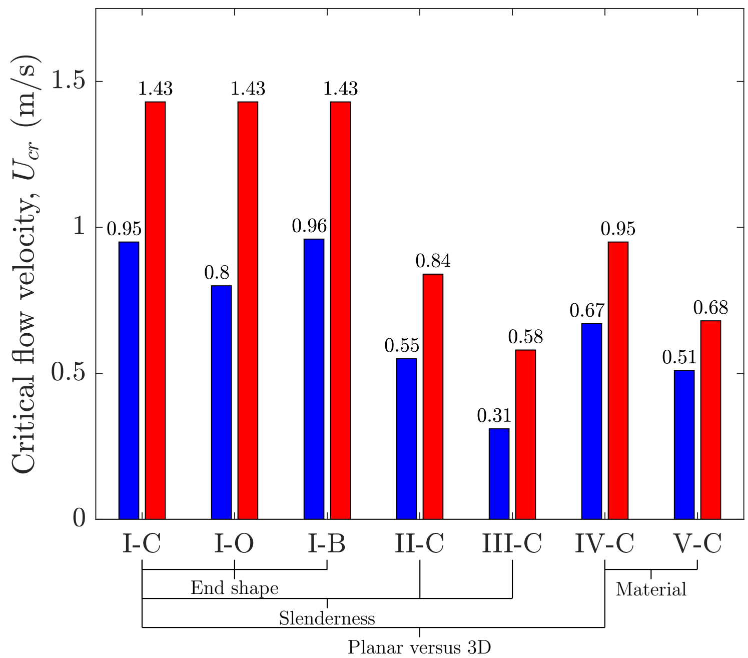

Figure 3.12: Summary of the results showing the critical flow velocities for instabilities. Blue (the shorter) and red (the taller) columns at each case, correspond to the onset of flutter and static divergence, respectively.

divergence, cylinders IV and V completely inverted themselves, with an angle of almost 180°, thus with the free-end pointing downstream. The dynamics of cylinder IV-C right after the threshold of flutter is shown in Fig. 3.11; the plots therein can be compared to the similar ones of Fig. 3.4. The polar trajectory of the motion of Fig. 3.11(a), the clustered points in the Poincaré map of Fig. 3.11(b), the unsteadiness in the time traces shown in Fig. 3.11(c), the dominant frequency of motion in Fig. 3.11(d), as well as the untidy limit cycle phase-space plots of Fig. 3.11(e,f), indicate an unsteady, near-intermittent 3D motion, yet with a strong harmonic component.

3.3.3 Critical flow velocities and frequencies

The dimensionless critical flow velocity and frequency associated with flutter and critical flow velocity of static divergence for all scenarios investigated are presented in Table 3.3. As can be seen, the dimensionless parameters do not completely coalesce to a single value for all cases, because the dynamics of the system is also governed by other parameters such as the

Table 3.3: Dimensionless critical flow velocities and frequencies.

Cylinder	I-C	I-O	I-B	II-C	III-C	IV-C	V
u_{cf}	0.62	0.52	0.62	0.54	0.40	0.62	0.41
ω_{cf}	1.88	2.25	1.87	2.23	2.32	2.36	2.74
u_{cb}	0.93	0.93	0.93	0.82	0.75	0.88	0.55

length-to-diameter ratio affecting the frictional flow effects, internal damping characteristics, and sensitivity to initial imperfections.

The quantitative summary of the results in dimensional form is presented in Fig. 3.12. In each pair of columns, the shorter one corresponds to the first instability (flutter) and the taller one corresponds to the second instability (static divergence). Each pair can be compared to its counterpart to analyze the influence of various system parameters.

3.4 The mechanisms of flutter and static divergence

We consider a simplified 2D form of the equation of motion to gain some insight into the mechanisms of the two instabilities, neglecting the distributed flow-related frictional forces along the cylinder and material damping forces to simplify the discussion. This form of the equation of motion in dimensionless form is given by [24]:

$$\begin{aligned}\frac{\partial^4\eta}{\partial\xi^4} &+ \left(\frac{1}{2}c_b u^2 + \chi\alpha u^2\right)\frac{\partial^2\eta}{\partial\xi^2} - 2\chi\beta^{\frac{1}{2}}u\frac{\partial^2\eta}{\partial\xi\partial\tau} + \left(1+\beta(\chi-1)\right)\frac{\partial^2\eta}{\partial\tau^2}\\ &+ \left[-\left(\frac{1}{2}c_b u^2 + f\chi u^2\right)\frac{\partial\eta}{\partial\xi} + (f-1)\,\chi\beta^{\frac{1}{2}}u\frac{\partial\eta}{\partial\tau}\right]\delta\left(\xi-1\right)\\ &+ \left(1+\beta\left(f\chi-1\right)\right)\chi_e\frac{\partial^2\eta}{\partial\tau^2}\delta\left(\xi-1\right)=0, \end{aligned} \tag{3.2}$$

in which the non-zero force at the upstream end of the cylinder has been embedded via the Dirac delta function. In this equation $\xi = x/L$ is the dimensionless axial coordinate, running along the undeformed long cylinder axis, with origin at the clamped end, and τ is the dimensionless time.

The other symbols in the equation stand for the following: $\eta = w/L$ is the nonlinear lateral deflection; c_b is the base drag coefficient at the free end; $\chi = (D_{ch}^2 + D^2)/(D_{ch}^2 - D^2)$, where D_{ch} is the equivalent hydraulic diameter of the test-section; thus, in our case, $\chi \simeq 1$;

$\alpha = v/U$ is the ratio of the axial flow velocity just upstream of the cylinder to that over the cylinder, in our case just less than unity; $\beta = \rho_f A/(\rho_f A + m)$, the ratio of the virtual mass to total mass per unit length, in our case in the range of 0.53-0.66; f is a streamline parameter related to free-end shape: $f \to 1$ for a well streamlined end and $f \to 0$ for a blunt one; χ is related to the fluid-flow momentum change at the free end and it is of the order of unity; χ_e is a geometric parameter related to free-end shape, typically very small, $\mathcal{O}(10^{-2})$. The negative Coriolis term, the third one in Eq. (3.2), is noted, which is destabilizing.

Considering a putative oscillation of the cylinder of period T, the work done by the fluid flow on the cylinder, ΔW, can be computed from Eq. (3.2) in the manner described in Appendix B, yielding

$$\Delta W \;=\; \int_0^T \left\{ \left[\,(2-f)\,\chi\beta^{\frac{1}{2}}u\right]\dot{\eta}^2 + \left[\,(f-\alpha)\,\chi u^2\right]\dot{\eta}\eta' \right\}\Bigg|_{\xi=1} d\tau, \tag{3.3}$$

where $\dot{(\;)} = \partial(\;)/\partial\tau$ and $(\;)' = \partial(\;)/\partial\xi$.

It is recalled that in the experiments the dimensionless critical flow velocity for flutter $u = u_{cf} < 1$, and since $f < 1$, for such flow velocities the first term in Eq. (3.3) is dominant. The second term can be either positive or negative depending on the value of f and α; since f ranges from 0 to 1, while α is close to unity, $f - \alpha$ is generally negative, or if positive quite small; also, $\dot{\eta}\eta' > 0$ for first-mode oscillations. Therefore, for sufficiently small $u < 1$, the first term is dominant, with the second playing a very minor role.

The dominant first term in Eq. (3.3) is always positive, thus energy is transferred from the fluid to the cylinder ($\Delta W > 0$) at small values of u, irrespective of f. Once u is high enough, yet still small, to yield a ΔW large enough to overcome frictional and material damping, amplified oscillations are generated, i.e. flutter. This happens irrespective of the values of f, i.e. of the shape of the free end. In the experiments, flutter did materialize in all cases with different end-shapes. The experimental values of u_{cf} for cylinder I with ogival, conical, and blunt end-shapes are fairly close (Table 3.3), although f for I-C and I-O is quite different from that for I-B; here it should be remarked that even though the first term in Eq. (3.3) is dominant, the onset of flutter is controlled by the combined effect of both terms in Eq. (3.3).

Physically, the flutter is associated with the negative Coriolis term, the third term in Eq.

(3.2), which gives rise to the first term in Eq. (3.3): any deflection of the pipe tends to be exaggerated by this Coriolis effect, resisted by the flexural restoring force.

The static instability, divergence, is examined by ignoring all time-dependent terms in Eq. (3.2), i.e. by considering

$$\frac{\partial^4\eta}{\partial\xi^4} + \left(\tfrac{1}{2}c_b + \chi\alpha\right) u^2 \frac{\partial^2\eta}{\partial\xi^2} - \left(\tfrac{1}{2}c_b + f\chi\right) u^2 \frac{\partial\eta}{\partial\xi}\delta(\xi - 1) = 0. \tag{3.4}$$

The second term represents a compressive load, and the third a shear force at the free end. Both are proportional to u^2 and therefore a static divergence is inevitable for high u, irrespective of the specific values of f, c_b, χ and α (all of which are positive), in agreement with the experimental observations. For example, taking $\alpha = 0.9$ and $\chi = 1$ (unconfined), for (f, c_b)=(0.8, 0.2), (0.6, 0.4) and (0, 1.2), we obtain $u_{cb} = 2.25$, 2.32 and 2.35, respectively. Moreover, in the shear force, a higher f is associated with a lower c_b, and *vice versa*, so that u_{cb} should not greatly depend on the shape of the free end. Indeed, in the experiments, $u_{cb} = 0.93$ in all cases (cases I-C, I-O and I-B) in Table 3.3 ($U_{cb} = 1.43$ m/s in Fig. 3.12). For the case of cylinder III-C, U_{cb} = ranges from 1.73 m/s to 1.80 m/s, using the aforementioned set of calculated u_{cb} values, whereas in the experiments $u_{cb} = 0.75$ and $U_{cb} = 0.58$ m/s.

Nevertheless, the discrepancy between the experimental $u_{cb} = 0.93$ and 0.75 and the theoretical $u_{cb} = 2.25 - 2.35$ is unusually high. It can be explained by the fact that the solutions of Eq. (3.4) presume that the system is at equilibrium prior to the onset of static divergence, which was not the case in the experiments; static divergence developed directly from an oscillatory state of the cylinder, which means that it is beyond the prediction capabilities of linear theory. In this regard, it is interesting to note that agreement was better for the [24] experiments, for a vertical system and confined air-flow, in which there was a brief post-flutter stabilization of the system, prior to the onset of static divergence.

Of course, for our case here, as stated before, static divergence could have arisen via a saddle-node bifurcation, the predication of which requires a nonlinear model. Utilizing the [23] model, the dimensionless critical flow velocity for the saddle-node bifurcation is

$$u = \left[\frac{\pi}{2\varepsilon C_D}\kappa'\right]^{1/2}, \tag{3.5}$$

where $\varepsilon = L/D$, $C_D = 1.1$ is the normalized drag coefficient for a circular cylinder [17]; κ' is a normalized flow speed [23], a dimensionless constant, indicating the ratio of hydrodynamic

Table 3.4: Qualitative dynamical characteristics of conventional and inverted cantilevered cylinders in axial flow.

System	Instabilities with increasing flow velocity	Sensitivity to free-end shape
Conventional cylinder	Weak static divergence, strong flutter	Very strong
Inverted cylinder	Weak flutter, strong static divergence	Very weak

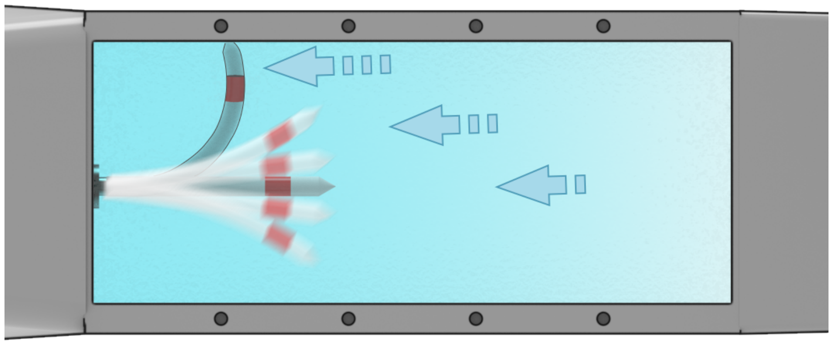

Figure 3.13: Graphical illustration of the qualitative dynamics observed with increasing flow velocity: the cylinder is subjected to flutter, followed by an abrupt static divergence.

to elastic restoring forces. Taking κ' =9.2, as for slender flags, we obtain $u = 1.22$ for systems I-O, I-C and I-B of Table 3.3, which corresponds to $U_{cb} = 1.88$ m/s, not too far from the experimental $U_{cb} = 1.43$ m/s of Fig. 3.12. For system III-C, $U_{cb} = 0.94$ m/s, less close to the experimental $U_{cb} = 0.58$ m/s, but still closer that the results obtained via Eq. (3.4). We can therefore conclude that the observed static divergence arose via a saddle-node bifurcation, as suggested by [23], rather than pitchfork bifurcation.

The foregoing are in sharp contrast to the case of cylinders in axial flow directed from the clamped end towards the free end. In that case, the free-end shape greatly affects stability. Indeed, for a blunt end, neither flutter nor divergence occur [5].

3.5 Concluding remarks

The fluid-elastic instability of inverted cantilevered cylinders in axial flow, i.e. with flow directed from the free end towards the clamped one, has been investigated. Study of this reverse flow configuration is not only curiosity-driven because of the fascinating dynamical behaviour it displays, but also because of real-world applications it is related to.

A series of water tunnel experiments were conducted to investigate the influence of varying system parameters, namely, end-piece shape, cantilever length-to-diameter ratio, planar versus 3D motions and material properties, on the dynamical behaviour and stability of this fluid-elastic system. To this end, three lengths of silicone-rubber cylinders with an embedded thin metal strip (cylinders I, II and III), a hollow silicone-rubber one (cylinder IV) and a santoprene one (cylinder V) were utilized. Also, three different free-end shapes were used in experiments with one of the cylinders, to investigate the effect of end-shape. In all cases, a more or less similar behaviour was captured: the cylinder was found to undergo turbulence buffeting, followed by weak movement-induced flutter-like oscillations in its first mode at relatively low flow velocity. These motions were unsteady and near-intermittent, nevertheless with a strong harmonic component; increasing flow velocity further, resulted in an increase in the amplitude and a decrease in frequency of these oscillations. Eventually, the cylinder was subjected to static divergence at high enough flow velocities. The sequence of flow-induced instabilities with increasing flow velocity is shown in Fig. 3.13. The mechanisms underlying these instabilities were briefly discussed. The static divergence was found to likely arise via a saddle-node bifurcation, rather than via a pitchfork bifurcation.

Varying the free end-shape was found to have only a marginal effect on the onset of flutter instability (refer to the first three pairs of columns in Fig. 3.12), and no effect on the onset of static divergence. Thus, qualitatively, the end-shape is unimportant, and quantitatively the effect is only marginal, as opposed to cylinders subjected to the opposite flow direction.

In general, the change in flow direction associated with the 'inverted cylinder' configuration, reverses all the essential features of the dynamics, *vis-à-vis* the 'conventional cylinder' configuration, as shown in Table 3.4.

The onset of both instabilities dropped to quite low values for increasing cylinder length-to-diameter ratio. The dynamical behaviour beyond the cylinder static divergence and impacting on the test section wall was found to be very complex, depending on the end-shape, the nonlinear impact forces and material of the cylinder. It was concluded that the frequency of the observed post-divergence motions in the case of cylinder III-C can be attributed to vortex shedding. The dominant frequency varied almost linearly with respect to flow velocity, with a Strouhal number in the range of 0.20-0.24. In the case of hollow cylinders with no metal strip, i.e. cylinders IV and V, post-divergence, the cylinders underwent very harsh motions and completely inverted themselves.

In all cases, with decreasing flow velocity, a hysteresis effect was observed. This behaviour was more pronounced in the case of the more flexible santoprene cylinder.

Acknowledgments

The financial support received from the Natural Sciences and Engineering Research Council of Canada (A.K.M., grant number 04957-2018), (M.P.P., grant number 06465-2018); the Solution Mining Research Institute (M.P.P., grant number U2017-3); and Pipeline Research Council International (M.P.P., grant number PR593-18700) is gratefully acknowledged. The first author is grateful to McGill University for a McGill Engineering International Tuition Award (MEITA).

Appendix A. Material damping of the elastomer cylinders

It was established long ago [44] that a two-parameter visco-hysteretic model captured adequately the internal damping characteristics of elastomer cylinders. The experimental methods used to determine the flexural rigidity and damping constants of elastomer cylinders are described in Appendix D of [39]. In this model the flexural term $EI(\partial^4 w/\partial x^4)$ is replaced by $EI\,[1 + (\alpha + \mu/\Omega)\,(\partial/\partial t)]\,(\partial^4 w/\partial x^4)$. In dimensionless terms, $(\partial^4\eta/\partial\xi^4)$ is replaced by

$$[1 + (\bar{\alpha} + \mu/\omega)\,\partial/\partial\tau]\,(\partial^4\eta/\partial\xi^4), \tag{A.1}$$

where $\bar{\alpha}$ and μ are the dimensionless viscoelastic and hysteretic damping coefficients, and the other parameters have been defined in Section 3.4.

Typical values for the Silastic A silicone-rubber cylinders used in these experiments are $\bar{\alpha} = 1.7\times10^{-4}$ and $\mu = 3.9\times10^{-2}$. For Silastic E cylinders, $\bar{\alpha} = 3.0\times10^{-4}$ and $\mu = 3.6\times10^{-2}$.

Appendix B. Energy transfer considerations for flutter

Here we consider the transfer of energy from the fluid to the cylinder, underlying the generation of flutter.

We first re-write Eq. (3.2) in the form

$$\sum_i F_i(\xi,\tau) = [...]\frac{\partial^2\eta}{\partial\tau^2}. \tag{B.1}$$

We then multiply each of the $F_i(\xi,\tau)$ by $\partial\eta/\partial\tau$ and integrate from $\xi = 0$ to $\xi = 1$ and from $\tau = 0$ to $\tau = T$, where T is the period of a putative cycle of oscillation. This gives ΔW as in

Eq. (3.3). Because the manipulations involved are not too straight-forward, the procedure is given here in detail for the first and third terms.

For the first term, integrating by parts gives

$$\begin{aligned}\Delta W_1 &= \int_0^T \int_0^1 \left[-\frac{\partial^4\eta}{\partial\xi^4}\right]\frac{\partial\eta}{\partial\tau}d\xi d\tau \\ &= -\int_0^T \left[\frac{\partial^3\eta}{\partial\xi^3}\frac{\partial\eta}{\partial\tau}\right]_0^1 d\tau + \int_0^T \left[\frac{\partial^2\eta}{\partial\xi^2}\frac{\partial^2\eta}{\partial\xi\partial\tau}\right]_0^1 d\tau \\ &\quad -\frac{1}{2}\int_0^T \int_0^1 \frac{\partial}{\partial\tau}\left(\frac{\partial^2\eta}{\partial\xi^2}\right)^2 d\xi d\tau. \end{aligned} \tag{B.2}$$

Having included the free-end shape force in the equation of motion, at the free end ($\xi = 1$), both $\partial^2\eta/\partial\xi^2$ and $\partial^3\eta/\partial\xi^3$ are zero; also, η and $\partial\eta/\partial\xi$ are zero at $\xi = 0$. Hence, the first two terms in Eq. (B.2) vanish. The last term gives $-\frac{1}{2}\int_0^1 (\partial^2\eta/\partial\xi^2)^2 \Big|_0^T d\xi$, and it also vanishes because of the periodicity assumption. Therefore, $\Delta W_1 = 0$, as it should be, because it arises from a a conservative force, derivable from a potential.

The third term gives

$$\begin{aligned}\Delta W_3 &= 2\chi\beta^{\frac{1}{2}}u\int_0^T \int_0^1 \left[\frac{\partial^2\eta}{\partial\xi\partial\tau}\right]\frac{\partial\eta}{\partial\tau}d\xi d\tau \\ &= 2\chi\beta^{\frac{1}{2}}u\int_0^T \int_0^1 \frac{\partial}{\partial\xi}\left(\frac{\partial\eta}{\partial\tau}\right)^2 d\xi d\tau = 2\chi\beta^{\frac{1}{2}}u\int_0^T \frac{1}{2}\left(\frac{\partial\eta}{\partial\tau}\right)^2\Big|_0^1 d\tau \\ &= \chi\beta^{\frac{1}{2}}u\int_0^T \left(\frac{\partial\eta}{\partial\tau}\right)^2\Big|_{\xi=1} d\tau, \end{aligned} \tag{B.3}$$

which is part of the first term of Eq. (3.3).

The fifth term, involving the Dirac delta function, gives

$$\Delta W_5 = -(f-1)\,\chi\beta^{\frac{1}{2}}u\int_0^T \left(\frac{\partial\eta}{\partial\tau}\right)^2\Big|_{\xi=1} d\tau, \tag{B.4}$$

which, combined with Eq. (B.3), gives the first term in Eq. (3.3).

References

[1] M. P. Païdoussis, Fluid-Structure Interactions: Slender Structures and Axial Flow, Vol. 2, second ed., Academic Press, 2016.

[2] M. P. Païdoussis, Dynamics of cylindrical structures in axial flow: A review, J. Fluids Struct. 107 (2021) 103374.

[3] W. R. Hawthorne, The early development of the Dracone flexible barge, Proc. Inst. Mech. Eng. 175 (1) (1961) 52–83.

[4] M. P. Païdoussis, Dynamics of flexible slender cylinders in axial flow. Part 1: theory, J. Fluid Mech. 26 (4) (1966) 717–736.

[5] M. P. Païdoussis, Dynamics of flexible slender cylinders in axial flow. Part 2: experiments, J. Fluid Mech. 26 (4) (1966) 737–751.

[6] M. P. Païdoussis, Dynamics of cylindrical structures subjected to axial flow, J. Sound Vib. 29 (3) (1973) 365–385.

[7] P. J. Holmes, Pipes supported at both ends cannot flutter, J. Appl. Mech. 45 (3) (1978) 619–622.

[8] M. P. Païdoussis, E. Grinevich, D. Adamovic, C. Semler, Linear and nonlinear dynamics of cantilevered cylinders in axial flow. Part 1: physical dynamics, J. Fluids Struct. 16 (6) (2002) 691–713.

[9] M. Kheiri, M. P. Païdoussis, Dynamics and stability of a flexible pinned-free cylinder in axial flow, J. Fluids Struct. 55 (2015) 204–217.

[10] Y. Perets, E. Sher, R. Harari, An experimental study on axial-flow-induced vibration of confined flexible rods with sequenced transverse rib roughness, Exp. Therm. Fluid Sci. 93 (2018) 86–95.

[11] S. S. Tabatabaei, M. Kheiri, J. Dargahi, Dynamics and stability of imperfect flexible cylinders in axial flow, J. Fluids Struct. 105 (2021) 103321.

[12] M. P. Païdoussis, Stability of towed, totally submerged flexible cylinders, J. Fluid Mech. 34 (2) (1968) 273–297.

[13] G. S. Triantafyllou, C. Chryssostomidis, Analytic determination of the buckling speed of towed slender cylindrical beams, ASME J. Energy Resour. Technol. 106 (2) (1984) 246–249.

[14] G. S. Triantafyllou, C. Chryssostomidis, Stability of a string in axial flow, ASME J. Energy Resour. Technol. 107 (4) (1985) 421–425.

[15] A. P. Dowling, The dynamics of towed flexible cylinders Part 1. Neutrally buoyant elements, J. Fluid Mech. 187 (1988) 507–532.

[16] A. P. Dowling, The dynamics of towed flexible cylinders Part 2. Negatively buoyant elements, J. Fluid Mech. 187 (1988) 533–571.

[17] G. I. Taylor, Analysis of the swimming of long and narrow animals, Proc. R. Soc. London 214 (1117) (1952) 158–183.

[18] M. J. Lighthill, Note on the swimming of slender fish, J. Fluid Mech. 9 (2) (1960) 305–317.

[19] M. J. Lighthill, Large-amplitude elongated-body theory of fish locomotion, Proc. R. Soc. London 179 (1055) (1971) 125–138.

[20] M. S. Triantafyllou, G. S. Triantafyllou, D. K. P. Yue, Hydrodynamics of Fishlike Swimming, Annu. Rev. Fluid Mech. 32 (1) (2000) 33–53.

[21] K. Singh, S. Michelin, E. De Langre, Energy harvesting from axial fluid-elastic instabilities of a cylinder, J. Fluids Struct. 30 (2012) 159–172.

[22] S. Rinaldi, M. P. Païdoussis, Theory and experiments on the dynamics of a free-clamped cylinder in confined axial air-flow, J. Fluids Struct. 28 (2012) 167–179.

[23] J. E. Sader, C. Huertas-Cerdeira, M. Gharib, Stability of slender inverted flags and rods in uniform steady flow, J. Fluid Mech. 809 (2016) 873–894.

[24] S. Rinaldi, M. P. Païdoussis, An improved theoretical model for the dynamics of a free–clamped cylinder in axial flow, J. Fluids Struct. 94 (2020) 102903.

[25] A. R. Abdelbaki, M. P. Païdoussis, A. K. Misra, A nonlinear model for a free-clamped cylinder subjected to confined axial flow, J. Fluids Struct. 80 (2018) 390–404.

[26] D. Kim, J. Cossé, C. H. Cerdeira, M. Gharib, Flapping dynamics of an inverted flag, J. Fluid Mech. 736 (2013) R1.

[27] P. S. Gurugubelli, R. K. Jaiman, Self-induced flapping dynamics of a flexible inverted foil in a uniform flow, J. Fluid Mech. 781 (2015) 657–694.

[28] J. E. Sader, J. Cossé, D. Kim, B. Fan, M. Gharib, Large-amplitude flapping of an inverted flag in a uniform steady flow – a vortex-induced vibration, J. Fluid Mech. 793 (2016) 524–555.

[29] M. Tavallaeinejad, M. P. Païdoussis, M. Legrand, M. Kheiri, Instability and the post-critical behaviour of two-dimensional inverted flags in axial flow, J. Fluid Mech. 890 (2020) A14.

[30] M. Tavallaeinejad, M. P. Païdoussis, M. F. Salinas, M. Legrand, M. Kheiri, R. M. Botez, Flapping of heavy inverted flags: a fluid-elastic instability, J. Fluid Mech. 904 (2020) R5.

[31] K. Moditis, M. P. Païdoussis, J. Ratigan, Dynamics of a partially confined, discharging, cantilever pipe with reverse external flow, J. Fluids Struct. 63 (2016) 120–139.

[32] M. F. J. Butt, M. P. Païdoussis, M. Nahon, Dynamics of a confined pipe aspirating fluid and concurrently subjected to external axial flow: An experimental investigation, J. Fluids Struct. 104 (2021) 103299.

[33] M. Chehreghani, A. R. Abdelbaki, A. K. Misra, M. P. Païdoussis, Experiments on the dynamics of a cantilevered pipe conveying fluid and subjected to reverse annular flow, J. Sound Vib. 515 (2021) 116480.

[34] A. M. Elmahdi, R. Lu, M. E. Conner, Z. Karoutas, E. Baglietto, Flow induced vibration forces on a fuel rod by LES CFD analysis, NURETH14-14th Int. Top. Meet. Nucl. React. Therm. Hydraul. Toronto, Ontario, Canada (2011).

[35] D. De Santis, A. Shams, Numerical modeling of flow induced vibration of nuclear fuel rods, Nucl. Eng. Des. 320 (2017) 44–56.

[36] E. Ter Hofstede, S. Kottapalli, A. Shams, Numerical prediction of flow induced vibrations in nuclear reactor applications, Nucl. Eng. Des. 319 (2017) 81–90.

[37] A. Cioncolini, J. Silva-Leon, D. Cooper, M. K. Quinn, H. Iacovides, Axial-flow-induced vibration experiments on cantilevered rods for nuclear reactor applications, Nucl. Eng. Des. 338 (2018) 102–118.

[38] X. Li, P. Qi, D. Li, S. Tan, P. Liu, Visualization experimental study on axial flow-induced vibration of slender cantilever rod for reactor, Ann. Nucl. Energy 160 (2021) 108357.

[39] M. P. Païdoussis, Fluid-Structure Interactions: Slender Structures and Axial Flow, Vol. 1, second ed., Academic Press, 2014.

[40] S. Rinaldi, Experiments on the dynamics of cantilevered pipes subjected to internal and/or external axial flow, Master's thesis, Department of Mechanical Engineering, McGill University, Montreal, QC, Canada (2009).

[41] M. P. Païdoussis, T. P. Luu, S. Prabhakar, Dynamics of a long tubular cantilever conveying fluid downwards, which then flows upwards around the cantilever as a confined annular flow, J. Fluids Struct. 24 (1) (2008) 111–128.

[42] E. Naudascher, D. Rockwell, Flow-Induced Vibrations: An Engineering Guide, Courier Corporation, 2012.

[43] J. Ryu, S. G. Park, B. Kim, H. J. Sung, Flapping dynamics of an inverted flag in a uniform flow, J. Fluids Struct. 57 (2015) 159–169.

[44] M. P. Païdoussis, P. E. Des Trois Maisons, Free vibration of a heavy damped vertical cantilevere, J. Appl. Mech. 38 (1971) 524–526.

CHAPTER 4

Dynamics of a Cantilevered Pipe Conveying Fluid and Counter-currently Subjected to Partially Confined External Axial Flows: Experimental Investigation I

Preface

The dynamics of system III, which involves a tubular beam subjected to simultaneous counter-current internal and external axial flows, is the main scope of the present thesis. This chapter deals with the first part of experiments on system III, using a bench-top-size apparatus. This experimental set-up involves a pressure vessel filled with water, a hanging flexible cantilevered pipe and a shorter concentric outer rigid tube. The fluid flows downward through the pipe, exits into the pressure vessel, flows upwards through the annular gap formed by the upper portion of the pipe and the outer rigid tube, and out of the pressure vessel. To achieve higher ratios of external-to-internal flow velocity, additional fluid may enter the pressure vessel at the bottom. Therefore, the system under study is a fluid-discharging cantilevered pipe subjected to a partially confined annular external flow. Interest in the matter mainly arises because this system replicates one of the modes of operation of brine-strings in solution-mined caverns, the so-called "product retrieval mode". The McGill FSI research group has been engaged in comprehensive fundamental research on this system, aiming to systematically explore various aspects of its dynamics. This chapter is a part of this ongoing research.

In the manuscript presented in this chapter [3], for various external-to-internal flow velocity ratios, and various confined lengths of the pipe, experiments were conducted to explore the dynamical behaviour of the system, including post-instability dynamics. The pipe loses stability by flutter. The results indicated that beyond instability, at high-enough flow rates, the flexible pipe contacts the outer rigid tube, with the contact involving single- or double-sided impacting, sticking and partial or complete circumferential rubbing.

Experiments on the dynamics of a cantilevered pipe conveying fluid and subjected to reverse annular flow

M. Chehreghani, A.R. Abdelbaki, A.K. Misra, M.P. Païdoussis*
Department of Mechanical Engineering, McGill University,
817 Sherbrooke Street West, Montreal, QC, Canada H3A 0C3.

Abstract: The dynamics of a pipe conveying fluid and counter-currently subjected to a partially confined external axial flow through a coaxial annular region over its upper portion has been investigated experimentally. Apart from its fundamental aspects, this flow configuration simulates one of the *modi operandi* of solution-mined caverns utilized for hydrocarbon storage. Beyond the instability, at sufficiently high flow rates, the flexible pipe impacts the rigid coaxial shorter outer tube. The effects of confinement length, i.e., the ratio of the confined length of the pipe to its total length, L'/L, and the ratio of external to internal flow velocities, U_o/U_i, on the onset of instability, as well as the dynamical behaviour of the system with impacting, have been investigated. It was found that for all L'/L ratios and a very small value of U_o/U_i, i.e., $U_o/U_i = 0.055$, the system loses stability via flutter in the second mode. Increasing the confinement length ratio expedited the aforementioned flutter. At higher U_o/U_i ratios, i.e., $U_o/U_i \geq 0.2$, the pipe is subjected to a static deformation, followed by more complex behaviour at higher flow velocities. The post-instability impact displays a rich dynamical behaviour with both periodic and chaotic components. Depending on the various system parameters, mainly the U_o/U_i and L'/L ratios and the internal flow velocity, several types of impacting/sticking behaviour were observed. The pipe may undergo single-sided or two-sided impacting, oscillation over the buckled position and partial or complete rubbing or sticking on the outer rigid tube.

Keywords: Flutter; Cantilevered pipes; External/internal axial flows; Impact with motion constraints; Chaos.

*Corresponding author.
E-mail addresses: mahdi.chehreghani@mail.mcgill.ca, ahmed.abdelbaki@mail.mcgill.ca, arun.misra@mcgill.ca, michael.paidoussis@mcgill.ca

4.1 Introduction

Applications of slender structures in contact with fluid are numerous. Pipelines, heat-exchangers, steam generators and brine-strings used to store hydrocarbons in salt caverns are among the many industrial applications of these systems. However, studies on this topic are also "curiosity driven" [1] and fundamental.

The literature on the dynamics of pipes conveying fluid is very extensive. This system has attracted scholars' attention extensively and is referred to as a paradigm in dynamics [2], as many of the so-called fluid-elastic instabilities can be illustrated with it. The literature review in this paper is selective, rather than all-inclusive. The interested reader is referred to [2] for a comprehensive discussion of studies on this subject.

It was demonstrated by Holmes and co-workers [3–5] that a Hopf bifurcation is responsible for instability of cantilevered pipes conveying fluid at sufficiently high flow velocities. Bajaj et al. [6] proved that the Hopf bifurcation can be either sub- or supercritical, depending on a parameter related to the pressure loss in the pipe.

The dynamics of a spring-constrained cantilevered pipe was examined both theoretically and experimentally by Païdoussis and Moon [7]. By means of analytical and numerical methods, the existence of chaotic regions was demonstrated. This study was pursued further by Païdoussis et al. [8]. Also, Semler [9] derived and solved the nonlinear equations of motion of either simply-supported or cantilevered pipes, indicating that chaotic motions may occur due to perturbations or motion-limiting constraints; refer to [10].

In a three-part study, the 3-D nonlinear dynamics of unrestrained and restrained cantilevered pipes conveying fluid was examined by Païdoussis an co-workers. Firstly, the pre-existing nonlinear equation of motion for planar motion of the system [11] was modified for three-dimensional motions of cantilevered tubular beams conveying fluid by Wadham-Gagnon et al. [12]. This study was then extended by Païdoussis et al. [13] to investigate the dynamics of the same system restrained by arrays of two or four springs or one spring located at a specific distance from the clamped end, and by Modarres-Sadeghi et al. [14] for a pipe with an end mass. Later on, research on the two- and three-dimensional dynamics of cantilevered pipes was undertaken by Modarres-Sadeghi et al. [15] to investigate the post-flutter dynamics of both horizontal and vertical pipes for flow velocities beyond the Hopf bifurcation; refer also to [16] and [17].

The first study on the dynamics of pipes simultaneously subjected to internal and external axial flows was conducted by Cesari and Curioni [18], predicting buckling instability of pipes with different boundary conditions. Thereafter, the dynamics of vertical pipes conveying fluid and concurrently subjected to an independent external axial flow was investigated by Hannoyer and Païdoussis [19]. For clamped-clamped pipes, the effect of the internal and external flows on the stability of the system was found to be additive, i.e., if either internal or external flow velocity is just less than the critical value for instability, an increase in the value of the velocity of the other flow would trigger instability. In contrast, if because of either internal or external flow a cantilevered pipe is just below the threshold of instability, by further increasing the other flow, the instability could be avoided.

Numerous studies have been conducted on the dynamics of a drill-string, e.g., by Bailey and Finnie [20], Finnie and Bailey [21], Den Hartog [22] and Grigoriev [23]. Also, Luu [24] has studied the stability of a long hanging cantilevered tubular beam conveying fluid which is also subjected to an external flow over its outer surface through an annular area formed by an outer rigid channel.

Thereafter, aiming at modelling the dynamics of a drill-string with a floating fluid-powered drill-bit, Païdoussis et al. [25] derived a mathematical formulation for a hanging cantilevered pipe discharging fluid downwards, which, after exiting from the free end, flows upwards over an annular region confined by a rigid concentric cylindrical channel; i.e., for two counter-current interdependent axial flows. For system parameters associated with a real drill-string system, as well as those for a bench-top-size experiment, computations were carried out. For relatively low degrees of confinement by the outer rigid channel, the internal flow was found to be dominant; at low flow rates, an increase in the damping caused by the existence of the annular flow stabilized the system. On the other hand, for higher degrees of confinement, the annular flow was found to be dominant, which leads to destabilization of the system, precipitating flutter at relatively low internal flow velocities. The dynamics of a system with reverse flow directions was investigated by Qian et al. [26]; for a drill-string-like system, theoretical results demonstrated that divergence may take place in the case of relatively high degree of confinement. Also, Fujita and Moriasa [27] studied the same system for both flow configurations, i.e., as in [25] and [26].

Motivated by applications in salt-cavern hydrocarbon storage systems, Moditis et al. [28, 29] investigated the dynamics of a hanging flexible cantilevered pipe, coaxial with a shorter rigid outer tube, taking into account the discontinuity in the external flow velocity within and outside the annulus. Moreover, a series of experiments were conducted in a bench-top-sized system to validate the analytical results. It was found that the full-scale system undergoes divergence rather than flutter. Also, an asymptotic behaviour was obtained as the length of the pipe was increased. Subsequently, a numerical study on the same system was carried out by Kontzialis et al. [30]. Results were in good agreement with existing experimental data. A linear model was also derived by Minas et al. [31] to investigate the dynamics of a system in which the flow discharges radially at the end of the pipe through a special end-piece; refer also to [32].

Later on, instead of a Heaviside step function as in [29], a logistic function was used to model the discontinuity in the external flow velocity by Abdelbaki et al. [33]. It was concluded that the proposed model could better predict the onset of instability and the frequency of oscillations as compared to [29]. Thereafter, a weakly nonlinear model was derived by Abdelbaki et al. [34] to study the dynamics of a hanging discharging cantilevered pipe simultaneously subjected to a fully-confined external axial flow in the reverse direction. In [35], the previous study was extended to the case of a cantilevered pipe discharging fluid and subjected to a partially-confined external axial flow. An oscillatory instability, i.e., flutter in the second mode, was predicted at sufficiently high flow velocities. Also, it was predicted that increasing flow velocity results in increased amplitude and frequency of oscillations. Moreover, generally, a longer or a tighter annulus destabilizes the system.

The foregoing literature survey demonstrates that, to the best of authors' knowledge, so far, no experimental study has been carried out to investigate the behaviour of the system studied by Moditis [29] with impacting. Also, lack of experiments to investigate the effect of some system parameters is evident. Therefore, the main purpose of the present study is the systematic experimental investigation of the dynamics of a cantilevered pipe discharging fluid and subjected to a reverse annular axial flow over its upper portion, as shown in Fig. 4.1. The pipe may impact on the coaxial shorter outer rigid tube at high enough flow velocities.

Using a bench-top-size apparatus, the onset of instability as well as the dynamical behaviour of the system after occurrence of impact is investigated for various ratios of confinement length, $r_{ann} = L'/L$, and various ratios of external to internal flow velocities, U_o/U_i; refer to Fig. 4.1(a). Not only is this system of interest because it displays a rich dynamical behaviour, but for its practical applications for hydrocarbon storage in salt-mined caverns; the present study would be helpful in determining safe ranges of the flow velocities, so as to prevent catastrophic damages.

In the present paper, experiments on the the dynamical behaviour of a hanging can-

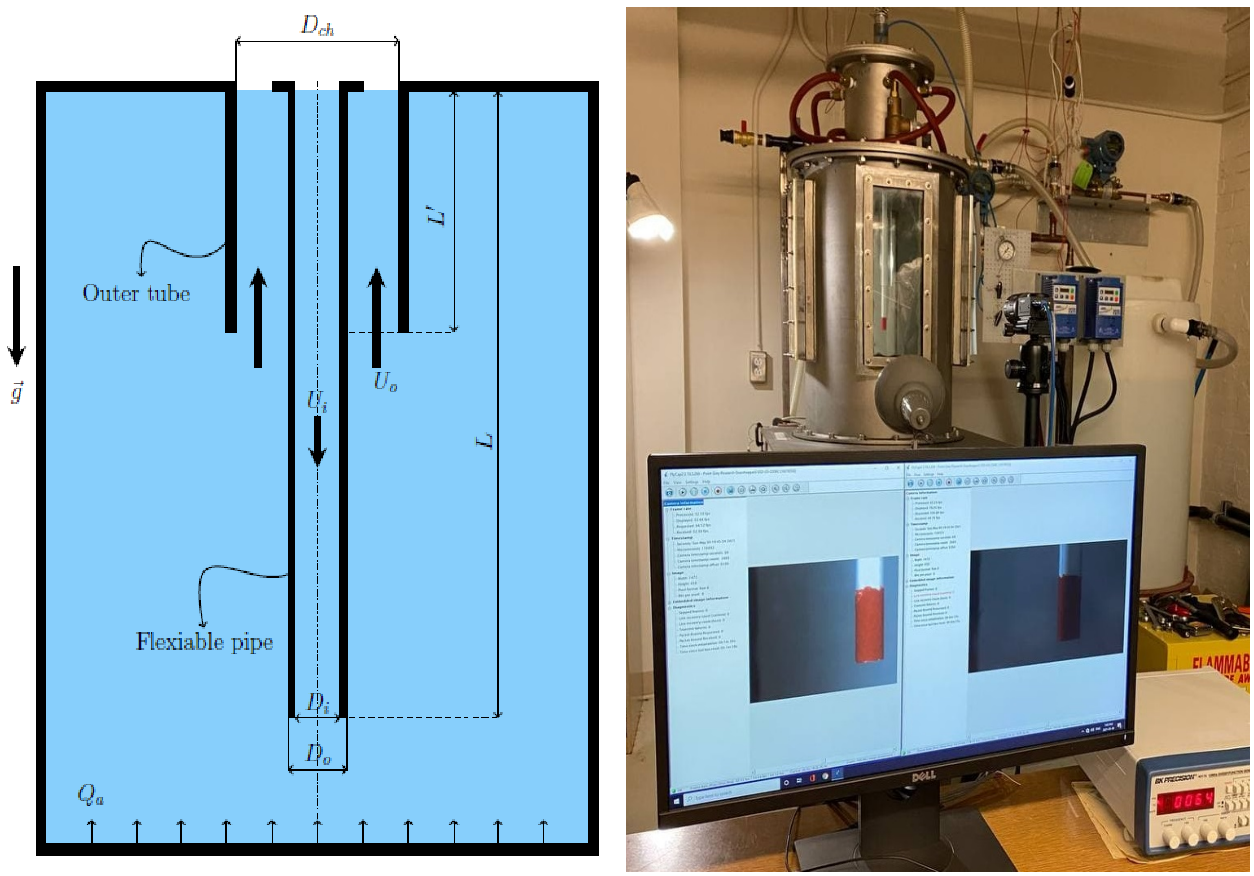

(a) (b)

Figure 4.1: (a) Schematic view of the system under consideration; Q_a denotes the additional volume of the fluid into the tank to modify the U_o/U_i ratio; (b) the SMRI/PRCI apparatus with a dual-camera system used to track the motion of the pipe tip.

tilevered pipe concurrently subjected to internal-discharging and annular-aspirating flows are described. In Section 2, a description of the apparatus, data acquisition system, experimental methodology and data analysis are described. In Section 3, the results of the experiments conducted in this study are presented. Finally, Section 4 is devoted to a summary of the results and conclusions.

4.2 Experimental apparatus and procedure

4.2.1 Test section

The bench-top-size apparatus used in this experimental investigation is shown in Fig. 4.1. The test-section consists of a cylindrical stainless steel pressure vessel filled with water, with four symmetrically placed rectangular plexiglas windows for viewing and access to the test chamber.

The test specimen is a flexible Silastic RTV pipe cast from silicone-rubber mixture. The pipe material properties as well as its dimensions are summarized is Table 4.1. Surrounding the pipe, a rigid coaxial plexiglas tube of diameter D_{ch} =31.5 mm creates an annulus over the upper portion of the pipe. Both the pipe and the outer plexiglas tube are cantilevered from their top ends. To investigate the effect of confinement length fraction, i.e., the ratio of the length of the confined region to the total length of the pipe, $r_{ann} = L'/L$ — refer to Fig. 4.1(a) — three different lengths of the plexiglas outer tube were used, namely, $L' = 109$ mm, $L' = 206.5$ mm and $L' = 304.5$ mm, which correspond to $r_{ann} = 0.253$, $r_{ann} = 0.478$ and $r_{ann} = 0.705$, respectively. In what follows, these are referred to as $r_{ann} \simeq 1/4$, 1/2 and 3/4 experiments for brevity.

The pipe discharges fluid downwards, which, upon exiting the pipe, flows upwards, and enters the surrounding annular region over the upper portion of the pipe. There is also an additional inlet at the bottom of the pressure vessel, Q_a — refer to Fig. 4.1(a). Two electric centrifugal pumps are responsible for drawing water from the bottom of a storage tank which is located beside the pressure vessel. The first pump provides the internal flow, i.e., flow in the pipe, and the other one supplies additional flow to the pressure vessel from the bottom, Q_a, so that desired ratios of the external flow velocity to the internal one, U_o/U_i, can be obtained. When $Q_a = 0$, by continuity $U_o = 0.055U_i$, and thus $U_o/U_i = 0.055$. To achieve $U_o/U_i > 0.055$, the second pump has to be used, providing Q_a.

This flow configuration is quite similar to one of the *modi operandi* for hydrocarbon storage in salt-mined caverns.

Table 4.1: Material properties and dimensions of the flexible pipe used in the experiments.

Material	EI [N m^2]	m [kg m^{-1}]	L [mm]	D_i [mm]	D_o [mm]
Silicone-rubber	7.37×10^{-3}	0.191	441	6.35	16

4.2.2 Data acquisition

To determine the volumetric flow rates associated with each of the two pumps, two magnetic flow-meters are used, thereby determining the internal flow rate, Q_i, and the additional inlet flow, Q_a. Hence the outlet flow rate, Q_o, is determined by $Q_o = Q_i + Q_a$. Therefore, the internal flow velocity, U_i, and the external flow velocity, U_o, can be determined using the known geometry of the system.

To ensure the integrity of the pressure vessel and avoid leakages, the mean pressure in the test-section is measured via a conventional Bourdon tube pressure gauge. The gauge is installed on the bleed line.

The motion of the centroid of the 'red-marked' area near the free-end of the pipe (refer to Fig. 4.1(b)) is tracked, using two synchronized cameras perpendicular to each other . More specifically, through two transparent windows of the pressure vessel at 90° to each other, the motion of a point approximately located at 18 mm above the pipe free end is followed by two identical FLIR Grasshopper3 2.3 MP cameras. These cameras are levelled and placed at identical height and distance from the two windows. To ensure synchronization of the two cameras, a function generator is used to trigger them.

These two cameras are focused on the red-marked part of the flexible cantilevered pipe used to facilitate the post-processing of the recorded videos. The video recording system is set to capture the videos at a frame rate of 64 fps. In each processed frame, the marker was detected and was then tracked in the next frames. The pixel location of the centroid of the marker in each frame was used to determine the displacements. The known width of the marker, i.e., the outer diameter of the pipe, was used as reference.

4.2.3 Experimental methodology

The experiments were designed to investigate the effects of the confinement length fraction, $r_{ann} = L'/L$, and the ratio of external to internal flow velocity, U_o/U_i, ranging from 0.055 to 0.8, on the dynamics of the system. For this purpose, after installing the flexible pipe, the outer plexiglas tube of the desired length, corresponding to $r_{ann} \simeq 1/4$, 1/2 or 3/4, was installed. For specific values of U_o/U_i, the internal flow velocity was increased step-wise to instability, and beyond to impacting. At each step, firstly the system was kept running for a while to attain steady state. Then, the motion of the marked section of the pipe was tracked and recorded for a duration of 300 seconds using the dual-camera system. To ensure consistency and guarantee validity of the results, the experiments were repeated for at least a second time.

4.2.4 Data analysis

The recorded videos were subsequently loaded into an image processing Matlab (Mathworks, Inc.) script to obtain the displacement-time series. The time series from both front and side cameras, at each velocity step, were then smoothed using a polynomial spline. These data were further processed to determine the nature of the motions by plotting phase portraits, PSDs, bifurcation diagrams, etc.

It is worth mentioning that in the displacement analysis, for each experiment, the initial location of the pipe at zero flow velocity, i.e., $U_i = U_o = 0$, that is, right prior to the first velocity step, serves as a reference.

4.3 Results

4.3.1 Experimental results for $r_{ann} \simeq 1/4$

4.3.1.1 Results for $U_o/U_i = 0.055$

Fig. 4.2(a) shows the experimental bifurcation diagram for $U_o/U_i = 0.055$, presenting the rms of displacement amplitude as a function of the internal flow velocity, U_i. The relationship between the dimensional and dimensionless flow velocities is presented in the Appendix. At low internal flow velocities, i.e., $U_i < 2$ m/s, the pipe remained almost stationary without changing its original undeformed shape. However, very weak motions

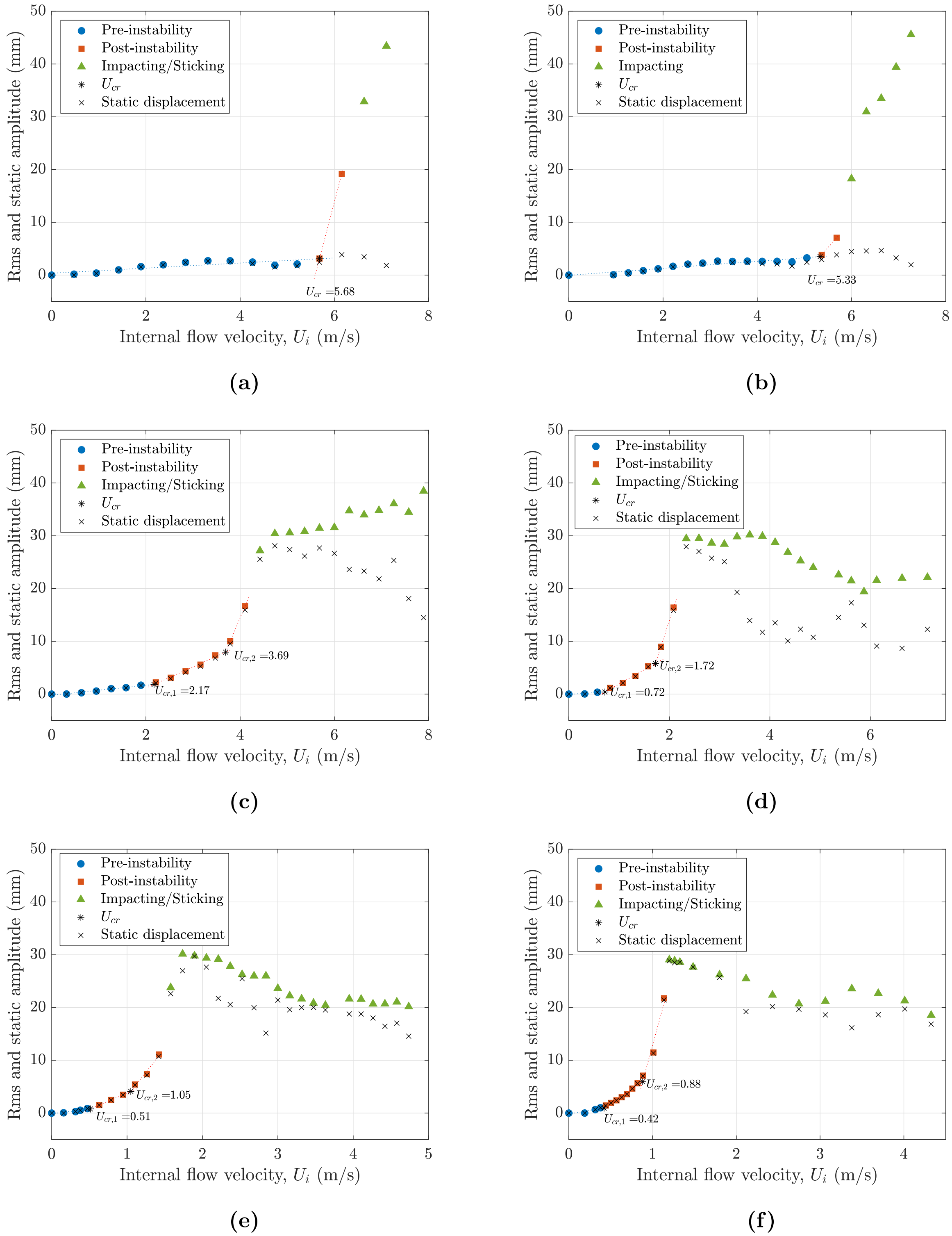

Figure 4.2: Bifurcation diagrams showing the static and rms amplitude of oscillations versus the internal flow velocity, U_i, for $r_{ann} \simeq 1/4$ and (a) $U_o/U_i = 0.055$; (b) $U_o/U_i = 0.1$; (c) $U_o/U_i = 0.2$; (d) $U_o/U_i = 0.4$; (e) $U_o/U_i = 0.6$; (f) $U_o/U_i = 0.8$.

initiated at $U_i = 2.37$ m/s. Increasing the flow velocity further, the amplitude of these oscillations increased, reaching a plateau at $U_i \simeq 4$ m/s with a maximum amplitude of approximately 3.3 mm. However, no dominant frequency could be determined, and therefore these oscillations were likely excited by flow turbulence, or they resulted from accentuation of imperfections in the pipe or in the clamping of the upper end. At $U_i \simeq 5.5$ m/s the oscillations became considerably stronger, with a dominant frequency of $f \simeq 1.45$ Hz at $U_i = 5.68$ m/s, indicating the onset of flutter in the second mode. Increasing the flow velocity further gave rise to notably higher amplitude oscillations. Eventually, the pipe executed one- or two-sided impacting with the outer rigid tube, starting at $U_i = 6.63$ m/s.

One important observation here is that during the experiments, the pipe always tended to move towards one side of the surrounding channel. This behaviour might be attributed to an initial curvature of the pipe or to accentuation of small initial eccentricity of the pipe relative to the outer rigid tube.

Fig. 4.3 presents the average PSD, i.e., power spectral density of the average of the time series signals that comes from each camera, at post-flutter flow velocities. In all cases, the PSDs exhibit a more or less dominant frequency of oscillation which remains almost constant with increasing flow velocity. The smaller peak in Fig. 4.3(b) corresponds to harmonic of the second-mode frequency of $\simeq$1.45 Hz. However, this smaller peak became weaker at higher flow velocities, as can be seen in Fig. 4.3(c,d).

The dynamics of the system at the onset of impacting can be characterized further by considering the sample results shown in Figs. 4.4 and 4.3(c). The time traces captured by the front and side cameras shown in Fig. 4.4(a) and the polar trajectory of the pipe tip in Fig. 4.4(b) demonstrate the unsteadiness, three-dimensionality and chaotic nature of the oscillations. Moreover, phase portraits of the front, side and combined displacements depicted in Fig. 4.4(c-e), respectively, indicate a 3D periodic motion; yet, due to the fact that the motion is very unsteady and nearly intermittent according to the time traces in Fig. 4.4(a), they fill the phase space, all the way to the origin, thereby not resulting in a clean limit cycle. Also, the Poincaré map in Fig. 4.4(f) is diffuse and suggests the existence of a chaotic component in the dynamical behaviour of the system.

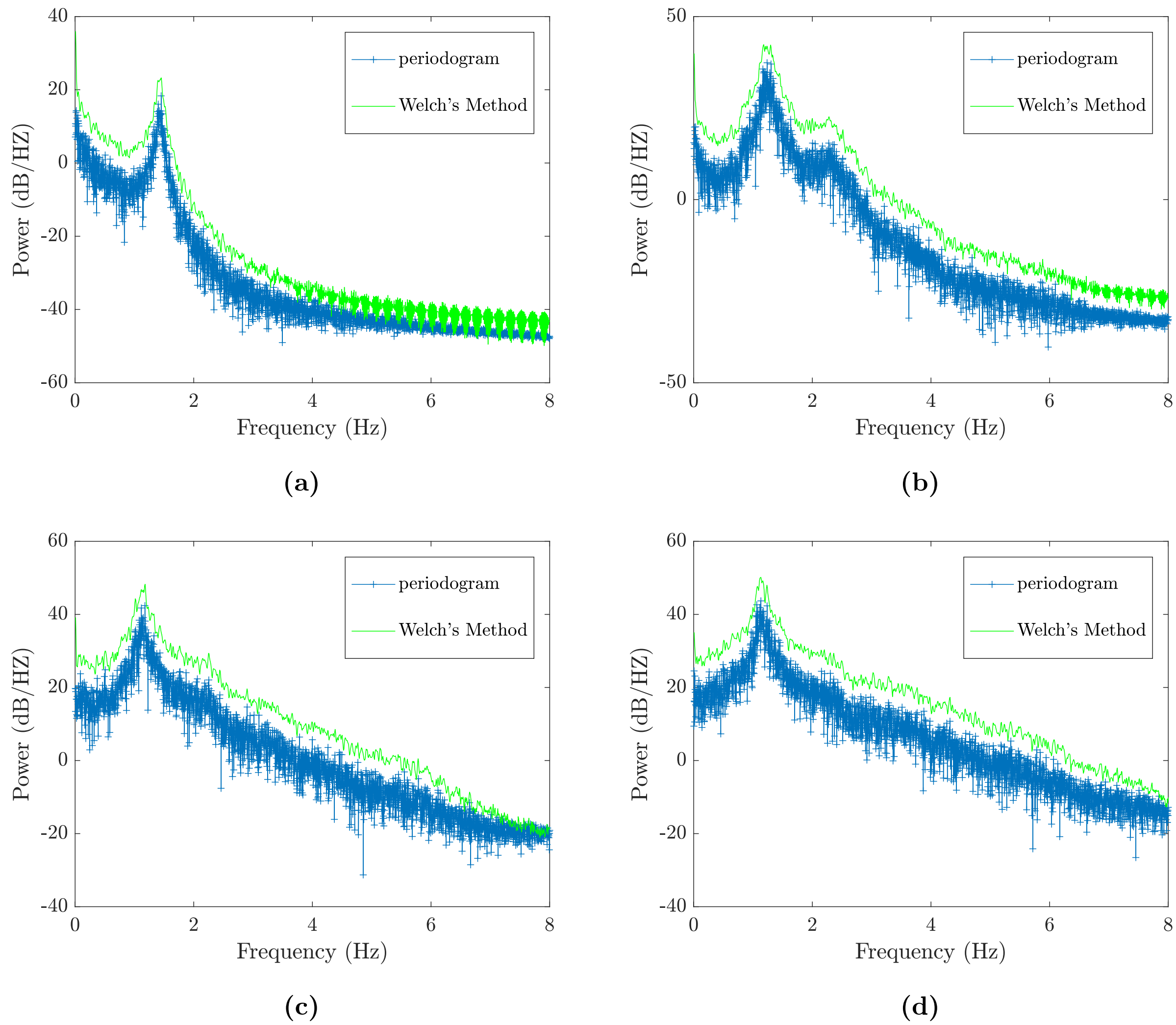

Figure 4.3: PSD plots for $U_o/U_i = 0.055$ and $r_{ann} \simeq 1/4$ at (a) $U_i = 5.68$ m/s; (b) $U_i = 6.16$ m/s; (c) $U_i = 6.63$ m/s; (d) $U_i = 7.10$ m/s.

4.3.1.2 Results for $U_o/U_i > 0.055$

For the velocity ratio of $U_o/U_i = 0.1$, qualitatively, the same behaviour as in $U_o/U_i = 0.055$ was observed — refer to Fig. 4.2(b); the system loses stability via flutter in the second mode at $U_i = 5.33$ m/s. One- or two-sided impacting on the outer rigid tube began at $U_i = 6$ m/s.

In contrast, for $U_o/U_i \geq 0.2$, as can be seen in Fig. 4.2(c-f) a different dynamical behaviour was observed. For $U_o/U_i = 0.2$, two significant increases in the slope, at $U_i = 2.17$ m/s and $U_i = 3.69$ m/s, can be observed. However, before touching the annulus, deformations were static with a very weak superimposed oscillatory component. At $U_i = 4.42$ m/s the pipe stuck to the outer rigid and oscillated about its buckled position while it partially rubbed around the rim of the outer tube, as can be seen in Fig. 4.5(a). In the PSD plot shown in Fig. 4.5(b), there is no sharply defined frequency. The same behaviour occurred at higher flow velocities. At $U_i = 6.32$ m/s, although the pipe was mostly stuck on the rim of the outer tube, it could sometimes detach and completely rub around its full circumference. At $U_i = 7.26$ m/s the oscillations were strong enough to determine a frequency of $f = 2.39$ Hz; refer to Fig. 4.5(f).

For $U_o/U_i = 0.4$, the first instability at $U_i = 0.72$ m/s is static and the second one at $U_i = 1.72$ is a static deformation with a weak superimposed oscillatory component; refer to Fig. regarding impacting; that is, partial or complete rubbing with no dominant frequency of oscillations. However, at $U_i = 7.14$ m/s the oscillations were strong enough to determine a frequency of $f = 2.26$ Hz.

For $U_o/U_i = 0.6$, both instabilities at $U_i = 0.51$ m/s and $U_i = 1.05$ m/s were static; see Fig. 4.2(e). The same applies in the case of $U_o/U_i = 0.8$, at $U_i = 0.42$ m/s and 0.88 m/s, refer to Fig. 4.2(f). After the initiation of impacting, the pipe rubbed against a part of the outer tube with weak oscillations about the buckled position.

One interesting observation here is the dynamical behaviour of the pipe when it is stuck on the outer tube, as shown in Fig. 4.6(c). The Poincaré map in Fig. 4.6(d) and probability density function of both front and side displacements in Fig. 4.6(e,f) indicate that the very weak oscillations about the buckled position have a strong periodic component.

4.3.2 Experimental results for $\boldsymbol{r_{ann} \simeq 1/2}$

The experimental bifurcation diagrams showing the rms of amplitude of displacement as a function of the internal flow velocity, U_i, for U_o/U_i ranging from 0.055 to 0.8 are presented in Fig. 4.7. Qualitatively, two distinct dynamical behaviours could be observed for $U_o/U_i = 0.055$ and $U_o/U_i > 0.055$. For $U_o/U_i = 0.055$, the system becomes unstable via flutter in the second mode. On the other hand, for $U_o/U_i > 0.055$, the system undergoes a static deformation followed by one or two oscillatory instabilities before initiation of impacting.

For $U_o/U_i = 0.055$, the pipe is subjected to one- or two-sided impacting with the outer rigid tube at $U_i \geq 6.63$ m/s. Increasing the flow velocity further, the harmonics become

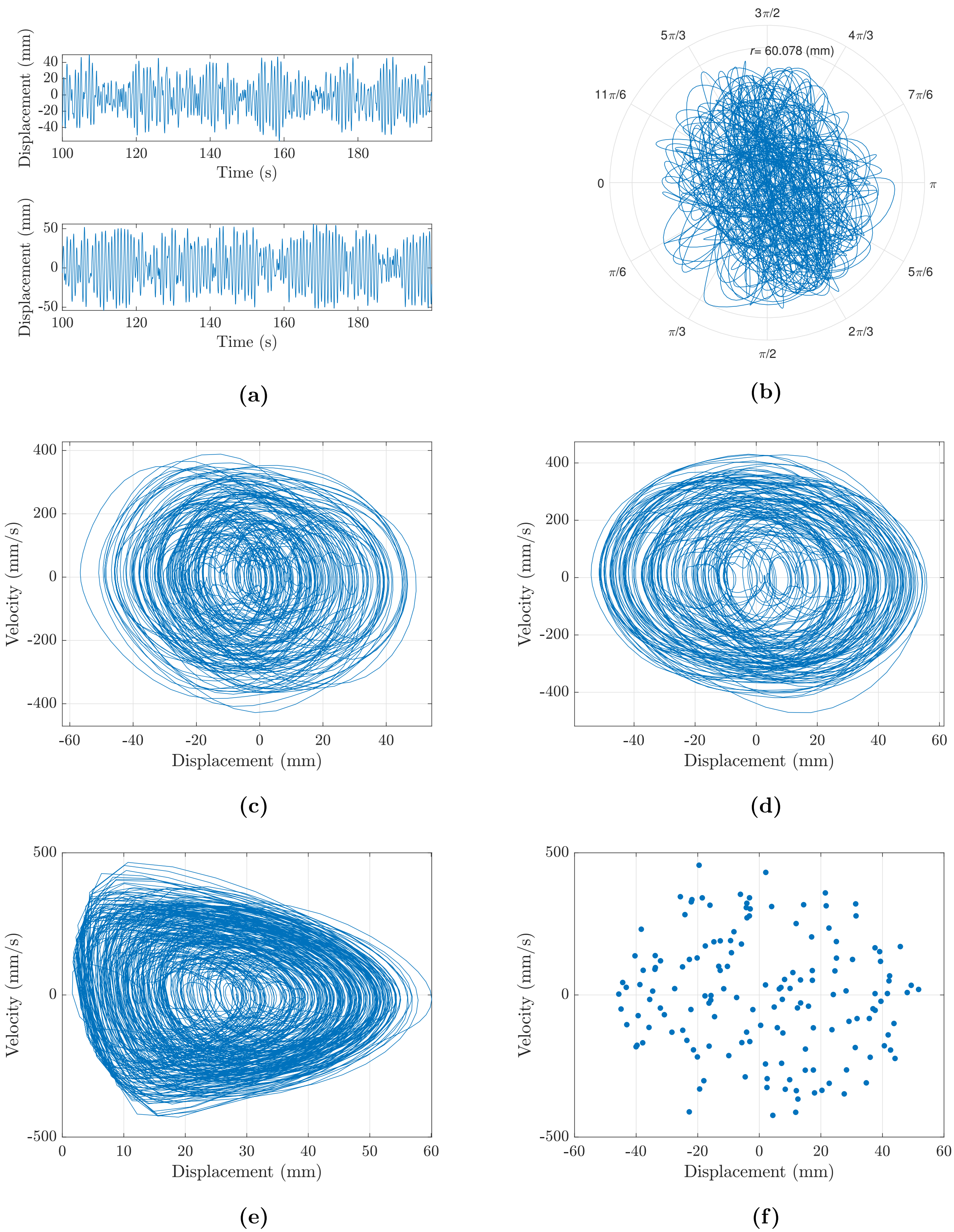

Figure 4.4: (a) Time series for $U_o/U_i = 0.055$ and $r_{ann} \simeq 1/4$ at $U_i = 6.63$ m/s; (b) polar plot; (c)-(e) phase portraits of the front, side and combined displacements, respectively; (f) Poincaré map of the oscillation.

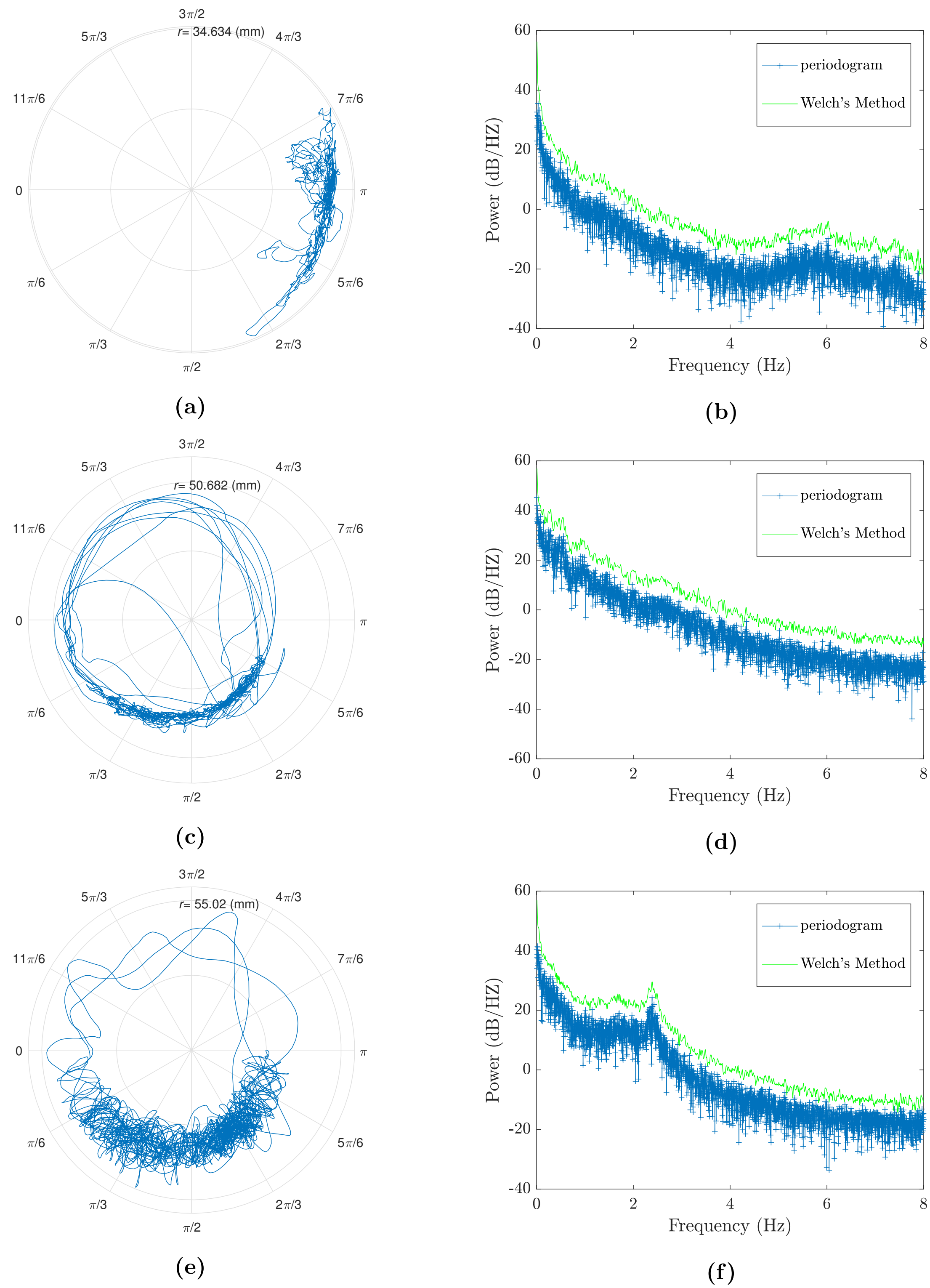

Figure 4.5: Impacting behaviour for $U_o/U_i = 0.2$ and $r_{ann} \simeq 1/4$, illustrated by means of polar plots and PSDs, at (a) and (b) $U_i = 4.42$ m/s; (c) and (d) $U_i = 6.32$ m/s; (e) and (f) $U_i = 7.26$ m/s.

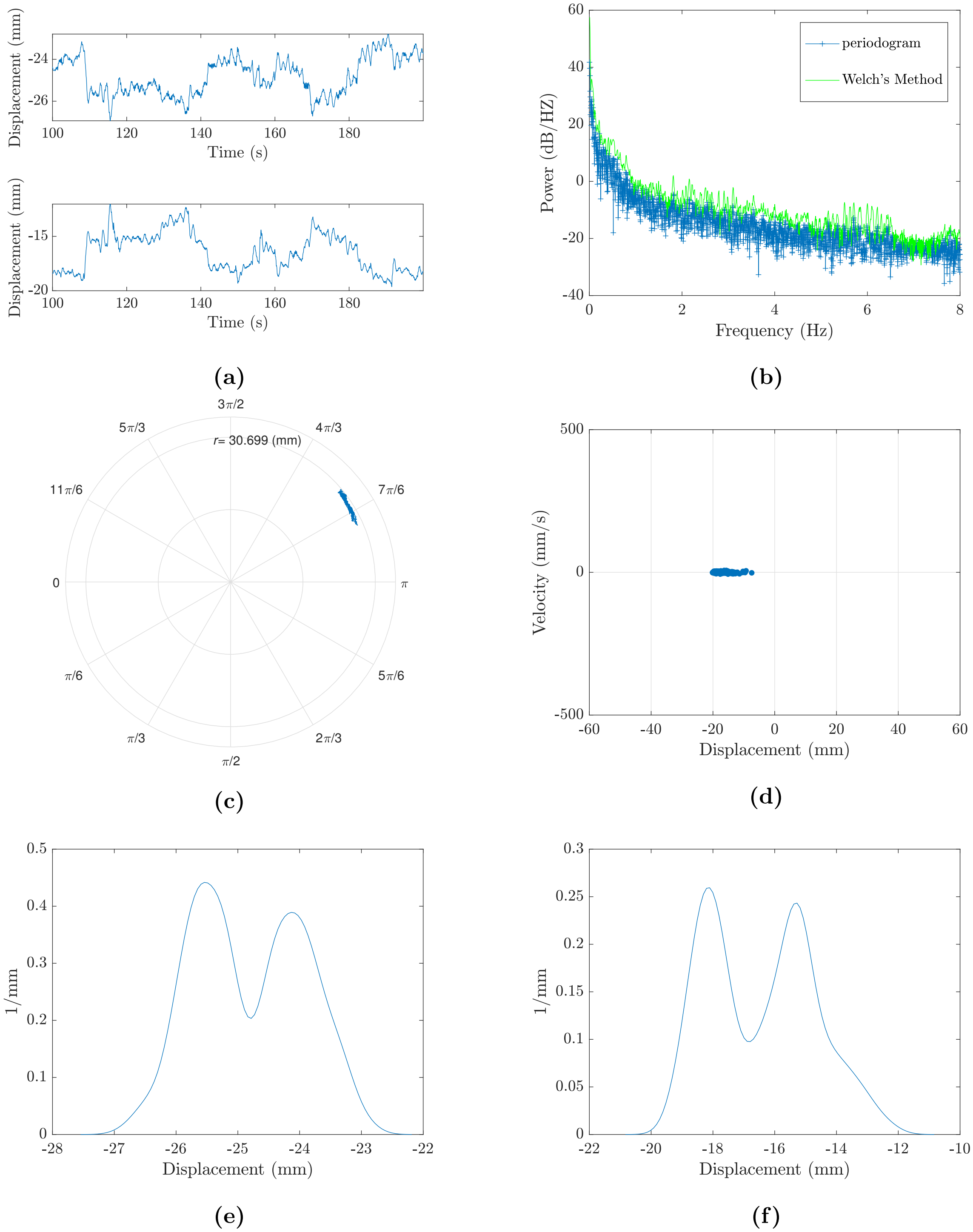

Figure 4.6: (a) Time series at $U_i = 1.74$ m/s for $U_o/U_i = 0.6$ and $r_{ann} \simeq 1/4$; (b) PSD; (c) polar plot; (d) Poincaré map; (e) PDF of front displacement; (f) PDF of side displacement.

stronger, as shown in the PSD plots of Fig. 4.8. These plots can be compared with those for $r_{ann} \simeq 1/4$ in Fig. 4.3 where the harmonics also disappear at higher flow velocities.

For $U_o/U_i = 0.1$, in contrast to $r_{ann} \simeq 1/4$, at first the pipe was subjected to a static deformation, which can be interpreted as buckling in the first mode since the amplitude increases with increasing flow velocity. This static instability developed at $U_i = 1.19$ m/s. Increasing the flow velocity further, the pipe was subjected to second-mode flutter at $U_i =$ 4.03 m/s. This flutter, however, was weak; the dominant frequency of $f = 1.91$ Hz in the PSD plot at $U_i = 4.42$ m/s is not so strong. At higher flow rates, the pipe started to touch the outer tube.

In agreement with the results for $U_o/U_i = 0.1$, for $U_o/U_i > 0.1$, as shown in Fig. 4.7(c-f) the pipe undergoes more than one instability before it hits the outer rigid tube; the second instability, however, is not always flutter in the second mode. For $U_o/U_i = 0.2$, first a static instability developed at $U_i = 1.06$ m/s; then an oscillatory instability, i.e., flutter in the second mode, materialized at $U_i = 1.69$ m/s. A frequency of $f = 2.09$ Hz was determined for oscillations at $U_i = 2.21$ m/s. The pipe tended to move toward one side of the rigid tube, and started to rub on it at $U_i = 2.53$ m/s.

For $U_o/U_i = 0.4$ (Fig. 4.7(d)), a static instability occurred at $U_i = 0.47$ m/s, followed by another instability at $U_i = 0.82$ m/s in the form of very weak oscillations superimposed on a static deformation. The same behaviour was observed at $U_i = 1.07$ m/s. The frequency of oscillations was not steady; a spectrum of frequencies ranging from 0 to 3 Hz was measured. At higher flow velocities, the pipe first rubbed against the outer rigid tube with a dominant frequency of 1.63 Hz.

The dynamical behaviour of the pipe and the PSD plots at higher flow velocities are presented in Fig. 4.9; a dominant frequency of $f = 0.98$ Hz was determined at $U_i = 2.08$ m/s, as shown in Fig. 4.9(b). The peaks observed at $U_i = 2.34$ m/s at $f = 1.17$ Hz and $f = 5.63$ Hz correspond to the second and third modes of the pipe. At $U_i = 2.59$ m/s, the peaks are around $f = 0.93$ Hz and $f = 5.48$ Hz.

For $U_o/U_i = 0.6$ the static instability at $U_i = 0.26$ m/s is followed by second mode flutter. The onset of this oscillatory instability, according to the Fig. 4.7(e), was found to be $U_i = 0.55$ m/s. The dominant frequency at $U_i = 0.63$ m/s and $U_i = 0.79$ m/s was found

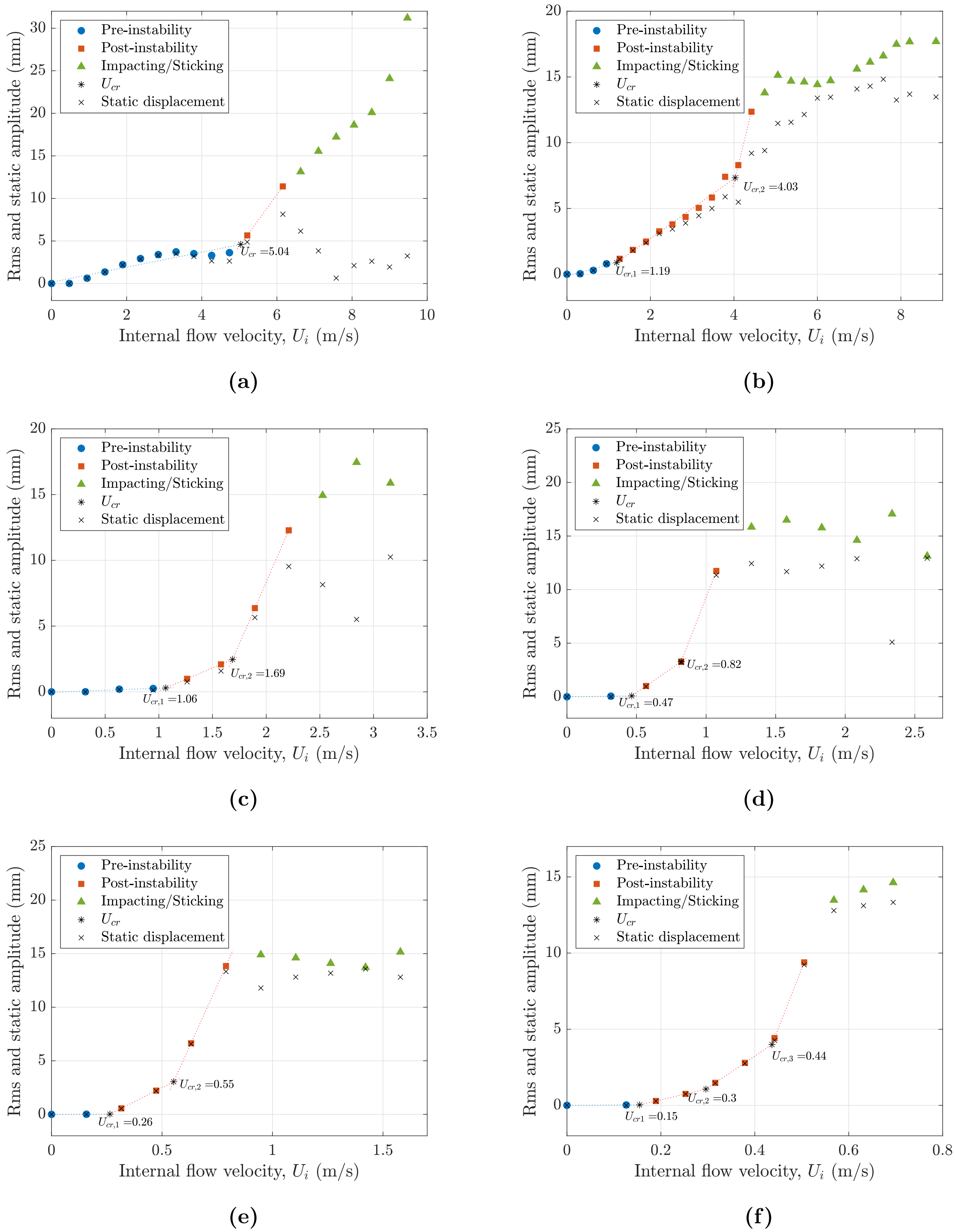

Figure 4.7: Bifurcation diagrams showing the static and rms amplitude of oscillations versus the internal flow velocity, U_i, for $r_{ann} \simeq 1/2$ and (a) $U_o/U_i = 0.055$; (b) $U_o/U_i = 0.1$; (c) $U_o/U_i = 0.2$; (d) $U_o/U_i = 0.4$; (e) $U_o/U_i = 0.6$; (f) $U_o/U_i = 0.8$.

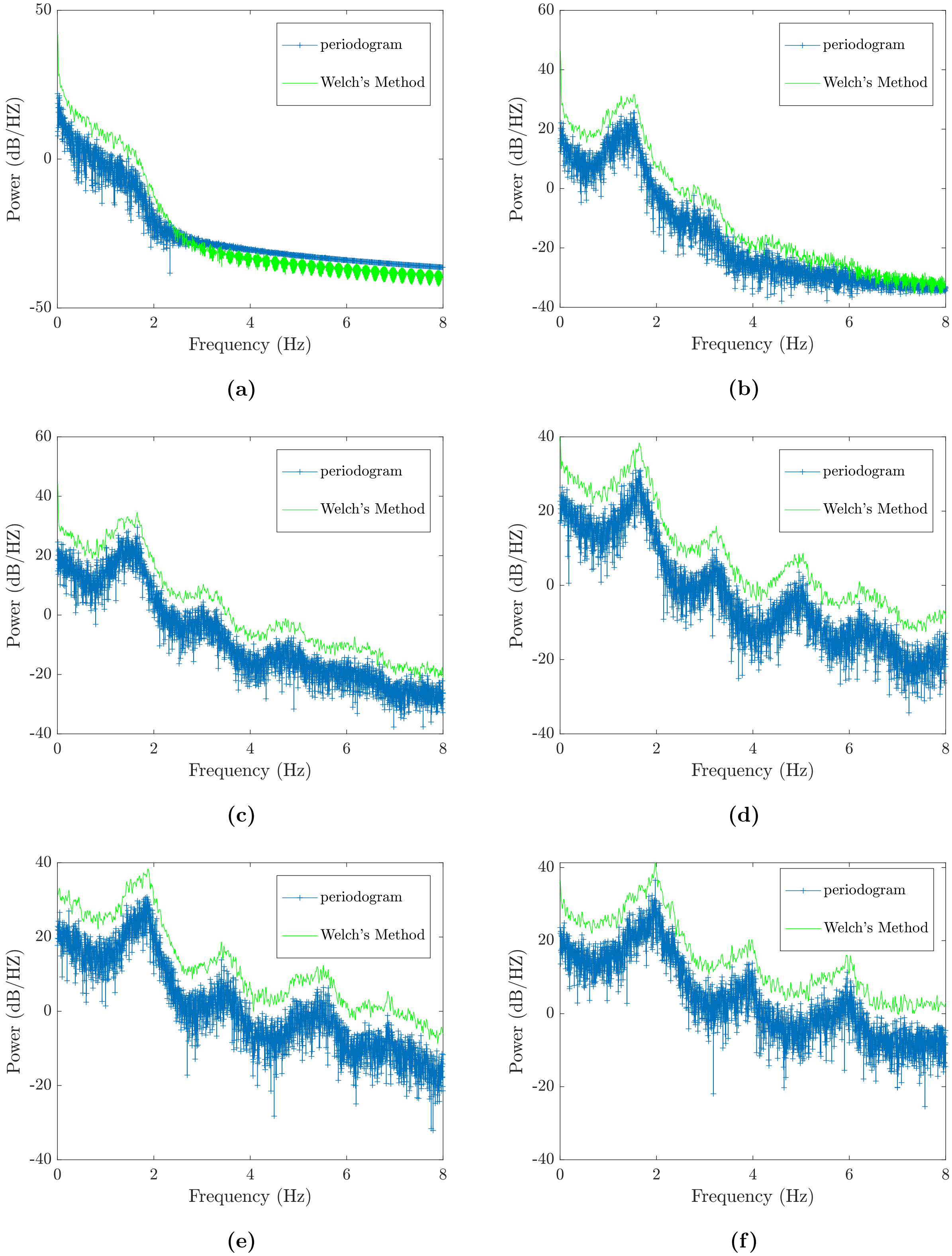

Figure 4.8: PSD plots for $U_o/U_i = 0.055$ and $r_{ann} \simeq 1/2$ at (a) $U_i = 5.21$ m/s; (b) $U_i = 6.16$ m/s; (c) $U_i = 6.63$ m/s; (d) $U_i = 7.10$ m/s; (e) $U_i = 7.58$ m/s; (f) $U_i = 8.05$ m/s.

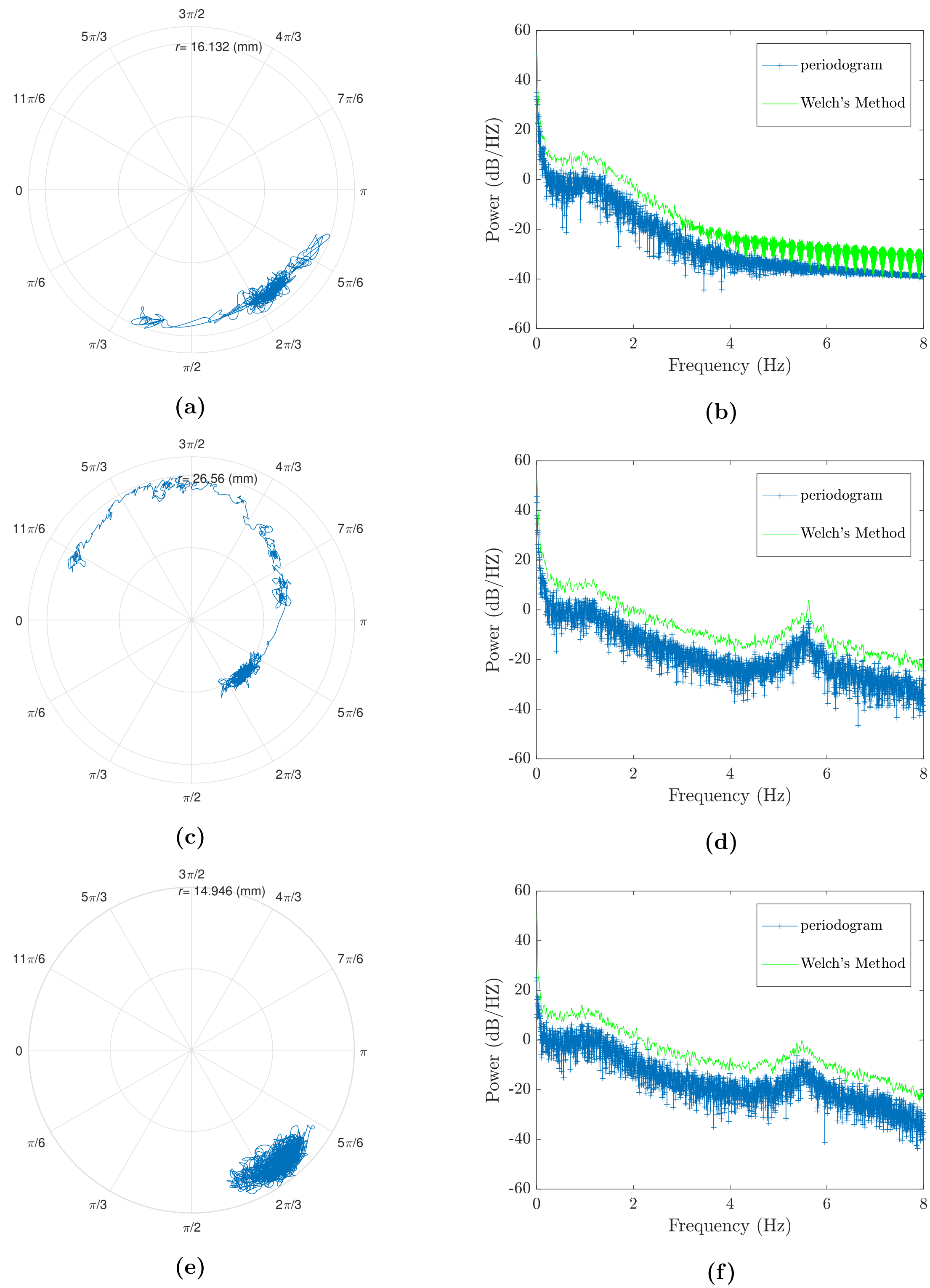

Figure 4.9: High frequency oscillations for $U_o/U_i = 0.4$ and $r_{ann} \simeq 1/2$ shown by means of polar plots and PSDs at high flow velocities: (a) and (b) $U_i = 2.08$ m/s; (c) and (d) $U_i = 2.34$ m/s; (e) and (f) $U_i = 2.59$ m/s.

to be $f = 2.27$ Hz and $f = 2.40$, respectively. In the latter, the oscillations were about an inclined state of the pipe.

Increasing the flow rate further, ultimately, contact between the pipe and the outer rigid tube in a form of partial rubbing was initiated. This impact mostly excited the frequency of $f = 1.34$ Hz and its harmonic at $f \simeq 2.88$ Hz. At higher flow velocities, the frequency spectra were rich but with frequency content mostly around the first and second mode frequencies, at $f \simeq 0.6$ Hz and $f \simeq 1.2$ Hz, respectively. At the maximum attainable flow velocity in this case, i.e., $U_i = 1.58$ m/s, however, oscillations were in the second and third modes; similar to that of $U_o/U_i = 0.4$ and $U_i = 2.59$ m/s.

Interestingly, for $U_o/U_i = 0.8$, the static instability at $U_i = 0.15$ m/s is followed by two oscillatory instabilities, namely, flutter in the first mode and in the second mode at higher flow rates, as shown in Fig. 4.7(f). The pipe started to partially rub on the surrounding tube at $U_i = 0.54$ m/s.

4.3.3 Experimental results for $r_{ann} \simeq 3/4$

In this section experimental results for the longest annulus, namely, $r_{ann} = 0.705$ are presented. Rms displacement as a function of the internal flow velocity, U_i, $U_o/U_i = 0.055, 0.1, 0.2, 0.4, 0.6$ and 0.8, are shown in Fig. 4.10. One significant difference, as compared to the case of $r_{ann} \simeq 1/2$ is that the post-buckling oscillatory instability for $U_o/U_i \geq 0.1$ never materialized, as the pipe developed a static deformation, touching the outer tube, and remained in contact with it thereafter.

For $U_o/U_i = 0.055$, as shown in Fig. 4.11(a), the pre-instability weak oscillations are not of a specific frequency, but a range of frequencies, mostly close to the first mode, as it has the lowest internal damping. At $U_i = 5.21$ m/s, these oscillations became stronger and at $U_i = 5.68$ m/s an oscillatory instability developed; refer to the PSDs of Fig. 4.11(b,c). Although the dominant frequencies in these PSDs are not sharply defined, they are close to the second-mode frequency. At $U_i = 6.16$ m/s, one-sided impacting occurred. At still higher flow velocities one- or two-sided impacting was observed; see Fig. 4.11(d-f). By further increasing the flow velocity, the pipe sticks to the outer tube and a kind of chattering behaviour was observed. Eventually, at the maximum attainable flow velocity in this experiment, i.e., $U_i = 9.95$ m/s, the pipe detached and irregular oscillations around the annulus took place,

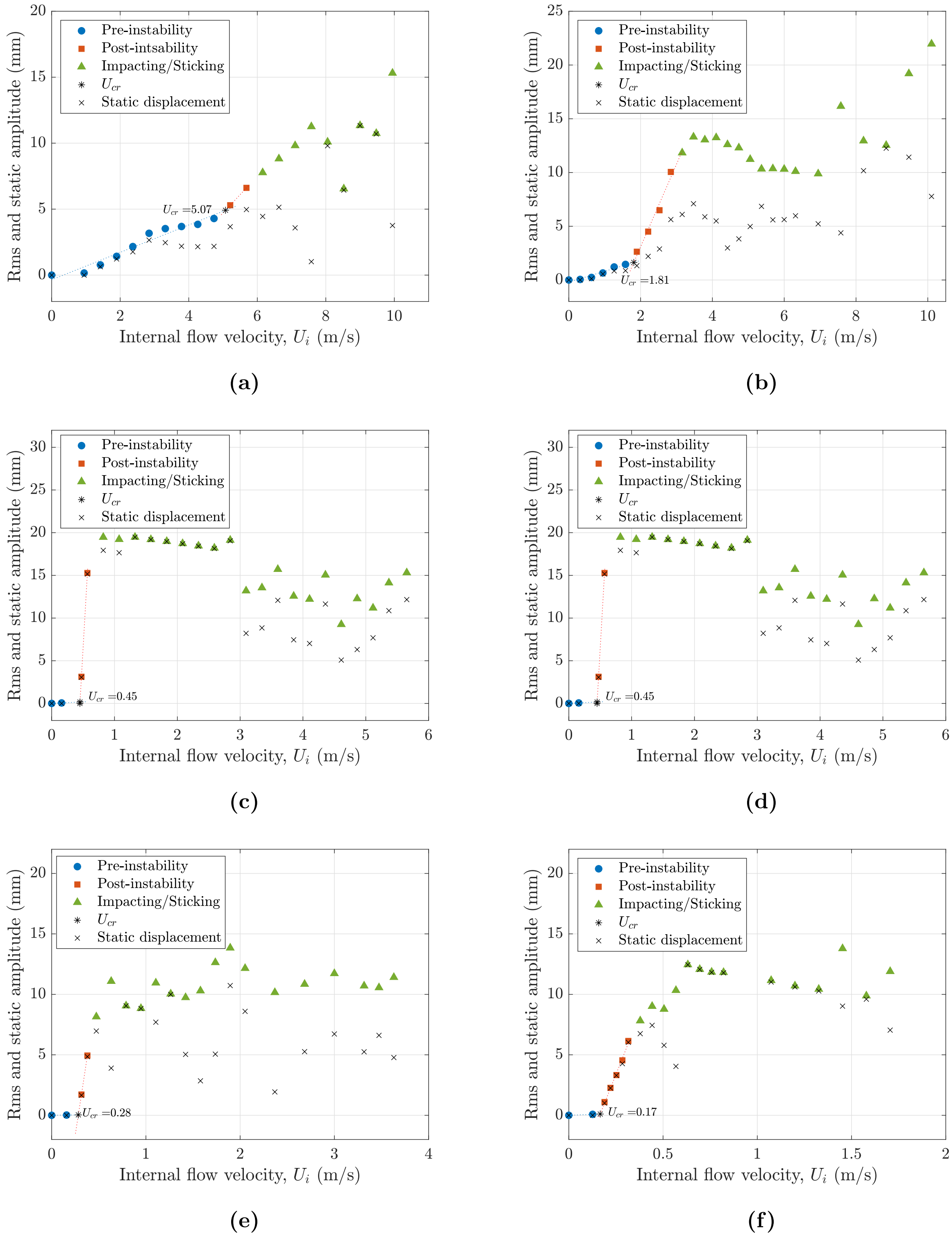

Figure 4.10: Bifurcation diagrams showing the static and rms amplitude of oscillations versus the internal flow velocity, U_i, for $r_{ann} \simeq 3/4$ and (a) $U_o/U_i = 0.055$; (b) $U_o/U_i = 0.1$; (c) $U_o/U_i = 0.2$; (d) $U_o/U_i = 0.4$; (e) $U_o/U_i = 0.6$; (f) $U_o/U_i = 0.8$.

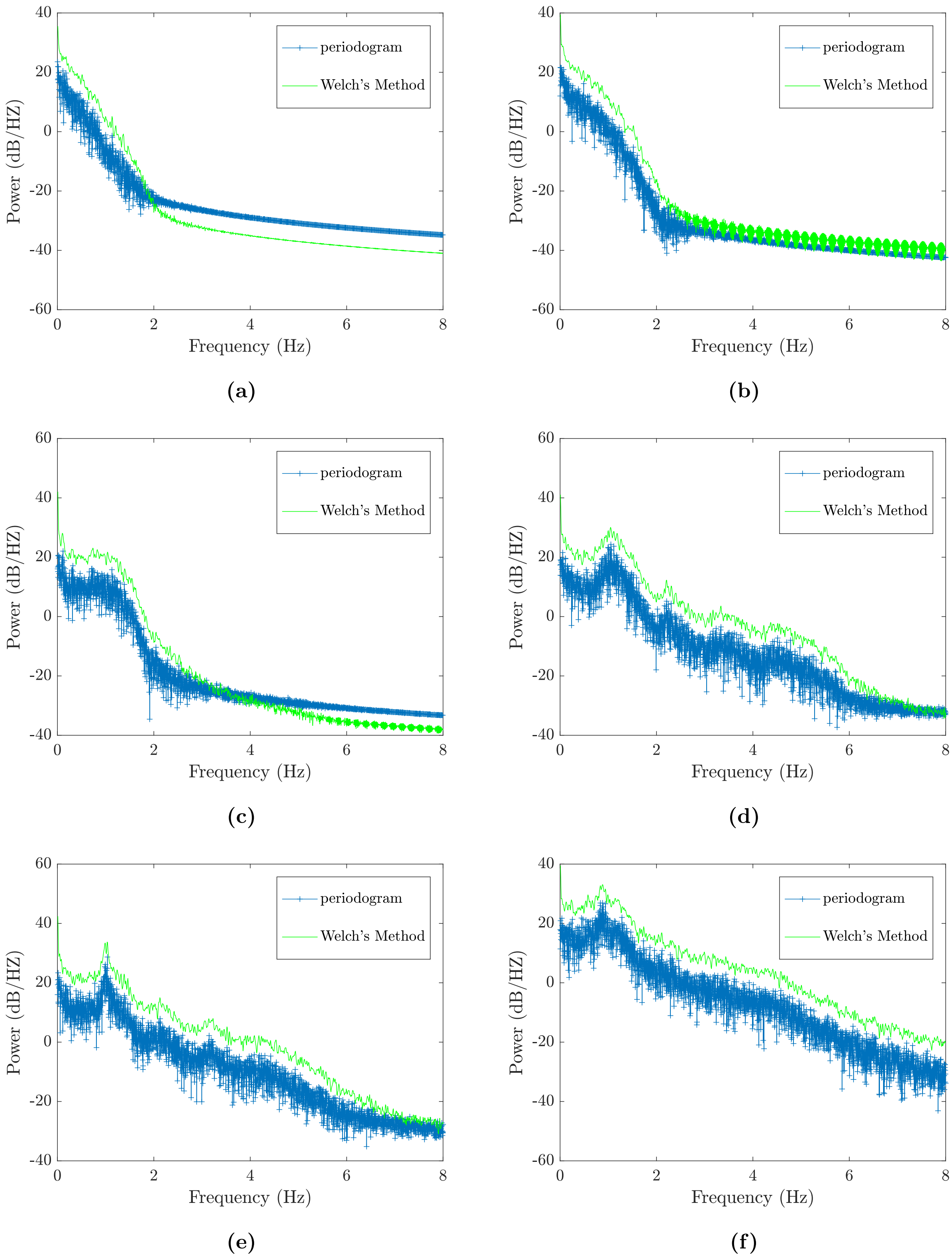

Figure 4.11: PSD plots for $U_o/U_i = 0.055$ and $r_{ann} \simeq 3/4$ at (a) $U_i = 4.47$ m/s; (b) $U_i = 5.21$ m/s; (c) $U_i = 5.68$ m/s; (d) $U_i = 6.16$ m/s; (e) $U_i = 6.63$ m/s; (f) $U_i = 7.10$ m/s.

as shown in Fig. 4.12(a-d).

For $U_o/U_i = 0.1$ (Fig. 4.10(b)), a static instability emerged at $U_i = 1.81$ m/s with

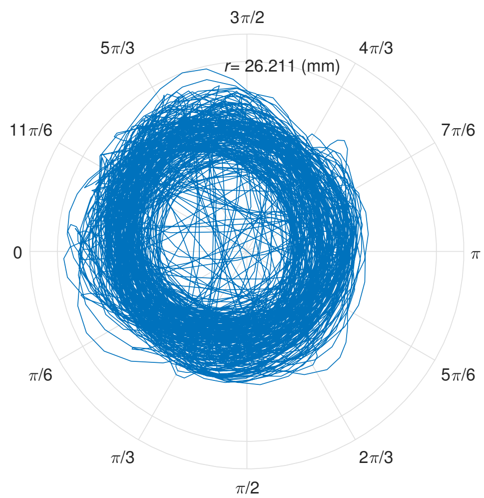

(a)

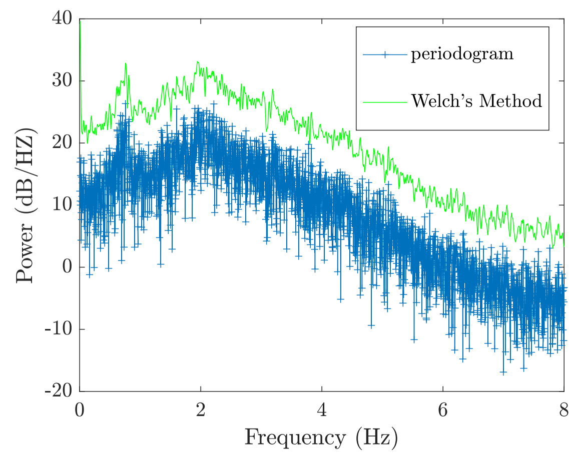

(b)

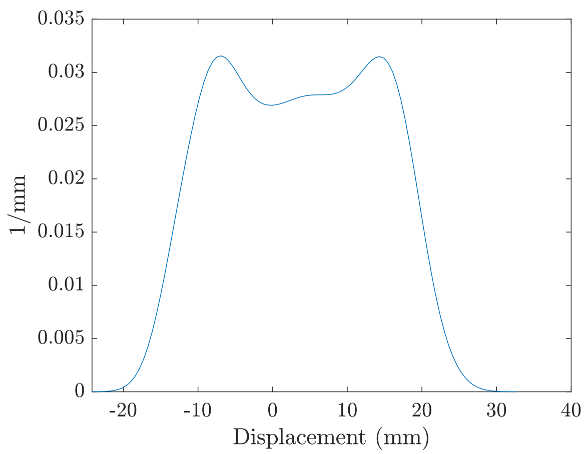

(c)

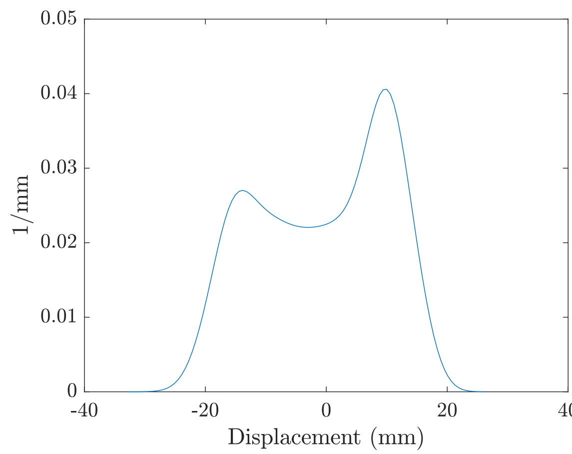

(d)

Figure 4.12: (a) Polar plot of the system at $U_i = 9.95$ m/s for $U_o/U_i = 0.055$ and $r_{ann} \simeq 3/4$; (b) PSD; (c) PDF of front displacement; (d) PDF of side displacement.

a weak oscillatory component superimposed. This oscillatory component developed further at higher flow rates, but a flutter instability never arose prior to inititation of impacting. At $U_i = 3.16$ m/s, the pipe partially, and at higher flows completely, rubbed against the surrounding tube. Increasing the flow velocity to $U_i = 7.58$ m/s, a similar behaviour to displayed in Fig. 4.12 was observed. At still higher flow, namely $U_i = 8.84$ m/s, the pipe stuck on the outer tube, and only a chattering kind of motion was observed; however, it detached itself at higher flow velocities, as can be seen on the right hand side of Fig. 4.10(b).

For $U_o/U_i = 0.2$ (Fig. 4.10(c)), a static instability was detected at $U_i = 0.85$ m/s. Very weak oscillations at $U_i = 0.95$ m/s and 1.26 m/s were mostly about an inclined position, with no sharply defined frequency, but a range of frequencies close to the first-mode frequency. The post-impacting dynamical behaviour is presented in Fig. 4.13; one-sided impacting and rubbing at $U_i = 1.58$ m/s, rubbing at $U_i = 1.89$ m/s, which then changes to sticking at $U_i = 2.84$ m/s. Fig. 4.13(f) indicates a dominant frequency of $f = 1.95$ Hz for the small oscillations about the inclined state of the pipe when it is stuck on the outer rigid tube. The pipe detached itself at higher flow rates and its behaviour was more or less similar to that for $U_o/U_i = 0.1$. Therefore, the dynamics of the pipe at higher U_is are not discussed here further for brevity.

For $U_o/U_i = 0.4$ (Fig. 4.10(d)), the sharp increase in the slope at $U_i = 0.45$ m/s is due to the static deformation; the pipe was inclined and only very small motions about the buckled position took place. At $U_i = 0.82$ m/s, the pipe chattered against the buckled position by partially rubbing on the outer tube. At higher flows, first it got stuck and then detached itself at $U_i = 3.09$ m/s. The frequency of oscillations about the buckled position was found to be about 2 Hz.

Qualitatively, the same stability behaviour as for $U_o/U_i = 0.4$ was observed for $U_o/U_i = 0.6$: static instability followed by impacting. One important note is that, at $U_i = 0.47$ m/s, the pipe only lightly touched the outer tube; therefore, one can specify it as the threshold of flutter about the buckled position; see Figs. 4.10(e) and 4.14(b).

Finally, for $U_o/U_i = 0.8$ (Fig. 4.10(f)), the pipe became inclined at very small flow velocities and a static instability at $U_i = 0.17$ m/s was indicated. Right after impacting started, i.e., at $U_i = 0.38$ m/s, where slow one-sided impacting was observed, the oscillations occurred with $f = 0.38$ Hz. However, at higher flow velocities, the dominant frequency of the oscillations was found to be around 2 Hz.

4.4 Summary and conclusion

The dynamics of a pipe simultaneously subjected to internal and reverse, partially-confined, external flows has been investigated experimentally in this study. The pipe is cantilevered vertically and discharges fluid downwards in a large reservoir. The fluid exits

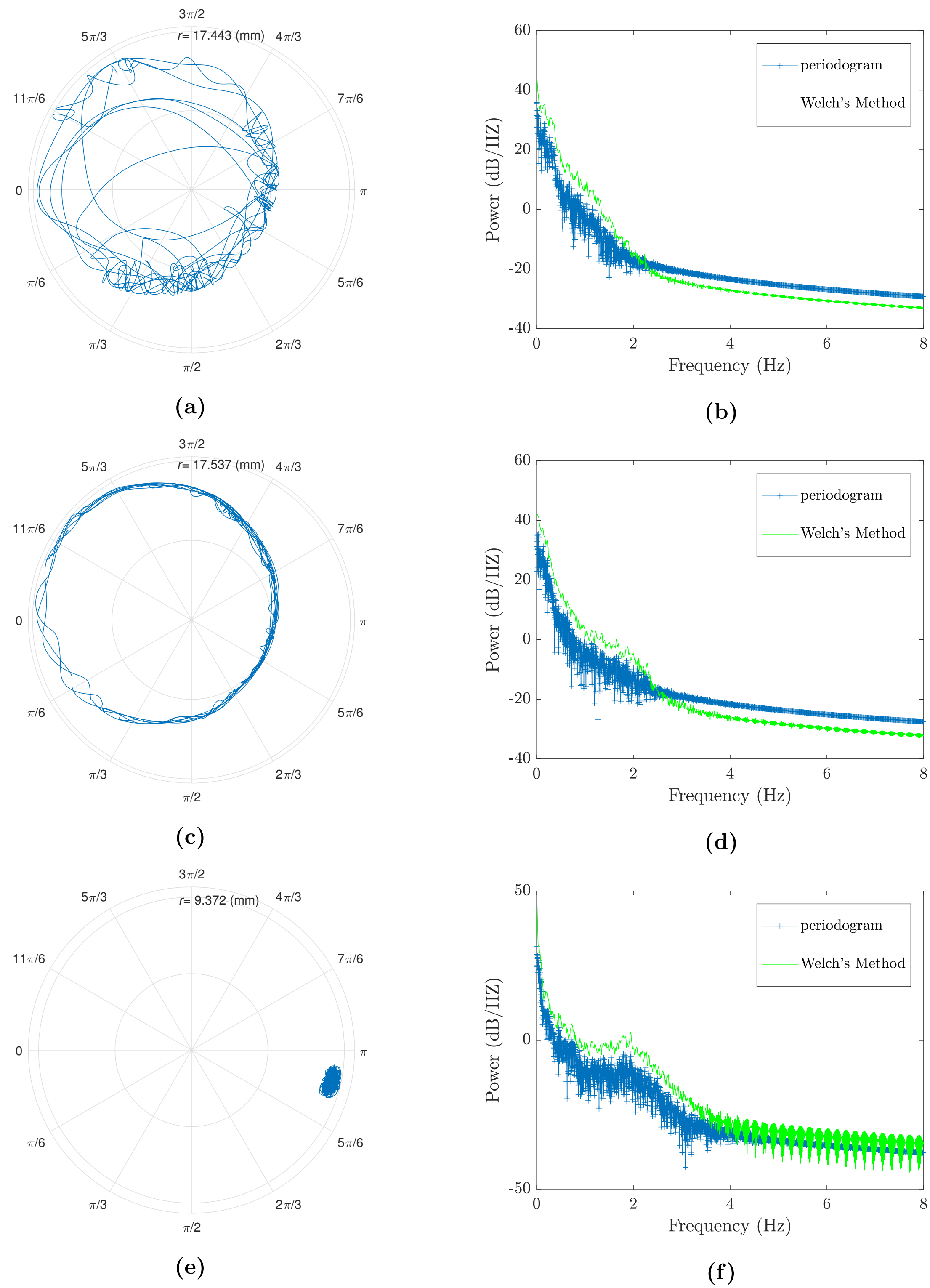

Figure 4.13: Dynamical behaviour of the system for $U_o/U_i = 0.2$ and $r_{ann} \simeq 3/4$ illustrated by means of polar plots and PSDs, at (a) and (b) $U_i = 1.58$ m/s; (c) and (d) $U_i = 1.89$ m/s; (e) and (f) $U_i = 2.84$ m/s.

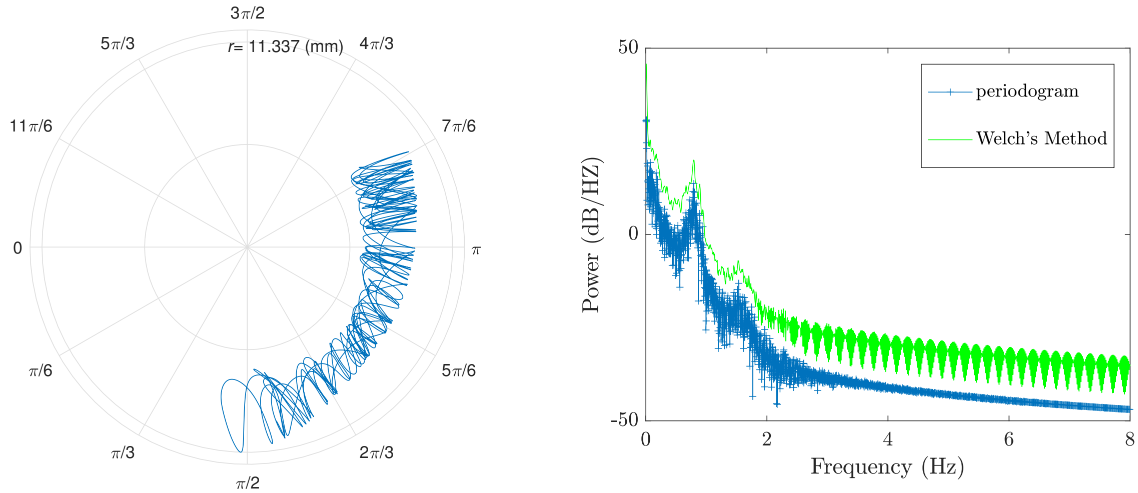

(a) **(b)**

Figure 4.14: Dynamical behaviour of the system for $U_o/U_i = 0.6$ and $r_{ann} \simeq 3/4$ right after the pipe started lightly touching the annulus, at $U_i = 0.47$ m/s, (a) polar plot; (b) PSD.

Table 4.2: Summary of the results showing the critical internal flow velocities in m/s for instability.

	$r_{ann} \simeq 1/4$		$r_{ann} \simeq 1/2$		$r_{ann} \simeq 3/4$
U_o/U_i	$U_{cr,1}$	$U_{cr,2}$	$U_{cr,1}$	$U_{cr,2}$	U_{cr}
0.055	5.68	-	5.04	-	5.07
0.1	5.41	-	1.19	4.03	1.81
0.2	2.17	3.69	1.06	1.69	0.85
0.4	0.72	1.72	0.47	0.82	0.45
0.6	0.51	1.05	0.26	0.55	0.28
0.8	0.42	0.88	0.15	0.3	0.17

the reservoir through an annulus surrounding the upper part of the pipe. Three sets of experiments were conducted to investigate the influence of varying the confinement ratio; i.e., the length of the annulus to the length of the flexible pipe, $r_{ann} = L'/L$, on the dynamical behaviour and stability of the system. For each L'/L, six ratios of external to internal flow velocities were tested, namely $U_o/U_i = 0.055$, 0.1, 0.2, 0.4, 0.6, and 0.8. For the lowest ratio of U_o/U_i tested, the pipe was found to undergo flutter in the second mode at relatively high

Table 4.3: The dynamical behaviour of the system right after the initiation of impacting.

r_{ann}	U_o/U_i	U_i	Observed dynamical behaviour of the pipe
1/4	0.055	6.63	Oscillations (f = 1.18 Hz)
	0.1	6.32	Oscillations (f = 1.02 Hz)
	0.2	4.42	Rubbing against part of the outer tube
	0.4	2.34	Rubbing against part of the outer tube
	0.6	1.58	Rubbing against part of the outer tube
	0.8	1.2	Rubbing against part of the outer tube
1/2	0.055	6.63	Oscillations (f = 1.65 Hz)
	0.1	4.74	Rubbing against part of the outer tube
	0.2	2.53	Rubbing against part of the outer tube
	0.4	1.33	Rubbing against part of the outer tube
	0.6	0.95	Rubbing/chattering against part of the outer tube (f =1.6 Hz)
	0.8	0.57	Rubbing/chattering against part of the outer tube (f =2.66 Hz)
3/4	0.055	6.16	Oscillations (f = 1.05 Hz)
	0.1	3.16	Rubbing against part of the outer tube
	0.2	1.58	Rubbing around the annulus
	0.4	0.82	Rubbing/chattering against part of the outer tube (f = 0.80 Hz)
	0.6	0.47	Oscillating while lightly touching and detaching (f = 0.79 Hz)
	0.8	0.38	Oscillations about the buckled position (f = 0.37 Hz)

flow velocity. The amplitude of oscillations increased with increasing flow velocity and the pipe eventually began to hit the rigid tube forming the annulus.

Increasing the ratio of external to internal flow velocities was found to have a significant destabilizing effect on the system. The onset of instability drops to quite low values with increasing U_o/U_i, as shown in Table 4.2. Moreover, in some cases, noticeably high amplitude static deflections were observed before flutter instability, which suggests that the pipe may undergo a static buckling at even lower flow velocities. Increasing the confinement ratio, r_{ann}, to $r_{ann} > 1/4$, was also found to destabilize the pipe, as seen in Table 4.2. The static deflections at low flow velocities were found to be more pronounced at higher r_{ann}, and the pipe started to hit/rub against the outer rigid tube before any oscillatory motion was observed. This can also be due to the narrowness of the annulus that prevents an oscillatory instability from developing.

The dynamical behaviour beyond the pipe touching/hitting the rigid tube has also been discussed in this study. A summary of the dynamical behaviour at flow velocities right after the initiation of impacting is presented in Table 4.3. At lower ratios of U_o/U_i the pipe continued to oscillate after hitting the rigid tube, and the oscillations seemed to be periodic with a chaotic component. At higher U_o/U_i, the pipe generally rubbed itself against the rigid outer tube; yet, at higher confinement ratios, the pipe was observed to detach itself from the rigid channel at higher flow velocities, and display periodic oscillations.

Acknowledgment

The financial support by the Natural Sciences and Engineering Research Council of Canada (NSERC), the Solution Mining Research Institute (SMRI), and Pipeline Research Council International (PRCI) is acknowledged. The first author is also grateful to McGill University for a McGill Engineering International Tuition Award (MEITA).

Appendix. Dimensionless parameters

Although in this study all the results have been described in terms of dimensional parameters, it is also common in the fluid-structure interaction community to use dimensionless internal and external flow velocities as follows:

$$u_i = \left(\frac{M_i}{EI}\right)^{1/2} LU_i, \qquad u_o = \left(\frac{\rho_f A_o}{EI}\right)^{1/2} LU_o, \tag{A.1}$$

where $M_i = \rho_f A_f$, ρ_f is the fluid density, $A_f = \frac{1}{4}\pi D_i^2$ and $A_o = \frac{1}{4}\pi D_o^2$, with D_i and D_o being the internal and external pipe diameter, respectively. L is the length of the pipe and EI is its flexural rigidity.

For the pipe used in the experiments in this paper, $u_i = 0.9142 \times [U_i \text{ (m/s)}]$ and $u_o = 2.3034 \times [U_o \text{ (m/s)}]$.

References

[1] M. Païdoussis, Calvin Rice Lecture: Some curiosity-driven research in fluid structure interactions and its current applications, ASME J. Press. Vessel Technol. 115 (1) (1993) 2–14.

[2] M. Païdoussis, Fluid-Structure Interactions: Slender Structures and Axial Flow, Vol. 1, 2nd edition, Academic Press, 2014.

[3] P. Holmes, Bifurcations to divergence and flutter in flow-induced oscillations: a finite dimensional analysis, J. Sound Vib. 53 (4) (1977) 471–503.

[4] P. Holmes, Pipes supported at both ends cannot flutter, J. Appl. Mech. 45 (3) (1978) 619–622.

[5] P. Holmes, J. Marsden, Bifurcation to divergence and flutter in flow-induced oscillations: an infinite dimensional analysis, Automatica 14 (4) (1978) 367–384.

[6] A. Bajaj, P. Sethna, T. Lundgren, Hopf bifurcation phenomena in tubes carrying a fluid, SIAM J. Appl. Math. 39 (2) (1980) 213–230.

[7] M. Païdoussis, F. Moon, Nonlinear and chaotic fluidelastic vibrations of a flexible pipe conveying fluid, J. Fluids Struct. 2 (6) (1988) 567–591.

[8] M. Païdoussis, G. Li, R. Rand, Chaotic motions of a constrained pipe conveying fluid: comparison between simulation, analysis, and experiment, J. Applied Mechanics 58 (1991) 559–565.

[9] C. Semler, Nonlinear dynamics and chaos of a pipe conveying fluid, Ph.D. thesis, Department of Mechanical Engineering, McGill University (1991).

[10] M. Païdoussis, C. Semler, Nonlinear and chaotic oscillations of a constrained cantilevered pipe conveying fluid: a full nonlinear analysis, Nonlinear Dyn. 4 (6) (1993) 655–670.

[11] C. Semler, G. Li, M. Païdoussis, The non-linear equations of motion of pipes conveying fluid, J. Sound Vib. 169 (5) (1994) 577–599.

[12] M. Wadham-Gagnon, M. Païdoussis, C. Semler, Dynamics of cantilevered pipes conveying fluid. Part 1: Nonlinear equations of three-dimensional motion, J. Fluids Struct. 23 (4) (2007) 545–567.

[13] M. Païdoussis, C. Semler, M. Wadham-Gagnon, S. Saaid, Dynamics of cantilevered pipes conveying fluid. Part 2: dynamics of the system with intermediate spring support, J. Fluids Struct. 23 (4) (2007) 569–587.

[14] Y. Modarres-Sadeghi, C. Semler, M. Wadham-Gagnon, M. Païdoussis, Dynamics of cantilevered pipes conveying fluid. Part 3: Three-dimensional dynamics in the presence of an end-mass, J. Fluids Struct. 23 (4) (2007) 589–603.

[15] Y. Modarres-Sadeghi, M. Païdoussis, C. Semler, Three-dimensional oscillations of a cantilever pipe conveying fluid, Int. J. Non. Linear. Mech. 43 (1) (2008) 18–25.

[16] L. Wang, T. Jiang, H. Dai, Three-dimensional dynamics of supported pipes conveying fluid, Acta Mech. Sin. 33 (6) (2017) 1065–1074.

[17] J. Duan, K. Chen, Y. You, R. Wang, J. Li, Three-dimensional dynamics of vortex-induced vibration of a pipe with internal flow in the subcritical and supercritical regimes, Int. J. Nav. Archit. Ocean Eng. 10 (6) (2018) 692–710.

[18] F. Cesari, S. Curioni, Buckling instability in tubes subject to internal and external axial fluid flow, in: Proc. 4th Conf. Dimens., Hungarian Academy of Science, Budapest, 1971, pp. 301–311.

[19] M. Hannoyer, M. Païdoussis, Instabilities of tubular beams simultaneously subjected to internal and external axial flows, ASME J. Mech. Des. 100 (2) (1978) 328–336.

[20] J. Bailey, I. Finnie, An analytical study of drill-string vibration, ASME J. Eng. Ind. 82 (2) (1960) 122–127.

[21] I. Finnie, J. Bailey, An experimental study of drill-string vibration, ASME J. Eng. Ind. 82 (2) (1960) 129–135.

[22] J. Den Hartog, John Orr memorial lecture: recent cases of mechanical vibration, South African Mech. Eng. 19 (3) (1969) 53–68.

[23] J. Grigoriev, Stability of a drill tube column with an initial curvature in the axial stream, J. Bauman Moscow State Tech. Univ. Mashinostronye 5 (1978) 23–28.

[24] T. Luu, On the dynamics of three systems involving tubular beams conveying fluid, Master's thesis, Department of Mechanical Engineering, McGill University, Canada (1983).

[25] M. Païdoussis, T. Luu, S. Prabhakar, Dynamics of a long tubular cantilever conveying fluid downwards, which then flows upwards around the cantilever as a confined annular flow, J. Fluids Struct. 24 (1) (2008) 111–128.

[26] Q. Qian, L. Wang, Q. Ni, Vibration and stability of vertical upward-fluid-conveying pipe immersed in rigid cylindrical channel, Acta Mech. Solida Sin. 21 (5) (2008) 331–340.

[27] K. Fujita, A. Moriasa, Stability of cantilevered pipes subjected to internal flow and external annular axial flow simultaneously, in: ASME 2015 Press. Vessel. Pip. Conf., Boston, MA, USA; PVP2015-45141, 2015.

[28] K. Moditis, The dynamics of hanging tubular cantilevers in axial flow: An experimental and theoretical investigation, Master's thesis, Department of Mechanical Engineering, McGill University (2014).

[29] K. Moditis, M. Païdoussis, J. Ratigan, Dynamics of a partially confined, discharging, cantilever pipe with reverse external flow, J. Fluids Struct. 63 (2016) 120–139.

[30] K. Kontzialis, K. Moditis, M. Païdoussis, Transient simulations of the fluid–structure interaction response of a partially confined pipe under axial flows in opposite directions, ASME J. Press. Vessel Technol. 139 (3) (2017).

[31] S. Minas, M. Païdoussis, F. Daneshmand, Experimental and analytical investigation of hanging tubular cantilevers with discharging axial and radial flow, in: ASME 2017 Int. Mech. Eng. Congr. Expo., Tampa, FL, USA; IMECE2017-70466, 2017.

[32] M. Païdoussis, A. Abdelbaki, M. Butt, K. Moditis, A. Misra, M. Nahon, Dynamics of a pipe subjected to internal and confined external flow, in: ASME Press. Vessel. Pip. Conf., San Antonio, TX, USA; PVP2019-93227, 2019.

[33] A. Abdelbaki, A. Misra, M. Païdoussis, Dynamics of a tubular cantilever simultaneously subjected to internal and partially-confined external axial flows, in: ASME 2018 Int. Des. Eng. Tech. Conf. and Comput. Inf. Eng. Conf., Québec City, QC, Canada; DETC2018-86176, 2018.

[34] A. Abdelbaki, M. Païdoussis, A. Misra, A nonlinear model for a hanging tubular cantilever simultaneously subjected to internal and confined external axial flows, J. Sound Vib. 449 (2019) 349–367.

[35] A. Abdelbaki, M. Païdoussis, A. Misra, A nonlinear model for a hanging cantilevered pipe discharging fluid with a partially-confined external flow, Int. J. Non-Linear Mech. 118 (2020) 103290.

CHAPTER 5

Dynamics of a Cantilevered Pipe Conveying Fluid and Counter-currently Subjected to Partially Confined External Axial Flows: Experimental Investigation II

Preface

Following the work presented in the previous chapter, this chapter presents the second part of the experiments on system III, using the same bench-top-size apparatus. In the previous chapter, the effect of annulus-to-pipe length ratio, i.e. the ratio of the confined length of the pipe to its total length, was studied. The manuscript presented in this chapter [4], focuses on utilizing qualitative and quantitative nonlinear dynamics tools, to explore the nature of the motions of the pipe, also investigating the influence of the other main system parameters on the dynamics. These parameters involve the (i) external flow confinement (annular gap size), (ii) pipe length-to-diameter ratio, (iii) pipe material, (iv) flow constriction at the upstream or downstream end of the annular region, and (v) eccentric positioning of the outer rigid tube relative to the central pipe.

Dynamics of a hanging fluid-discharging pipe subjected to reverse external flow: an experimental investigation

Mahdi Chehreghani, Ahmed Shaaban, Arun K. Misra, Michael P. Païdoussis*

Department of Mechanical Engineering, McGill University,

817 Sherbrooke Street West, Montreal, QC, Canada H3A 0C3.

Abstract: The present paper discusses and analyzes experiments on the dynamics of hanging cantilever tubular beams conveying fluid downwards and subjected to partially-confined reverse external axial flow. A bench-top-size facility, consisting of a reservoir filled with water, a hanging flexible pipe conveying fluid downwards and a shorter outer rigid tube surrounding the pipe at its upper portion containing an upwards flow, was utilized. A non-contacting optical approach was employed to obtain the displacement time-series of pipe motions from which, using qualitative and quantitative nonlinear dynamics tools, the nature of the motions was explored. The oscillatory motions observed were found to be unsteady with both periodic and chaotic content. The influence of some system parameters on the dynamics, namely, external flow confinement, pipe slenderness, pipe material, placement of a constraint at the external annular flow inlet/outlet, and eccentric positioning of the outer rigid tube relative to the central pipe, was examined. It was found that varying the system parameters in some cases gives rise to quite interesting qualitative or quantitatively changes in this Fluid-Structure Interaction (FSI) system.

Keywords: Pipes conveying fluid; Flutter; Static divergence; Annular confinement; Eccentricity; Slenderness; Flow separation; Axial flow; Chaos.

5.1 Introduction

The dynamics of slender structures conveying fluid or subjected to external flow is an enduring research topic, with the first paper published on the subject more than eighty years ago [1]. Pipelines, high-speed trains, nuclear reactors and renewable energy harvesters are among the many engineering applications in which a slender body interacts with fluid. Biological and physiological examples may be found in locomotion of slender fish, blood vessels

*Corresponding author.

E-mail addresses: mahdi.chehreghani@mail.mcgill.ca, ahmed.shaaban@mail.mcgill.ca, arun.misra@mcgill.ca, michael.paidoussis@mcgill.ca

and vocal cords. In addition to many studies in this area being "application oriented", several are "curiosity-driven" and fundamental [2], focusing on understanding the underlying FSI of the observed phenomena.

The fairly simple system of a pipe conveying fluid and its many variations, such as pipes with added supports, masses, linear and nonlinear springs and dashpots and end-nozzles, display a rich dynamical behaviour. Indeed, the fluid-elastic system of a pipe conveying fluid has become a *paradigm* in dynamics [2, 3], serving as a model problem to illustrate known dynamical concepts or as a tool to explore new classes of dynamical behaviour.

It is known that the gyroscopic conservative system of a pipe with supported ends cannot flutter [4], despite the prediction of coupled-mode flutter by linear theory. Cantilevered pipes, on the other hand do flutter [5]; they are subjected to either a sub- or supercritical Hopf bifurcation into periodic motions (flutter) at sufficiently high flow velocities, depending on the system parameters [6]. When a fluttering cantilevered pipe is constrained by a nonlinear motion-restraining spring, the existence of a period-doubling route to chaos was demonstrated [7]. For an extensive review of the subject, the interested reader is referred to [2, 8].

In parallel, work on the dynamics of cylindrical bodies immersed in axial flow has been conducted quite extensively, for instance by Païdoussis [9], Triantafyllou and Chryssostomidis [10, 11], Dowling [12], Rinaldi and Païdoussis [13, 14], Sader et al. [15] and Perets et al. [16], citing only some important studies on the subject. For the sake of brevity, these studies are not discussed here; the interested reader is referred to [17].

We next consider the dynamics of cantilevered pipes simultaneously subjected to internal and external axial flows. This system loses stability via flutter or static divergence, depending on the system parameters. Perhaps the first study on the dynamics of this system was by Cesari and Curioni [18], who predicted buckling instability of pipes with different boundary conditions. Hannoyer and Païdoussis [19] examined the dynamics of hanging tubular beams subjected to independent concurrent internal and external axial flows. For clamped-clamped pipes, the internal and external flows had a synergistic effect on instability of the system. For cantilevered pipes, however, the effect of the two flows was antagonistic in some cases; moreover, it was found that the onset of instability greatly depends on the shape of the free end. For example, for a blunt end, the internal flow is dominant and, although flutter arises at sufficiently high flow velocities, increasing the external flow velocity may re-stabilize the system. For a more or less streamlined end-piece, the dynamical behaviour is quite complex, i.e. both static and dynamic instabilities occur. Later on, stability of *internally/externally tapered* pipes subjected to internal and/or external flow was investigated both theoretically and experimentally by Hannoyer and Païdoussis [20, 21].

Motivated by some applications, such as modelling the dynamics of heat-exchanger and boiler internals, the dynamics of clusters of cylinders subjected to concurrent internal and external flows was studied in [22]. Another engineering application-motivated research on the dynamics of pipes subjected to both internal and external flows is that of drill-strings. Some early work was carried out by Bailey and Finnie [23], Finnie and Bailey [24] and Den Hartog [25]. Later on, Luu [26] investigated the dynamics of a long hanging cantilevered pipe discharging fluid downwards, which upon exiting the pipe flows upwards through an annulus formed by the pipe and a concentric outer rigid tube. Also, the case of an inclined pipe with internal and annular flows was studied by Wang and Bloom [27].

A mathematical model associated with an idealized drill-string system with a floating fluid-powered drill-bit was derived by Païdoussis et al. [28]. In this study, the flow configuration was similar to that of Luu [26]; i.e., the internal and annular flows were counter-current and interdependent. It was concluded that for a relatively slightly confined system, the internal flow is dominant in the dynamics; quite the reverse for a more confined system where the annular flow is dominant, precipitating flutter at relatively low internal flow rates.

Qian et al. [29] studied a drill-string-like system, but with reverse flow directions, i.e. with annulus discharging and the pipe aspirating fluid. For a relatively confined external flow, they predicted theoretically that the system is subjected to static divergence, rather than to an oscillatory instability. Fujita and Moriasa [30] examined the same system for both conventional and reverse flow configurations. Recently, Abdollahi et al. [31] investigated the stability of a rotating pipe conveying fluid in an annular fluid-filled channel, aiming at a more realistic modelling of drill-strings. See also Ghasemloonia et al. [32] for a review on this topic.

A pipe subjected to counter-current internal and external flows is an idealized model for the storage and subsequent retrieval of hydrocarbons in solution-mined caverns. These caverns are formed by leaching underground salt deposits. Thereafter, a part of the brine is replaced by liquid or gaseous hydrocarbons. In one of the *modi operandi*, one fluid is pushed through a central long pipe of the order of a kilometer, while displacing the other fluid to exit the cavern through a shorter annulus around the pipe. Motivated by this application, Moditis et al. [33] extended the work of Païdoussis et al. [28] to the case of a pipe conveying fluid and subjected to a partially confined external axial flow over its upper portion through a concentric shorter outer rigid tube. The dynamics of the system was also examined experimentally, using a bench-top-sized apparatus. The theoretical calculations predicted flutter for parameters corresponding to the bench-top system, but static divergence (buckling) for the full-scale system. Thereafter, Kontzialis et al. [34] conducted a numerical study on the same system, obtaining results in good agreement with the available experiments.

Later on, Abdelbaki et al. [35] derived a weakly-nonlinear model to examine the dynamics of a hanging tubular cantilevered beam counter-currently subjected to a partially-confined annular flow. For the system parameters investigated, a Hopf bifurcation leading to limit-cycle oscillations was predicted at high-enough flow velocities. Also, it was concluded that, generally, a longer or a narrower annulus would precipitate the instability earlier.

Minas and Païdoussis [36] extended the work of Moditis et al. [33] to explore the dynamics of a radially discharging pipe, as well as higher ratios of annular to internal flow velocity, both theoretically and experimentally. Also, the dynamics of the system with the opposite flow configuration (aspirating pipe, discharging annulus) was studied. Chehreghani et al. [37] explored the influence of the confinement length on the dynamics of the same system. The post-instability dynamics and impacting of the pipe on the coaxial shorter outer rigid tube were also studied.

A more comprehensive literature survey on the dynamics of cantilevered pipe subjected to internal and reverse external annular flows may be found in [38]. Nevertheless, it is manifest from the foregoing that a systematic parametric experimental work is required to fully investigate the dynamics of this system. This lacuna motivated us to conduct a systematic experimental work to characterize the influence of some of the main system parameters on the dynamics of the system, namely external flow confinement (annular gap size), pipe slenderness, pipe material, eccentricity between the pipe and the surrounding cylindrical channel, and external flow constriction at the inlet or outlet of the annulus. Some, but not all, of the experimental results on the effect of external flow confinement reported here has previously been presented in Chehreghani et al. [39].

The repercussions of operating solution-mined caverns at flow velocities beyond the critical for fluid-elastic instabilities are severe. Beyond the onset of flutter, the amplitude of the central pipe oscillation grows, eventually resulting in repeated impact of the pipe on the outer tube, causing fretting wear of the pipe and possible breakage, with part of the pipe ending up at the bottom of the cavern. If the pipe is subject to static divergence (buckling) instead of flutter, the outcome may be the same. The pipe only touches the outer tube intermittently, switching from one side to the other; or, if "sticking" occurs, the buckled pipe chatters against the outer tube at high frequency, again resulting in fretting wear and possible damage.

Making use of the bench-top apparatus shown schematically in Fig. 5.1, the threshold of instability as well as the post-instability behaviour of the system was explored, for various ratios of the external (annular) to internal flow velocities, U_o/U_i. The flow configuration studied here, besides being of interest for its fundamental aspects, simulates the mode of retrieval of the hydrocarbon product stored in salt-mined caverns. Therefore, the present study would be useful in diagnosing the cause of brine-string breakages [40, 41], as well as delimiting the safe ranges of the flow velocities in practice.

The rest of the paper is organized as follows. The experimental apparatus and methodology are described in Section 5.2. The main dimensionless parameters involved are provided in Section 5.3. Experimental results on the effect of the external flow confinement are presented in Section 5.4. Section 5.5 gives a brief summary of the results on the effect of annular confinement length ratio, and Section 5.6 on the effect of pipe slenderness. Experimental results on the influence of external flow constriction are discussed in Section 5.7, on the influence of pipe material properties in Section 5.8, and on the influence of an eccentricity between the pipe and the surrounding annular region in Section 5.9. Finally, Section 5.10 is devoted to the conclusions from the work reported in this paper.

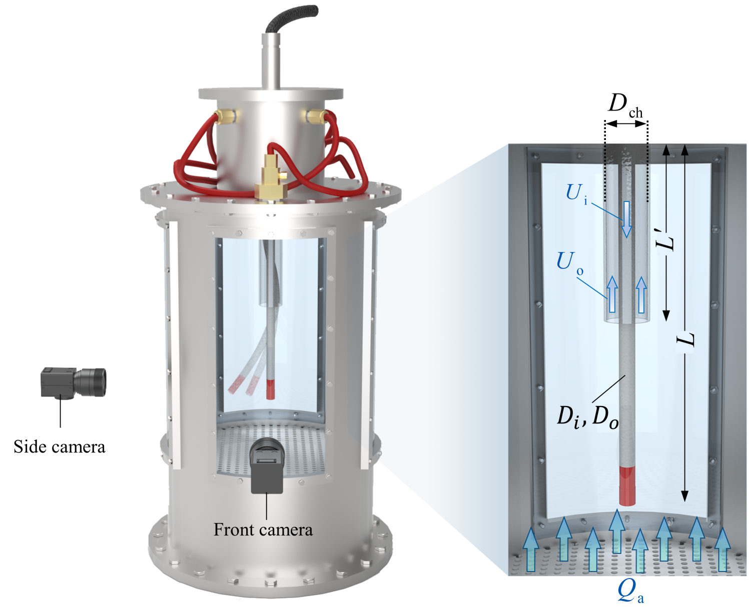

Figure 5.1: Schematic view of the SMRI-PRCI apparatus and the synchronized dual-camera system. Internal flow with velocity U_i, and the flow in the surrounding annular region with velocity U_o, as well as parameters related to the geometry are shown in the zoomed view. Q_a denotes the additional fluid entering the pressure vessel to achieve higher values of U_o/U_i. Approximate size of the pressure vessel: 0.5 m in diameter; 1 m in height.

5.2 Apparatus and methodology

5.2.1 Experimental setup

The SMRI-PRCI apparatus in the FSI laboratory at McGill University, shown schematically in Fig. 5.1, was utilized. This set-up consists a pressure vessel, a flexible pipe, a coaxial transparent shorter rigid plexiglas tube surrounding the upper portion of the pipe, two centrifugal pumps with digital controllers, two magnetic flow meters, a conventional Bourdon tube pressure gauge and a water storage tank. The pressure vessel has four rectangular transparent windows, symmetrically placed, allowing access and viewing of the dynamics of the flexible pipe.

Properties of the flexible pipes are presented in Table 5.1. EI denotes the flexural rigidity, m mass per unit length, L length, D_o outer diameter and D_i inner diameter of the pipe. The silicone-rubber (silastic RTV) pipes were cast in-house from a mixture of liquid silicone-rubber. For details on casting the elastomer pipes the interested reader is referred

Table 5.1: Properties of the flexible pipes used in the experiments.

Pipe	Material	EI [N m^2]	m [kg m^{-1}]	L [mm]	D_o [mm]	D_i [mm]
A	Silicone–rubber	7.37×10^{-3}	0.191	441	16.0	6.35
B	Silicone–rubber	7.37×10^{-3}	0.191	221	16.0	6.35
C	Santoprene	37.3×10^{-3}	0.086	443	13.0	9.50

to Appendix D of Païdoussis [2]. Pipe C was a commercial santoprene hose. The frequency of first-mode oscillations of pipes A, B and C in air are 1.09 Hz, 2.63 Hz and 2.10 Hz, respectively. Païdoussis and Des Trois Maisons [42] have postulated that a two-parameter Kelvin-Voigt model is sufficient to capture the internal damping characteristics of elastomer pipes. A description of the two-parameter visco-hysteretic Kelvin-Voigt model and typical values of the associated coefficients may be found in Rinaldi [43] and Appendix D of Païdoussis [2]. The modal logarithmic decrements of the damping for the silicone-rubber pipes used in these experiments for the n^{th} beam-mode can be approximated by $\delta_n = 0.0521n - 0.0151$, based on a linear interpolation of the measured modal logarithmic decrement of the first three modes. It should be stressed, however, that the flow-induced damping is overwhelmingly more significant than the structural damping. Therefore, neither does the structural damping model, nor the values of the coefficients involved play a significant role in the dynamics of the system [28, 44].

As shown in Fig. 5.1, the flexible cantilevered pipe discharges fluid downwards in the pressure vessel with flow velocity, U_i. Upon exiting the pipe, the fluid is aspirated with velocity U_o in the upwards direction, in the annulus between the upper portion of the pipe and the surrounding cylindrical plexiglas tube. Therefore, the external flow around the pipe is partially confined. To achieve higher U_o/U_i, additional flow, with volumetric rate Q_a, was added into the pressure vessel from the bottom. To this end, one pump pushed water from the storage tank into the pipe, thereby providing the internal flow in the pipe, Q_i, while the other pump provided the additional water to the bottom of the pressure vessel from the storage tank. Hence, the external flow rate is $Q_o = Q_i + Q_a$, and therefore $U_o A_{ch} = U_i A_i + Q_a$, where $A_{ch} = (\pi/4)\,(D_{ch}^2 - D_o^2)$ is the cross-sectional area of the annulus between the outer tube and the pipe and $A_i = (\pi/4)\,D_i^2$ is the internal cross-sectional area of the pipe.

The outer rigid tube had a diameter of $D_{ch} = 54$ mm and a length of $L' = 206.5$ mm for

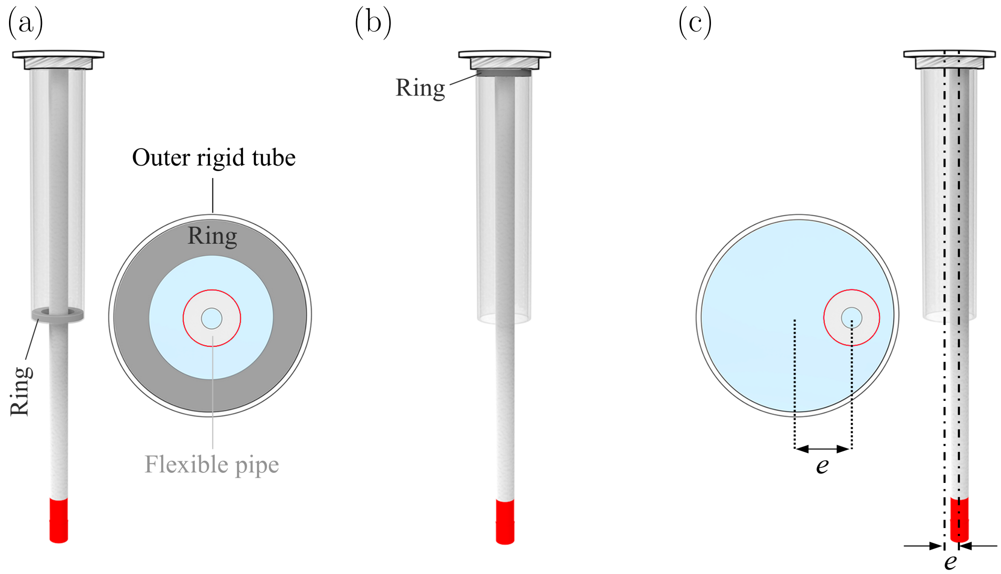

Figure 5.2: Schematic plot depicting (a) the placement of a flow-constricting rigid ring of inner diameter D_{ir} at the inlet (lower end) of the outer rigid tube and the cross-sectional view showing the pipe, the rigid ring and the outer rigid tube; (b) the placement of the rigid ring at the outlet (top end) of the outer rigid tube; (c) elevation and cross-sectional views of the off-centre placement of the outer rigid tube with respect to the central pipe; e denotes the eccentricity.

experiments with pipe A and C, and a length of $L' = 109$ mm for experiments with pipe B. Therefore, for all the cases we have $r_{ann} = L'/L \simeq 1/2$ – refer to Fig. 5.1.

For experiments on the effect of annular flow constriction a constraint was placed at the inlet or outlet of the annular region, namely a ring of thickness $t_r = 12$ mm, outer diameter $D_{or} = D_{ch} = 54$ mm and various inner diameter sizes, D_{ir}; it was pressure-fitted at the bottom (entrance) or top (exit) of the annular region, as shown in Fig. 5.2(a,b), respectively. More details are provided in Section 5.7.

For experiments on the eccentric system, the outer rigid tube was mounted with a pre-determined eccentricity, e, with respect to the undeformed state of the pipe, as shown in Fig. 5.2(c). Further details are provided in Section 5.9.

5.2.2 Data acquisition and processing

From the known geometry of the system and measurement of Q_i and Q_a, by means of two magnetic flow meters, the internal and annular (external) flow velocities, U_i and U_o can be determined.

A conventional Bourdon tube pressure gauge was utilized to measure the static pressure in the vessel. This pressure was monitored and recorded for ensuring the integrity of the apparatus.

To measure the motion of the pipe, a non-contacting optical technique was used. To this end, a 38 mm long region at the free-end of the pipe was marked in red. The motion of the centroid of this "red-marked" region at the pipe tip was tracked and recorded via two synchronized FLIR Grasshopper3 high-speed cameras from the two perpendicular windows of the pressure vessel. These cameras are referred to as "front" and "side" cameras throughout the paper, as shown in Fig. 5.1. The two cameras were triggered via a function generator, thereby assuring synchronization.In each experiment, the undeformed state of the pipe submerged in quiescent fluid served as a reference for measuring deformation.

The flow velocity was increased gradually to instability, and further on to impact on the plexiglas tube. At each flow velocity increment, after waiting adequately to ensure a steady state condition, the motion of the pipe tip was recorded.

A video-processing Matlab (Mathworks, Inc.) script was utilized to obtain displacement-time series from the videos recorded via the dual-camera system. More specifically, the script converts each recorded frame into a binary image. In each frame, when the red marker is detected, the centroid of the red area in pixel units can also be determined. Thereafter, the centroid location in pixel units can be converted into millimeters using the known dimensions of the marker to obtain the displacement time-series signal. Eventually, the time series signal was post-processed to identify the dynamics of the system, employing tools such as bifurcation diagrams, wavelet transforms, Poincaré maps, PSDs, phase plane plots, and via quantitative measures such as the PDF, auto-correlation function and Lyapunov exponents.

5.3 Dimensionless parameters

In this paper, the data is presented in terms of dimensionless parameters in order to facilitating comparison of the results to existing or future work, and in this parametric study enabling a more "apples to apples" comparison.

The conventional dimensionless internal and external (annular) flow velocities, u_i and u_o,

Table 5.2: Multiplicative factors to convert the dimensionless to dimensional terms.

Pipe	A	B	C
$U_i(\mathrm{m/s})/u_i$	1.094	2.183	1.637
$U_o(\mathrm{m/s})/u_o$	0.4341	0.866	1.197
$(U_o/U_i)\,/\,(u_o/u_i)$	0.397	0.397	0.731
$f(\mathrm{Hz})/\omega$	0.108	0.430	0.291

and dimensionless frequency, ω, utilized in the past [28, 33], are as follows:

$$u_i = \left(\frac{\rho_f A_i}{EI}\right)^{1/2} LU_i, \quad u_o = \left(\frac{\rho_f A_o}{EI}\right)^{1/2} LU_o, \quad \omega = \left(\frac{m + \rho_f A_i + \rho_f A_o}{EI}\right)^{1/2} L^2\Omega, \tag{5.1}$$

where ρ_f is the density of the fluid, water in this case, $A_i = \frac{\pi}{4}D_i^2$, $A_o = \frac{\pi}{4}D_o^2$, and $\Omega = 2\pi f$ is the radian frequency, f being in Hz. Other symbols are the same as in Table 5.1.

In order to provide a better "feel" for the reader, dimensional results are also presented in some cases. The multiplicative factors for conversion from the dimensionless to dimensional terms for the three pipes used in these experiments are provided in Table 5.2. Please note that $u_o/u_i = (D_o/D_i)\,(U_o/U_i)$.

Throughout the paper, some parameters related to the geometry of the system are also used (see Figs. 5.1 and 5.2), namely

$$\alpha_{ch} = \frac{D_{ch}}{D_o}, \quad r_{ann} = \frac{L'}{L}, \quad \varepsilon = \frac{L}{D_o}, \quad \bar{g}_r = \frac{D_{ir} - D_o}{D_h}, \quad \bar{e} = \frac{2e}{D_h}, \tag{5.2}$$

where α_{ch} is a dimensionless parameter associated with the annular confinement (annular gap size), in which D_{ch} is the inner diameter of the outer rigid tube. The confinement parameter, $\chi = (D_{ch}^2 + D_o^2)\,/\,(D_{ch}^2 - D_o^2)$, may also be used; for a relatively unconfined pipe $\chi \to 1$ and for a very narrow annulus $\chi \to \infty$. Also, r_{ann} is a parameter associated with confinement length ratio, L' being the confined length of the pipe. ε is pipe slenderness. Furthermore, $\bar{g}_r$ is a dimensionless parameter pertinent to the gap size between the rigid ring and the pipe, in which D_{ir} is the inner diameter of the ring used in experiments on flow constriction, and $D_h = D_{ch} - D_o$ is the hydraulic diameter of the annular region. $\bar{e}$ is a dimensionless parameter associated with eccentricity, e being the eccentricity between the

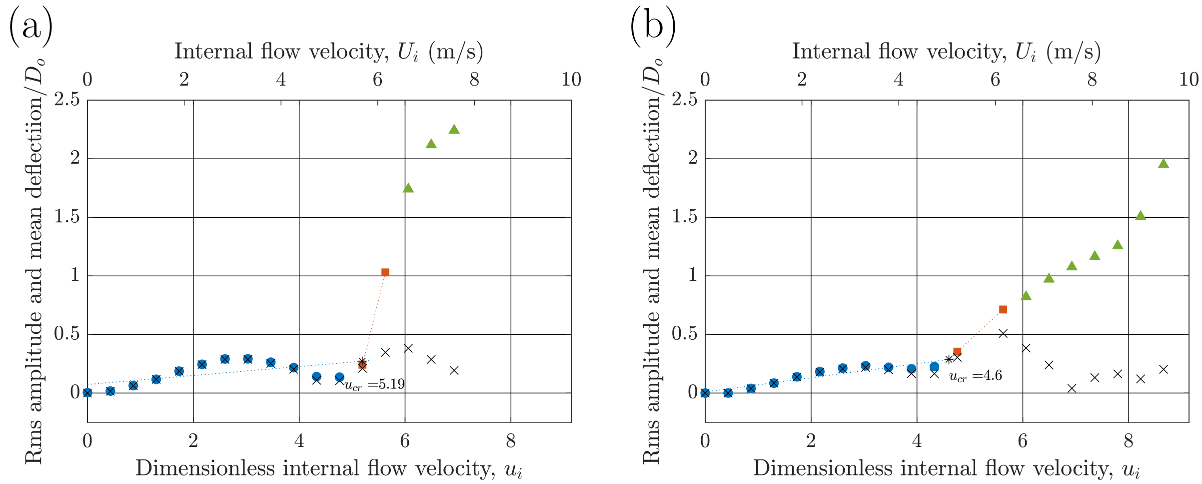

Figure 5.3: Bifurcation diagrams showing the rms amplitude of total displacement and the mean deflection versus u_i for interdependent internal and external flows (Q_a =0) and (a) α_{ch} = 3.37 (D_{ch}=54 mm and U_o/U_i =0.015); (b) α_{ch} = 1.97 (D_{ch} =31.5 mm and U_o/U_i=0.055). Rms amplitude: (●) pre-instability, (■) instability, (▲) impact; (×) mean deflection; ($*$) critical flow for instability.

outer rigid tube and the undeformed state of the pipe in eccentric system experiments.

The linear equation of motion for a partially confined, vertical cantilevered pipe discharging water and subjected to reverse axial external flow in the dimensionless form as given by Moditis et al. [33] is provided in Appendix A. To facilitate the discussion pertinent to the influence of some parameters, the expressions for the mass, damping and stiffness matrices of the discretized equation of motion are presented in Appendix B.

5.4 Results on the effect of external flow confinement

In this section, results on the influence of the size of the annular gap between the pipe and the outer rigid tube are presented; i.e., the parameter varied is the annular confinement ratio, α_{ch}, refer to Eq. (5.2) . Here, the results for a wider outer rigid tube with $\alpha_{ch} = 3.37$ ($D_{ch} = 54$ mm, $\chi = 1.19$) are compared to those of Chehreghani et al. [37] for a narrower outer rigid tube with $\alpha_{ch} = 1.97$ ($D_{ch} = 31.5$ mm, $\chi = 1.69$) and the same other system parameters. The fixed parameters are as follows: pipe A with slenderness $\varepsilon = 27.56$, and the rigid outer tube with annular confinement length ratio, $r_{ann} = 0.468 \simeq 1/2$ ($L' = 206.5$).

5.4.1 *Interdependent internal and external flow*

In the first set of experiments, no additional flow was added into the pressure vessel from the bottom; i.e., $Q_a = 0$, and the internal and external flow were interdependent: $U_o A_{ch} = U_i A_i$. This means that by changing the confinement (annular gap size), U_o/U_i is also affected. Here, for the wider gap ($\alpha_{ch} = 3.37$, $D_{ch} = 54$ mm, $\chi = 1.19$), we have $U_o/U_i = 0.015$ ($u_o/u_i = 0.038$) and for the narrower one ($\alpha_{ch} = 1.97$, $D_{ch} = 31.5$ mm, $\chi = 1.69$), we have $U_o/U_i = 0.055$ ($u_o/u_i = 0.138$).

The experimental bifurcation diagrams for the wider (U_o/U_i =0.015) and the narrower (U_o/U_i =0.055) annular gap size are presented in Fig. 5.3(a, b), respectively. [Note that in all the bifurcation diagrams presented through the paper, the rms of (total displacement)$/D_o$ as well as (pipe mean deflection)$/D_o$ are plotted as a function of u_i.] The dynamical behaviour is qualitatively similar. Quantitatively, however, increasing the size of the annular gap resulted in an increase in the critical flow velocity, namely from $u_{cr} = 4.60$ to $u_{cr} = 5.19$, and also in an increase in the amplitude of oscillations. The character of motion of the pipe changes at u_{cr}, as discussed in the two paragraphs that follow.

As seen in Fig. 5.3(a), for very small u_i, the pipe remained almost stationary at its undeformed initial shape. Increasing u_i resulted in very weak random first-mode oscillations in addition to a small static deformation ($1.30 < u_i < 5.19$); these random motions with a limited amplitude were likely excited by turbulence buffeting, or they may have arisen partly from accentuation of initial imperfections. As can be seen in Fig. 5.4(a), no dominant frequency can be determined in this range of u_i. At $u_i = 5.19$, weak small amplitude second-mode oscillations initiated, as can be seen in Fig. 5.3(a) and Fig. 5.4(a). The determination of u_{cr} by the intersection of two linear fits of (i) small unsteady turbulence-induced motions and (ii) more regular fast-rising oscillation amplitudes has been shown in practice to be the best approach [44]. Increasing the internal flow velocity further to u_i =5.63, resulted in remarkably more powerful second-mode oscillations with a dominant frequency of $\omega = 14.3$ (=1.54 Hz), as shown in Fig. 5.4(a), and a sharp increase in the rms amplitude, demonstrated in the bifurcation diagram of Fig. 5.3(a). The self-excited second-mode flutter observed is a "movement-induced instability" in the Naudascher and Rockwell [45] categorization in which the fluctuating forces are associated with movements of the structure.

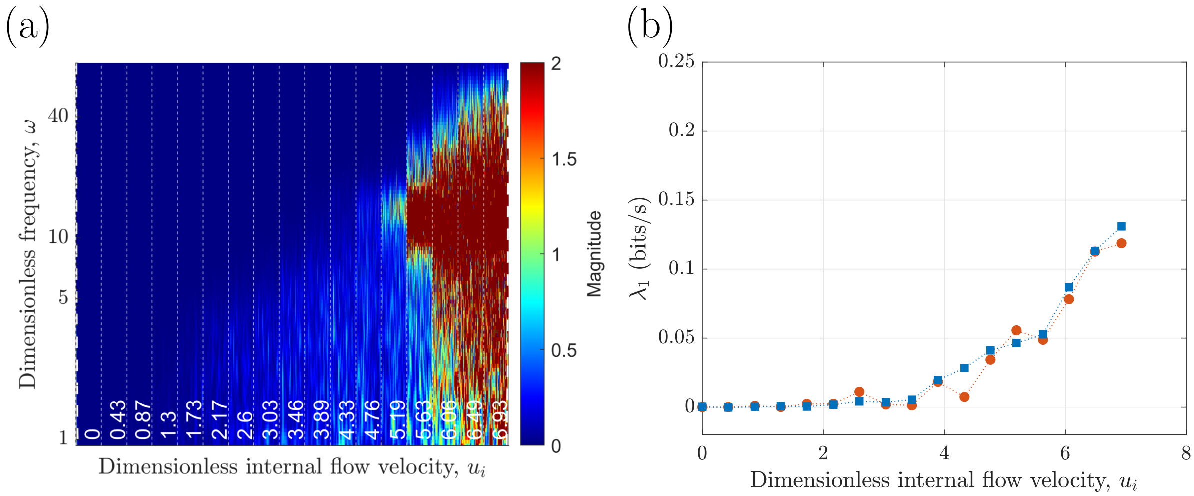

Figure 5.4: (a) Morse wavelet scalogram in which the vertical strips indicate values of the internal flow velocity; (b) variation of the largest Lyapunov exponent of the front (●) and side (■) displacement time series as a function of internal flow velocity.

As seen in Fig.5.3(a), increasing flow velocity further to $u_i = 6.06$ resulted in oscillations of higher amplitude and the pipe impacted on one side of the surrounding rigid tube; then, at still higher flows, a combination of two-sided impacting and rotational motions materialized.

The high amplitude oscillations observed at u_i=5.63 (Fig. 5.3(a)) can be explored further by means of the analysis in Fig. 5.5. The time traces of Fig. 5.5(a) and the front versus side displacement plot of Fig. 5.5(b) suggest an unsteady and near-intermittent oscillation, in which, albeit having a strong periodic component($\omega = 14.3$), the amplitude and the plane of oscillations (direction of motions) vary in a chaotic manner. The pseudo-phase space plot of the combined front and side motions shown in Fig. 5.5(c) provides more evidence on the existence of both periodic and chaotic content in the oscillations. The double-hump shape of the probability density function of the oscillatory part of the combined motion (Fig. 5.5(d)), the scattered, albeit with some structure, shape of the Poincaré map ((Fig. 5.5(e))), and the fairly rapid decay and unsteadiness of the autocorrelation function of the combined oscillatory displacement (Fig. 5.5(f)) confirm the intermittent nature of the oscillations with both periodic and chaotic content.

The largest Lyapunov exponent, λ_1, from the experimental time-series was estimated using an efficient version of the algorithm by Wolf et al. [46]. As shown in Fig. 5.4(b), λ_1,

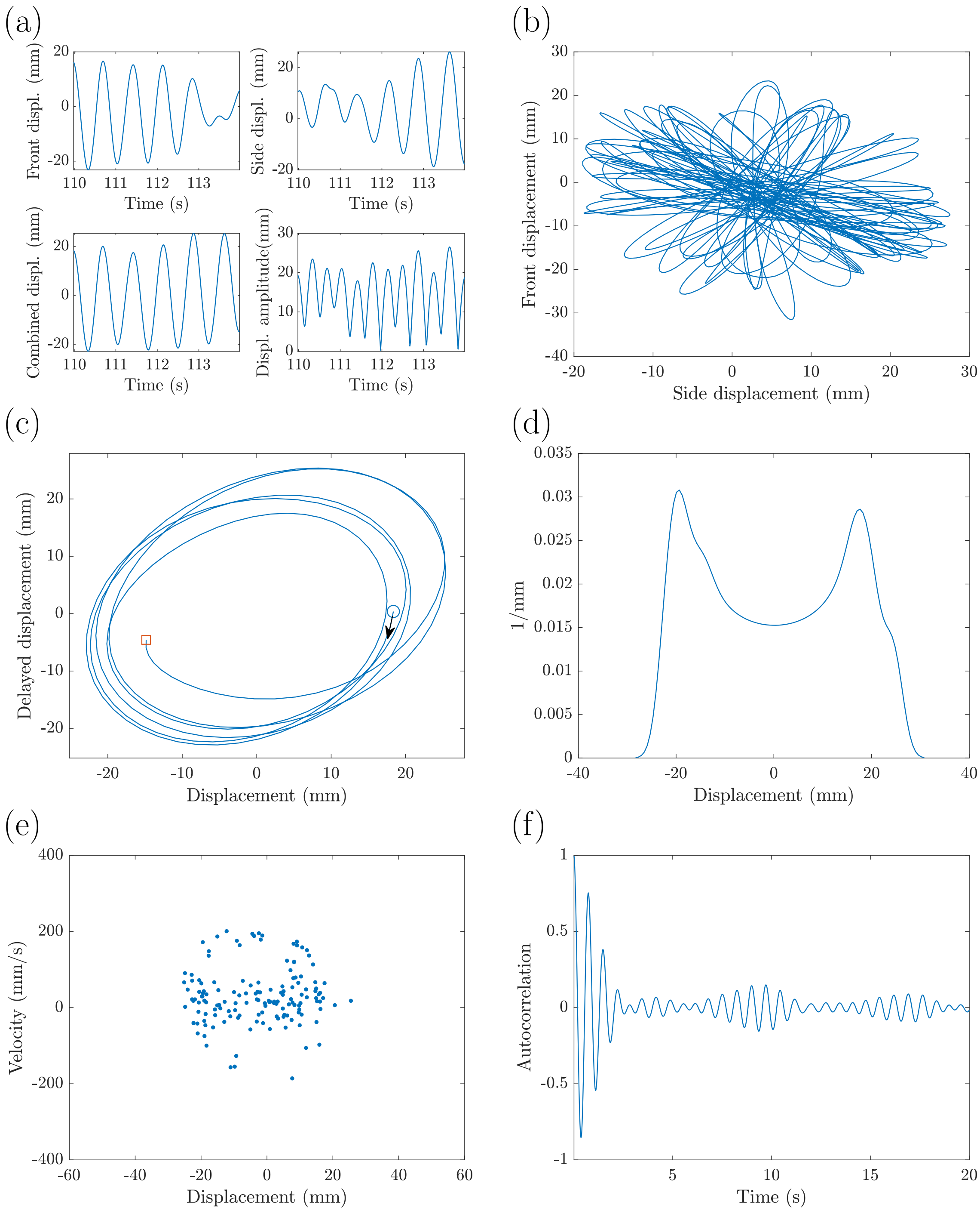

Figure 5.5: Dynamics of the system at $u_i = 5.63$ ($U_i = 6.16$ m/s) for the wider outer rigid tube ($\alpha_{ch} = 3.37$), with interdependent internal and external flows ($U_o/U_i = 0.015$) and the parameters given in Section 5.4.1 by means of (a) time traces; (b) front versus side displacement; (c) pseudo-phase space of the combined displacement; (d) PDF of the combined displacement; (e) Poincaré map; (f) autocorrelation of the combined displacement.

despite being small, increases with flow velocity. Remarkably, when the pipe impacts on the outer rigid tube, λ_1 increases with a greater slope. Therefore, with increasing flow velocity the chaotic content of the oscillations is enhanced. This enhancement in the chaotic content with flow velocity, in addition to the analysis provided in Fig. 5.5, suggests that the system may follow the intermittency route to chaos; that is, long periods of periodic motion with bursts of chaos [47].

Physically, careful investigation of Eqs. (A.1), (B.1), (B.2) and (B.3) reveals that varying α_{ch} (and hence χ), affects the virtual mass, the Coriolis and the centrifugal forces in a complicated manner. In addition, a more confined annulus means a higher u_o. In agreement with the experimental results provided in Fig. 5.3, based on the calculations conducted, increasing the annular gap size (increasing α_{ch}, decreasing χ) tends to stabilize the system.

5.4.2 Independent internal and external flows

In this case, the influence of the parameter of interest, that is the annular confinement (solely $\alpha_{ch} = D_{ch}/D_o$), was isolated from variations in U_o/U_i. This requires having the same value of U_o/U_i for both the wider and narrower outer tube via independently controlled internal and external flows. To this end, the same pipe and outer rigid tube as in Section 5.4.1 were used, but with appropriate amounts of additional fluid entering from the bottom of the pressure vessel, $Q_a \neq 0$, to achieve higher values of U_o/U_i, namely 0.2, 0.4 and 0.8. Comparing the results provided here for a wider annular gap size (D_{ch}=54 mm, $\alpha_{ch} = 3.37$) with those of Chehreghani et al. [37] for a narrower annular gap size (D_{ch}=31.5 mm, $\alpha_{ch} = 1.97$) allows us to characterize solely the influence of external flow confinement.

Experimental bifurcation diagrams presenting the rms amplitude of displacement and the mean deflection versus u_i for α_{ch}= 3.37 (wider outer tube), and U_o/U_i=0.2, 0.4 and 0.8 are presented in Fig. 5.6(a, c, e), respectively. They are compared to their counterparts with the same U_o/U_i but α_{ch} =1.97 (narrower outer tube) in Fig. 5.6(b,d, f).

Generally, for independent external and internal flows and α_{ch} =3.37, compared to that of interdependent flows (U_o/U_i =0.015), two interesting dynamical features are noticed. Firstly, at relatively small flows ($u_i = 0.87 - 1.73$ for $U_o/U_i = 0.2$, $u_i = 0.43 - 0.98$ for $U_o/U_i = 0.4$, and $u_i = 0.23 - 0.58$ for $U_o/U_i = 0.8$), fairly powerful first-mode oscillations took place as shown in Fig. 5.7(a-c), followed by mixed first- and weak second-mode oscillations at

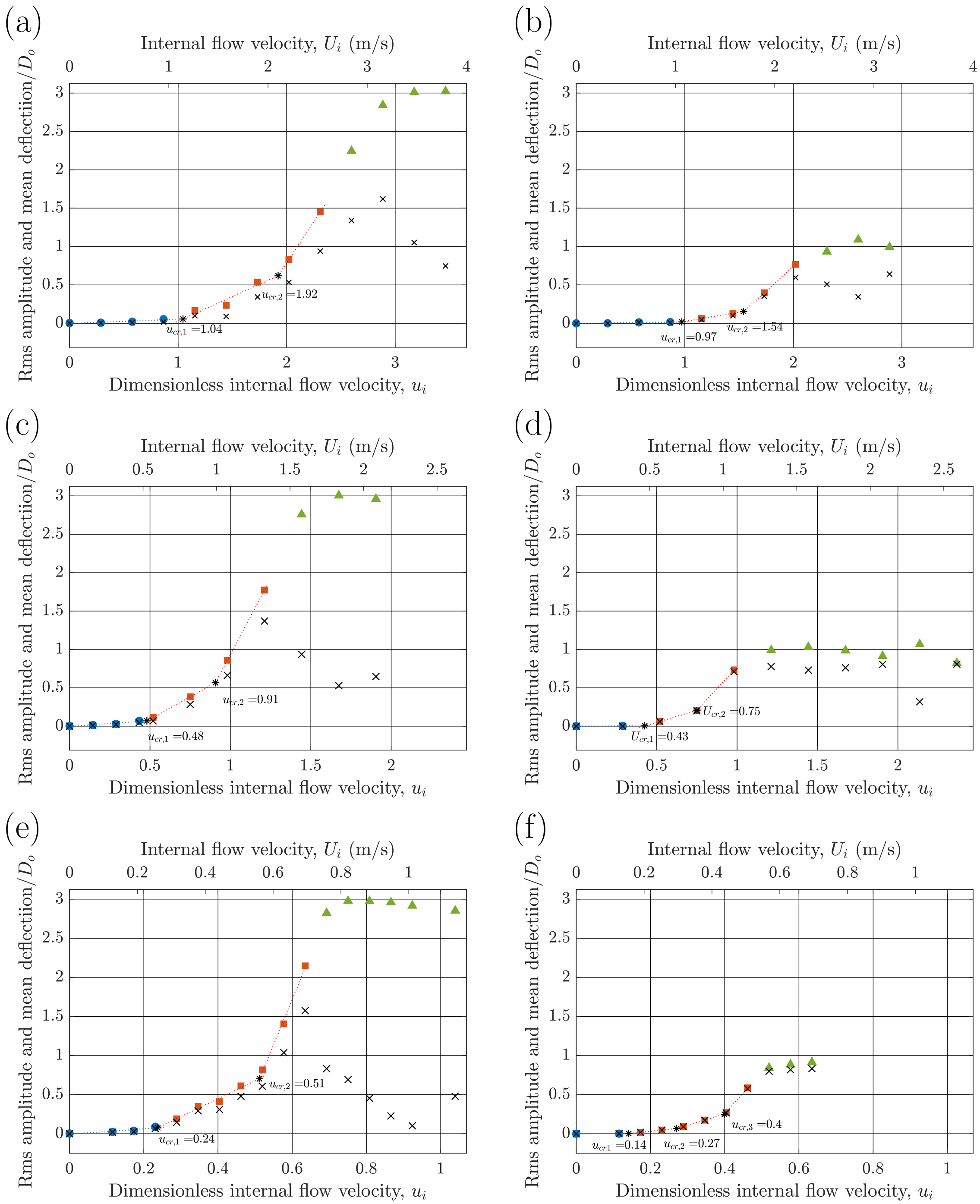

Figure 5.6: Bifurcation diagrams showing the rms amplitude of total displacement and the mean deflection as a function of u_i for independent internal and external flows ($Q_a \neq 0$). For the wider annulus, $\alpha_{ch} = 3.37$ (D_{ch}=54 mm): (a) $U_o/U_i = 0.2$; (c) 0.4; (e) 0.8. For the narrower annulus, $\alpha_{ch} = 1.97$ (D_{ch} =31.5 mm): (b) $U_o/U_i = 0.2$; (d) 0.4; (f) 0.8. Rms amplitude: (●) pre-instability, (■) instability, (▲) impact; (×) mean deflection; (∗) critical flow for instability.

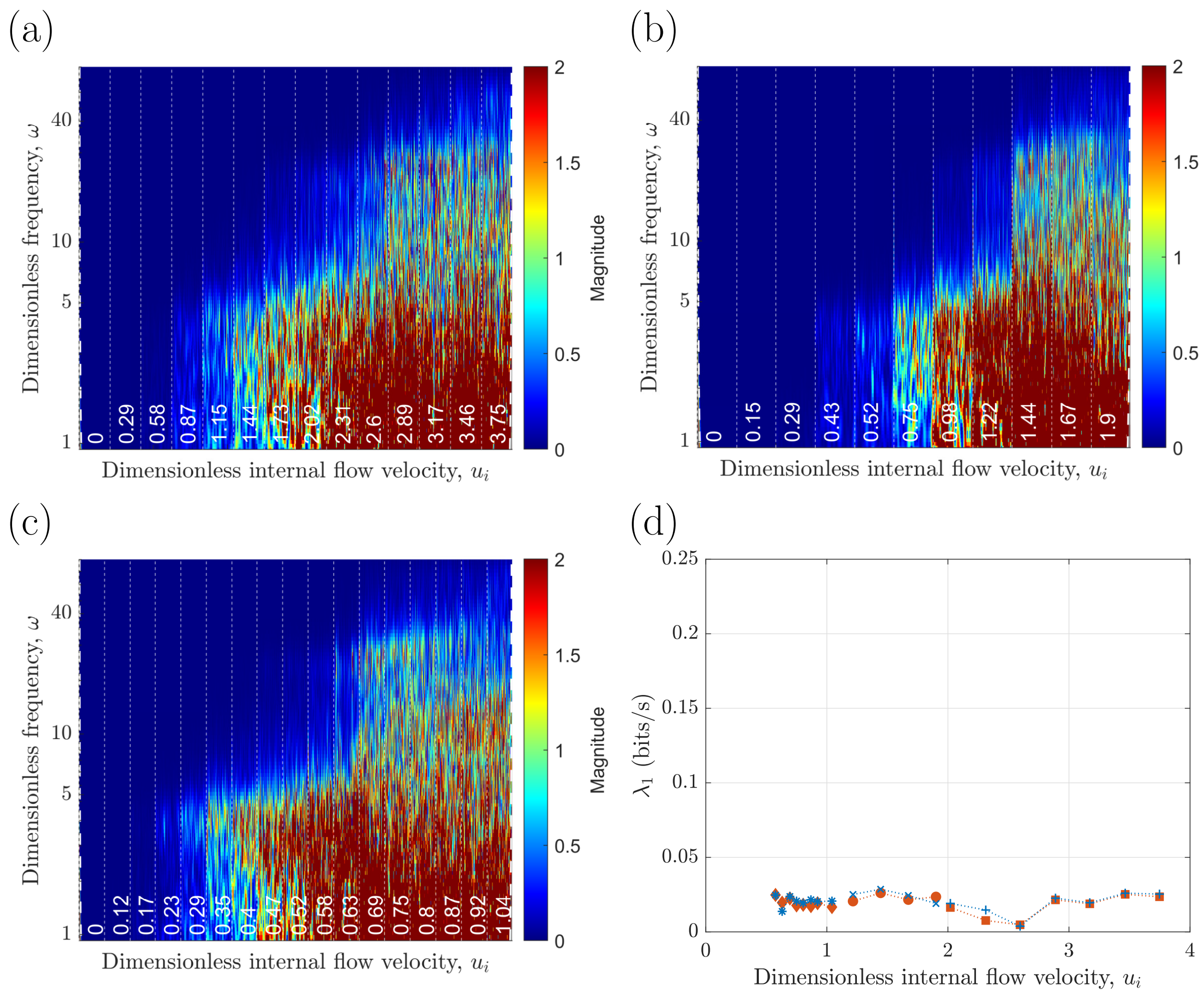

Figure 5.7: Morse wavelet scalogram in which the vertical strips indicate values of the internal flow velocity for $\alpha_{ch} = 3.37$ and $U_o/U_i =$ (a) 0.2, (b) 0.4, and (c) 0.8. (d) Variation of the largest Lyapunov exponent of the front and side displacement time series versus u_i for $\alpha_{ch} = 3.37$ and $U_o/U_i = 0.2$: front (■) and side (+); $U_o/U_i = 0.4$: front (●) and side (×); $U_o/U_i = 0.8$: front (♦) and side ($*$).

higher u_i prior to the onset of impacting on the outer rigid tube, whereas for interdependent flows (U_o/U_i =0.015), prior to the onset of second mode flutter, the pipe was only subjected to a static deformation (see Fig. 5.4(a)). Secondly, for $Q_a \neq 0$, at sufficiently high flow velocities, the pipe partially or completely rubbed against the rim of the outer tube, rather than undergoing the one- or two-sided impacting observed for interdependent flows. This chattering behaviour resulted in powerful low frequency oscillations, shown in Fig. 5.7(a-c).

In terms of the effect of increasing the confinement, a stabilizing influence was observed, for all U_o/U_i investigated. For the wider outer tube and U_o/U_i =0.2, first-mode oscillations at $u_i = 1.15$ commenced. At u_i =2.02 a weak second-mode component began to appear, as shown in the scalogram of Fig. 5.7(a), resulting in mixed first- and second-mode oscillations at higher u_i (the PSDs are not shown for brevity). For the narrower annular region and U_o/U_i=0.2, the dynamics is reported as follows: static deformation at relatively small flows, followed by weak mixed-mode oscillations superimposed on the mean static deflection at higher flow rates. For higher U_o/U_i, namely, 0.4 and 0.8, the trend is similar to that of U_o/U_i =0.2, as shown in Fig. 5.6(c-f) and Fig. 5.7(b, c).

In terms of chaos, in the range of the flow velocities achievable in the experiment, the chaotic component was very weak with the largest Lyapunov exponent, $\lambda_1 \simeq 0$, as shown in Fig. 5.7(d). The small non-zero λ_1 suggests that the oscillation, although predominantly periodic, inherently contains a rather weak chaotic component. Yet, λ_1, even after touching the outer tube, appears not to grow with flow velocity, as the pipe stuck on the outer tube rather than impacting on it, and therefore the enhanced chaotic content observed in Fig. 5.4(b) never materialized in this case.

For the physical explanation of the effect of the size of the annular gap on stability of the system, a similar discussion to the case of interdependent flows can be made: with increasing the annular gap confinement (a narrower gap size), the combined effect of the virtual mass, the Coriolis and the centrifugal force is destabilizing. For higher U_o/U_i these effects multiply with a larger u_o, refer to Eq. (A.1). Hence, for higher U_o/U_i, the destabilizing effect of confinement is more pronounced; see Fig. 5.6.

5.5 The effect of annulus-to-pipe length ratio

Using outer rigid tubes of different lengths, the influence of varying confinement length ratio, $r_{ann} = L'/L$, was previously investigated by Chehreghani et al. [37]. The ratios of $r_{ann} \simeq 1/4, 1/2$ and $3/4$, all with the same annular gap size $\alpha_{ch} = 1.97$ and using pipe A, were investigated. Therefore, the effect of this parameter is not discussed at length here. In general, it was concluded that increasing r_{ann} has a destabilizing effect on the pipe. Table 5.3 presents the critical flow velocities for various values of r_{ann}.

Increasing r_{ann} affects the added mass, Coriolis force, the viscous forces in the normal and longitudinal directions, the centrifugal force as well as the terms related to the pressure at the

Table 5.3: The effect of r_{ann} on the dimensionless critical internal flow velocities of pipe A with $\alpha_{ch} = 1.97$.

	$r_{ann} \simeq 1/4$		$r_{ann} \simeq 1/2$		$r_{ann} \simeq 3/4$
U_o/U_i	$u_{cr,1}$	$u_{cr,2}$	$u_{cr,1}$	$u_{cr,2}$	u_{cr}
0.055	5.19	-	4.61	-	4.63
0.1	4.94	-	1.09	3.68	1.65
0.2	1.98	3.37	0.97	1.54	0.78
0.4	0.66	1.57	0.43	0.75	0.41
0.6	0.47	0.96	0.24	0.50	0.26
0.8	0.38	0.80	0.14	0.27	0.15

inlet of the annular region in a complicated manner, mainly by influencing the limits of the integrals of Eq. (B.4) and the terms associated with the Heaviside step function and Dirac delta function in Eq. (A.1). Based on the calculations conducted for the higher confinement length, the destabilizing forces appear to be predominant, compared to the stabilizing ones.

5.6 The effect of pipe slenderness

To investigate the influence of pipe length-to-diameter ratio, $\varepsilon = L/D$, the dynamics of pipe B, which has the same properties as pipe A but is shorter (see Table 5.1), is compared to that of pipe A. To isolate the effect of pipe slenderness and facilitate comparison with the experiments carried out with pipe A, a shorter outer rigid tube was used, so that the ratio of the outer tube length to that of the pipe was kept approximately constant, i.e. r_{ann} =1/2. In experiments with both pipes, a coaxial outer rigid tube ($\bar{e} = 0$) with the annular confinement $\alpha_{ch} = 3.37$ ($D_{ch} = 54$ mm) that corresponds to $\chi = 1.19$ was used. The system parameters for experiments with pipe B are as follows: slenderness $\varepsilon = 13.81$ and outer rigid tube with $r_{ann} = 0.493 \simeq 1/2$ ($L' = 109$); whereas for pipe A: slenderness $\varepsilon = 27.56$ and $r_{ann} = 0.468 \simeq 1/2$ ($L' = 206.5$).

The critical flow velocities for the onset of instability of pipe A and B are presented in Table 5.4. It is noted that increasing ε has a very weak stabilizing effect for the cases with $Q_a \neq 0$, i.e. higher U_o/U_i ratios. For interdependent internal and external flows, in which U_o/U_i =0.015 is small, the effect is destabilizing.

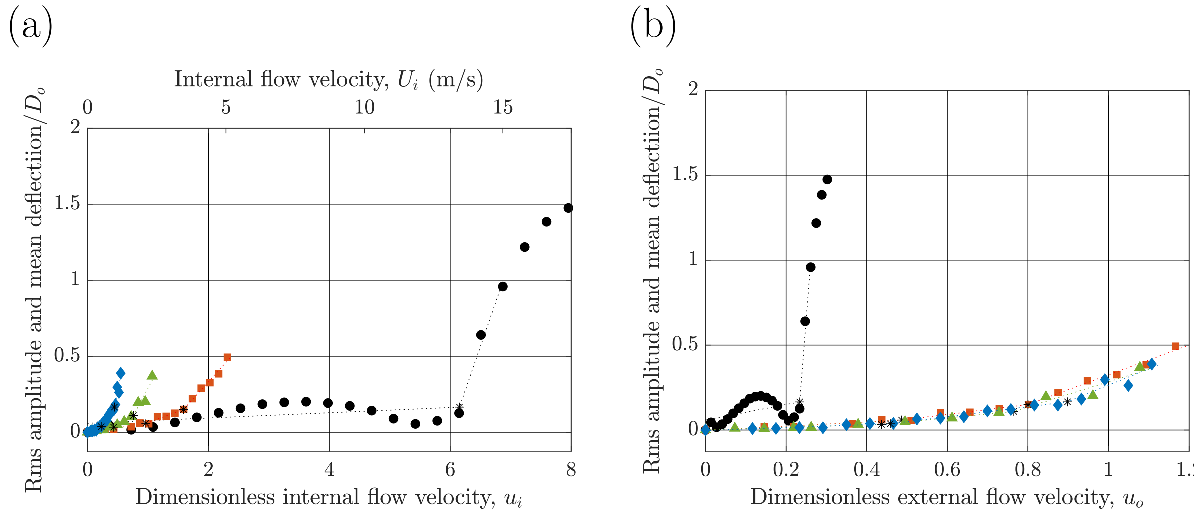

Figure 5.8: Bifurcation diagrams showing the rms amplitude of total displacements as a function of (a) u_i; (b) u_o; for pipe B ($\varepsilon = 13.81$) and U_o/U_i= 0.015: (●); 0.2: (■); 0.4: (▲); 0.8: ♦; ($*$) critical flow for instability.

Bifurcation diagrams showing the rms amplitude of displacement and the mean deflection as a function of u_i and u_o are presented in Fig. 5.8(a, b), respectively. As can be seen, for higher U_o/U_i, the dynamics is mostly external-flow dependent, as all the curves in Fig. 5.8(b) approximately collapse into one curve, except for the small value of U_o/U_i =0.015.

The experimental results provided in this section reveal that, qualitatively, the dynamics of pipe B is similar to that of pipe A, shown in Fig. 5.3(a) and Fig. 5.6(a,c,e). The critical flow velocities are related to pipe slenderness in a complex manner, depending on the viscous forces in the longitudinal and normal directions associated with the external flow. In particular, careful investigation of the Eq. (A.1) shows that all the terms including ε are multiplied by c_f, a dimensionless friction coefficient pertinent to the external-flow viscous forces, and u_o or u_o^2. However, artificially multiplying all the terms involving ε by 10 was found to have only a marginal stabilizing effect on the critical flow velocities, in agreement with the experimental results for $U_o/U_i = 0.2 - 0.8$. It is noted that in the case of $U_o/U_i = 0.015$, the value of u_o at the onset of instability is small and almost equal for the two pipes: $u_o = 0.20$ for pipe A and $u_o = 0.23$ for pipe B, and thus the stabilizing influence of increasing ε may have become very marginal due to the small values of u_o. On the other hand, for $U_o/U_i = 0.015$, the frequency-dependent κ_u term in Eq. (A.1) is smaller for pipe A than pipe B, because

Table 5.4: Critical flow velocities of the instability of pipe A ($\varepsilon = 27.56$) and pipe B ($\varepsilon = 13.81$).

	Pipe A		Pipe B	
U_o/U_i	$u_{cr,1}$	$u_{cr,2}$	$u_{cr,1}$	$u_{cr,2}$
0.015	5.19		6.15	
0.2	1.04	1.92	0.97	1.59
0.4	0.48	0.91	0.43	0.76
0.8	0.24	0.51	0.23	0.44

the frequency is smaller, resulting in a smaller u_{cr} for pipe A.

5.7 The effect of flow constriction at the upstream or downstream end of the annular region

It is known that structures subjected to tightly confined annular external flow are exposed to annular- and leakage-flow-induced instabilities. For leakage-flow-induced instability to materialize, neither is the cylinder (pipe) required to be very flexible, nor the flow velocities to be high. The system undergoes instability, provided that the geometry has the potential to cause the phenomenon. Leakage-flow-induced instabilities are capable of causing catastrophic failures, giving rise to forces of the order of tens of tons [17]. As a 'rule of thumb', it is believed that a constriction at the upstream end of a tightly-confined channel tends to destabilize the system, whereas a constriction at the downstream end tends to promote stability.

In practical applications such as solution mining, sometimes ring-shaped stabilizers are added on the brine-string in the annular region. In the light of the possible occurrence of leakage-flow-induced instability, using such stabilizers may have a deleterious effect. Therefore, for the system under study, the effect of inserting a ring-shaped obstruction at the inlet or outlet of the annular region formed by the pipe and the outer rigid tube was explored, as illustrated in Fig. 5.2(a, b).

5.7.1 Obstruction at the annular region inlet

The investigate the effect of the external flow constriction on the stability of the system as well as the amplitude of oscillations, a ring of thickness $t_r = 12$ mm, outer diameter $D_{or} = D_{ch} = 54$ mm and various inner diameter sizes, namely, $D_{ir} = 41$, 32 or 25 mm was pressure-fitted at the bottom (inlet) of the annular region to constrain the annular flow, as shown in Fig. 5.2(a); these ring sizes correspond to $\bar{g}_r = (D_{ir} - D_o)/D_h$ =0.66, 0.42 and 0.24, respectively. The fixed system parameters were as follows: pipe A with $\varepsilon = 27.56$, rigid outer tube with $r_{ann} = 0.468 \simeq 1/2$ ($L' = 206.5$), $\alpha_{ch} = 3.37$ ($D_{ch} = 54$ mm) corresponding to $\chi = 1.19$, and $\bar{e} = 0$. The results can be compared to those of Section 5.4 with the same pipe and outer rigid tube, but with no obstruction in the annular flow ($\bar{g}_r$ =1).

Bifurcation diagrams illustrating the rms amplitude of displacement and the mean

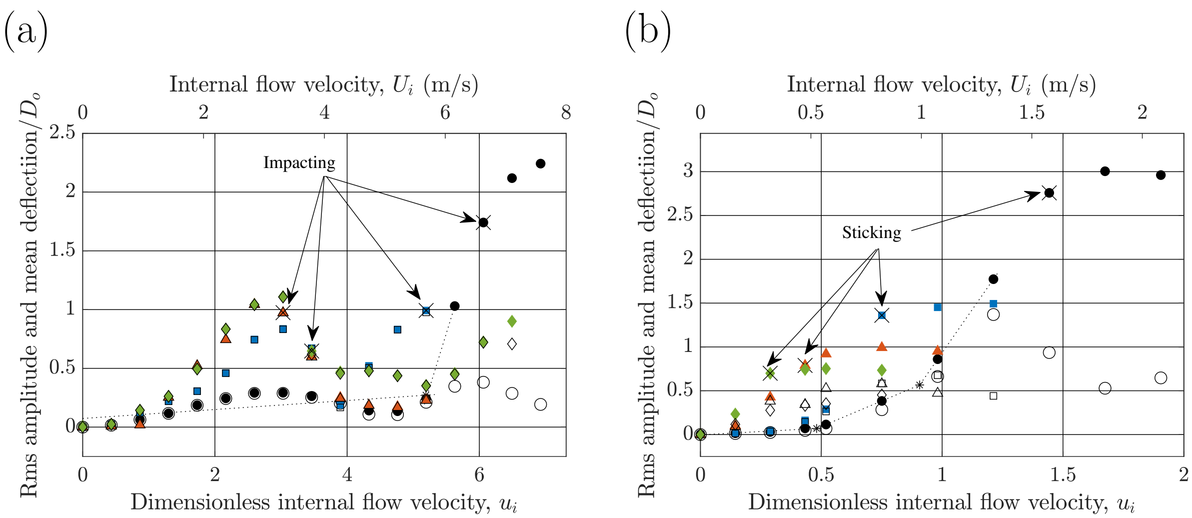

Figure 5.9: Bifurcation diagrams showing the rms amplitude of total displacement and the mean deflection versus u_i for investigating the effect of placement of an obstruction at the inlet of the outer rigid tube for pipe A with $\alpha_{ch} = 3.37$ (D_{ch}=54 mm). (a) Interdependent internal and external flows (Q_a =0, U_o/U_i =0.015); (b) U_o/U_i=0.4. Filled markers show the rms amplitude and hollow markers show the mean static deflection: $\bar{g}_r$ =1 (no ring): (●), $\bar{g}_r$ =0.66: (■), $\bar{g}_r$ =0.42: (▲), $\bar{g}_r$ =0.24: (♦).

deflection versus u_i for $U_o/U_i = 0.015$ ($Q_a = 0$) and $U_o/U_i = 0.4$ ($Q_a \neq 0$) are presented in Fig. 5.9(a, b), respectively. As can be seen, for interdependent flows ($Q_a = 0$) and all ring sizes, placement of the constraint at the inlet increases the deflection of the pipe by exaggerating its static deformation, resulting in impacting of the pipe on the inner rim of the ring. For higher U_o/U_i and tight enough rings, i.e. $\bar{g}_r$ =0.42 and 0.25, both static and oscillatory components of the deformation increase severely. This behaviour may well be due to the leakage-flow-induced instability mechanism. Hence, the system may acquire energy from the flow giving rise to flutter, when the negative damping outweighs the positive dissipation due to structural and flow-induced damping in the system.

5.7.2 Obstruction at the annular region outlet

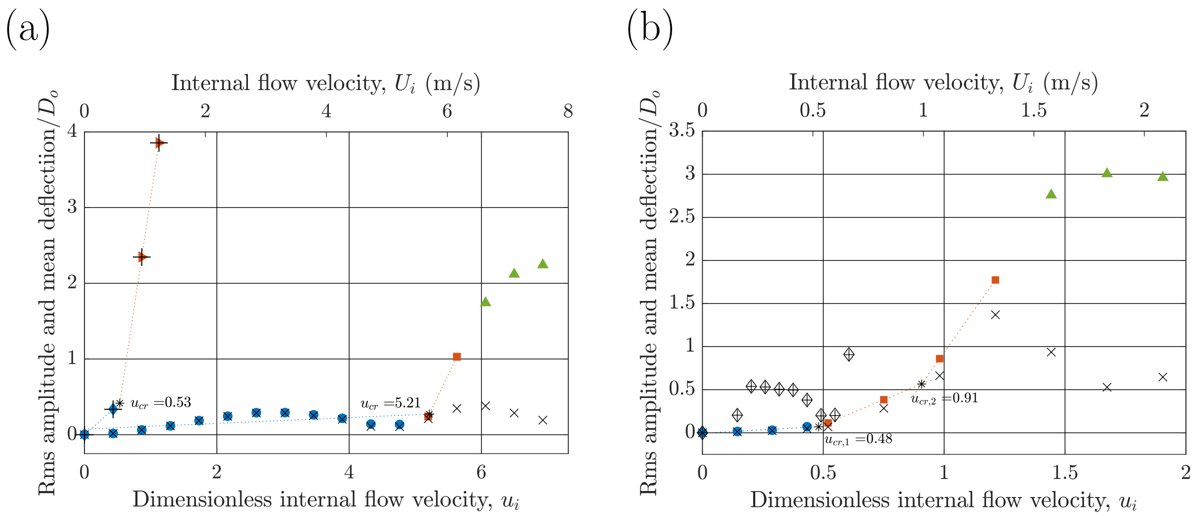

Figure 5.10: Bifurcation diagrams showing the rms amplitude of total displacement and the mean deflection versus u_i for investigating the effect of placement of an obstruction at the outlet of the outer rigid tube for pipe A with α_{ch} = 3.37 (D_{ch}=54 mm) and (a) interdependent internal and external flows (Q_a =0, U_o/U_i =0.015); (b) U_o/U_i=0.4. Rms amplitude: (●) pre-instability and no ring, (◆) pre-instability and $\bar{g}_r$ =0.05, (■) instability and no ring, (▶) instability and $\bar{g}_r$ =0.05, (▲) impact and no ring, (◇) data points for $\bar{g}_r$ = 0.10; (×) mean deflection and no ring, (+) mean deflection for the cases with a ring; (∗) critical flow for instability.

In this set of experiments, placement of an obstruction at the outlet of the annular region was investigated. A ring of thickness t_r = 12 mm, outer diameter $D_{or} = D_{ch}$ = 54 mm and inner diameter, D_{ir} =20 or 18 mm was pressure-fitted at the outlet (top) of the annular region. These ring inner diameter sizes correspond to $\bar{g}_r = (D_{ir} - D_o)/D_h$ =0.10 and 0.05, respectively. Other system parameters are the same as Section 5.7.1. The results can be compared to those of Section 5.4 with the same pipe and outer rigid tube, but with no obstruction at the outer tube.

Fig. 5.10 compares the rms amplitude of total displacement and mean deflection as a function of u_i for the cases with and without a constraint at the outlet. It was observed that obstruction of the external flow at the outlet increased the pressure inside the pressure vessel

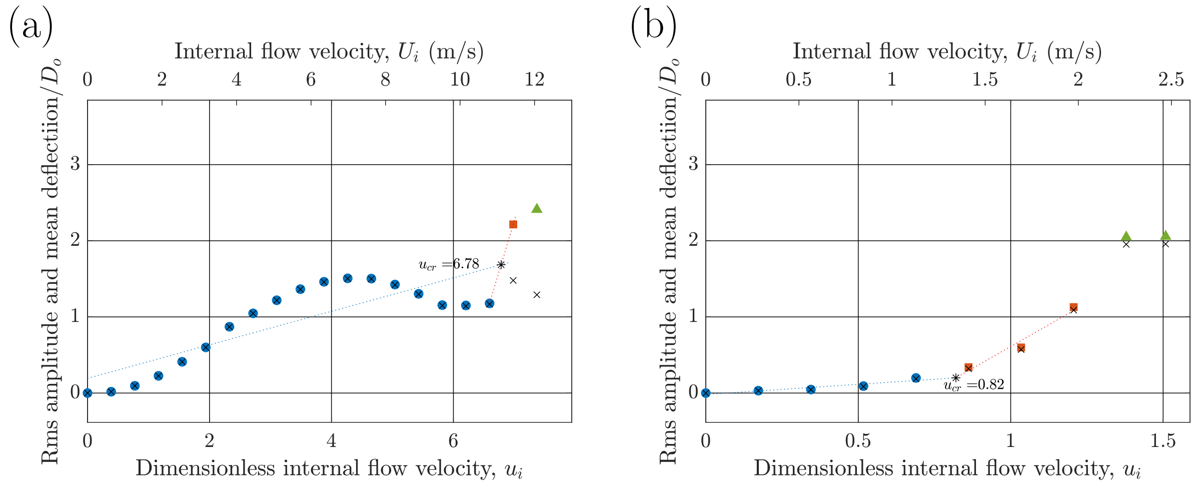

Figure 5.11: Bifurcation diagrams showing the rms amplitude of total displacements and the mean deflection versus u_i for the pipe C and, (a) interdependent internal and external flows (U_o/U_i=0.033); (b) independent internal and external flows (U_o/U_i =0.4). Rms amplitude: (●) pre-instability, (■) instability, (▲) impact; (×) mean deflection; (∗) critical flow for instability.

considerably. This build-up of pressure may be responsible for the large amplitude static deflection at relatively small flow velocities. As can be seen in Fig. 5.10(a), for U_o/U_i = 0.015 the increase in the slope of the bifurcation diagram is very severe, but the oscillatory component is very weak. For U_o/U_i =0.4, the turbulence buffeting region for the case with no ring is replaced by a bell-shaped curve, followed by a static divergence.

The instabilities in this case take place at relatively small flows, suggesting that the increase in pressure resulting from placement of the obstruction at the downstream end of the annulus may well be the mechanism for the static divergence observed: small perturbations in the system are exaggerated severely because of the high-pressure.

5.8 The effect of pipe material

To examine the influence of material properties on the dynamics, experiments with pipe C, which is a commercial santoprene pipe, were conducted. Pipe C is stiffer compared to pipe A. The pipe stiffness as well as its geometry are given in Table 5.1. The system parameters are as follows: pipe C with $\varepsilon = 34.08$, outer rigid tube with $r_{ann} = 0.466 \simeq 1/2$ ($L' = 206.5$) and $\alpha_{ch} = 4.15$ ($D_{ch} = 54$ mm) corresponding to $\chi = 1.12$.

Bifurcation diagrams showing the rms displacement and mean deflection versus u_i for interdependent internal and external flows (U_o/U_i =0.033 in this case), and for U_o/U_i =0.4 are presented in Fig. 5.11(a, b), respectively. The results can be compared to those for pipe A and the same outer tube: in Fig. 5.3(a) for interdependent flows (U_o/U_i =0.015), and in Fig. 5.6(c) for U_o/U_i =0.4. It is noted that pipe C, the stiffer pipe, has higher dimensionless critical flow velocities, namely for interdependent internal and external flows $u_{cr} = 6.78$ and for $U_o/U_i = 0.82$, as compared to $u_{cr} = 5.19$ and $u_{cr} = 0.48$ for pipe A. This demonstrates that u_i is not a sufficient dimensionless parameter to collapse the dynamics. Note that EI, is already included in the expression for u_i, given in Eq. (5.1). However, the dynamics of the system also depends on other parameters, such as internal damping characteristics, frequency-dependent damping (κ_u in Eq. (A.1)), gravity parameter, γ, mass parameter associated with the internal flow, β_i, and mass parameter associated with the external flow, β_o, the latter three expressed as

$$\gamma = \frac{(m + M_i - M_o)}{EI} g L^3, \quad \beta_i = \frac{M_i}{m + M_i + M_o}, \quad \beta_o = \frac{M_o}{m + M_i + M_o}, \tag{5.3}$$

where m is the pipe mass, $M_i = \rho_f A_i$ denotes the mass of the internal fluid per unit length, and $M_o = \rho_f A_o$ is the added mass associated with the external flow per unit length, in which ρ_f is the density of the fluid (water in this case); $A_i = (\pi/4)d_i^2$ and $A_o = (\pi/4)d_o^2$ are the inner and outer cross-sectional area of the pipe, respectively. For pipe A we have $\gamma = 2.47$, $\beta_i = 0.07$ and $\beta_o = 0.47$; for pipe C, $\gamma = 0.55$, $\beta_i = 0.25$ and $\beta_o = 0.46$. Since the two pipes have almost the same β_o, we have investigated only the effect of γ and β_i on u_{cr} based on the model of Eq. (A.1). The calculations revealed that u_{cr} increases with increasing γ and β_i, the effect of increasing β_i being more pronounced. Therefore, increasing u_{cr} in the case of experiments with pipe C might be attributed to the greater value of β_i; alternatively, to the higher values of frequency-dependent damping (the first mode frequency of pipe C measured in air is 2.10 Hz, as compared to 1.09 Hz for pipe A).

Qualitatively, compared to pipe A, the oscillations were weaker and with a wider frequency bandwidth in the PSDs for pipe C (not shown here, for brevity). The largest Lyapunov exponent for pipe C at the onset of instability was $\lambda_1 \simeq$0.15 bits/s for $U_o/U_i = 0.033$, compared to $\lambda_1 \simeq 0.05$ for pipe A (shown in Fig. 5.4(b)), showing that pipe C had a stronger chaotic component. For U_o/U_i =0.4, however, the chaotic component was similar for the two pipes, i.e. $\lambda_1 \simeq 0$. It is noted that at the onset of instability the rms of displacement of pipe C for $U_o/U_i = 0.033$ is greater than that of pipe A for $U_o/U_i = 0.015$, as shown in Figs. 5.11(a) and 5.3(a), respectively. For U_o/U_i =0.4, however, the rms amplitude of displacements for the two pipes are similar. The larger amplitude of oscillations results in an increase in the contribution of nonlinearities in the system response. Comparing the amplitude of oscillations at the onset of instability for pipes A and C, suggests that the increase in the chaotic component in the case of the interdependent flows may be attributed to the larger amplitude of oscillations.

5.9 The effect of eccentricity

To explore the effect of an eccentric placement of the rigid outer tube with respect to the central flexible pipe, the outer rigid tube was mounted with a predetermined eccentricity, e, with respect to the pipe centreline, as in Fig. 5.2(c). In this case, other system parameters are as follows: pipe A with $\varepsilon = 27.56$, the rigid outer tube with $r_{ann} = 0.468 \simeq 1/2$ ($L' = 206.5$) and $\alpha_{ch} = 3.37$ ($D_{ch} = 54$ mm) that corresponds to $\chi = 1.19$.

5.9.1 Interdependent internal and external flow

In experiments with interdependent internal and external flows ($U_o/U_i = 0.015$), $e = 4$, 8 and 14 mm, corresponding to $\bar{e} = 0.208$, 0.416 and 0.727, respectively, were investigated. The results are presented in Fig. 5.12. As seen, an eccentricity between the central pipe and the outer rigid tube resulted in a remarkable increase in the static deflection of the pipe in the bell-shaped region prior to any oscillatory instability.

Given the smaller gap between one side of the pipe and the surrounding channel, the exaggerated static deflection gave rise to impacting at relatively smaller flows.

5.9.2 Independent internal and external flow

In these experiments for U_o/U_i=0.2, 0.4 and 0.8, $e = 4$ mm ($\bar{e} = 0.208$) and 8 mm ($\bar{e} = 0.416$) were tried. The bifurcation diagrams for $\bar{e} = 0.416$ and U_o/U_i =0.2 and 0.8 are shown in Fig. 5.13. The bifurcation diagrams can be compared to those of Fig. 5.6(a, e) for the same U_o/U_i, but for a concentric system. Also, the critical flow velocity for the onset of instability for the concentric and eccentric systems ($\bar{e} \simeq 0.208$ and 0.416) are compared in Table 5.5.

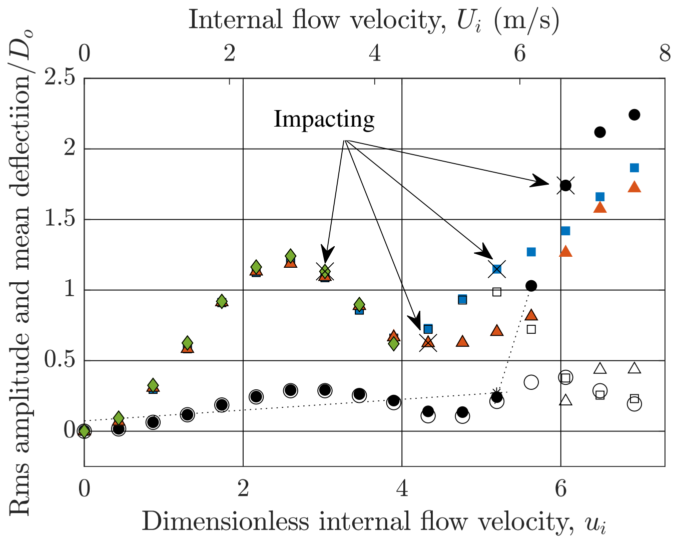

Figure 5.12: Bifurcation diagram presenting the rms amplitude of total displacements and the mean deflection as a function of u_i showing the effect of eccentricity for pipe A, U_o/U_i= 0.015. (●) Rms amplitude and (○) mean deflection for concentric system. (■) Rms amplitude and (□) mean deflection for $\bar{e}$ = 0.208. (▲) Rms amplitude and (△) mean deflection for $\bar{e}$ = 0.416. (♦) Rms amplitude and (◇) mean deflection for $\bar{e}$ = 0.727.

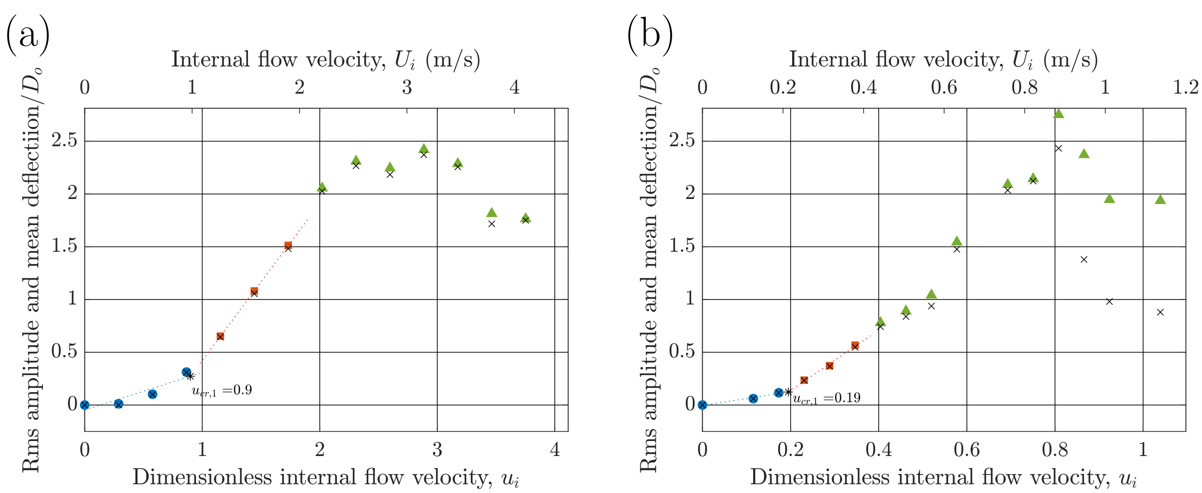

Figure 5.13: Bifurcation diagrams showing the rms amplitude of total displacements as a function of u_i for the eccentrically located pipe A, $\bar{e}$ = 0.416 and (a) U_o/U_i =0.2; (b) U_o/U_i =0.8. Rms amplitude: (●) pre-instability, (■) instability, (▲) impact; (×) mean deflection; (∗) critical flow for instability.

Table 5.5: Comparing $u_{cr,1}$ for pipe A with different values of dimensionless eccentricity with respect to the outer tube.

U_o/U_i	$\bar{e} = 0$	$\bar{e} \simeq 0.208$	$\bar{e} \simeq 0.416$
0.015	5.19	-	-
0.2	1.04	0.94	0.9
0.4	0.48	0.48	0.46
0.8	0.24	0.28	0.19

Two important changes can be observed: (i) the second instability region in the bifurcation diagrams of the concentric system disappeared in the case of the eccentric one, resulting in impacting on the outer tube at relatively smaller flows; (ii) the amplitude of motions increased for the eccentric system compared to those for concentric one.

5.10 Conclusion

In the present systematic experimental investigation, the dynamics of a hanging pipe discharging fluid downwards into a reservoir and subjected to a partially confined reverse external axial flow through a shorter annulus over the upper portion of the pipe was examined. Besides scientific curiosity in exploring the rich dynamical behaviour this system displays, interest in the matter arises because of its engineering applications, specifically in the retrieval mode of operation of the solution-mined hydrocarbon storage caverns.

For various ratios of the external to internal flow velocities, U_o/U_i, a series of experiments were carried out to study and characterize the influence of the following system parameters: (i) external flow confinement, (ii) pipe slenderness, (iii) placement of a constraint at the inlet or outlet of the annular gap, (iv) pipe material, and (v) the eccentric mounting of the surrounding annulus relative to the central pipe.

Generally, for interdependent external and internal flows, the pipe underwent turbulence buffeting at low flow velocities, followed by second-mode flutter at higher flows. For independent external and internal flows, the pipe was subjected to turbulence buffeting also, followed by static deflection of the pipe or weak first-mode oscillations, and eventually by second- or mixed-mode oscillations. These motions were quite unsteady, with a dominant periodic component and some chaotic content. Varying the system parameters in some cases resulted in remarkably different dynamical behaviour, qualitatively and/or quantitatively. The underlying fluid-structure interaction mechanisms resulting in these variations were briefly discussed.

In all cases, the onset of instabilities decreased to lower flows by increasing U_o/U_i. Increasing the annular gap size (decreasing the confinement) and pipe stiffness was found to have a stabilizing effect in general. On the other hand, placement of a constraint at the inlet of the annulus or eccentric positioning of the outer rigid tube with respect to the central pipe had a destabilizing effect on the system. The destabilizing influence of placement of a constraint at the annular gap outlet was significant, leading to very large static deformation at relatively small flow velocities. Increasing pipe slenderness had a destabilizing effect for the very small $U_o/U_i = 0.015$, and only a marginal stabilizing effect for higher U_o/U_i.

CRediT authorship contribution statement

M. Chehreghani: Experiments, Writing – Original Draft. **A. Shaaban**: Experiments, Writing – Review & Editing. **A.K. Misra**: Funding acquisition, Supervision, Writing – Review & Editing. **M.P. Païdoussis**: Funding acquisition, Supervision, Writing – Review & Editing.

Acknowledgments

The financial support of the Natural Sciences and Engineering Research Council of Canada (A.K.M., grant number 04957-2018; M.P.P., grant number 06465-2018), the Solution Mining Research Institute (M.P.P., grant number U2017-3) and Pipeline Research Council International (M.P.P., grant number PR593-18700) is gratefully acknowledged. The first author is thankful to McGill University for a McGill Engineering International Tuition Award (MEITA). Thanks also go to Mr. Aram Bahmani for helping with some schematic graphical designs.

Appendix A. The linear equation of motion of the basic system

The linear equation of motion for a cantilevered pipe discharging fluid downwards and simultaneously subjected to reverse axial external flow in dimensionless form was derived by

Moditis et al. [33]; it is

$$
\begin{aligned}
&\eta'''' + \Big\{\gamma - \frac{1}{2}\varepsilon c_f u_o^2(1+h)\big[1 - H(\xi - r_{ann})\big] - \frac{1}{2}u_o^2\big(1+K_1\big)\delta_D(\xi - r_{ann})\Big\}\eta' \\
&\quad + \Big\{ - \gamma(1-\xi) + \frac{1}{2}\varepsilon c_f u_o^2(1+h)(r_{ann} - \xi)\big[1 - H(\xi - r_{ann})\big] - (\Gamma - \Pi_{iL} + \Pi_{oL}) \\
&\quad + \frac{1}{2}u_o^2\big(1+K_1\big)\big[1 - H(\xi - r_{ann})\big]\Big\}\eta'' + \Big\{1 + \beta_o(\chi - 1)\big[1 - H(\xi - r_{ann})\big]\Big\}\ddot{\eta} \\
&\quad + \Big\{2u_i\sqrt{\beta_i} - 2u_o\chi\sqrt{\beta_o}\big[1 - H(\xi - r_{ann})\big]\Big\}\dot{\eta}' + \Big\{u_i^2 + \chi u_o^2\big[1 - H(\xi - r_{ann})\big]\Big\}\eta'' \\
&\quad + \frac{1}{2}c_f\varepsilon u_o\sqrt{\beta_o}\big[1 - H(\xi - r_{ann})\big]\dot{\eta} + \kappa_u\Big\{1 + \big[1 - H(\xi - r_{ann})\big]\Big(\frac{1+\alpha_{ch}^{-3}}{(1-\alpha_{ch}^{-2})^2} \\
&\quad - 1\Big)\Big\}\dot{\eta} = 0,
\end{aligned}
\tag{A.1}
$$

where $(\ )' = \partial(\ )/\partial\xi$, $\dot{(\ )} = \partial(\ )/\partial\tau$, and H denotes the Heaviside step function, and δ_D the Dirac delta function. In this equation, in addition to some of the dimensionless parameters introduced in Section 5.3, the following parameters are used: $\xi = x/L$ is the dimensionless axial coordinate, alongside the undeformed state of the central pipe, with origin at the cantilever fixed end; $\eta = w/L$ is the dimensionless lateral displacement of the pipe; $\tau = \big[(EI)/(m+\rho_f A_i+\rho_f A_o)\big]^{1/2}(t/L^2)$ is the dimensionless time; $\beta_i = (\rho_f A_i)/(m+\rho_f A_i+\rho_f A_o)$ is the ratio of the internal fluid mass to the total mass; $\beta_o = (\rho_f A_o)(m+\rho_f A_i+\rho_f A_o)$ is the ratio of the virtual (added) mass associated with the external flow to the total mass; $\gamma = \big[(m+\rho_f A_i - \rho_f A_o)gL^3\big]/(EI)$ is a dimensionless parameter related to the gravity; $\Gamma = \big[T(L)L^2\big]/(EI)$ is a dimensionless parameter relevant to the longitudinal tension at the free end; $\alpha = D_i/D_o$; $h = D_o/D_h$; $\kappa_u = (k_u L^2)/[EI(M_t+\rho_f A_i+\rho_f A_o)]^{1/2}$ is a dimensionless parameter associated with the viscous-drag coefficient and $c_f = (4/\pi)C_f$ is a dimensionless frictional coefficient associated with the external flow viscous forces in the longitudinal and normal directions. Additionally, $\Pi_{iL} = (A_i p_i(L)L^2)/(EI)$ and $\Pi_{oL} = (A_o p_o(L)L^2)/(EI)$ are dimensionless parameters related to the pressure measured at the pipe free end, just inside and outside of the pipe, respectively. Also, $\Pi_{iL} = \alpha^2\Pi_{oL} - (1/2)u_i^2 + (A_i\rho_f g h_e L^2)/(EI)$, where $\Pi_{oL} = (1/2)\varepsilon c_f h r_{ann} u_o^2 + (1/2)u_o^2\big(1+K_1\big) + (A_o\rho_f g L^3)/(EI)$, in which $0.8 \leqslant K_1 \leqslant 0.9$ is a parameter related to the head-loss associated with the quiescent fluid aspirated into the annular region at $\xi = r_{ann}$, and h_e is the head-loss due to the abrupt expansion of the flow exiting the pipe into the pressure vessel at the free end.

Making use of Galerkin's technique, the dimensionless equation of the motion, i.e. Eq.

(6.44), can be discretized to a set of N ordinary differential equations, represented in matrix form as follows:

$$\mathrm{M}\ddot{\mathrm{q}} + \mathrm{C}\dot{\mathrm{q}} + \mathrm{K}\mathrm{q} = 0, \tag{A.2}$$

where M, C and K are mass, damping and stiffness matrices, respectively. The expressions of these matrices are given in Appendix B.

Appendix B. The expressions for mass, damping and stiffness matrices

M, C and K in Eq.(A.2), mass, damping and stiffness matrices, respectively, are as follows:

$$\mathrm{M}_{ij} = a_{ij}(0,1) + \beta_o(\chi - 1)a_{ij}(0, r_{ann}), \tag{B.1}$$

$$\begin{aligned}\mathrm{C}_{ij} = {} & 2u_i\sqrt{\beta_i}b_{ij}(0,1) - 2u_o\sqrt{\beta_o}\chi b_{ij}(0,r_{ann}) + \frac{1}{2}c_f\varepsilon u_o\sqrt{\beta_o}a_{ij}(0,r_{ann}) \\ & + k_u a_{ij}(0,1) + k_u\Big[\frac{1+\alpha_{ch}^{-3}}{(1-\alpha_{ch}^{-2})^2} - 1\Big]a_{ij}(0,r_{ann}),\end{aligned} \tag{B.2}$$

$$\begin{aligned}\mathrm{K}_{ij} = {} & \Lambda_j^4 a_{ij}(0,1) + \gamma b_{ij}(0,1) - \frac{1}{2}\varepsilon c_f u_o^2\big[(1+h)b_{ij}(0,r_{ann})\big] + \chi u_o^2 c_{ij}(0,r_{ann}) \\ & + \frac{1}{2}\varepsilon c_f u_o^2(1+h)\big[r_{ann}c_{ij}(0,r_{ann}) - d_{ij}(0,r_{ann})\big] - \gamma\big[c_{ij}(0,1) - d_{ij}(0,1)\big] \\ & - \frac{1}{2}u_o^2(1+K_1)\phi_i|_{\xi=r_{ann}}\phi_j'|_{\xi=r_{ann}} - (\Gamma - \Pi_{iL} + \Pi_{oL})c_{ij}(0,1) \\ & + \frac{1}{2}u_o^2(1+K_1)c_{ij}(0,r_{ann}) + u_i^2 c_{ij}(0,1),\end{aligned} \tag{B.3}$$

where Λ_j is the j^{th} eigenvalue of the cantilevered Euler-Bernoulli beam characteristic equation and the following integrals are defined in order to have a more compact notation:

$$\begin{aligned}a_{ij}(a,b) &= \int_a^b \phi_i\phi_j d\xi, \quad b_{ij}(a,b) = \int_a^b \phi_i\phi_j' d\xi, \\ c_{ij}(a,b) &= \int_a^b \phi_i\phi_j'' d\xi, \quad d_{ij}(a,b) = \int_a^b \xi\phi_i\phi_j'' d\xi,\end{aligned} \tag{B.4}$$

in which ϕ_j is the the j^{th} normalized cantilevered Euler-Bernoulli beam eigenfunction.

References

[1] F. J. Bourrières, Sur un phénomène d'oscillation auto-entretenue en mécanique des fluides réels, in: Publications Scientifiques et Techniques du Ministère de l'Air. France, No. 147., 1939.

[2] M. P. Païdoussis, Fluid-Structure Interactions: Slender Structures and Axial Flow, Vol. 1, 2nd edition, Academic Press, Oxford, 2014.

[3] M. P. Païdoussis, G. X. Li, Pipes conveying fluid: a model dynamical problem, J. Fluids Struct. 7 (2) (1993) 137–204.

[4] P. J. Holmes, Pipes supported at both ends cannot flutter, J. Appl. Mech. 45 (3) (1978) 619–622.

[5] R. W. Gregory, M. P. Païdoussis, Unstable oscillation of tubular cantilevers conveying fluid. Part II: Experiments, Proc. R. Soc. London, Ser. A 293 (1435) (1966) 528–542.

[6] A. K. Bajaj, P. R. Sethna, T. S. Lundgren, Hopf bifurcation phenomena in tubes carrying a fluid, SIAM J. Appl. Math. 39 (2) (1980) 213–230.

[7] M. P. Païdoussis, F. C. Moon, Nonlinear and chaotic fluidelastic vibrations of a flexible pipe conveying fluid, J. Fluids Struct. 2 (6) (1988) 567–591.

[8] M. P. Païdoussis, Pipes conveying fluid: A fertile dynamics problem, J. Fluids Struct. 114 (2022) 103664.

[9] M. P. Païdoussis, Dynamics of flexible slender cylinders in axial flow. Part 1: theory, J. Fluid Mech. 26 (4) (1966) 717–736.

[10] G. S. Triantafyllou, C. Chryssostomidis, Analytic determination of the buckling speed of towed slender cylindrical beams, ASME J. Energy Resour. Technol. 106 (2) (1984) 246–249.

[11] G. S. Triantafyllou, C. Chryssostomidis, Stability of a string in axial flow, ASME J. Energy Resour. Technol. 107 (4) (1985) 421–425.

[12] A. P. Dowling, The dynamics of towed flexible cylinders Part 1. Neutrally buoyant elements, J. Fluid Mech. 187 (1988) 507–532.

[13] S. Rinaldi, M. P. Païdoussis, Theory and experiments on the dynamics of a free-clamped cylinder in confined axial air-flow, J. Fluids Struct. 28 (2012) 167–179.

[14] S. Rinaldi, M. P. Païdoussis, An improved theoretical model for the dynamics of a free–clamped cylinder in axial flow, J. Fluids Struct. 94 (2020) 102903.

[15] J. E. Sader, C. Huertas-Cerdeira, M. Gharib, Stability of slender inverted flags and rods in uniform steady flow, J. Fluid Mech. 809 (2016) 873–894.

[16] Y. Perets, E. Sher, R. Harari, An experimental study on axial-flow-induced vibration of confined flexible rods with sequenced transverse rib roughness, Exp. Therm. Fluid Sci. 93 (2018) 86–95.

[17] M. P. Païdoussis, Fluid-Structure Interactions: Slender Structures and Axial Flow, Vol. 2, 2nd edition, Academic Press, Oxford, 2016.

[18] F. Cesari, S. Curioni, Buckling instability in tubes subject to internal and external axial fluid flow, in: Proc. 4th Conf. Dimens., Hungarian Academy of Science, Budapest, 1971, pp. 301–311.

[19] M. J. Hannoyer, M. P. Païdoussis, Instabilities of tubular beams simultaneously subjected to internal and external axial flows, ASME J. Mech. Des. 100 (2) (1978) 328–336.

[20] M. J. Hannoyer, M. P. Païdoussis, Dynamics of slender tapered beams with internal or external axial flow—Part 1: Theory, J. Appl. Mech. 46 (1) (1979) 45–51.

[21] M. J. Hannoyer, M. P. Païdoussis, Dynamics of slender tapered beams with internal or external axial flow—Part 2: Experiments, J. Appl. Mech. 46 (1) (1979) 52–57.

[22] M. P. Païdoussis, P. Besançon, Dynamics of arrays of cylinders with internal and external axial flow, J. Sound Vib. 76 (3) (1981) 361–379.

[23] J. J. Bailey, I. Finnie, An analytical study of drill-string vibration, ASME J. Eng. Ind. 82 (2) (1960) 122–127.

[24] I. Finnie, J. J. Bailey, An experimental study of drill-string vibration, ASME J. Eng. Ind. 82 (2) (1960) 129–135.

[25] J. P. Den Hartog, John Orr memorial lecture: recent cases of mechanical vibration, South African Mech. Eng. 19 (3) (1969) 53–68.

[26] T. P. Luu, On the dynamics of three systems involving tubular beams conveying fluid, Master's thesis, Department of Mechanical Engineering, McGill University, Canada (1983).

[27] X. Wang, F. Bloom, Dynamics of a submerged and inclined concentric pipe system with internal and external flows, J. Fluids Struct. 13 (4) (1999) 443–460.

[28] M. P. Païdoussis, T. P. Luu, S. Prabhakar, Dynamics of a long tubular cantilever conveying fluid downwards, which then flows upwards around the cantilever as a confined annular flow, J. Fluids Struct. 24 (1) (2008) 111–128.

[29] Q. Qian, L. Wang, Q. Ni, Vibration and stability of vertical upward-fluid-conveying pipe immersed in rigid cylindrical channel, Acta Mech. Solida Sin. 21 (5) (2008) 331–340.

[30] K. Fujita, A. Moriasa, Stability of cantilevered pipes subjected to internal flow and external annular axial flow simultaneously, in: ASME 2015 Press. Vessel. Pip. Conf., Boston, MA, USA; PVP2015-45141, 2015.

[31] R. Abdollahi, R. Firouz-abadi, M. Rahmanian, On the stability of rotating pipes conveying fluid in annular liquid medium, J. Sound Vib. 494 (2021) 115891.

[32] A. Ghasemloonia, D. G. Rideout, S. D. Butt, A review of drillstring vibration modeling and suppression methods, J. Pet. Sci. Eng. 131 (2015) 150–164.

[33] K. Moditis, M. P. Païdoussis, J. Ratigan, Dynamics of a partially confined, discharging, cantilever pipe with reverse external flow, J. Fluids Struct. 63 (2016) 120–139.

[34] K. Kontzialis, K. Moditis, M. P. Païdoussis, Transient Simulations of the Fluid–Structure Interaction Response of a Partially Confined Pipe Under Axial Flows in Opposite Directions, ASME J. Press. Vessel Technol. 139 (3), 031303 (10 2016).

[35] A. R. Abdelbaki, M. P. Païdoussis, A. K. Misra, A nonlinear model for a hanging cantilevered pipe discharging fluid with a partially-confined external flow, Int. J. Non. Linear. Mech. 118 (2020) 103290.

[36] S. L. Minas, M. P. Païdoussis, Dynamics of a shrouded cantilevered pipe subjected to internal and annular flows, J. Sound Vib. 490 (2021) 115729.

[37] M. Chehreghani, A. R. Abdelbaki, A. K. Misra, M. P. Païdoussis, Experiments on the dynamics of a cantilevered pipe conveying fluid and subjected to reverse annular flow, J. Sound Vib. 515 (2021) 116480.

[38] M. P. Païdoussis, Dynamics of a cantilevered pipe subjected to internal and reverse external axial flow: A review, J. Fluids Struct. 106 (2021) 103349.

[39] M. Chehreghani, A. Shaaban, A. K. Misra, M. P. Païdoussis, Dynamics of cantilevered pipes conveying fluid and subjected to reverse annular external flow: experimental investigation of the influence of external flow confinement, in: C. Habchi, P. Moussou (Eds.), Proc. 12th Int. Conf. Flow-Induced Vib., l. zimmer, Edition, Paris, 2022, pp. 17–22.

[40] J. L. Ratigan, Brine string integrity and model evaluation, in: Proc. Process. SMRI Fall Meet. Galveston, TX, USA, 2008, pp. 13–14.

[41] P. Bérest, A. Réveillère, D. Evans, M. Stöwer, Review and analysis of historical leakages from storage salt caverns wells, Oil Gas Sci. Technol. d'IFP Energies Nouv. 74 (2019) 27.

[42] M. P. Païdoussis, P. E. Des Trois Maisons, Free vibration of a heavy damped vertical cantilever, J. Appl. Mech. 38 (1971) 524–526.

[43] S. Rinaldi, Experiments on the dynamics of cantilevered pipes subjected to internal and/or external axial flow, Master's thesis, Department of Mechanical Engineering, McGill University, Montreal, QC, Canada (2009).

[44] M. Chehreghani, I. Gholami, A. K. Misra, M. P. Païdoussis, Fluid-elastic instability of inverted cantilevered cylinders in axial flow, J. Fluids Struct. 115 (2022) 103778.

[45] E. Naudascher, D. Rockwell, Flow-Induced Vibrations: An Engineering Guide, Courier Corporation, North Chelmsford, MA, 2012.

[46] A. Wolf, J. B. Swift, H. L. Swinney, J. A. Vastano, Determining Lyapunov exponents from a time series, Phys. D Nonlinear Phenom. 16 (3) (1985) 285–317.

[47] F. C. Moon, Chaotic and Fractal Dynamics: Introduction for Applied Scientists and Engineers, John Wiley & Sons, New York, 2008.

Complementary discussion on system III - experimental investigation

To clarify and expand on what is included in the manuscript presented in Chapter 5 [4], further discussion is provided here.

As discussed, all bifurcation diagrams for various ratios of U_o/U_i in Fig. 5.8(b) collapse into one curve, except for the small value of $U_o/U_i = 0.015$. This suggests that for higher U_o/U_i, the dynamics mainly depends on the external flow, whereas for $U_o/U_i = 0.015$, it depends mostly on the internal flow. The reason the behavior for $U_o/U_i = 0.015$ is different from those of higher U_o/U_i ratios is likely related to the different flow configurations: for $U_o/U_i = 0.015$, there is no additional fluid entering from the bottom of the pressure vessel, resulting in interdependent internal and external flows (refer to Fig. 5.1). In contrast, for higher U_o/U_i ratios, additional fluid enters the pressure vessel, making the internal and external flows independent. It might also be related to the values of U_o/U_i themselves, as $U_o/U_i = 0.015$ is much lower than the other values tested in the experiments. To confirm this, further investigation may be necessary.

CHAPTER 6

Dynamics of a Cantilevered Pipe Conveying Fluid and Partially Subjected to a Confined Counter-current External Axial Flow of a Different Fluid: A Theoretical Investigation

Preface

The manuscript presented in this chapter [5], focuses on developing a linear analytical model for system III, representing an idealized brine-string in a salt-mined cavern. The objective is to predict fluid-elastic instabilities of brine-strings during product retrieval in salt-mined caverns, aligning with the final objective of the current thesis, which is to provide the tools for preventing fluid-elastic instabilities causing catastrophic failures and thereby avoiding the associated financial and ecological repercussions.

The earlier analytical models developed, have not successfully predicted the critical flow velocities in full-scale brine-strings. Attempting to predict a more realistic range of critical flow velocities for the full-scale system, the model developed in this manuscript has taken the presence of two fluids of different densities (the brine and the product), as well as the product pressure at the well-head into account. The system parameters used to obtain the numerical results in this manuscript were carefully chosen in consultation with operators of salt-caverns, ensuring their relevance.

Dynamics of a cantilevered pipe conveying fluid and partially subjected to a confined counter-current external axial flow of a different fluid

M. Chehreghani, A.K. Misra, M.P. Païdoussis*

Department of Mechanical Engineering, McGill University,

817 Sherbrooke Street West, Montreal, QC, Canada H3A 0C3.

Abstract: A linear analytical model has been developed for prediction of fluid-elastic instabilities of brine-strings during product retrieval in salt-mined caverns. These caverns are utilized for storage and subsequent retrieval of hydrocarbons, hydrogen gas or compressed air in Compressed Air Energy Storage (CAES) plants. The retrieval operation involves pumping brine downwards through a long cantilevered pipe ("brine-string") into the cavern, causing the lighter-than-brine gaseous or liquid "product" stored in the cavern to flow upwards and out of the cavern through a shorter annular passage formed by a concentric casing surrounding the upper portion of the pipe. The presence in the cavern of two different fluids with a variable interface level is taken into account. Employing a Newtonian derivation of the equation of motion solutions were obtained via the Galerkin modal decomposition technique, demonstrating that the brine-string may develop buckling or flutter at high-enough flow rates, depending on the system parameters. Extensive computations investigated the influence of system parameters on the dynamics. It is shown that simplifying the system by considering a single fluid in the cavern, and so for the flows within and around the brine-string, leads to unrealistically high critical flow velocity predictions.

Keywords: Flow-induced instability; Axial flow; Hanging tubular cantilever; Fluid-conveying pipe; Brine-string in salt-mined caverns; Flutter; Static divergence.

6.1 Introduction

An alternative title for this paper could be "The fluid-elastic instabilities of an idealized brine-string in salt-mined caverns", as investigating the dynamics of this system is the motivation behind this study.

Salt caverns are formed by drilling a well into underground salt deposits, and then leaching the salt by pumping fresh water down through a vertical pipe, the "brine-string". The injected fresh water dissolves the minerals, and the resulting brine is brought to the surface by injecting additional fresh water. A huge underground cavern is left behind, filled with brine, which can be used for storage and subsequent retrieval of liquid and gaseous hydrocarbons such as crude oil, natural gas, ethylene or hydrogen [1, 2]. These steps are shown schematically in Fig. 6.1. Salt-mined caverns can also serve as storage facilities for hydrogen gas or compressed air in CAES plants, aiding in the abatement of energy consumption peaks and valleys [3].

A schematic view of the system under consideration is shown in Fig. 6.2(a). This system consists of a long cantilevered pipe (the "brine-string"), typically thousands of meters long (usually 1-2 km), extending from the ground all the way down to nearly the bottom of the cavern, and a shorter concentric annular region formed by a rigid "casing" surrounding the pipe at its upper portion. The outer rigid casing is cemented onto the overburden and caprock, and extends slightly into the cavern. A substantial portion of the brine string lies below the casing enclosure [1].

Solution-mined caverns can be used in two different *modi operandi*: the "storage" and the "production" or "retrieval" modes [2, 4, 5]. The latter case, shown schematically in Fig. 6.2(b), is the focus of this paper. In this mode, which has a similar configuration as that of drill-strings utilized for oil exploration [6], brine is pumped into the brine-string, and the lighter-than-brine hydrocarbons are retrieved through the annulus for sale at a commercially propitious time; for this, as high an extraction flow rate as possible is desirable. However, the drawback of high extraction rates is that, at high flow velocities, the brine-string might undergo fluid-elastic instability, potentially causing impacting on the rigid casing. In severe cases, repeated impacting may lead to damage or even breakage of the brine-string. In fact, operators and engineers have grappled with the challenge of limiting flow-induced vibrations and suppressing fluid-elastic instabilities in brine-strings for many years, as these have been identified as probable causes of the breakages or permanent deformation; see, for instance, the damaged, permanently deformed brine string taken out from a gas and a liquid storage cavern shown in Fig. 6.3(a,b). Over the past few decades, twenty-one accidents involving gas and petroleum leaks have been documented in salt caverns [1, 7]. These incidents not only have serious financial repercussions, as repair and replacement costs are very high, but also cause serious environmental damage. Therefore, it is crucial to comprehend the dynamics

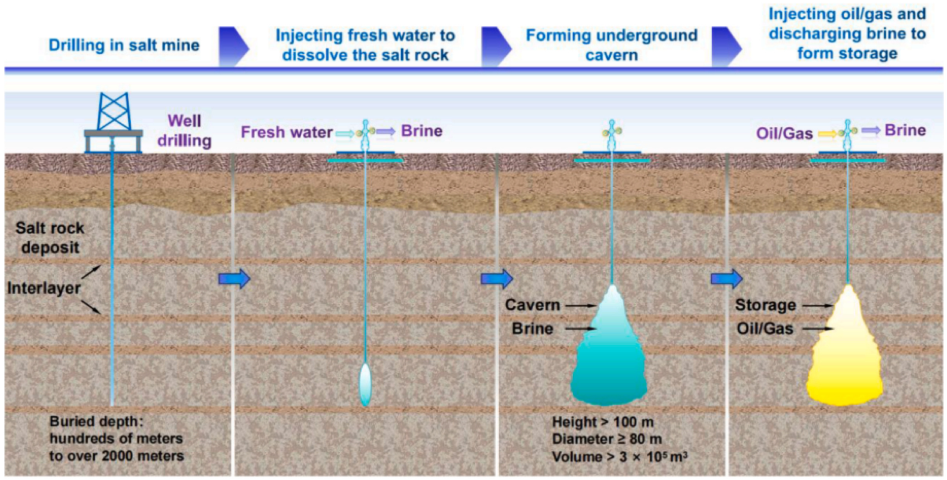

Figure 6.1: Formation of salt caverns: site selection, leaching salt deposit through fresh water injection, forming a cavern filled with brine, brine removal through gas or liquid injection in order to store hydrocarbons therein (after Liu et al. [3]). For a clearer viewing, please refer to the coloured online version.

of brine-strings, so as to prevent such catastrophic accidents. Hence, research is directed towards determining the safe upper limit for the flow velocity in the brine-string, ensuring that the system remains stable, avoiding divergence or flutter [8–10].

Extensive research has been conducted on the dynamics of the fluid-elastic system of pipes conveying fluid since at least 1939 [11]. The great attention paid to the study of this system is mainly due to its capacity of displaying a rich dynamical behaviour, despite its relatively simple analytical modelling and ease of physical realization [9, 12]. Numerous researchers have investigated a variety of configurations of this system. Examples include pipes with additional supports and lumped masses, linear and nonlinear springs, motion-restraining constraints, free-end nozzles, initially curved and imperfectly supported pipes, among other variations [13–22]. A pipe with supported ends is a gyroscopic conservative system and is only subject to static divergence at sufficiently high flow velocities [23, 24]. Cantilevered pipes, however, become unstable by flutter; they lose stability via a Hopf bifurcation into limit cycle oscillations. This bifurcation can be either subcritical or supercritical, depending on the system parameters [25–27]. The book by Païdoussis [12], along with a more recent review [9], provides a comprehensive overview of the extensive research conducted on

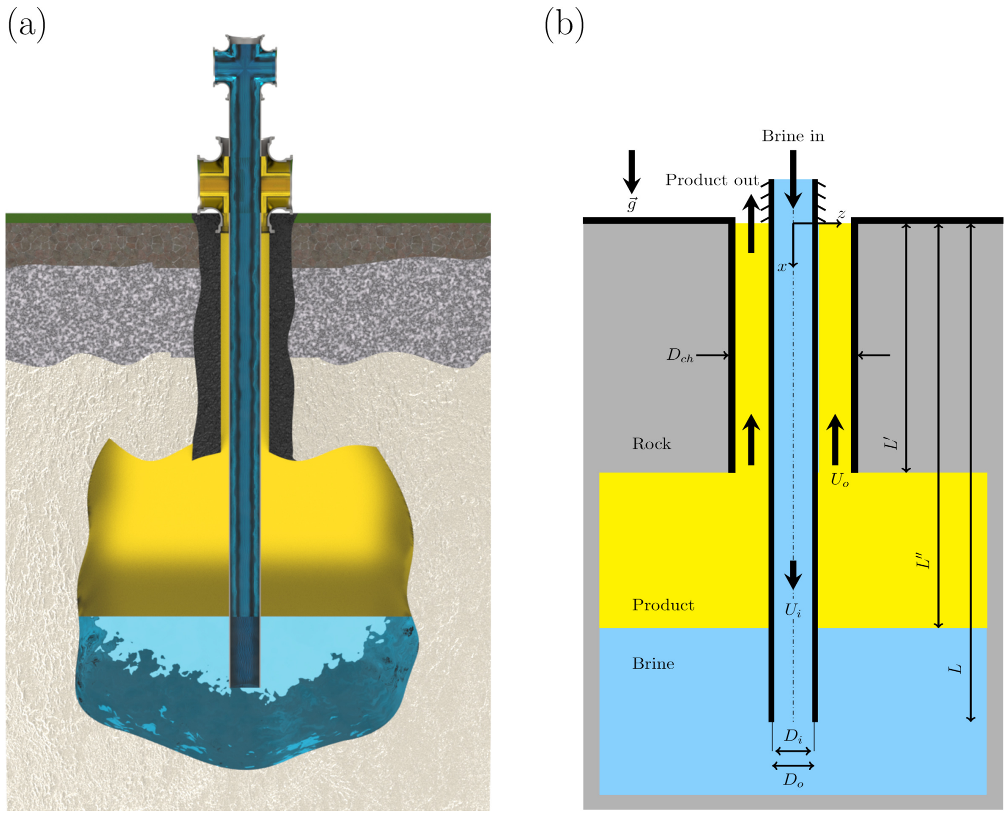

Figure 6.2: Schematic view of the system under consideration: (a) a brine-string in a typical solution-mined cavern; (b) an idealized model of the product retrieval operation. For a clearer viewing, please refer to the coloured online version.

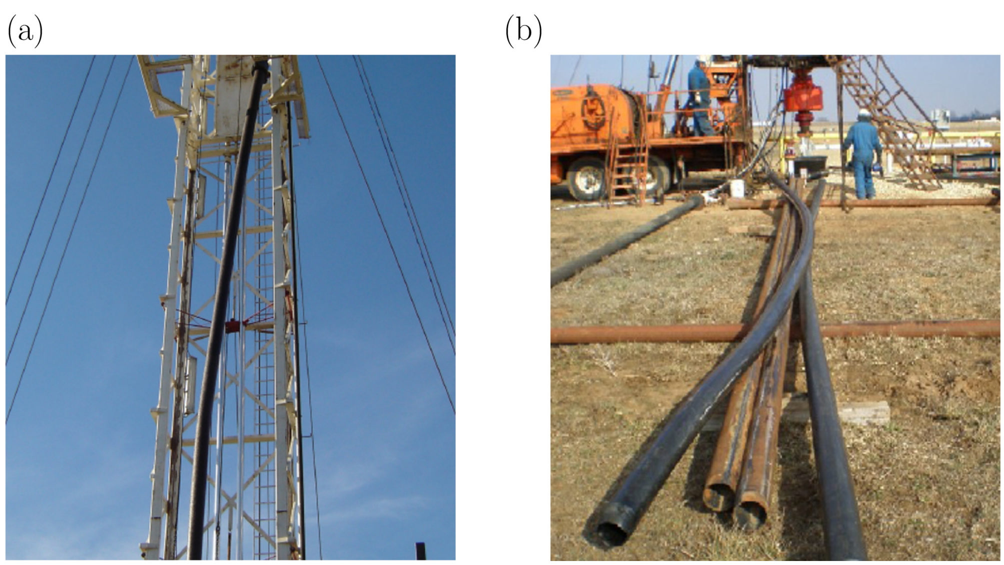

Figure 6.3: Brine string damage (after Ratigan [1]): (a) in a gas storage well; (b) in a liquid storage cavern.

the dynamics of pipes conveying fluid.

Next, we consider the dynamics of tubular beams subjected to simultaneous internal and external axial flows. Cesari and Curioni [28] were perhaps the first to study the dynamics of this system, predicting static divergence of pipes with different boundary conditions. Later on, the dynamics of hanging fluid-conveying pipes subjected to an independent external axial flow was examined by Hannoyer and Païdoussis [29]. For pipes with both ends clamped, the influence of the internal and external flows on stability is synergistic, i..e. when the velocity of either the internal or external flow is slightly below the critical threshold for instability, an increase in the velocity of the other flow would induce instability. For cantilevered pipes, on the other hand, in some cases, the effect of the internal and external flows on instability is not additive; i.e. if the pipe is just at the threshold of instability due to either internal or external flow, further increasing the other flow could prevent instability. It was also found that stability is significantly affected by the shape of the free end. Particularly, with a blunt end, internal flow is dominant, and although flutter occurs at high flow rates, increasing the external flow velocity might potentially stabilize the system. In scenarios involving a more streamlined end-piece, the dynamics becomes more complicated, involving both static and dynamic instabilities.

Besides curiosity-driven research, research into the dynamics of pipes under concurrent internal and external axial flows has also been driven by specific engineering applications. This includes attempts to model the dynamics of heat-exchangers and boiler internals [30, 31]. Also, some studies were conducted directed towards understanding the dynamics of the hydraulically powered drill-string system; some of the early work on this, by Bailey and Finnie [32], Finnie and Bailey [33] and Den Hartog [34], dates back to the 1960s.

Later, the stability of long vertical cantilevered pipes subjected to counter-current internal and external axial flows was studied by Luu [35]. This study involved interdependent internal and external axial flows, i.e. the fluid exiting the pipe flowed upwards through the annular region between the pipe and a rigid outer tube surrounding the pipe.

Another important study, modelling the drill-string system with a floating fluid-powered drill-bit, was conducted by Païdoussis et al. [6]. The pipe was subjected to counter-current and interdependent internal and annular flows, a flow configuration similar to that of Luu

[35]. It was shown that in a system with a slight or moderate degree of annular confinement, internal flow governs the dynamics and the system loses stability via flutter. In relatively more confined systems, the annular flow dominates the dynamics, leading to flutter at relatively lower flow velocities.

Dynamics of a hanging pipe conveying fluid upwards and subjected to counter-current and interdependent annular flow, i.e. the system studied in [6, 35] but with the reverse flow configuration, was examined by Qian et al. [36]. It was concluded that, depending upon the system parameters, both flutter or divergence may materialize. In particular, a system with a relatively tightly confined external annular flow loses stability via static divergence rather than flutter. Later on, the dynamics of the system with both conventional flow (as in Païdoussis and et al. [6]) and reverse flow (as in Qian et al. [36]) was studied by Fujita and Moriasa [37].

Another engineering application motivating research on pipes simultaneously subjected to internal and external axial flows is that of brine-strings in salt-mined caverns. The McGill Fluid-Structure Interactions research group has been conducting comprehensive fundamental research on this, in order to systematically explore the different aspects of the dynamics of this system, theoretically, experimentally, and via Computational Fluid Dynamics (CFD) models [4, 8, 10, 38–45]. It is evident from these studies that the complexity of the dynamics of this system is considerable.

The model developed by Païdoussis et al. [6] was modified in Moditis [46] and Moditis et al. [4] to take the discontinuity in the external flow confinement into account; thereby, developing a model for a system with confined external axial flow only over the upper segment of the pipe through a co-axial shorter outer rigid cylindrical tube. Additionally, the dynamics of the system was studied experimentally in a bench-top-sized apparatus. For parameters corresponding to the bench-top system, numerical results predicted that the system undergoes an oscillatory instability. For the full-scale system, however, attempts to tackle the problem of a brine-string of length $L > 450$ m, using the conventional Galerkin technique, were not successful. For $L < 450$, the model predicted static divergence (buckling) , but at unrealistically high flow velocities. For $L > 450$, implementing an asymptotic analysis based on the work of Doaré and de Langre [47] and of de Langre et al. [48] resulted again in estimating an unrealistically high critical flow velocity. Later, Kontzialis et al. [49] studied the same system via a numerical approach, obtaining results that closely align with the bench-top experimental data.

Thereafter, Abdelbaki et al. [39] extended the model developed by Moditis et al. [4] to derive a weakly-nonlinear model. For the parameters pertinent to the bench-top-scale system, at sufficiently high flow rates, a Hopf bifurcation leading to limit-cycle oscillations was predicted.

Minas and Païdoussis [8] examined the dynamics of the system studied by Moditis et al. [4], but with independent internal and external flows, to investigate the effect of higher external-to-internal flow velocity ratios. For the same system, Chehreghani et al. [43] examined the effect of the confinement length, as well as the post-instability dynamics and impacting of the pipe on the shorter coaxial outer rigid tube. Later, Chehreghani et al. [10] conducted a systematic experimental parametric study to explore the influence of the main system parameters: annular confinement (annular gap size), slenderness and material of the pipe, eccentricity between the pipe and the outer cylindrical rigid tube, and flow obstruction at the inlet/outlet of the annular region, for various external-to-internal flow velocity ratios.

Other researchers have also studied the dynamics of the system involving a reversed flow direction, where the pipe aspirates and the annulus discharges fluid [41, 44, 45]. These studies are not discussed here for the sake of brevity.

A fuller review of the studies on pipes subjected to counter-current external and internal flows may be found in [9, 40]. Nevertheless, from the forgoing literature survey one can conclude that the analytical model in these studies has not been successful in predicting critical flow velocities in real, full-scale systems, despite being successful in predicting them in the bench-top laboratory system. For instance, the results obtained by Moditis et al. [4] via an asymptotic approach suggest a critical internal flow velocity greater than 20 m/s (in some cases greater than 50 m/s), while the case histories presented in Ratigan (2008) [1] for real-world applications indicate that several brine-strings have experienced failure at considerably lower flows. Additionally, the Moditis [46] and Moditis et al. work [4] fails to tackle the problem involving long pipes ($L > 450$), typically found in full-scale systems.

In the models developed to-date, the presence of fluids of different densities as well as the product pressure at the well-head were ignored. In an attempt to obtain a more realistic prediction of critical flow velocities for full-scale systems, we eliminate these simplifications in this paper, and develop a linear analytical model for the system shown in Fig. 6.2(b). The system parameters used to obtain the numerical results obtained in the present paper, were selected in consultation with salt-cavern operators, thus ensuring relevance. The purpose of this study is to predict safe ranges of flow rates in brine-strings operating in the retrieval mode, so as to prevent fluid-elastic instabilities causing catastrophic failures and thus avoid the attendant financial and ecological repercussions.

The rest of the paper is structured as follows. Detailed derivation of the theoretical model is presented in Section 6.2. Numerical results and pertinent discussion are presented in Section 6.3. The influence of the main brine-string system parameters on the dynamics is discussed in Section 6.4. Finally, Section 6.5 is devoted to the concluding remarks.

6.2 Model development

6.2.1 Derivation of the equation of motion

In the present study, following the formulations in [4] and [6] with modifications in the external flow modelling, a linear theoretical model for the dynamics of the brine string system, shown schematically in Fig. 6.2, is derived.

An idealized model of the brine-string in salt-mined caverns in the retrieval mode can be described as follows. A flexible hanging cantilevered pipe of length L, inner diameter D_i, and outer diameter D_o, is located at the centre of the cavern; refer to Fig. 6.2(b). The pipe is confined at its upper portion by a rigid outer tube (cemented casing) of length L' and diameter D_{ch}. The pipe discharges brine with density ρ_b and viscosity μ_b downwards into the cavern with velocity U_i. This generates a partially confined external axial flow of the product (of density ρ_p, and viscosity μ_p) with flow velocity U_o upwards in the annulus. Below the confined region, the pipe is immersed in the product down to a level L'', below which the pipe is immersed in brine.

Let the x-axis be the axial coordinate, along the undeformed state of the central pipe, as shown in Fig. 6.2(b), with origin at its fixed end, while the z-axis is in the lateral direction. Considering small deflections, a balance of forces acting on an element of the deformed pipe shown in Fig. 6.4(a) yields

$$\frac{\partial T}{\partial x} - \frac{\partial}{\partial x}\Big(Q\frac{\partial w}{\partial x}\Big) + M_t g - (F_{in} + F_{en})\frac{\partial w}{\partial x} + F_{it} - F_{et} = 0, \tag{6.1}$$

$$\frac{\partial}{\partial x}\Big(T\frac{\partial w}{\partial x}\Big) + \frac{\partial Q}{\partial x} - M_t\frac{\partial^2 w}{\partial t^2} + F_{in} + F_{en} + (F_{it} - F_{et})\frac{\partial w}{\partial x} = 0, \tag{6.2}$$

where T is the tension in the pipe, Q denotes the transverse shear force, w is the lateral displacement of the pipe, M_t is the pipe mass per unit length, g is the gravitational acceleration, and t is the time; F_{it} and F_{in} are the tangential and normal hydrodynamic forces on the pipe due to the internal flow, while F_{et} and F_{en} are those due to the external flow.

Making use of the classical Euler-Bernoulli beam theory, denoting the flexural rigidity of the central pipe by EI, the transverse shear force is given by

$$Q = -\frac{\partial}{\partial x}\Big(EI\frac{\partial^2 w}{\partial x^2}\Big). \tag{6.3}$$

In Eq. (6.3), the material damping in the pipe has been neglected, as the flow-induced damping is considerably more significant [6, 50, 51].

The normal and tangential forces associated with the internal flow, F_{in} and F_{it}, can be obtained via Païdoussis' approach [52], by a balance of the forces acting on an element δx of the internal fluid, shown in Fig. 6.4(b), in the x- and z-directions, yielding

$$F_{it} - F_{et}\frac{\partial w}{\partial x} = M_{fi}g - \frac{\partial}{\partial x}(A_i p_i), \tag{6.4}$$

$$-\Big(F_{in} + F_{it}\frac{\partial w}{\partial x}\Big) = M_{fi}\Big(\frac{\partial}{\partial t} + U_i\frac{\partial}{\partial x}\Big)^2 w + \frac{\partial}{\partial x}(A_i p_i\frac{\partial w}{\partial x}), \tag{6.5}$$

where $M_{fi} = \rho_b A_i$, in which ρ_b is the density of the fluid in the pipe (brine) and $A_i = (\pi/4)D_i^2$. Also, p_i is the pipe internal pressure, and $\big(\frac{\partial}{\partial t} + U_i\frac{\partial}{\partial x}\big)^2$ stands for repeated application of the operator in the parentheses.

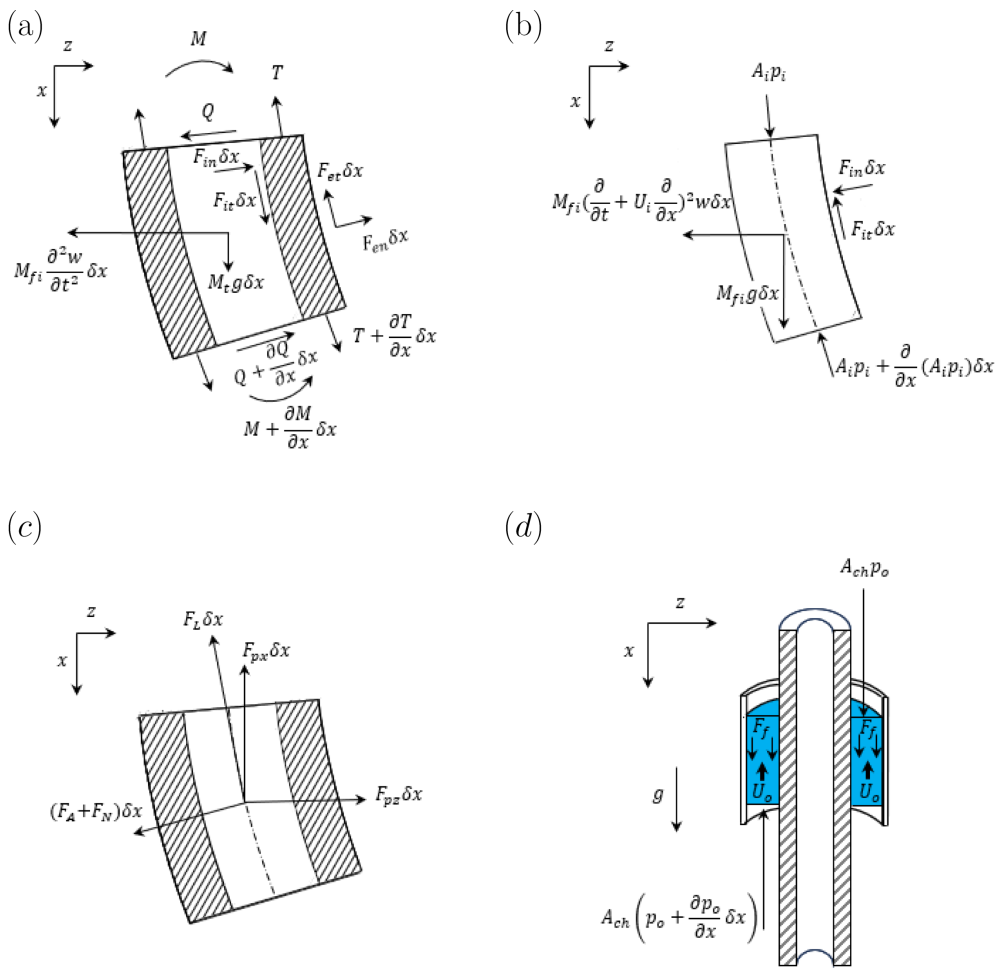

Figure 6.4: Schematic views showing (a) forces acting on an element δx of the deformed pipe; (b) forces acting on an element δx of the internally flowing fluid; (c) forces acting on an element δx of the externally flowing fluid; (d) forces acting on an annular fluid element of length δx.

Substitution of Eqs. (6.4) and (6.5) into Eqs. (6.1) and (6.2) and using Eq. (6.3) results in the following expressions for the forces in the x- and z-directions:

$$\frac{\partial T}{\partial x} + M_t g + \left[M_{fi} g - \frac{\partial}{\partial x}(A_i p_i)\right] - F_{en}\frac{\partial w}{\partial x} - F_{et} = 0, \tag{6.6}$$

$$\begin{aligned} EI\frac{\partial^4 w}{\partial x^4} - \frac{\partial}{\partial x}(T\frac{\partial w}{\partial x}) + M_t\frac{\partial^2 w}{\partial t^2} + \left[M_{fi}(\frac{\partial}{\partial t} + U_i\frac{\partial}{\partial x})^2 w + \frac{\partial}{\partial x}(A_i p_i\frac{\partial w}{\partial x})\right] - F_{en} \\ + F_{et}\frac{\partial w}{\partial x} = 0. \end{aligned} \tag{6.7}$$

For small lateral displacements, it is presumed that the inviscid hydrodynamic forces are predominant. Hence, the external flow-field can be simplified: the inviscid and viscous hydrodynamic forces associated with the external flow can be obtained separately, rather than by direct usage of the Navier-Stokes equations. To this end, (i) the inviscid hydrodynamic forces are derived by modelling the flow as the superposition of the perturbations caused by lateral vibrations of the pipe in the mean inviscid axial flow [53], and (ii) the viscosity-related forces are added to the system separately. This approach has been proven to provide acceptable results. For a detailed discussion on this, the interested reader in referred to [52].

Fig. 6.4(c) shows the external flow-related forces acting on an element of the pipe: the lateral inviscid hydrodynamic force, F_A, the frictional normal and longitudinal viscous forces, F_N and F_L, respectively, and the hydrostatic forces in the x- and z-direction, F_{px} and F_{pz}, respectively. Projection of these forces in the x- and z-direction, while retaining terms up to first-order, leads to

$$-F_{en}\frac{\partial w}{\partial x} - F_{et} = -F_L - F_{px}, \tag{6.8}$$

$$-F_{en} + F_{et}\frac{\partial w}{\partial x} = (F_A + F_N) - F_{pz} + F_L\frac{\partial w}{\partial x}. \tag{6.9}$$

For a thin boundary layer and by means of potential flow theory, the added mass per unit length associated with the acceleration of the external flow due to pipe motion can be expressed [54] as follows: $M_o = \chi\rho_p A_0$, for $0 < x < L'$, $M_o = \rho_p A_0$, for $L' < x < L''$ and $M_o = \rho_b A_0$, for $L'' < x < L$; where $A_o = \pi D_o^2/4$, $\chi = (D_{ch}^2 + D_o^2)/(D_{ch}^2 - D_o^2)$ is a parameter associated with the degree of confinement of the flow passing through the annular gap, and ρ_p is the density of the product. Denoting by $r_\rho = \rho_b/\rho_p$ the brine/product density ratio, the following expression is obtained for the added mass:

$$M_o = \rho_p A_o\big[\chi + (1-\chi)H(x-L') + (r_\rho - 1)H(x-L'')\big], \tag{6.10}$$

where $H(x-L')$ and $H(x-L'')$ are the Heaviside step functions.

The relative fluid-body velocity is defined as follows:

$$\mathrm{V}_{\mathrm{rel}} = \big(\frac{\partial u}{\partial t} - U_o(x)\big)\hat{\imath} + \frac{\partial w}{\partial t}\hat{\jmath}, \tag{6.11}$$

where u and w are displacements in the x- and z-direction, respectively. The two components of velocity in the longitudinal and normal directions are

$$u_L = \big[\frac{\partial u}{\partial t} - U_o(x)\big]\cos(\theta) + \frac{\partial w}{\partial t}\sin(\theta) \approx \frac{\partial u}{\partial t} - U_o(x), \tag{6.12}$$

$$u_N = -\big[\frac{\partial u}{\partial t} - U_o(x)\big]\sin(\theta) + \frac{\partial w}{\partial t}\cos(\theta) \approx U_o(x)\frac{\partial w}{\partial x} + \frac{\partial w}{\partial t}. \tag{6.13}$$

The inviscid force per unit length in the transverse direction can be written as [55]

$$F_A = M_o\Big[\frac{\partial u_N}{\partial t} - \frac{\partial}{\partial x}(u_N u_L)\Big]. \tag{6.14}$$

Substituting Eqs. (6.12) and (6.13) into Eq. (6.14), retaining only first-order terms, and assuming that the external flow velocity vanishes over the unconfined portion of the pipe, $x > L'$, hence $U_o(x) = -U_o\big[1 - H(x - L')\big]$, results in

$$\begin{aligned} F_A = {} & \rho_p A_o\big[\chi + (1-\chi)H(x-L') + (r_\rho - 1)H(x - L'')\rho\big]\frac{\partial^2 w}{\partial t^2} \\ & + 2U_o\chi\rho_p A_o\big[H(x-L') - 1\big]\frac{\partial^2 w}{\partial x \partial t} + \chi\rho_p A_o U_o^2\big[1 - H(x-L')\big]\frac{\partial^2 w}{\partial x^2}, \end{aligned} \tag{6.15}$$

where the terms on the right-hand side are associated with inertia, Coriolis and centrifugal forces, respectively.

Based on the semi-empirical formulas of Taylor [56], further developed in [54], the viscous forces in the longitudinal and normal directions, as modified for the problem at hand, are

$$F_L = \frac{1}{2}\rho_p D_o C_T U_o^2\big[1 - H(x-L')\big], \tag{6.16}$$

$$F_N = \frac{1}{2}\rho_p D_o C_N U_o\Big\{\big[1 - H(x-L')\big]\frac{\partial w}{\partial t} - U_o\big[1 - H(x-L')\big]\frac{\partial w}{\partial x}\Big\} + k\frac{\partial w}{\partial t}, \tag{6.17}$$

where C_T and C_N are the friction coefficients in the longitudinal and normal direction, respectively. The viscous-drag coefficient, k, is associated to lateral motion of the cylinder in quiescent fluid (with no mean external flow).

Supposing that the assumption of a thin boundary layer holds, based on a two-dimensional flow analysis, the expression for k in Eq. (6.17) can be adopted from Chen et al. [50], Sinyavskii et al. [57] and Moditis et al. [4], yielding

$$k = k_{up}\Big\{\frac{1+\bar{\gamma}^3}{(1-\bar{\gamma}^2)^2}\big[1-H(x-L')\big] + \big[H(x-L')-H(x-L'')\big] + r_\rho\sqrt{\frac{\nu_b}{\nu_p}}H(x-L'')\Big\}, \tag{6.18}$$

where, ν_b and ν_p are the kinematic viscosities of the brine and product, respectively. As in Ref. [57], $k_{up} = 2\sqrt{2}\rho_p A_0 \,\mathrm{Re}(\Omega)/\sqrt{\tilde{s}}$, in which $\mathrm{Re}(\Omega)$ denotes the real part of the radian frequency of oscillations, $\tilde{s} = \mathrm{Re}(\Omega)D_o^2/(4\nu_p)$, and $\bar{\gamma} = D_o/D_{ch}$.

For the hydrostatic forces, we adopt the expressions derived in [54]. The hydrostatic forces in the x- and z-directions are given as follows:

$$F_{px} = -\frac{\partial}{\partial x}(A_o p_o) + A_o\frac{\partial p_o}{\partial x}, \tag{6.19}$$

$$F_{pz} = A_o\frac{\partial}{\partial x}(p_o\frac{\partial w}{\partial x}). \tag{6.20}$$

Inside the annulus, the pressure variation is associated with friction and gravity. Below the annulus, the pressure loss due to friction is negligible. Therefore, the pressure distribution below the annulus is assumed to be hydrostatic. Also, for the fluid entering the annular region, the influence of the entrance is assumed to be confined to an infinitesimally short region in the vicinity of $L'^- < x < L'^+$.

Considering the forces acting on an annular fluid element, as shown in Fig. 6.4(d), for $0 < x < L'$ one can write

$$-A_{ch}\frac{\partial p_o^{(1)}}{\partial x} + F_f + A_{ch}\rho_p g = 0, \tag{6.21}$$

in which $p_o^{(1)}$ is the pressure distribution within the annulus, and F_f is the total annular friction force acting on the annular flow element of cross-sectional area $A_{ch} = \pi\big(D_{ch}^2 - D_o^2\big)/4$.

It can be presumed that the wall shear stresses acting on the inner and outer annular surfaces are equal. Consequently, $F_f/S_{tot} = F_L^{(1)}/S_o$, where $S_{tot} = \pi(D_{ch}+D_o)$ and $F_L^{(1)} = \frac{1}{2}\rho_p D_o C_T U_o^2$. Hence,

$$F_f = \frac{S_{tot}}{S_o}F_L^{(1)}. \tag{6.22}$$

Substituting Eq. (6.22) into Eq. (6.21), one obtains

$$-A_{ch}\frac{\partial p_o^{(1)}}{\partial x} + \frac{S_{tot}}{S_o}F_L^{(1)} + A_{ch}\rho_p g = 0.$$

Denoting the hydraulic diameter by $D_h = D_{ch} - D_o$, the pressure gradient within the annulus ($0 \leq x < L'$) simplifies to

$$A_o\frac{\partial p_o^{(1)}}{\partial x} = F_L^{(1)}\Big(\frac{D_o}{D_h}\Big) + A_o\rho_p g. \tag{6.23}$$

Integrating Eq. (6.23) yields

$$p_o^{(1)}(x) = \Big[\frac{F_L^{(1)}}{A_o}\Big(\frac{D_o}{D_h}\Big) + \rho_p g\Big]x + p_o|_{x=0}, \tag{6.24}$$

which is the external pressure distribution for $0 < x < L'$, where $p_o|_{x=0}$ is the product pressure at the well-head ($x = 0$).

Since it is assumed that the pressure distribution below the annulus is hydrostatic, for $L' < x < L''$ one can write

$$\frac{\partial p_o^{(2)}}{\partial x} = \rho_p g, \tag{6.25}$$

where $p_o^{(2)}$ is the external pressure distribution in the region below the annulus and above the interface level. Integrating Eq. (6.25) yields

$$p_o^{(2)}(x) = \rho_p g x + c_1. \tag{6.26}$$

The constant of integration, c_1, is determined next. Considering the head loss associated with the fluid entering the annular region at $x = L'$, one can write

$$p_o^{(2)}|_{x=L'^+} = \tfrac{1}{2}\rho U_o^2 + p_o^{(1)}|_{x=L'^-} + \rho g h_1, \tag{6.27}$$

where $h_1 = (K_1 U_o^2)/(2g)$ is the head-loss due to the sudden contraction for the fluid entering the annular region, in which K_1 is 0.8-0.9 for the problem at hand [58].

Combining Eqs. (6.24), (6.26) and (6.27), the constant c_1 is found to be

$$c_1 = \tfrac{1}{2}\rho_p U_o^2 + \frac{F_L^{(1)}}{A_o}\Big(\frac{D_o}{D_h}\Big)L' + \rho_p g h_1 + p_o|_{x=0}. \tag{6.28}$$

Substituting Eq. (6.28) into Eq. (6.26), the pressure in the region $L' < x < L''$ can be written as follows:

$$p_o^{(2)}(x) = \rho_p g x + \tfrac{1}{2}\rho U_o^2 + \frac{F_L^{(1)}}{A_o}\Big(\frac{D_o}{D_h}\Big)L' + \rho_p g h_1 + p_o|_{x=0}. \tag{6.29}$$

The hydrostatic pressure distribution for $L'' < x < L$ is governed by

$$\frac{\partial p_o^{(3)}}{\partial x} = \rho_b g, \tag{6.30}$$

where $p_o^{(3)}$ is the external pressure distribution below the interface level, which upon integration yields

$$p_o^{(3)}(x) = \rho_b g x + c_2. \tag{6.31}$$

The constant c_2 can be found by equating the pressure obtained at the interface level ($x = L''$) using Eqs. (6.29) and (6.31). This leads to the following expression for the pressure in the region $L'' < x \leq L$:

$$p_o^{(3)}(x) = \rho_p g x + \rho_p(r_\rho - 1)g(x - L'') + \frac{F_L^{(1)}}{A_o}\Big(\frac{D_o}{D_h}\Big)L' + \frac{1}{2}\rho_p U_o^2 + \rho_p g h_1 + p_o|_{x=0}. \tag{6.32}$$

Hence, in view of Eqs. (6.24), (6.29) and (6.32), the external pressure can be written as

$$\begin{aligned} p_o(x) = {} & \frac{F_L^{(1)}}{A_o}\Big(\frac{D_o}{D_h}\Big)x - \frac{F_L^{(1)}}{A_o}\Big(\frac{D_o}{D_h}\Big)(x - L')H(x - L') \\ & + \big[\frac{1}{2}\rho_p U_o^2 + \rho_p g h_1\big]H(x - L') + p_o|_{x=0} \\ & + \rho_p g x + \rho_p(r_\rho - 1)g(x - L'')H(x - L''). \end{aligned} \tag{6.33}$$

The external pressure gradient is

$$\begin{aligned} \frac{\partial p_o}{\partial x} = {} & \frac{F_L^{(1)}}{A_o}\Big(\frac{D_o}{D_h}\Big)(1 - H(x - L')) + \big[\frac{1}{2}\rho U_o^2 + \rho_p g h_1\big]\delta_D(x - L') \\ & + \rho_p g + \big[\rho_p(r_\rho - 1)g\big]H(x - L''), \end{aligned} \tag{6.34}$$

where $\delta_D(x - L')$ is the Dirac delta function.

Note that the well-head pressure, $p_o|_{x=0}$, is governed by regulation, assuring that the product will not hydraulically fracture the salt formation right below the casing shoe [59]. More specifically, regulations restrict the product pressure at the casing shoe depth, $p_o|_{x=L'}$, to not exceed a value, cr, times L'. Hence, $p_o|_{x=L'} \leq crL'$. Typically, $cr = 0.7 - 0.9$ psi/ft ($\simeq$ 16,000-20,000 Pa/m). Evaluating the right-hand side of Eq. (6.29), one can obtain the maximum allowable pressure at the well-head, $p_{o,\max}|_{x=0}$. An upper bound for the maximum allowable pressure is obtained at zero external flow velocity, and therefore, from Eq. (6.29):

$$p_{o,\max}|_{x=0} \leq (cr - \rho_p g)L'. \tag{6.35}$$

Substituting Eqs. (6.16) and (6.19) into Eq. (6.8) and subsequently Eq. (6.8) into Eq. (6.6) results in

$$\frac{\partial}{\partial x}(T - A_i p_i + A_o p_o) + M_t g + M_{fi} g - A_o \frac{\partial p_o}{\partial x} - \frac{1}{2}\rho_p D_o C_T U_o^2 \big[1 - H(x - L')\big] = 0. \tag{6.36}$$

The tensioning and pressurization term, $(T - A_i p_i + A_o p_o)$, can be determined by integrating Eq. (6.36) from x to L, yielding

$$\begin{aligned}(T - A_i p_i + A_o p_o) =&(M_t + M_{fi} - \rho_p A_o) g (L - x) \\ &- \frac{1}{2}\rho_p D_o C_T U_o^2 \Big(\frac{D_o}{D_h} + 1\Big)(L' - x)\big[1 - H(x - L')\big] \\ &- A_o\big(\frac{1}{2}\rho_p U_o^2 + \rho_p g h_1\big)\big[1 - H(x - L')\big] \\ &+ A_o \rho_p (r_\rho - 1) g (x - L'') H(x - L'') \\ &- A_o \rho_p (r_\rho - 1) g (L - L'') + (T - A_i p_i + A_o p_o)|_{x=L},\end{aligned} \tag{6.37}$$

in which, via an energy balance for the fluid at $x = L$, the external pressure at the tip of the pipe, $p_o|_{x=L}$, and the internal pressure at the tip, $p_i|_{x=L}$, are related to each other through

$$p_i|_{x=L} = p_o|_{x=L} - \frac{\rho_b U_i^2}{2} + \rho_b g h_2, \tag{6.38}$$

where $h_2 = (K_2 U_i^2)/(2g)$, with $K_2 = 1$, is the head-loss associated with the sudden enlargement (expansion) of the internal flow into the surrounding fluid [58]. Also, $p_o|_{x=L}$ can be computed by evaluating Eq. (6.33) at $x = L$, which yields

$$\begin{aligned}p_o|_{x=L} =&\frac{1}{2A_o} C_T \rho_p D_o U_o^2 \Big(\frac{D_o}{D_h}\Big) L' + \frac{1}{2}\rho_p U_o^2 + \rho_p g h_1 + p_o|_{x=0} + \rho_p g r_\rho L \\ &+ \rho_p g L''(1 - r_\rho).\end{aligned} \tag{6.39}$$

6.2.2 The equation of motion

Substitution of Eqs. (6.15), (6.16), (6.17) and (6.20) into Eq. (6.9), subsequent substitution of the result into Eq. (6.7) and use of Eq. (6.37) results in the equation of motion in the z-direction:

$$\begin{aligned}
&EIw'''' + \Big\{\big(M_t + M_{fi} - \rho_p A_o\big)g - \frac{1}{2}\rho_p D_o C_T U_o^2\Big(\frac{D_o}{D_h}+1\Big)\big[1 - H(x-L')\big] \\
&- A_o\big(\frac{1}{2}\rho_p U_o^2 + \rho_p g h_1\big)\delta_D(x-L') - A_o\rho_p(r_\rho - 1)gH(x-L'')\Big\}w' \\
&+ \Big\{\big(-M_t - M_{fi} + \rho_p A_o\big)g(L-x) + \frac{1}{2}\rho_p D_o C_T U_o^2\Big(\frac{D_o}{D_h}+1\Big)(L'-x)\big[1-H(x-L')\big] \\
&+ A_o\big(\frac{1}{2}\rho_p U_o^2 + \rho_p g h_1\big)\big[1-H(x-L')\big] - A_o\rho_p(r_\rho-1)g(x-L'')H(x-L'') \\
&+ A_o\rho_p(r_\rho-1)g(L-L'') - (T - A_i p_i + A_o p_o)|_{x=L}\Big\}w'' + M_t\ddot{w} + M_{fi}\ddot{w} \\
&+ 2U_i M_{fi}\dot{w}' + M_{fi}U_i^2 w'' + \rho_p A_o\Big[\chi + (1-\chi)H(x-L') + (r_\rho - 1)H(x-L'')\Big]\ddot{w} \\
&- 2U_o\chi\rho_p A_o\big[1-H(x-L')\big]\dot{w}' + U_o^2\chi\rho_p A_o\big[1-H(x-L')\big]w'' \\
&+ \frac{1}{2}\rho_p D_o C_N U_o\big[1-H(x-L')\big]\dot{w} - \frac{1}{2}\rho_p D_o C_N U_o^2\big[1-H(x-L')\big]w' \\
&+ k_{up}\Big\{\frac{1+\bar{\gamma}^3}{(1-\bar{\gamma}^2)^2}\big[1-H(x-L')\big] + \big[H(x-L') - H(x-L'')\big] + r_\rho\sqrt{\frac{\nu_b}{\nu_p}}H(x-L'')\Big\}\dot{w} \\
&+ \frac{1}{2}\rho_p D_o C_T U_o^2\big[1-H(x-L')\big]w' = 0,
\end{aligned} \tag{6.40}$$

where $(\ )' = \partial(\ )/\partial x$, $\dot{(\ )} = \partial(\ )/\partial t$, and $p_i|_{x=L}$ and $p_0|_{x=L}$ can be found using Eqs. (6.38) and (6.39).

The associated boundary conditions are the classical ones for a clamped-free beam:

$$w|_{x=0} = w'|_{x=0} = w''|_{x=L} = w'''|_{x=L} = 0. \tag{6.41}$$

The relationship between the internal and external flow velocities can be obtained through conservation of mass, that is

$$U_o = \frac{D_i^2}{D_{ch}^2 - D_o^2} r_\rho U_i. \tag{6.42}$$

6.2.3 The non-dimensional equation of the motion

Eq. (6.40) may be rendered dimensionless through the use of the following dimensionless parameters:

$$
\begin{aligned}
&\xi = \frac{x}{L}, \quad \eta = \frac{w}{L}, \quad \tau = \Big(\frac{EI}{M_t + M_{fi} + \rho_p A_o}\Big)^{1/2}\frac{t}{L^2}, \quad u_i = \Big(\frac{M_{fi}}{EI}\Big)^{1/2} L U_i,\\
&u_o = \Big(\frac{\rho_p A_o}{EI}\Big)^{1/2} L U_o, \quad \beta_i = \frac{M_{fi}}{M_t + M_{fi} + \rho_p A_o}, \quad \beta_o = \frac{\rho_p A_o}{M_t + M_{fi} + \rho_p A_o},\\
&\gamma = \frac{(M_t + M_{fi} - \rho_p A_o) g L^3}{EI}, \quad \Gamma = \frac{T|_{x=L} L^2}{EI}, \quad c_N = \frac{4}{\pi} C_N, \quad c_T = \frac{4}{\pi} C_T,\\
&\gamma_p = \frac{A_o \rho_p g L^3}{EI}, \quad r_{ann} = \frac{L'}{L}, \quad r_{if} = \frac{L''}{L}, \quad \alpha = \frac{D_i}{D_o}, \quad \alpha_{ch} = \frac{D_{ch}}{D_o},\\
&\Pi_{iL} = \frac{A_i p_i|_{x=L} L^2}{EI}, \quad \Pi_{oL} = \frac{A_o p_o|_{x=L} L^2}{EI}, \quad h = \frac{D_o}{D_h},\\
&\kappa_{up} = \frac{k_{up} L^2}{[EI(M_t + M_{fi} + \rho A_o)]^{1/2}}, \quad \varepsilon = \frac{L}{D_o}, \quad \omega = \Big(\frac{M_t + M_{fi} + \rho_p A_o}{EI}\Big)^{1/2} L^2 \Omega.
\end{aligned}
\tag{6.43}
$$

The dimensionless equation of motion is

$$
\begin{aligned}
&\eta'''' + \Big\{\gamma - \frac{1}{2}\varepsilon c_T u_o^2 (1+h)\big[1 - H(\xi - r_{ann})\big] - \big[\frac{1}{2}u_o^2(1+K_1)\big]\delta_D(\xi - r_{ann})\\
&\quad - \gamma_p (r_\rho - 1) H(\xi - r_{if})\Big\}\eta' + \Big\{ -\gamma(1-\xi) + \frac{1}{2}\varepsilon c_T u_o^2(1+h)(r_{ann} - \xi)\big[1 - H(\xi - r_{ann})\big]\\
&\quad + \frac{1}{2}u_o^2(K_1 + 1)\big[1 - H(\xi - r_{ann})\big] + \gamma_p (r_\rho - 1)(r_{if} - \xi) H(\xi - r_{if})\\
&\quad + \gamma_p (r_\rho - 1)(1 - r_{if}) - (\Gamma - \Pi_{iL} + \Pi_{oL})\Big\}\eta'' + \Big\{1 + \beta_o(\chi - 1)\big[1 - H(\xi - r_{ann})\big]\\
&\quad + \beta_o (r_\rho - 1) H(\xi - r_{if})\Big\}\ddot{\eta} + 2\Big\{u_i\sqrt{\beta_i} - u_o\sqrt{\beta_o}\chi\big[1 - H(\xi - r_{ann})\big]\Big\}\dot{\eta}' + \Big\{u_i^2\\
&\quad + \chi u_o^2\big[1 - H(\xi - r_{ann}\big]\Big\}\eta'' + \frac{1}{2}c_N \varepsilon u_o \sqrt{\beta_o}\big[1 - H(\xi - r_{ann})\big]\dot{\eta}\\
&\quad + \kappa_{up}\Big\{\frac{1 + \alpha_{ch}^{-3}}{(1 - \alpha_{ch}^{-2})^2}\big[1 - H(x - L')\big] + \big[H(x - L') - H(x - L'')\big]\\
&\quad + r_\rho \sqrt{\frac{\nu_b}{\nu_p}} H(x - L'')\Big\}\dot{\eta} - \frac{1}{2}(c_N - c_T)\varepsilon u_o^2\big[1 - H(\xi - r_{ann})\big]\eta' = 0,
\end{aligned}
\tag{6.44}
$$

where $(\ )' = \partial(\ )/\partial\xi$, $\dot{(\ )} = \partial(\ )/\partial\tau$. Also, making use of Eqs. (6.38), (6.39) and (6.43), the values Π_{iL} and Π_{oL} can be related to each other as follows:

$$
\Pi_{iL} = \alpha^2 \Pi_{oL} - \frac{1}{2}u_i^2 + \frac{A_i \rho_b g h_2 L^2}{EI},
\tag{6.45}
$$

where

$$\Pi_{oL} = \frac{1}{2}c_T h r_{ann}\varepsilon u_o^2 + \Pi_{o0} + \frac{1}{2}u_o^2(1+K_1) + \gamma_p r_\rho + \frac{A_o\rho_p(1-r_\rho)gL''L^2}{EI}, \tag{6.46}$$

in which $\Pi_{o0} = (A_o p_o|_{x=0}L^2)/EI$.

The associated clamped-free boundary conditions in dimensionless form are

$$\eta|_{\xi=0} = \eta'|_{\xi=0} = \eta''|_{\xi=1} = \eta'''|_{\xi=1} = 0. \tag{6.47}$$

Finally, the relationship between the internal and external flow velocities in dimensionless form is

$$u_o = \frac{\alpha}{\alpha_{ch}^2 - 1}\sqrt{r_\rho}u_i. \tag{6.48}$$

6.2.4 Solution procedure

Making use of Galerkin's modal decomposition technique, the dimensionless equation of the motion, i.e. Eq. (6.44), can be discretized. Let $\tilde{\eta}(\xi,\tau)$ be an approximate solution, and one can write

$$\eta(\xi,\tau) \approx \tilde{\eta}(\xi,\tau) = \sum_{j=1}^{N}\phi_j(\xi)q_j(\tau), \tag{6.49}$$

in which $\phi_j(\xi)$ are appropriate comparison functions satisfying both essential and natural boundary conditions of the problem, in this case the normalized cantilevered Euler-Bernoulli beam eigenfunctions; $q_j(\tau)$ are the corresponding generalized coordinates. N in the truncated series denotes the number of modes in the Galerkin scheme approximation. Substituting Eq. (6.49) into Eq. (6.44), multiplying by $\phi_i(\xi)$ and subsequently integrating over the normalized domain, i.e. from $\xi = 0$ to $\xi = 1$, a set of N ordinary differential equations are obtained, which may be written in matrix form as follows:

$$\mathbf{M}\ddot{\mathbf{q}} + \mathbf{C}\dot{\mathbf{q}} + \mathbf{K}\mathbf{q} = \mathbf{0}, \tag{6.50}$$

where $\mathbf{M}$, $\mathbf{C}$ and $\mathbf{K}$ are the mass, damping and stiffness matrices, respectively, expressions for which are given in the Appendix; $\mathbf{q}$=$\{q_1, q_2, ..., q_N\}^T$, $\dot{\mathbf{q}}$=d$\mathbf{q}$/dτ and $\ddot{\mathbf{q}}$=d$\dot{\mathbf{q}}/d\tau$.

Eq. (6.50), involves the following integrals:

$$\begin{aligned} a_{ij}(a,b) &= \int_a^b \phi_i\phi_j d\xi, \quad b_{ij}(a,b) = \int_a^b \phi_i\phi_j' d\xi, \\ c_{ij}(a,b) &= \int_a^b \phi_i\phi_j'' d\xi, \quad d_{ij}(a,b) = \int_a^b \xi\phi_i\phi_j'' d\xi. \end{aligned} \tag{6.51}$$

These integrals may be evaluated in closed form if the limits of integration are 0 and 1, and the values for cantilevered beams may be found for instance in [12]. For other sets of integral limits, however, numerical integration needs to be employed. In this study, the numerical integration was perfumed using the seventh degree Newton–Cotes formula.

Seeking oscillatory solutions, let

$$\mathbf{q} = \mathbf{A}e^{\Lambda\tau}, \tag{6.52}$$

where A is a time-independent complex vector and Λ is a complex number. Substituting Eq. (6.52) in Eq. (6.50) and rearranging the resulting equations yields to the following eigenvalue problem for the state vector of $\mathbf{Z} = \begin{Bmatrix} \mathbf{q} \\ \Lambda\mathbf{q} \end{Bmatrix}$, that is

$$\begin{bmatrix} 0 & \mathbf{I} \\ \mathbf{M^{-1}K} & -\mathbf{M^{-1}C} \end{bmatrix}\mathbf{Z} = \Lambda\mathbf{Z}. \tag{6.53}$$

We express $\Lambda_j = \mathrm{i}\omega_j$, where ω_j is complex eigenfrequency and $\mathrm{i} = \sqrt{-1}$. Solving the eigenvalue problem for incremental internal flow velocities, the stability of the system may be investigated. The imaginary part of the eigenfrequency is associated with damping of the system. If, for a specific u_i, all $\mathrm{Im}(\omega_j) > 0$, the system is stable. If for some value of u_i we obtain $\mathrm{Im}(\omega_j) < 0$, the system is unstable. Thus, at the critical flow velocity $u_i = u_{i,cr}$, we have $\mathrm{Im}(\omega_j) = 0$. The real part of the eigenfrequency is related to the frequency of oscillations. Therefore, if $\mathrm{Im}(\omega_j) < 0$ while $\mathrm{Re}(\omega_j) = 0$, the system undergoes a static divergence (buckling), and if $\mathrm{Im}(\omega_j) < 0$ while $\mathrm{Re}(\omega_j) \neq 0$, the system undergoes flutter (an oscillatory instability), which is associated with a Hopf bifurcation.

To ensure convergence, an increasing number of modes were used in the Galerkin approximation, $N = 20$ up to 26, to achieve convergence in the first ten eigenfrequencies for flow velocities up to the critical, within a margin of less than 2%.

In Section 4, for each set of system parameters, the eigenvalue problem of Eq. (6.53) is solved for incremental flow velocities, and the critical flow velocity obtained is based on the first-detected instability.

Table 6.1: Dimensionless critical flow velocity, $u_{i,cr}$ and the mode of instability for the bench-scale-system parameters. F2: flutter in the second mode

r_{ann}	Ref. [4]	Ref. [39]	Present
$\simeq 1/4$	6.69 (F2)	6.69 (F2)	6.68 (F2)
$\simeq 1/2$	6.47 (F2)	6.44 (F2)	6.44 (F2)
$\simeq 3/4$	6.44 (F2)	6.42 (F2)	6.45 (F2)

6.3 Numerical results and discussion

6.3.1 Validation

The model developed underwent validation against simpler systems available in the literature in which a single fluid in the cavern was considered: (a) a bench-top-scale system subjected to internal and external flow of water; (b) relatively short brine-strings in caverns with water.

6.3.1.1 Bench-top-scale system

Results were obtained for the bench top-scale system parameters as in Moditis et al. [4] and Abdelbaki et al. [39]. The properties and dimensions of this system are as follows. A flexible pipe of length $L = 431$ mm, inner diameter $D_i = 6.35$ mm, outer diameter $D_o = 16$ mm, flexural rigidity $EI = 7.37 \times 10^{-3}$ N m^2 and mass per unit length $M_t = 0.191$ kg/m. Surrounding the upper portion of the flexible pipe, a rigid outer tube of inner diameter $D_{ch} = 31.5$ mm, and three different lengths, namely $L' = 109$ mm, 206.5 mm and 304.5 mm (corresponding to $r_{ann} = 0.253$, 0.479 and 0.706, respectively) were considered. The associated dimensionless parameters are: $\alpha = 0.397$, $\alpha_{ch} = 1.97$, $\beta_i = 7.41 \times 10^{-2}$, $\beta_o = 0.470$, $\gamma = 2.69$, $\varepsilon = 26.9$ and $h = 1.03$.

The critical dimensionless internal flow velocities and the mode of instability predicted by this model are presented in Table 6.1 and they are compared to those reported in [4] and [39]. The results obtained by the present model are in excellent agreement with those of [4, 39].

Fig. 6.5 shows a typical Argand diagram obtained via the present model for the bench-

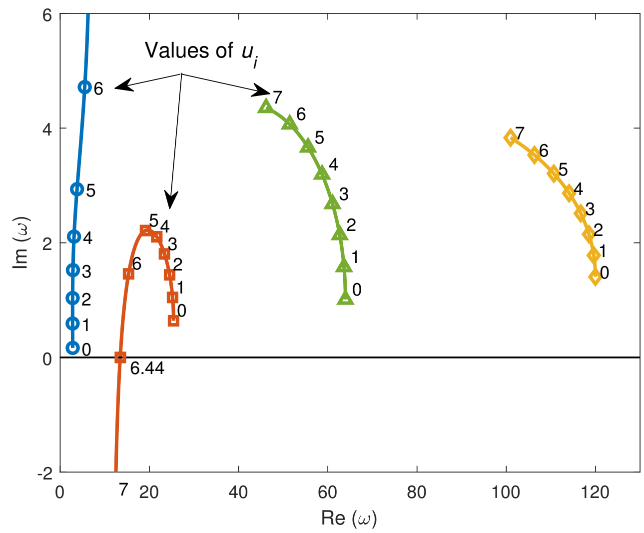

Figure 6.5: A typical Argand diagram for the system parameters associated with the bench-top-scale system with $r_{ann} \simeq 1/2$, given in Section 6.3.1.1 undergoing second mode flutter at $u_i = 6.44$. Mode 1 (○), Mode 2 (□), Mode 3 (△), Mode 4 (◇).

top-scale system with $r_{ann} \simeq 1/2$. In this diagram, the first four modes of the system are shown for incremental values of u_i from 0 to $u_{i,cr}$ and beyond, wherein the imaginary part of the dimensionless eigenfrequencies, Im(ω), is plotted against its real part, Re(ω). With increasing u_i, at $u_{i,cr} = 6.44$ the second mode crosses the real axis at a non-zero real value, indicating a Hopf bifurcation and loss of stability by second mode flutter, in agreement with previous work.

6.3.1.2 Relatively short brine-strings in caverns with single fluid

Another set of calculations was conducted using the parameters of a relatively short brine-string system analyzed in Ref. [4]. This enables validation of the current model using system parameters that more closely resemble those of a full-scale brine-string system, while still utilizing a single-fluid (water). The properties and dimensions of this system are as follows: Brine-string length $L = 200$ m, inner diameter $D_i = 0.159$ m, outer diameter $D_o = 0.1778$ m, flexural rigidity $EI = 3.47 \times 10^6$ N m^2 and mass per unit length $M_t = 38.7$ kg/m; length of the outer rigid casing $L' = 100$ m. The results are compared to those obtained by Moditis et al. [4] for three values of confinement, namely $\alpha_{ch} = D_{ch}/D_o = 1.6$, 2 and 2.8; corresponding to the inner diameter of the outer casing $D_{ch} = \alpha_{ch} D_o = 0.284$ m, 0.356 m and 0.498 m. As per Ref. [4], the well-head pressure is given a value of $p_o|_{x=0} = 0$, and the friction coefficients in the normal and longitudinal direction are $C_N = C_T = 0.0125$. The other associated dimensionless parameters are: $\alpha = 0.894$, $\beta_i = 0.238$, $\beta_o = 0.298$, $\gamma = 763.6$, $\varepsilon = 1.125 \times 10^3$. In what follows, this system is referred to as "A-water-water system" for brevity.

The dimensionless critical flow velocities and the mode of instability predicted by this model for the A-water-water system are presented in Table 6.2 and they are in excellent agreement with those obtained in Ref. [4].

Another comparison was carried out for a water-filled brine-string system with the same dimensions as in A-water-water system, but this time, for a constant $\alpha_{ch} = 1.676$, the brine-string length was varied from $L = 10$ m to 300 m, accordingly so was $\varepsilon = L/D_o$, while keeping $r_{ann} = L'/L$ constant. The results are compared in Fig. 6.6, showing an excellent agreement to those reported in Ref. [4]. It should be noted that the cantilever length, L, has been used in the non-dimensionalization of the internal flow velocity, u_i, provided in Eq. (6.43). Consequently, u_i is not an appropriate dimensionless term for studying the influence of length on the dynamics of the system. More suitable dimensionless terms have been employed by Doaré and de Langre [47] for hanging fluid-conveying pipes, and by de Langre et al. [48] for cylinders in axial flow. In this investigation, however, we have not redefined the dimensionless quantities. Instead, we have used a new dimensionless flow velocity, u_i/ε, to study the influence of length on the dynamics of the system. This new dimensionless parameter allows investigating the effect of the length (slenderness).

6.3.2 Results of the present model for system parameters associated with typical full-scale systems

This section presents theoretical results pertinent to long brine-string-like systems.

The properties and dimensions of a sample system, hereafter referred to as system B, are as follows: Brine-string length $L = 1283$ m, inner diameter $D_i = 0.159$ m, outer diameter $D_o = 0.1778$ m, flexural rigidity $EI = 3.47 \times 10^6$ N m^2 and mass per unit length $M_t = 38.7$ kg/m; length of the outer rigid casing $L' = 1085$ m and inner diameter $D_{ch} = 0.298$ m. These values are similar to those for the A-water-water system, but the length is considerably longer

Table 6.2: Dimensionless critical flow velocity, $u_{i,cr}$ and the mode of instability for the system introduced in Section 6.3.1.2 with $L = 200$ m and various α_{ch}. Di: static divergence in the ith mode, Fi: flutter in the ith mode

α_{ch}	Ref. [4]	Present
1.6	14.0* (D1)	14.3 (D1)
2	23.3* (F1)	23.6 (F1)
2.8	25.0* (F5)	25.0 (F5)

*These values are obtained from Fig.11 in Ref. [4] by a plot digitizer, and they might not be exact to three significant figures.

(more appropriate for a real brine-string). The density of brine is $\rho_b = 1200$ kg/m^3, and its viscosity $\mu_b = 3.6$ cP. Taking the product in the cavern to be propane, $\rho_p = 508$ kg/m^3 and $\mu_p = 0.095$ cP. The friction coefficients in the normal and longitudinal direction are $C_N = 0.5C_T = 0.0125$, which is appropriate for rough cylinders [52]. The interface level is given a value of $L'' = 1281$ m, 1213 m, and 1145 m, for the greatest, intermediate and smallest value of interface level, respectively. The well-head pressure is $p_o|_{x=0} = 1000$ psi ($\simeq 6.895$ MPa).

The associated dimensionless parameters are as follows: $r_{ann} = 0.846$, $r_{if} = 0.998$, 0.945 or 0.892, $\alpha = 0.894$, $\beta_i = 0.317$, $\beta_o = 0.168$, $\gamma = 2.983 \times 10^5$, $\varepsilon = 7.216 \times 10^3$. For this system, the conversion factor between the dimensional and dimensionless internal flow velocity is U_i (m/s)$/u_i = 0.297$, and the frequencies is Ω (rad/s)$/\omega = 1.305 \times 10^{-4}$.

To highlight the importance of taking the presence of two different fluids in the cavern, results are compared for two cases: the B-brine-propane system (in which the two fluids are brine and propane) and the B-brine-brine system (in which it is assumed that the cavern is filled only with brine). In the latter case, the well-head pressure, $p_o|_{x=0}$, can be neglected. The Argand diagrams for the two cases are shown in Fig. 6.7(a,b). It is noted that both systems lose stability by static divergence; the B-brine-propane system in the second mode at $u_{i,cr} = 44.10$ ($U_{i,cr} = 13.12$ m/s), and the B-brine-brine system in the first mode at $u_{i,cr} = 60.07$ ($U_{i,cr} = 17.87$ m/s). Thus, both the critical flow velocity and the mode of

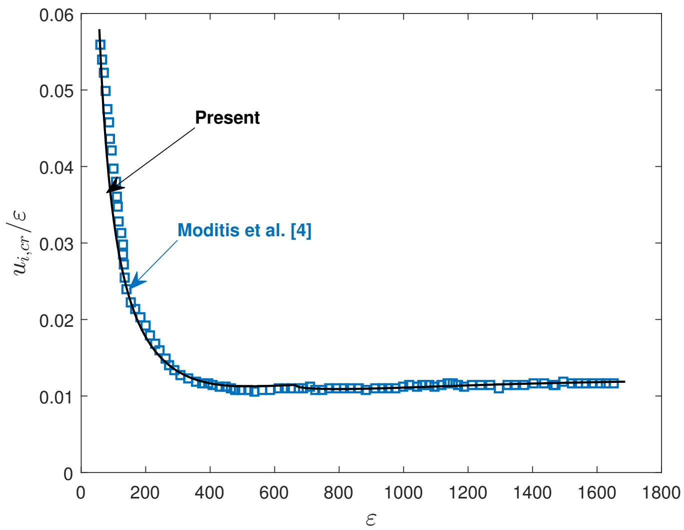

Figure 6.6: Variation of $u_{i,cr}/\varepsilon$ with increasing ε for the system parameters as in Section 6.3.1.2 with $r_{ann} = 0.85$ and $\alpha_{ch} = 1.676$.

instability change, highlighting the significant influence of considering the presence of two distinct fluids within the cavern.

Further calculations were conducted using several other typical brine-string systems, namely systems I-V, given in Table 6.3. Taking the product in the cavern to be propane, and for brine-strings made of steel with $E = 206$ GPa, the associated dimensionless parameters are given in Table 6.4, with the conversion factor between the dimensionless and dimensional terms and the relationship between internal and/or external flow velocities given in Table 6.5. The value of well-head pressure in the calculations for all cases was taken to be $p_o|_{x=0} = 0.5p_{o,\max}|_{x=0}$; refer to Eq. (6.35).

The critical flow velocity and the mode of instability for systems I-V are provided in Table 6.6, in which results are given for $C_N = C_T = 0.0125$ and $C_N = 0.5C_T = 0.0125$, the latter being pertinent for rough cylinders. One can conclude that, generally, a cylinder with more roughness would have a lower critical flow velocity than a smoother one. It is evident that the critical flow velocity and mode of instability varies from one case to another, depending on the system parameters.

It can be concluded from the results presented in Table 6.6 that, the effect of interface level ratio, r_{if} on the critical flow velocity is not monotonic; in any case, the effect is minor.

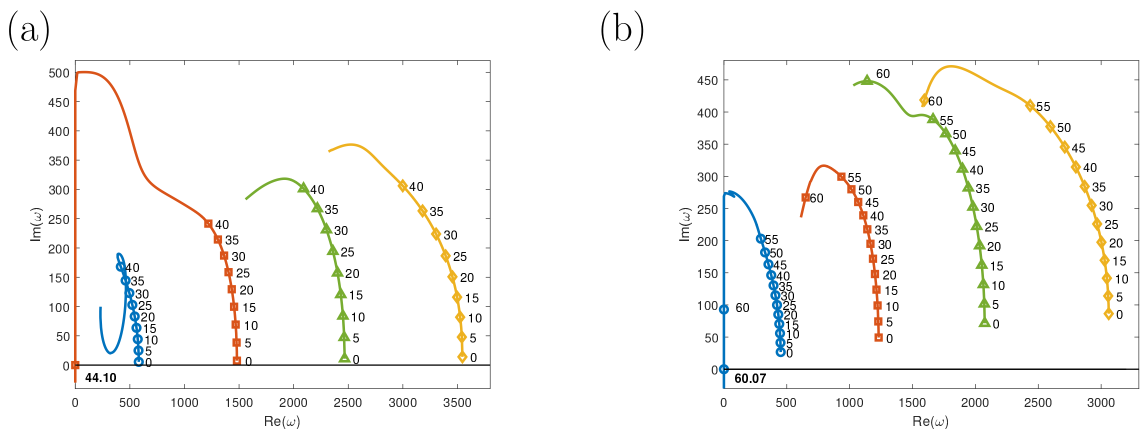

Figure 6.7: Argand diagram for system B, defined in Section 6.3.2, in which the two fluids in the cavern are: (a) brine-propane (greatest r_{if}); (b) brine-brine. The first one undergoes static divergence in the second mode at $u_i = 44.10$, and the second static divergence in the first mode at $u_i = 60.07$. Mode 1 (○), Mode 2 (□), Mode 3 (△), Mode 4 (◇).

Table 6.3: Dimensions of some typical brine-string systems.

Case	Brine-string				Production casing		Interface level (m)		
	L (m)	D_i (m)	D_o (m)	M_t (kg/m)	L' (m)	D_{ch} (m)	Greatest r_{if} *	Moderate r_{if} *	Smallest r_{if} *
I	1315	0.224	0.244	60	1070	0.318	1313	1222	1131
II	1062	0.225	0.244	60	600	0.321	1061	861	660
III	812	0.381	0.406	125	411	0.508	810	641	472
IV	1038	0.373	0.406	163	614	0.578	1036	855	674
V	257	0.124	0.140	25	198	0.206	256	235	213

* At its greatest value for interface level, the cavern would hold nearly the maximum product capacity possible, whereas for the smallest value of interface level, the cavern is full of brine and the product would be present only at the level of the annular region between the brine-string and outer casing. The moderate interface level is the average situation.

Table 6.4: Dimensionless parameters associated with the systems of Table 6.3. In these calculations, the two fluids in the brine-string and storage cavern are brine and propane.

Case	α	α_{ch}	β_i	β_o	γ	ε	h	r_{ann}
I	0.918	1.303	0.361	0.181	1.796×10^5	5.389×10^3	3.297	0.814
II	0.922	1.316	0.363	0.181	0.995×10^5	4.352×10^3	3.169	0.565
III	0.938	1.251	0.418	0.201	0.084×10^5	2.000×10^3	3.980	0.506
IV	0.919	1.424	0.364	0.183	0.317×10^5	2.557×10^3	2.360	0.591
V	0.886	1.471	0.306	0.165	0.035×10^5	1.836×10^3	2.121	0.770

Table 6.5: Multiplicative factors to convert the dimensionless to dimensional terms and the relationship between internal and/or external flow velocities associated with the systems of Table 6.3. In these calculations, the two fluids in the brine-string and storage cavern are brine and propane.

Case	U_i (m/s)/u_i	U_o (m/s) /u_o	u_o/u_i	U_o/U_i	$(U_o/U_i)/(u_o/u_i)$	Ω (rad/s)/ω
I	0.356	0.503	2.020	2.850	1.411	1.628×10^{-4}
II	0.429	0.609	1.939	2.749	1.417	2.436×10^{-4}
III	1.169	1.687	2.550	3.671	1.442	9.307×10^{-4}
IV	0.748	1.056	1.375	1.942	1.412	4.349×10^{-4}
V	1.249	1.701	1.168	1.590	1.361	26.90×10^{-4}

Table 6.6: Critical flow velocity, $u_{i,cr}$, and the mode of instability for the systems of Table 6.3. Di: static divergence in the ith mode, Fi: flutter in the ith mode. The dimensional values of $U_{i,cr}$ (m/s) are given in parentheses.

Case	$C_N = C_T = 0.0125$			$C_N = 0.5C_T = 0.0125$		
	Greatest r_{if}	Moderate r_{if}	Smallest r_{if}	Greatest r_{if}	Moderate r_{if}	Smallest r_{if}
I	16.66 (5.93 m/s)	16.24 (5.78 m/s)	16.94 (6.03 m/s)	11.91 (4.24 m/s)	11.63 (4.14 m/s)	12.11 (4.31 m/s)
	D1	F1	D1	D1	F1	D1
II	18.25 (7.83 m/s)	18.23 (7.82 m/s)	18.41 (7.90 m/s)	13.19 (5.66 m/s)	13.12 (5.63 m/s)	13.29 (5.70 m/s)
	D1	F4	F2	D1	F4	F2
III	6.00 (7.02 m/s)	5.80 (6.78 m/s)	5.55 (6.49 m/s)	4.42 (5.17 m/s)	4.32 (5.05 m/s)	4.14 (4.84 m/s)
	D1	D1	D1	F1	D1	D1
IV	20.73 (15.51 m/s)	20.75 (15.52 m/s)	20.76 (15.53 m/s)	15.16 (11.34 m/s)	15.12 (11.31 m/s)	15.20 (11.37 m/s)
	D1	F4	D1	D1	F4	D1
V	9.65 (12.05 m/s)	9.54 (11.91 m/s)	9.44 (11.79 m/s)	7.21 (9.01 m/s)	7.13 (8.90 m/s)	7.06 (8.82 m/s)
	D1	D1	D1	D1	D1	D1

For instance, for case I and $C_N = 0.5C_T = 0.0125$, the values of critical flow velocity are fairly close, ranging between 11.63 to 12.11.

Fig. 6.8 shows Argand diagrams for two cases: (i) case I with $C_N = 0.5C_T = 0.0125$ and the greatest r_{if}, where a static divergence in the first mode takes place at $u_i = 11.91$ ($U_i = 4.24$ m/s); (ii) case IV with $C_N = 0.5C_T = 0.0125$ and the moderate r_{if}, predicting flutter in the fourth mode at $u_i = 15.12$ ($U_i = 11.31$ m/s).

6.4 Parametric study

In this parametric study, the reference system against which the results are compared is the B-brine-propane system, introduced in Section 6.3.2. The influence of the main system parameters on the dynamics of the brine-string system was studied, focusing on the effect of well-head pressure, the ratio between brine and product densities, the annular flow confinement (α_{ch}), the confinement length ratio (r_{ann}), and the brine-string length (or its slenderness, ε).

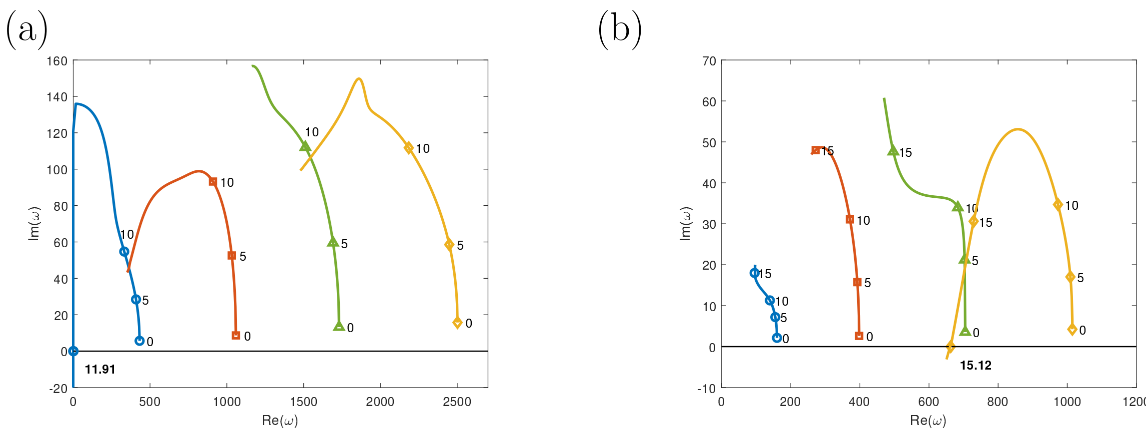

Figure 6.8: Argand diagram for (a) Case I with $C_N = 0.5C_T = 0.0125$ and the greatest r_{if} subject to static divergence in the first mode at $u_i = 11.91$; (b) Case IV with $C_N = 0.5C_T = 0.0125$ and the moderate r_{if} subject to flutter in the fourth mode at $u_i = 15.12$. Mode 1 (○), Mode 2 (□), Mode 3 (△), Mode 4 (◇).

6.4.1 The effect of well-head pressure

The effect of external pressure being stabilizing is well known for pipes with supported ends. Also, it is known that a pipe with supported ends will buckle if the internal pressure exceeds the external one sufficiently, independently of internal flow velocity [12]. However, for a cantilevered pipe subjected to external flow of different density, the influence of pressure is not obvious.

To assess the potential impact of pressure on the dynamics of the system under investigation, calculations were carried out for three different values of the well-head pressure, namely $p_o|_{x=0} = 0$, $p_o|_{x=0} = 0.5p_{o,\max}|_{x=0}$ or $p_o|_{x=0} = p_{o,\max}|_{x=0}$; refer to Eq. (6.35). The results are presented in Table 6.7. It can be concluded that, in general, the effect of the well-head pressure, albeit marginal, is stabilizing. For instance, the critical flow velocity for the greatest r_{if} increases from $u_{i,cr} = 42.53$ for $p_o|_{x=0} = 0$ to 45.52 for $p_o|_{x=0} = p_{o,\max}|_{x=0}$.

6.4.2 The effect of brine-to-product density ratio

Next, the influence of the product density was investigated. To this end, calculations were conducted for the B-brine-propane system, the B-crude-oil-brine system and the B-brine-brine system. The results are presented in Table 6.8. It can be concluded that, the lower the density of the product is, the lower the critical flow velocity would be. For instance, compar-

Table 6.7: Dimensionless critical flow velocity, $u_{i,cr}$ and the mode of instability for B-brine-propane system with different values of well-head-pressure. Di: static divergence in the ith mode, Fi: flutter in the ith mode

$p_o\|_{x=0} = 0$			$p_o\|_{x=0} = 0.5p_{o,\max}\|_{x=0}$			$p_o\|_{x=0} = p_{o,\max}\|_{x=0}$		
Greatest r_{if}	Moderate r_{if}	Smallest r_{if}	Greatest r_{if}	Moderate r_{if}	Smallest r_{if}	Greatest r_{if}	Moderate r_{if}	Smallest r_{if}
42.53 (D2)	42.56 (B2)	44.07 (F1)	44.10 (D2)	44.10 (F1)	45.72 (F1)	45.52 (F1)	45.59 (F1)	47.30 (D2)

Table 6.8: Dimensionless critical flow velocity, $u_{i,cr}$ and the mode of instability for system B with three different brine-to-product density and viscosity ratios. Di: static divergence in the ith mode, Fi: flutter in the ith mode

Propane with $SG = 0.508$ and $\mu_p = 0.095$ cP			Crude oil with $SG = 0.800$ and $\mu_p = 3.5$ cP			Brine with $SG = 1.2$ and $\mu_b = 3.6$ cP
Greatest r_{if}	Moderate r_{if}	Smallest r_{if}	Greatest r_{if}	Moderate r_{if}	Smallest r_{if}	Only brine in the cavern
44.10 (D2)	44.10 (F1)	45.72 (F1)	53.25 (F1)	53.29 (F1)	54.43 (D1)	60.07 (D1)

ing the results obtained for propane and crude oil, one can conclude that an approximately 57% increase in the density of the product has resulted in an approximately 21% increase in the critical flow velocity. Therefore, for very light liquid products, it is crucial to consider the presence of two different fluids within the cavern.

6.4.3 The effect of external flow confinement

The influence of α_{ch} on the brine-string system was also examined. A higher value of α_{ch} is associated with a less confined system, leading to a lower annular flow velocity, u_o, as can be concluded from Eq. (6.48).

Calculations were carried out for various values of $\alpha_{ch} = D_{ch}/D_o$ by changing the value of D_{ch}, while the remaining parameters are as in the B-brine-propane system. The results are presented in Fig. 6.9, in which the dimensionless internal critical flow velocity is plotted against α_{ch}. Additionally, the associated type of instability at each value of α_{ch} is indicated. As shown, in the case of a highly confined or effectively unconfined brine string system ($\alpha_{ch} < 1.7$ or $\alpha_{ch} > 3.6$), the system becomes unstable via flutter, whereas it loses stability by static divergence for moderately confined systems ($1.7 < \alpha_{ch} < 3.6$). Quantitatively, as shown in Fig. 6.9, $u_{i,cr}$ increases continuously and significantly with increasing α_{ch} (i.e., for less confinement) up to $\alpha_{ch} = 3.6$. Thereafter, the critical flow velocity reaches a plateau, indicating that the system is effectively unconfined, and α_{ch} has a negligible influence on the

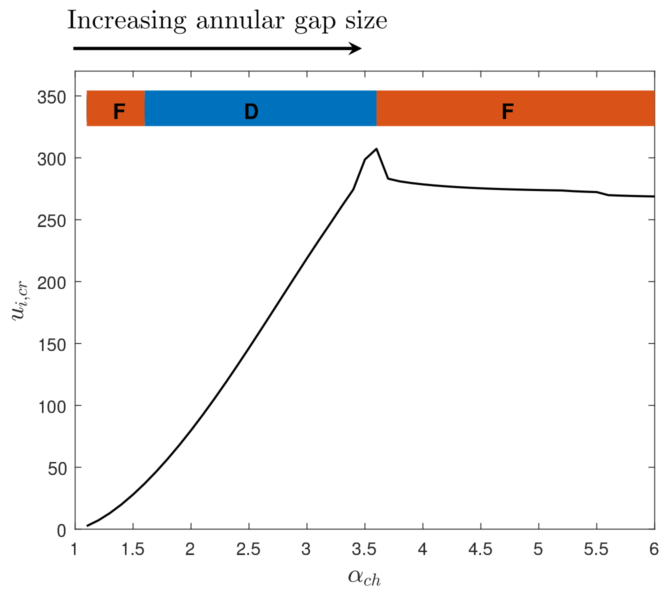

Figure 6.9: Variation of $u_{i,cr}$ with the annular gap confinement, $\alpha_{ch} = D_{ch}/D_o$. To achieve various values of α_{ch}, the parameter that is varied is the diameter of the outer casing, D_{ch}, while the remaining parameters are as in B-brine-propane system defined in Section 6.3.2

critical flow velocity.

6.4.4 The effect of confinement length ratio

The influence of the confinement length ratio, $r_{ann} = L'/L$ on the critical velocity was explored next. To this end, calculations were carried out for various values of L', while the remaining parameters are as in the B-brine-propane system defined in Section 6.3.2. The higher the value of r_{ann}, the larger is the upper portion of the brine-string subjected to annular flow.

Figure 6.10 presents the results, where the dimensionless internal critical flow velocity is plotted against r_{ann}. Additionally, the corresponding type of instability at each value of r_{ann} is indicated. As shown, increasing the confined length portion of the brine-string (or equivalently increasing the production casing length) destabilizes the system. This destabilization is quite significant and monotonic. In particular, $u_{i,cr}$ decreases from approximately 260 for an unconfined brine-string to about 42 for a brine-string that is almost entirely confined.

Increasing r_{ann} influences the dynamics qualitatively as well. A brine-string immersed in fluid, effectively without any annular flow ($r_{ann} \leq 0.05$), undergoes flutter in the eighth

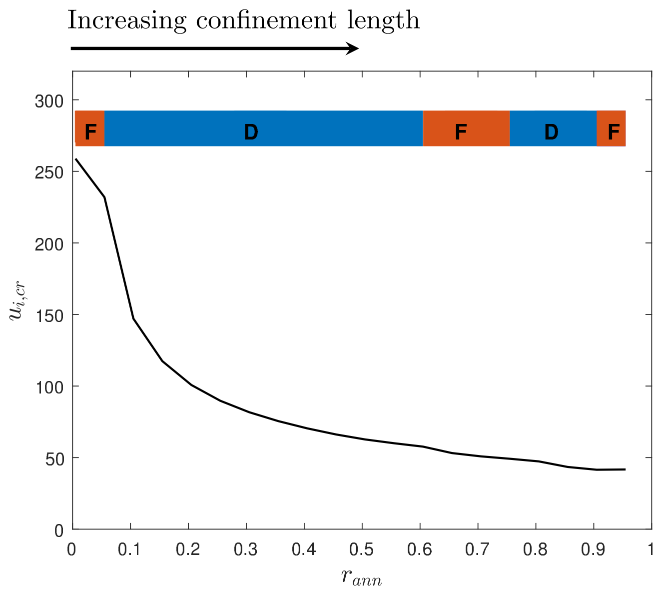

Figure 6.10: Variation of $u_{i,cr}$ with the annular confinement length, $r_{ann} = L'/L$. To achieve various values of r_{ann}, the parameter that is varied is the length of the outer casing, L', while the remaining parameters are as in the B-brine-propane system defined in Section 6.3.2.

mode; this oscillatory instability is succeeded by a static divergence for higher values of confinement length ratio, $0.05 < r_{ann} < 0.65$. For still higher r_{ann} the instability type becomes more sensitive to r_{ann}, alternating between divergence and flutter in the first mode.

6.4.5 The effect of pipe slenderness

The influence of the brine-string slenderness, $\varepsilon = L/D_o$, on the onset of instability was investigated via calculations with various values of brine-string length, L, while the remaining parameters are as in the B-brine-propane system, defined in Section 6.3.2. As discussed in Section 6.3.1.2, the brine-string length, L, appears in the relationship between the dimensional and dimensionless internal flow velocities, given in Eq. (6.43); therefore, u_i is not a suitable dimensionless parameter to investigate the influence of length on the onset of instability. Hence, a modified dimensionless velocity is used, that is u_i/ε. The relationship between the dimensional U_i and this modified dimensionless velocity is independent from L, thereby allowing the exploration of the effect of the length (slenderness).

As shown in Fig. 6.11, increasing the brine-string slenderness results initially in a very significant reduction of the onset of instability. However, for sufficiently slender (long) brine-

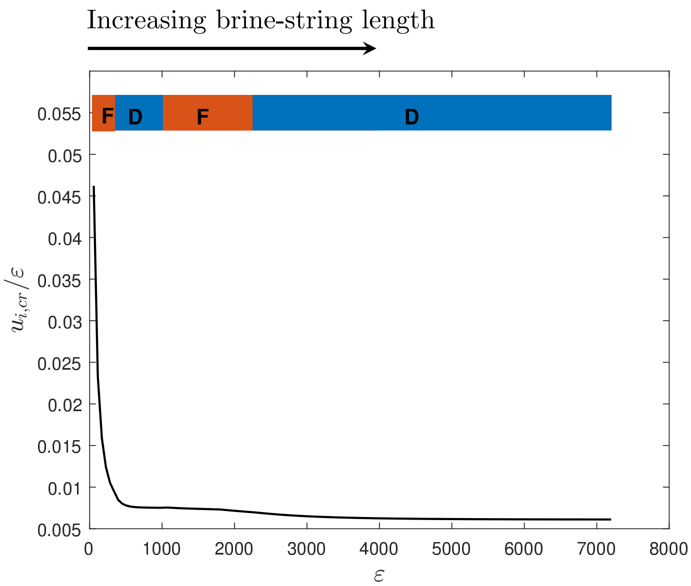

Figure 6.11: Variation of $u_{i,cr}/\varepsilon$ with the brine-string slenderness, $\varepsilon = L/D_o$. To achieve various values of ε, the parameter that is varied is the brine-string length, L, while the remaining parameters are as in B-brine-propane system introduced in Section 6.3.2

strings, the onset of instability becomes almost independent of ε; an asymptotic behaviour is observed, where as ε approaches a near-plateau, and a further increase in L has no influence on the dynamics. This asymptotic behaviour has been reported before by Doaré and de Langre [47] for a similar simpler system, namely for long hanging fluid-conveying pipes. The predominant effect of gravity-induced tension, which results in stabilizing the upper portion of very long pipes has been identified as the cause of this asymptotic system behaviour. In other words, the gravity-induced tension makes the upper portion of very long pipes effectively rigid, and therefore above a critical length, the flow velocity required to induce instability becomes independent of the pipe length. It is also noted that for a long enough brine-string, the system is subjected to static divergence, rather than flutter.

6.5 Conclusion

A linear theoretical model has been developed to predict fluid-elastic instabilities in brine-strings during product retrieval in salt-mined caverns. The fluid mechanics and dynamics of the system are simplified, and the model consists of a fluid-discharging cantilevered flexible pipe subjected to a partially-confined reverse annular flow. Specifically, it is assumed that the entire system is immersed in a container containing two different fluids with a variable interface level and that the cantilevered pipe is subjected to an external flow through an annular region over its upper portion, formed by concentric cantilevered outer rigid casing.

The model developed was first validated against similar simpler systems.Theoretical results were obtained for system parameters pertinent to long brine-string-like systems. The results indicate that the brine-string system becomes subject to either buckling or flutter at sufficiently high flow velocities, depending on the system parameters. The analysis reveals that simplifying the system by considering only a single fluid in the cavern (brine) is non-conservative, resulting in significant overestimation of the critical flow velocity.

Next, the impact of key system parameters on the dynamics was explored, namely the influence of the brine-product interface level, the well-head pressure, the ratio between brine and product densities, external flow confinement (annular gap size), confined length portion, and brine-string slenderness.

The results have shown that the effect of interface level is marginal, and that the well-head pressure has a stabilizing effect. Moreover, the lighter the product, the lower the critical flow velocity. The results regarding the effect of confinement indicate that with an increase in the annular gap size, leading to a decrease in the annular flow velocity, the system becomes more stable. However, the effect of confinement reaches a threshold, beyond which its influence on the dynamics becomes marginal. Increasing the length of the outer casing (increasing the confinement length) leads to significantly lower critical flow velocities. The effect of increasing the brine-string length was also found to be destabilizing, but in an asymptotic manner; the critical flow velocity approaches a limiting value for sufficiently long systems, and any additional increase in L does not impact the dynamics.

Acknowledgments

The financial support of the Natural Sciences and Engineering Research Council of Canada (A.K.M., grant number 04957-2018; M.P.P., grant number 06465-2018), the Solution Mining Research Institute (M.P.P., grant number U2017-3) and Pipeline Research Council International (M.P.P., grant number PR593-18700) is gratefully acknowledged. The first author is thankful to McGill University for a McGill Engineering International Tuition Award (MEITA). Thanks also go to Mr. Aram Bahmani for helping with some schematic

designs.

CRediT authorship contribution statement

M. Chehreghani: Conceptualization, Methodology, Validation, Formal analysis, Investigation, Writing – Original Draft. **A.K. Misra**: Conceptualization, Funding acquisition, Supervision, Project administration, Writing – Review & Editing. **M.P. Païdoussis**: Conceptualization, Funding acquisition, Supervision, Project administration, Writing – Review & Editing.

Declaration of Competing Interest

The authors affirm that there are no known competing interests or personal relationships that might have influenced the findings presented in this paper.

Data availability

The data that support the findings of this study are available, upon request to the first author.

Appendix

The mass, damping and stiffness matrices in Eq.(6.50), **M**, **C** and **K**, are given here, as follows:

$$\mathrm{M}_{ij} = a_{ij}(0,1) + \beta_o(\chi - 1)a_{ij}(0, r_{ann}) - \beta_o(r_\rho - 1)\big[a_{ij}(0, r_{if}) - a_{ij}(0,1)\big], \tag{A.1}$$

$$\begin{aligned}\mathrm{C}_{ij} = {} & 2u_i\sqrt{\beta_i}b_{ij}(0,1) - 2u_o\sqrt{\beta_o}\chi b_{ij}(0, r_{ann}) + \frac{1}{2}c_N\varepsilon u_o\sqrt{\beta_o}a_{ij}(0, r_{ann}) \\ & + k_{up}\frac{1+\alpha_{ch}^{-3}}{(1-\alpha_{ch}^{-2})^2}a_{ij}(0, r_{ann}) + k_{up}\big[a_{ij}(0, r_{if}) - a_{ij}(0, r_{ann})\big] \\ & + r_\rho\sqrt{\frac{\nu_b}{\nu_p}}\big[a_{ij}(0,1) - a_{ij}(0, r_{if})\big],\end{aligned} \tag{A.2}$$

$$
\begin{aligned}
\mathrm{K}_{ij} = {} & \lambda_j^4 a_{ij}(0,1) + \gamma b_{ij}(0,1) - \frac{1}{2}\varepsilon c_T u_o^2 (1+h) b_{ij}(0, r_{ann}) \\
& - \Big[\frac{1}{2}u_o^2(1+K_1)\Big]\phi_i|_{\xi=r_{ann}}\phi_j'|_{\xi=r_{ann}} - \gamma_p(r_\rho - 1)\big[b_{ij}(0,1) - b_{ij}(0,r_{if})\big] \\
& - \gamma\big[c_{ij}(0,1) - d_{ij}(0,1)\big] + \frac{1}{2}\varepsilon c_T u_o^2\big[(1+h)\big[r_{ann}c_{ij}(0,r_{ann}) - d_{ij}(0,r_{ann})\big] \\
& + \Big[\frac{1}{2}u_o^2(1+K_1)\Big]c_{ij}(0,r_{ann}) + \gamma_p(r_\rho - 1)\big[r_{if}c_{ij}(0,1) - d_{ij}(0,1) \\
& - r_{if}c_{ij}(0,r_{if}) + d_{ij}(0,r_{if}) + (1-r_{if})c_{i,j}(0,1)\big] - (\Gamma - \Pi_{iL} + \Pi_{oL})c_{ij}(0,1) \\
& + u_i^2 c_{ij}(0,1) + \chi u_o^2 c_{ij}(0,r_{ann}) - \frac{1}{2}\varepsilon u_o^2 b_{i,j}(0,r_{ann})\big[c_N - c_T\big],
\end{aligned}
\tag{A.3}
$$

where λ_j is the jth eigenvalue of the characteristic equation of a cantilevered Euler-Bernoulli beam.

References

[1] J. L. Ratigan, Brine string integrity and model simulation, in: SMRI Tech. Conf., Galveston/Austin, TX, USA, pp. 273–293, 2008.

[2] J. L. Ratigan, Flow-induced buckling of brine injection strings in solution-mined storage caverns, in: SMRI Tech. Conf., Albuquerque, NM, USA, 2017.

[3] W. Liu, Q. Li, C. Yang, X. Shi, J. Wan, et al., The role of underground salt caverns for large-scale energy storage: A review and prospects, Energy Storage Mater. 63 (2023) 103045.

[4] K. Moditis, M. P. Païdoussis, J. Ratigan, Dynamics of a partially confined, discharging, cantilever pipe with reverse external flow, J. Fluids Struct. 63 (2016) 120–139.

[5] H. W. Fiedelman, J. O. Voigt, The Solution Mining Research Institute – an updated review, in: Seventh Symp. Salt, Kyoto, Japan, pp. 347–351, 1993.

[6] M. P. Païdoussis, T. P. Luu, S. Prabhakar, Dynamics of a long tubular cantilever conveying fluid downwards, which then flows upwards around the cantilever as a confined annular flow, J. Fluids Struct. 24 (2008) 111–128.

[7] P. Bérest, A. Réveillère, D. Evans, M. Stöwer, Review and analysis of historical leakages from storage salt caverns wells, Oil Gas Sci. Technol. d'IFP Energies Nouv. 74 (2019) 27.

[8] S. L. Minas, M. P. Païdoussis, Dynamics of a shrouded cantilevered pipe subjected to internal and annular flows, J. Sound Vib. 490 (2021) 115729.

[9] M. P. Païdoussis, Pipes conveying fluid: A fertile dynamics problem, J. Fluids Struct. 114 (2022) 103664.

[10] M. Chehreghani, A. Shaaban, A. K. Misra, M. P. Païdoussis, Dynamics of a hanging fluid-discharging pipe subjected to reverse external flow: An experimental investigation, J. Fluids Struct. 119 (2023) 103889.

[11] F. J. Bourrières, Sur un phénomène d'oscillation auto-entretenue en mécanique des fluides réels, in: Publications Scientifiques et Techniques du Ministère de l'Air. France, No. 147., 1939.

[12] M. P. Païdoussis, Fluid-Structure Interactions: Slender Structures and Axial Flow, Vol. 1, 2nd edition, Academic Press, 2014.

[13] J. L. Hill, C. P. Swanson, Effects of lumped masses on the stability of fluid conveying tubes, J. Appl. Mech. 37 (2) (1970) 494–497.

[14] S. S. Chen, J. A. Jendrzejczyk, General characteristics, transition, and control of instability of tubes conveying fluid, J. Acoust. Soc. Am. 77 (3) (1985) 887–895.

[15] Y. Modarres-Sadeghi, C. Semler, M. Wadham-Gagnon, M. P. Païdoussis, Dynamics of cantilevered pipes conveying fluid. Part 3: Three-dimensional dynamics in the presence of an end-mass, J. Fluids Struct. 23 (4) (2007) 589–603.

[16] M. H. Ghayesh, M. P. Païdoussis, Y. Modarres-Sadeghi, Three-dimensional dynamics of a fluid-conveying cantilevered pipe fitted with an additional spring-support and an end-mass, J. Sound Vib. 330 (12) (2011) 2869–2899.

[17] M. P. Païdoussis, F. C. Moon, Nonlinear and chaotic fluidelastic vibrations of a flexible pipe conveying fluid, J. Fluids Struct. 2 (6) (1988) 567–591.

[18] A. Czerwiński, J. Łuczko, Nonlinear vibrations of planar curved pipes conveying fluid, J. Sound Vib. 501 (2021) 116054.

[19] K. Zhou, Q. Ni, W. Chen, H. L. Dai, P. Hagedorn, L. Wang, Static equilibrium configuration and nonlinear dynamics of slightly curved cantilevered pipe conveying fluid, J. Sound Vib. 490 (2021) 115711.

[20] T. S. Lundgren, P. R. Sethna, A. K. Bajaj, Stability boundaries for flow induced motions of tubes with an inclined terminal nozzle, J. Sound Vib. 64 (4) (1979) 553–571.

[21] A. Shaaban, M. Chehreghani, A. K. Misra, M. P. Païdoussis, The dynamics of imperfectly supported hanging pipes conveying fluid: An experimental study, J. Fluids Struct. 121 (2023) 103951.

[22] M. Riazat, M. Kheiri, Three-dimensional nonlinear dynamics of imperfectly supported pipes conveying fluid, J. Fluids Struct. (2023) 104011.

[23] P. J. Holmes, Bifurcations to divergence and flutter in flow-induced oscillations: a finite dimensional analysis, J. Sound Vib. 53 (4) (1977) 471–503.

[24] P. J. Holmes, Pipes supported at both ends cannot flutter, J. Appl. Mech. 45 (3) (1978) 619–622.

[25] A. K. Bajaj, P. R. Sethna, T. S. Lundgren, Hopf bifurcation phenomena in tubes carrying a fluid, SIAM J. Appl. Math. 39 (2) (1980) 213–230.

[26] J. Rousselet, G. Herrmann, Dynamic behavior of continuous cantilevered pipes conveying fluid near critical velocities, J. Appl. Mech. 48 (4) (1981) 943–947.

[27] C. Semler, G. X. Li, M. P. Païdoussis, The non-linear equations of motion of pipes conveying fluid, J. Sound Vib. 169 (5) (1994) 577–599.

[28] F. Cesari, S. Curioni, Buckling instability in tubes subject to internal and external axial fluid flow, in: Proc. 4th Conf. Dimens., Hungarian Academy of Science, Budapest, 1971, pp. 301–311.

[29] M. J. Hannoyer, M. P. Païdoussis, Instabilities of tubular beams simultaneously subjected to internal and external axial flows, ASME J. Mech. Des. 100 (2) (1978) 328–336.

[30] M. P. Païdoussis, Flow-induced vibrations in nuclear reactors and heat exchangers: Practical experiences and state of knowledge, in: Pract. Exp. with Flow-Induced Vib. IAHR/IUTAM Symp., Karlsruhe, Germany, pp. 1–81, 1980.

[31] M. P. Païdoussis, P. Besançon, Dynamics of arrays of cylinders with internal and external axial flow, J. Sound Vib. 76 (3) (1981) 361–379.

[32] J. J. Bailey, I. Finnie, An analytical study of drill-string vibration, ASME J. Eng. Ind. 82 (2) (1960) 122–127.

[33] I. Finnie, J. J. Bailey, An experimental study of drill-string vibration, ASME J. Eng. Ind. 82 (2) (1960) 129–135.

[34] J. P. Den Hartog, John Orr memorial lecture: recent cases of mechanical vibration, South African Mech. Eng. 19 (3) (1969) 53–68.

[35] T. P. Luu, On the dynamics of three systems involving tubular beams conveying fluid, Master's thesis, Department of Mechanical Engineering, McGill University, Canada (1983).

[36] Q. Qian, L. Wang, Q. Ni, Vibration and stability of vertical upward-fluid-conveying pipe immersed in rigid cylindrical channel, Acta Mech. Solida Sin. 21 (5) (2008) 331–340.

[37] K. Fujita, A. Moriasa, Stability of cantilevered pipes subjected to internal flow and external annular axial flow simultaneously, in: ASME 2015 Press. Vessel. Pip. Conf., Boston, MA, USA; PVP2015-45141, 2015.

[38] A. R. Abdelbaki, M. P. Païdoussis, A. K. Misra, A nonlinear model for a hanging tubular cantilever simultaneously subjected to internal and confined external axial flows, J. Sound Vib. 449 (2019) 349–367.

[39] A. R. Abdelbaki, M. P. Païdoussis, A. K. Misra, A nonlinear model for a hanging cantilevered pipe discharging fluid with a partially-confined external flow, Int. J. Non-Linear Mech. 118 (2020) 103290.

[40] M. P. Païdoussis, A. R. Abdelbaki, M. F. J. Butt, M. Tavallaeinejad, K. Moditis, A. K. Misra, M. Nahon, J. L. Ratigan, Dynamics of a cantilevered pipe subjected to internal and reverse external axial flow: A review, J. Fluids Struct. 106 (2021) 103349.

[41] M. F. J. Butt, M. P. Païdoussis, M. Nahon, Dynamics of a confined pipe aspirating fluid and concurrently subjected to external axial flow: A theoretical investigation, J. Sound Vib. 509 (2021) 116148.

[42] F. Daneshmand, T. Liaghat, M. P. Païdoussis, A Coupled Two-Way Fluid–Structure Interaction Analysis for the Dynamics of a Partially Confined Cantilevered Pipe Under Simultaneous Internal and External Axial Flow in Opposite Directions, ASME J. Press. Vessel Technol. 144 (2) (2021) 21401.

[43] M. Chehreghani, A. R. Abdelbaki, A. K. Misra, M. P. Païdoussis, Experiments on the dynamics of a cantilevered pipe conveying fluid and subjected to reverse annular flow, J. Sound Vib. 515 (2021) 116480.

[44] A. Shaaban, M. Chehreghani, A. K. Misra, M. P. Païdoussis, Experiments on the dynamics of aspirating cantilevered pipes concurrently subjected to reverse external axial flow, J. Sound Vib. 561 (2023) 117817.

[45] M. F. J. Butt, M. Nahon, M. P. Païdoussis, Dynamics of a confined pipe aspirating fluid concurrently subjected to external axial flow: Experiments on confinement length effects, J. Sound Vib. 571 (2024) 118001.

[46] K. Moditis, The dynamics of hanging tubular cantilevers in axial flow: An experimental

and theoretical investigation, Master's thesis, Department of Mechanical Engineering, McGill University, Montreal, QC, Canada (2014).

[47] O. Doaré, E. de Langre, The flow-induced instability of long hanging pipes, Eur. J. Mech. - A/Solids 21 (5) (2002) 857–867.

[48] E. de Langre, M. P. Païdoussis, O. Doaré, Y. Modarres-Sadeghi, Flutter of long flexible cylinders in axial flow, J. Fluid Mech. 571 (2007) 371–389.

[49] K. Kontzialis, K. Moditis, M. P. Païdoussis, Transient Simulations of the Fluid–Structure Interaction Response of a Partially Confined Pipe Under Axial Flows in Opposite Directions, ASME J. Press. Vessel Technol. 139 (3) (2017).

[50] S. S. Chen, M. W. Wambsganss, J. A. Jendrzejczyk, Added mass and damping of a vibrating rod in confined viscous fluids, J. Appl. Mech. 43 (2) (1976) 325–329.

[51] M. Chehreghani, I. Gholami, A. K. Misra, M. P. Païdoussis, Fluid-elastic instability of inverted cantilevered cylinders in axial flow, J. Fluids Struct. 115 (2022) 103778.

[52] M. P. Païdoussis, Fluid-Structure Interactions: Slender Structures and Axial Flow, Vol. 2, 2nd edition, Academic Press, 2016.

[53] M. J. Lighthill, Note on the swimming of slender fish, J. Fluid Mech. 9 (2) (1960) 305–317.

[54] M. P. Païdoussis, Dynamics of cylindrical structures subjected to axial flow, J. Sound Vib. 29 (3) (1973) 365–385.

[55] M. J. Lighthill, Large-amplitude elongated-body theory of fish locomotion, Proc. R. Soc. London 179 (1055) (1971) 125–138.

[56] G. I. Taylor, Analysis of the swimming of long and narrow animals, Proc. R. Soc. London 214 (1117) (1952) 158–183.

[57] V. F. Sinyavskii, V. S. Fedotovskii, A. B. Kukhtin, Oscillation of a cylinder in a viscous liquid, Sov. Appl. Mech. 16 (1) (1980) 46–50.

[58] E. F. Brater, H. W. King, J. E. Lindell, C. Y. Wei, Handbook of Hydraulics for the Solution of Hydraulic Engineering Problems, 7th edition, McGraw-Hill, Boston, MA., 1996.

[59] Design and Operation of Solution-mined Salt Caverns for Liquid Hydrocarbon Storage, API recommended practice 1115, second edition (2018).

Complementary discussion on system III - theoretical investigation

To clarify and expand on what is included in the manuscript presented in Chapter 6 [5], further discussion is provided here.

The idealized model for stability of brine-strings in salt-mined caverns presented in the preceding chapter predicts more realistic critical flow velocities compared to previous models. Previous models ignored the presence of fluids with different densities. By incorporating the two-fluid model, we were able to achieve more realistic predictions of critical flow velocities for full-scale systems. This is because: (i) the brine/product density ratio, r_ρ, appears in many terms in the equation of motion; (ii) r_ρ indirectly affects the U_o/U_i ratio, allowing for relatively high U_o/U_i in the case of interdependent internal and external flows, refer to Eq. (6.42).

CHAPTER 7

Conclusions and Suggested Future Work

The focus of this thesis lies in investigating the FSI dynamics of slender cantilevered cylinders subjected to internal, external, or simultaneous internal and external axial flows. It specifically examines the dynamics of three closely related systems of slender tubular beams under internal and external axial flows through experimental exploration and/or the construction of an analytical fluid-structure interaction model. System I involves a slightly curved cantilevered pipe discharging/aspirating fluid. System II is an inverted cantilevered cylinder subjected to external axial flow, i.e. with the flow directed from the free end towards the clamped one. System III constitutes the primary focus of this study spanning three thesis chapters; it involves a hanging cantilevered pipe discharging fluid and subjected simultaneously to a partially-confined inverted axial flow along its upper portion, through the annulus created by a coaxial shorter outer rigid tube.

In the experimental studies, the flow velocity was incremented gradually until reaching instability and beyond. A non-contacting optical technique utilizing a perpendicular synchronized dual-camera system was employed to track and record the motion of the flexible cylinder at each flow velocity increment. Subsequently, the recorded videos underwent processing to extract the displacement time series signals. These signal were further analyzed to identify the nature of the dynamics, employing both qualitative and quantitative measurements. Analysis techniques included bifurcation diagrams, wavelet transforms, Poincaré maps, power spectral densities (PSDs), phase plane plots, probability density functions (PDFs), auto-correlation functions, and Lyapunov exponents.

An analytical model was developed for system III via a Newtonian derivation of the partial differential equations of motion. Employing the Galerkin modal decomposition technique, the equation of motion was discretized to yield a set of ordinary differential equations. Conducting numerical integration using the seventh degree Newton–Cotes formula and recasting the ordinary differential equations using the state-space vector resulted in an eigenvalue problem. Solving the eigenvalue problem for incremental flow velocities, the stability of the system was investigated and Argand diagrams for various system parameters were obtained.

In what follows, a summary of the findings for each system is provided, along with suggestions for future research.

7.1 Summary of findings

7.1.1 System I

In Chapter 2, the dynamics of a slightly curved clamped-free tubular beam conveying fluid, presented in Chehreghani et al. [1], was studied. Using a bench-top-size apparatus, four different cases were examined experimentally: (i), (ii) a water-discharging straight or curved pipe in a reservoir filled with air; (iii), (iv) a water-aspirating straight or curved pipe in a reservoir filled with water.

The results showed that both curved and straight discharging pipes undergo a self-excited oscillatory instability, namely flutter in the second mode, at high-enough flow rates. Analyzing the displacement signal revealed that the oscillation was predominantly periodic. The main difference between the dynamics of the slightly curved and straight discharging pipes was that the curved pipe was subject to a relatively large amplitude static deformation prior to the onset of the oscillatory instability. More specifically, prior to the onset of flutter, with increasing flow velocity, the initial curvature of the curved discharging pipe gradually amplified, with the pipe deforming in a first-mode and then in a second-mode shape. The deformation of the curved pipe took place in the plane of the initial curvature and therefore, it was 2D.

The aspirating curved pipe developed first-mode flutter at sufficiently high flow velocities. Prior and after the threshold of flutter, with increasing flow velocity, the aspirating curved pipe was subject to a gradually increasing static deformation. The amplitude of the static deformation for the curved pipe was relatively large; however, the amplitudes of the oscillatory part of the displacements were rather small, and were superimposed on the mean deflection of the pipe. The first-mode flutter-like oscillations took place about the mean deflected state and they were of a weak, unsteady, near-intermittent nature, with a larger chaotic content than for the straight aspirating pipe.

7.1.2 System II

In Chapter 3, which presents the study by Chehreghani et al. [2], water-tunnel experiments on inverted cantilevered cylinders in axial flow, i.e. cylinder subjected to flow directed from the free towards the fixed one, were described and analyzed. Utilizing silicone–rubber cylinders of three different lengths with an embedded thin metal strip, a hollow silicone–rubber and a santoprene one, as well as three different free-end shapes, the influence of the main system parameters was examined.

The sequence of qualitative dynamics observed in the experiments, with increasing flow velocity, was as follows: the inverted cylinder underwent turbulence buffeting, followed by weak unsteady and near-intermittent first-mode flutter-like oscillations at relatively low flows. At still higher flows, the amplitude of oscillations increased and eventually, at sufficiently high flows, abruptly, a large-amplitude static divergence materialized. By discussing the mechanisms underlying these instabilities, it was concluded that the static divergence likely resulted from a saddle–node bifurcation, rather than a pitchfork bifurcation. The onset of static divergence displayed notable hysteresis, suggesting a subcritical bifurcation. In the case of highly-pliable cylinders, the static divergence amplitude could be extremely large, such that the cylinder would invert itself, so that the free end of the cylinder would face downstream.

Increasing the cylinder slenderness resulted in a decrease of the critical flow velocities for the onset of both instabilities. It was found that the free end-shape has only a negligible effect on the onset of flutter instability, and no effect on the threshold of static divergence, in sharp contrast to the effect of this parameter for a cylinder subjected to flow in the conventional flow direction, i.e. flow directed from the fixed end towards the free one.

7.1.3 System III

System III was studied in Chapters 4-6, corresponding to manuscripts [3–5], respectively. These studies were motivated by applications in brine-strings in salt-mined caverns utilized for storage and subsequent retrieval of hydrocarbons, hydrogen gas or compressed air.

In the experiments, a bench-top-size apparatus, consisting of a pressure vessel filled with water, a hanging flexible pipe, discharging water downwards, and a shorter outer rigid tube surrounding the upper portion of the pipe and containing an upward flow, was utilized. To achieve higher external-to-internal flow velocity ratios, additional flow, could enter the pressure vessel from the bottom. To examine the influence of the principal system parameters, flexible pipes of two different lengths and materials, as well as the outer rigid tubes of various lengths and inner diameters were employed. Additionally, for experiments on the effect of annular flow obstruction, a constraint (a ring) was placed at the inlet or outlet of the annulus. To investigate the effect of eccentricity between the pipe and the outer rigid tube, the rigid tube was placed with a predetermined eccentricity with respect to the undeformed position of the pipe. Various external-to-internal flow velocity ratios were tested. It was observed that for interdependent external and internal flows, generally, the pipe was subjected to turbulence buffeting at low flows, followed by flutter in the second-mode at sufficiently high flow velocities. For independent external and internal flows the pipe underwent the following sequence of dynamical states: turbulence buffeting, followed by static deflection or weak first-mode oscillations, and eventually second- or mixed-mode oscillations. The observed flutter was quite unsteady, but predominantly periodic with some chaotic content. Generally, increasing the external-to-internal flow velocity ratio, confinement length, annular flow obstruction or eccentric positioning of the outer rigid tube with respect to the central pipe were all found to have a destabilizing effect. On the other hand, increasing the annular gap size (less confinement) and using a stiffer pipe were all found to have a stabilizing effect. Increasing pipe length-to-diameter ratio had a destabilizing effect for the very small external-to-internal flow velocity ratio of 0.015, and a rather negligible stabilizing effect for higher external-to-internal flow velocity ratios.

The analytical model developed for system III, which was obtained by simplifying the fluid mechanics and dynamics of the brine-string system, was utilized to predict fluid-elastic instabilities in this system. Numerical results indicated that, depending on the system parameters, the full-scale brine-string system may undergo buckling or flutter at sufficiently high flow velocities. It was shown that simplifying the system by considering only a single fluid (brine) in the cavern resulted in a significant overestimation of the critical flow velocity. The analysis revealed that well-head pressure has a stabilizing effect, while the influence of the brine-product interface level on dynamics is negligible. It was also concluded that decreasing the density of the product destabilizes the system. Increasing the annular gap size, which decreases the external-to-internal flow velocity ratio, stabilized the system; however, this effect approached a threshold, beyond which its influence on dynamics became essentially negligible. Increasing the confined length portion of the brine-string had a destabilizing influence. Extending the length of the brine-string was found to induce destabilization, albeit in an asymptotic manner; the critical flow velocity approached a limiting value for sufficiently long brine-strings, beyond which further increases in length had no effect on the dynamics.

The analytical model developed in Chapter 6 can be used for the simpler bench-top-scale experimental system considered in Chapters 4 and 5 with very little modification. Theoretical results for the bench-top-scale system parameters are in good qualitative and quantitative agreement with experimental observations in terms of the critical flow velocity and the mode of instability. Also, both the theory and the experiments are in agreement in terms of the effect of the principal system parameters on the dynamics of system III.

7.2 Future work

For system I, it would be interesting to conduct more experiments on pipes of various initially curved shapes. It may be possible to 3D print pipes with a first, second or higher mode curved shapes. Also, other types of geometric imperfections can be explored, for instance twisted pipes. Additionally, for aspirating pipes, it would be interesting to conduct experiments using a suction pump instead of experiments on pipes immersed in a pressurized vessel. To improve the flow-intake model for aspirating pipes, flow visualization would be insightful. Moreover, since curved pipes undergo large static deformation prior to an oscillatory instability, developing a geometrically exact nonlinear analytical model of the system would be interesting.

For system II, further investigation could provide insights on the mechanisms underlying the FSI dynamics of the system; specifically, to determine whether the observed static divergence arises via a saddle–node or a pitchfork bifurcation. Also, it would be interesting to apply external perturbations to the inverted cantilevered cylinder at relatively low flow velocities, to examine if a saddle-node bifurcation would materialize at low flows. Additionally, the effect of imperfections, such as an initially curved shape and imperfect clamping can be explored. Moreover, developing a geometrically exact nonlinear model of a free-clamped cylinder in axial flow with improved free-end boundary conditions and an initial curvature would be useful.

For system III, the effect of friction coefficients needs to be explored further. Specifically, it is necessary to investigate if the values of these coefficients, now routinely used, are appropriate. Additionally, developing an analytical model taking into account the impact forces and initial curvature of the pipe would be interesting. Also, for the system with reverse flow directions, i.e. the storage mode of operation with the annulus discharging the product into the cavern and the brine-string aspirating brine, it is needed to develop a similar analytical model to that for system III, in which the existence of two fluids in the cavern as well as the wellhead pressure are taken into account.

There are also some interesting systems of slender structures subjected to axial flow that can be further investigated. For instance, revisiting the system of a cantilevered pipe conveying fluid and subjected to motion-restraining spring constraints could involve the development of a geometrically exact nonlinear model for this system. Also, conducting fresh experiments on this system would be interesting. Additionally, wind and water tunnel experiments can be conducted to examine the influence of surface ridges on the dynamics of a cantilevered plate subjected to axial flow.

References

[1] M. Chehreghani, A. Shaaban, A. K. Misra, M. P. Païdoussis, Experimental investigation of the dynamics of slightly curved cantilevered pipes conveying fluid, Nonlinear Dyn. 111 (2023) 22101–22117.

[2] M. Chehreghani, I. Gholami, A. K. Misra, M. P. Païdoussis, Fluid-elastic instability of inverted cantilevered cylinders in axial flow, J. Fluids Struct. 115 (2022) 103778.

[3] M. Chehreghani, A. R. Abdelbaki, A. K. Misra, M. P. Païdoussis, Experiments on the dynamics of a cantilevered pipe conveying fluid and subjected to reverse annular flow, J. Sound Vib. 515 (2021) 116480.

[4] M. Chehreghani, A. Shaaban, A. K. Misra, M. P. Païdoussis, Dynamics of a hanging fluid-discharging pipe subjected to reverse external flow: An experimental investigation, J. Fluids Struct. 119 (2023) 103889.

[5] M. Chehreghani, A. K. Misra, M. P. Païdoussis, Dynamics of a cantilevered pipe conveying fluid and partially subjected to a confined counter-current external axial flow of a different fluid, J. Sound Vib. 590 (2024) 118574.

[6] M. P. Païdoussis, Fluid-Structure Interactions: Slender Structures and Axial Flow, Vol. 1, 2nd edition, Academic Press, Oxford, 2014.

[7] M. P. Païdoussis, Calvin Rice Lecture: Some curiosity-driven research in fluid structure interactions and its current applications, ASME J. Press. Vessel Technol. 115 (1) (1993) 2–14.

[8] M. S. Triantafyllou, G. S. Triantafyllou, D. K. P. Yue, Hydrodynamics of Fishlike Swimming, Annu. Rev. Fluid Mech. 32 (1) (2000) 33–53.

[9] M. P. Païdoussis, Pipes conveying fluid: A fertile dynamics problem, J. Fluids Struct. 114 (2022) 103664.

[10] M. Tavallaeinejad, A. Fereidoooni, M. P. Païdoussis, A. Grewal, V. Wickramasinghe, An application of cantilevered plates subjected to extremely large amplitude deformations: A self-starting mechanism for vertical axis wind turbines, J. Fluids Struct. 113 (2022) 103666.

[11] H. Ding, J. C. Ji, Vibration control of fluid-conveying pipes: a state-of-the-art review, Appl. Math. Mech. -Engl. Ed. 44 (9) (2023) 1423–1456.

[12] E. Naudascher, D. Rockwell, Flow-Induced Vibrations: An Engineering Guide, Courier Corporation, North Chelmsford, MA, 2012.

[13] F. J. Bourrières, Sur un phénomène d'oscillation auto-entretenue en mécanique des fluides réels, in: Publications scientifiques et techniques du ministère de l'Air (France), No. 147., 1939.

[14] L. A. Vega, Oceanocean thermal energy conversion, in: Meyers, R. A. (Ed.), Encyclopedia of Sustainability Science and Technology, Vol. 6, Springer, New York, NY, 2012, pp. 7296–7328.

[15] C. Zhou, Y. Yang, J. Wang, Q. Wu, Z. Gu, Y. Zhou, X. Liu, Y. Yang, H. Tang, Q. Ling, L. Wang, J. Zang, Ferromagnetic soft catheter robots for minimally invasive bioprinting, Nat. Commun. 12 (1) (2021) 1–12.

[16] M. F. Lumentut, M. I. Friswell, Powering smart pipes with fluid flow: Effect of velocity profiles, Comput. Struct. 258 (2022) 106680.

[17] H. Farokhi, M. P. Païdoussis, A. K. Misra, Nonlinear behaviour of cantilevered carbon nanotube resonators based on a new nonlinear electrostatic load model, J. Sound Vib. 419 (2018) 604–629.

[18] J. S. Chung, A. K. Whitney, Axial stretching oscillation of an 18,000-ft vertical pipe in the ocean, ASME J. Energy Resour. Tech. 105 (2) (1983) 195–200.

[19] M. P. Païdoussis, G. X. Li, Pipes conveying fluid: a model dynamical problem, J. Fluids Struct. 7 (2) (1993) 137–204.

[20] P. J. Holmes, Pipes supported at both ends cannot flutter, J. Appl. Mech. 45 (3) (1978) 619–622.

[21] T. B. Benjamin, Dynamics of a system of articulated pipes conveying fluid-I. theory, Proc. R. Soc. Lond. A. 261 (1307) (1961) 457–486.

[22] R. W. Gregory, M. P. Païdoussis, Unstable oscillation of tubular cantilevers conveying fluid. I. theory, Proc. R. Soc. Lond. A. 293 (1435) (1966) 512–527.

[23] A. K. Bajaj, P. R. Sethna, T. S. Lundgren, Hopf bifurcation phenomena in tubes carrying a fluid, SIAM J. Appl. Math. 39 (2) (1980) 213–230.

[24] Y. Modarres-Sadeghi, C. Semler, M. Wadham-Gagnon, M. P. Païdoussis, Dynamics of cantilevered pipes conveying fluid. Part 3: Three-dimensional dynamics in the presence of an end-mass, J. Fluids Struct. 23 (4) (2007) 589–603.

[25] M. P. Païdoussis, F. C. Moon, Nonlinear and chaotic fluidelastic vibrations of a flexible pipe conveying fluid, J. Fluids Struct. 2 (6) (1988) 567–591.

[26] M. P. Païdoussis, Dynamics of cylindrical structures in axial flow: A review, J. Fluids Struct. 107 (2021) 103374.

[27] M. P. Païdoussis, Fluid-Structure Interactions: Slender Structures and Axial Flow, Vol. 2, 2nd edition, Academic Press, Oxford, 2016.

[28] J. Massey, J. Forde, G. Parry, Cold-water corals and offshore hydrocarbon exploration operations on the irish atlantic margin, Workshop report, Irish Offshore Operators Association, Dublin (2014).

[29] M. J. Hannoyer, M. P. Païdoussis, Instabilities of tubular beams simultaneously subjected to internal and external axial flows, ASME J. Mech. Des. 100 (2) (1978) 328–336.

[30] J. P. Den Hartog, John Orr memorial lecture: recent cases of mechanical vibration, South African Mech. Eng. 19 (3) (1969) 53–68.

[31] M. P. Païdoussis, T. P. Luu, S. Prabhakar, Dynamics of a long tubular cantilever conveying fluid downwards, which then flows upwards around the cantilever as a confined annular flow, J. Fluids Struct. 24 (1) (2008) 111–128.

[32] J. L. Ratigan, Brine string integrity and model simulation, in: SMRI Tech. Conf., Galveston/Austin, TX, USA, pp. 273–293, 2008.

[33] X. Ge, Y. Li, X. Chen, X. Shi, H. Ma, H. Yin, N. Zhang, C. Yang, Dynamics of a partially confined, vertical upward-fluid-conveying, slender cantilever pipe with reverse external flow, Appl. Sci. 9 (7) (2019) 1425.

[34] J. L. Ratigan, Flow-induced buckling of brine injection strings in solution-mined storage caverns, in: SMRI Tech. Conf., Albuquerque, NM, USA, 2017.

[35] W. Liu, Q. Li, C. Yang, X. Shi, J. Wan, et al., The role of underground salt caverns for large-scale energy storage: A review and prospects, Energy Storage Mater. 63 (2023) 103045.

[36] K. Moditis, M. P. Païdoussis, J. Ratigan, Dynamics of a partially confined, discharging, cantilever pipe with reverse external flow, J. Fluids Struct. 63 (2016) 120–139.

[37] H. Ashley, G. Haviland, Bending vibrations of a pipe line containing flowing fluid, J. Appl. Mech. 17 (3) (1950) 229–232.

[38] G. W. Housner, Bending vibration of a pipeline containing flowing fluid, J. Appl. Mech. 19 (2) (1952) 205–208.

[39] V. P. Feodos'ev, Vibrations and stability of a pipe when liquid flows through it, Inzhenernyi Sb. 10 (1) (1951) 69–70.

[40] F. I. Niordson, Vibrations of a cylindrical tube containing flowing fluid, Kungliga Tekniska Hogskolans Handlingar (Stockholm) No. 73, 1953.

[41] R. H. Long, Experimental and theoretical study of transverse vibration of a tube containing flowing fluid, J. Appl. Mech. 22 (1) (1955) 65–68.

[42] G. H. Handelman, A note on the transverse vibration of a tube containing flowing fluid, Q. Appl. Math. 13 (3) (1955) 326–330.

[43] T. B. Benjamin, Dynamics of a system of articulated pipes conveying fluid. II. experiments, Proc. R. Soc. Lond. A. 261 (1961) 487–499.

[44] R. W. Gregory, M. P. Païdoussis, Unstable oscillation of tubular cantilevers conveying fluid. II. experiments, Proc. R. Soc. Lond. A. 293 (1435) (1966) 528–542.

[45] M. P. Païdoussis, E. B. Deksnis, Articulated models of cantilevers conveying fluid: the study of a paradox, J. Mech. Eng. Sci. 12 (4) (1970) 288–300.

[46] M. P. Païdoussis, Dynamics of tubular cantilevers conveying fluid, J. Mech. Eng. Sci. 12 (2) (1970) 85–103.

[47] J. L. Hill, C. P. Swanson, Effects of lumped masses on the stability of fluid conveying tubes, J. Appl. Mech. 37 (2) (1970) 494–497.

[48] S. S. Chen, Flow-induced instability of an elastic tube, in: Mech. Eng., ASME Paper No. 71-Vibr-39, 1971.

[49] O. Becker, Zum stabilitaetsverhalten des durchstroemten geraden rohres mit elastischer querstuetzung, Maschinenbautechnik 28 (1979) 325–327.

[50] S. S. Chen, J. A. Jendrzejczyk, General characteristics, transition, and control of instability of tubes conveying fluid, J. Acoust. Soc. Am. 77 (3) (1985) 887–895.

[51] W. S. Edelstein, S. S. Chen, Flow-induced instability of an elastic tube with a variable support, Nucl. Eng. Des. 84 (1) (1985) 1–11.

[52] W. H. Chen, C. N. Fan, Stability analysis with lumped mass and friction effects in elastically supported pipes conveying fluid, J. Sound Vib. 119 (3) (1987) 429–442.

[53] R. S. Reddy, S. Panda, G. Natarajan, Nonlinear dynamics of functionally graded pipes conveying hot fluid, Nonlinear Dyn. 99 (3) (2020) 1989–2010.

[54] M. P. Païdoussis, N. T. Issid, Dynamic stability of pipes conveying fluid, J. Sound Vib. 33 (3) (1974) 267–294.

[55] A. L. Thurman, C. D. Mote Jr., Nonlinear oscillation of a cylinder containing a flowing fluid, J. Eng. Ind. 91 (4) (1969) 1147–1155.

[56] J. Rousselet, G. Herrmann, Flutter of articulated pipes at finite amplitude, J. Appl. Mech. 44 (1) (1977) 154–158.

[57] P. J. Holmes, Bifurcations to divergence and flutter in flow-induced oscillations: a finite dimensional analysis, J. Sound Vib. 53 (4) (1977) 471–503.

[58] P. J. Holmes, J. E. Marsden, Bifurcation to divergence and flutter in flow-induced oscillations: an infinite dimensional analysis, Automatica 14 (4) (1978) 367–384.

[59] J. Rousselet, G. Herrmann, Dynamic behavior of continuous cantilevered pipes conveying fluid near critical velocities, J. Appl. Mech. 48 (4) (1981) 943–947.

[60] C. Semler, Nonlinear dynamics and chaos of a pipe conveying fluid, Ph.D. thesis, Department of Mechanical Engineering, McGill University (1991).

[61] G. S. Copeland, F. C. Moon, Chaotic flow-induced vibration of a flexible tube with end mass, J. Fluids Struct. 6 (6) (1992) 705–718.

[62] M. P. Païdoussis, C. Semler, Nonlinear and chaotic oscillations of a constrained cantilevered pipe conveying fluid: a full nonlinear analysis, Nonlinear Dyn. 4 (6) (1993) 655–670.

[63] C. Semler, G. X. Li, M. P. Paıdoussis, The non-linear equations of motion of pipes conveying fluid, J. Sound Vib. 169 (5) (1994) 577–599.

[64] C. Semler, M. P. Païdoussis, Intermittency route to chaos of a cantilevered pipe conveying fluid with a mass defect at the free end, J. Appl. Mech. 62 (4) (1995) 903–907.

[65] A. Sarkar, M. P. Païdoussis, A compact limit-cycle oscillation model of a cantilever conveying fluid, J. Fluids Struct. 17 (4) (2003) 525–539.

[66] M. Wadham-Gagnon, M. P. Païdoussis, C. Semler, Dynamics of cantilevered pipes conveying fluid. {P}art 1: Nonlinear equations of three-dimensional motion, J. Fluids Struct. 23 (4) (2007) 545–567.

[67] M. P. Païdoussis, C. Semler, M. Wadham-Gagnon, S. Saaid, Dynamics of cantilevered pipes conveying fluid. {P}art 2: dynamics of the system with intermediate spring support, J. Fluids Struct. 23 (4) (2007) 569–587.

[68] Y. Modarres-Sadeghi, M. P. Païdoussis, C. Semler, Three-dimensional oscillations of a cantilever pipe conveying fluid, Int. J. Non-Linear Mech. 43 (1) (2008) 18–25.

[69] L. Wang, T. L. Jiang, H. L. Dai, Three-dimensional dynamics of supported pipes conveying fluid, Acta Mech. Sin. 33 (6) (2017) 1065–1074.

[70] J. Duan, K. Chen, Y. You, R. Wang, J. Li, Three-dimensional dynamics of vortex-induced vibration of a pipe with internal flow in the subcritical and supercritical regimes, Int. J. Nav. Archit. Ocean Eng. 10 (6) (2018) 692–710.

[71] R. E. D. Bishop, I. Fawzy, Free and forced oscillation of a vertical tube containing a flowing fluid, Phil. Trans. R. Soc. Lond. A., Mathematical and Physical Sciences 284 (1316) (1976) 1–47.

[72] A. K. Misra, M. P. Païdoussis, K. S. Van, On the dynamics of curved pipes transporting fluid. Part I: Inextensible theory, J. Fluids Struct. 2 (3) (1988) 221–244.

[73] A. K. Misra, M. P. Païdoussis, K. S. Van, On the dynamics of curved pipes transporting fluid Part II: Extensible theory, J. Fluids Struct. 2 (3) (1988) 245–261.

[74] K. Zhou, Q. Ni, W. Chen, H. L. Dai, P. Hagedorn, L. Wang, Static equilibrium configuration and nonlinear dynamics of slightly curved cantilevered pipe conveying fluid, J. Sound Vib. 490 (2021) 115711.

[75] K. Zhou, H. R. Yi, H. L. Dai, H. Yan, Z. L. Guo, F. R. Xiong, Q. Ni, P. Hagedorn, L. Wang, Nonlinear analysis of L-shaped pipe conveying fluid with the aid of absolute nodal coordinate formulation, Nonlinear Dyn. 107 (1) (2022) 391–412.

[76] T. S. Lundgren, P. R. Sethna, A. K. Bajaj, Stability boundaries for flow induced motions of tubes with an inclined terminal nozzle, J. Sound Vib. 64 (4) (1979) 553–571.

[77] X. Jian, H. Yuying, Bifurcations of a cantilevered pipe conveying steady fluid with a terminal nozzle, Acta Mech. Sin. 16 (3) (2000) 264–272.

[78] S. Rinaldi, M. P. Païdoussis, Dynamics of a cantilevered pipe discharging fluid, fitted with a stabilizing end-piece, J. Fluids Struct. 26 (3) (2010) 517–525.

[79] C. Guo, C. Zhang, M. P. Païdoussis, Modification of equation of motion of fluid-conveying pipe for laminar and turbulent flow profiles, ASME J. Press. Vessel Technol. 26 (5) (2010) 793–803.

[80] K. Yamashita, T. Yagyu, H. Yabuno, Nonlinear interactions between unstable oscillatory modes in a cantilevered pipe conveying fluid, Nonlinear Dyn. 98 (4) (2019) 2927–2938.

[81] K. Zhou, Q. Ni, L. Wang, H. L. Dai, Planar and non-planar vibrations of a fluid-conveying cantilevered pipe subjected to axial base excitation, Nonlinear Dyn. 99 (4) (2020) 2527–2549.

[82] Q. Ni, Y. Wang, M. Tang, Y. Luo, H. Yan, L. Wang, Nonlinear impacting oscillations of a fluid-conveying pipe subjected to distributed motion constraints, Nonlinear Dyn. 81 (1-2) (2015) 893–906.

[83] A. M. Dehrouyeh-Semnani, H. Zafari-Koloukhi, E. Dehdashti, M. Nikkhah-Bahrami, A parametric study on nonlinear flow-induced dynamics of a fluid-conveying cantilevered pipe in post-flutter region from macro to micro scale, Int. J. Non-Linear Mech. 85 (2016) 207–225.

[84] T. Zhang, H. Ouyang, Y. O. Zhang, B. L. Lv, Nonlinear dynamics of straight fluid-conveying pipes with general boundary conditions and additional springs and masses, Appl. Math. Model. 40 (17-18) (2016) 7880–7900.

[85] J. Gu, T. Ma, M. Duan, Effect of aspect ratio on the dynamic response of a fluid-conveying pipe using the Timoshenko beam model, Ocean Eng. 114 (2016) 185–191.

[86] M. P. Païdoussis, Aspirating pipes do not flutter at infinitesimally small flow, J. Fluids Struct. 13 (3) (1999) 419–425.

[87] R. Hisamatsu, T. Utsunomiya, Free vibration and stability of a fully submerged pipe aspirating water: An experiment and new physical insights, J. Fluids Struct. 116 (2023) 103789.

[88] M. P. Païdoussis, T. P. Luu, Dynamics of a pipe aspirating fluid such as might be used in ocean mining, J. Energy Resour. Technol. 107 (2) (1985) 250–255.

[89] G. L. Kuiper, A. V. Metrikine, Dynamic stability of a submerged, free-hanging riser conveying fluid, J. Sound Vib. 280 (3-5) (2005) 1051–1065.

[90] G. L. Kuiper, A. V. Metrikine, Experimental investigation of dynamic stability of a cantilever pipe aspirating fluid, J. Fluids Struct. 24 (4) (2008) 541–558.

[91] M. P. Païdoussis, C. Semler, M. Wadham-Gagnon, A reappraisal of why aspirating pipes do not flutter at infinitesimal flow, J. Fluids Struct. 20 (1) (2005) 147–156.

[92] S. Rinaldi, Experiments on the dynamics of cantilevered pipes subjected to internal and/or external axial flow, Master's thesis, Department of Mechanical Engineering, McGill University, Montreal, QC, Canada (2009).

[93] D. B. Giacobbi, The dynamics of aspirating cantilevered pipes and pipes conveying variable density fluid, Master's thesis, Department of Mechanical Engineering, McGill University, Montreal, QC, Canada (2010).

[94] M. F. J. Butt, The dynamics of hanging tubular cantilevers simultaneously subjected to internal and external axial flows, Ph.D. thesis, Department of Mechanical Engineering, McGill University (2021).

[95] Y. Ma, Y. You, A. Feng, K. Chen, Experimental and analytical investigation of dynamic stability of a cantilevered pipe aspirating fluid, in: OnePetro, 32nd Int. Ocean Polar Eng. Conf., no. ISOPE-I-22-012, 2022.

[96] M. P. Païdoussis, J. P. Denise, Flutter of cylindrical shells conveying fluid, J. Sound Vib. 16 (3) (1971) 459–461.

[97] M. P. Païdoussis, J. P. Denise, Flutter of thin cylindrical shells conveying fluid, J. Sound Vib. 20 (1) (1972) 9–26.

[98] D. S. Weaver, T. E. Unny, On the dynamic stability of fluid-conveying pipes, J. Appl. Mech. 40 (1) (1973) 48–52.

[99] D. S. Weaver, B. Myklatun, On the stability of thin pipes with an internal flow, J. Sound Vib. 31 (4) (1973) 399–410.

[100] L. K. Shayo, C. H. Ellen, Theoretical studies of internal flow-induced instabilities of cantilever pipes, J. Sound Vib. 56 (4) (1978) 463–474.

[101] M. Amabili, Nonlinear Vibrations and Stability of Shells and Plates, Cambridge University Press, 2008.

[102] W. R. Hawthorne, The early development of the dracone flexible barge, Proc. IMechE. 175 (1) (1961) 52–83.

[103] M. P. Païdoussis, Dynamics of flexible slender cylinders in axial flow. Part 1: theory, J. Fluid Mech. 26 (4) (1966) 717–736.

[104] M. P. Païdoussis, Dynamics of flexible slender cylinders in axial flow. Part 2: experiments, J. Fluid Mech. 26 (4) (1966) 737–751.

[105] M. P. Païdoussis, Stability of towed, totally submerged flexible cylinders, J. Fluid Mech. 34 (2) (1968) 273–297.

[106] M. P. Païdoussis, Dynamics of cylindrical structures subjected to axial flow, J. Sound Vib. 29 (3) (1973) 365–385.

[107] E. de Langre, M. P. Païdoussis, O. Doaré, Y. Modarres-Sadeghi, Flutter of long flexible cylinders in axial flow, J. Fluid Mech. 571 (2007) 371–389.

[108] G. S. Triantafyllou, C. Chryssostomidis, Analytic determination of the buckling speed of towed slender cylindrical beams, ASME J. Energy Resour. Technol. 106 (2) (1984) 246–249.

[109] G. S. Triantafyllou, C. Chryssostomidis, Stability of a string in axial flow, ASME J. Energy Resour. Technol. 107 (4) (1985) 421–425.

[110] S. S. Chen, Vibration of nuclear fuel bundles, Nucl. Eng. Des. 35 (3) (1975) 399–422.

[111] M. P. Païdoussis, The dynamics of clusters of flexible cylinders in axial flow: theory and experiments, J. Sound Vib. 65 (3) (1979) 391–417.

[112] J. O. Gagnon, M. P. Païdoussis, Fluid coupling characteristics and vibration of cylinder cluster in axial flow. part I. theory, J. Fluids Struct. 8 (3) (1994) 257–291.

[113] J. O. Gagnon, M. P. Païdoussis, Fluid coupling characteristics and vibration of cylinder cluster in axial flow. part II. experiments, J. Fluids Struct. 8 (3) (1994) 293–324.

[114] P. Wang, C. W. Wong, Y. Zhou, Turbulent intensity effect on axial-flow-induced cylinder vibration in the presence of a neighboring cylinder, J. Fluids Struct. 85 (2019) 77–93.

[115] M. P. Païdoussis, D. Mateescu, W. G. Sim, Dynamics and stability of a flexible cylinder in a narrow coaxial cylindrical duct subjected to annular flow, J. Appl. Mech. 57 (1) (1990) 232–240.

[116] D. Mateescu, M. P. Païdoussis, F. Belanger, Unsteady annular viscous flows between oscillating cylinders. Part I: computational solutions based on a time-integration method, J. Fluids Struct. 8 (5) (1994) 489–507.

[117] D. Mateescu, M. P. Païdoussis, F. Belanger, Unsteady annular viscous flows between oscillating cylinders. Part II: A hybrid time-integration solution based on azimuthal fourier expansions for configurations with annular backsteps, J. Fluids Struct. 8 (5) (1994) 509–527.

[118] D. Mateescu, A. Mekanik, M. P. Païdoussis, Analysis of 2-D and 3-D unsteady annular flows with oscillating boundaries, based on a time-dependent coordinate transformation, J. Fluids Struct. 10 (1) (1996) 57–77.

[119] M. P. Païdoussis, B. K. Yu, Elastohydrodynamics and stability of towed slender bodies of revolution, AIAA J. Hydronaut. 10 (1976) 127–134.

[120] A. P. Dowling, The dynamics of towed flexible cylinders. Part 1. neutrally buoyant elements, J. Fluid Mech. 187 (1988) 507–532.

[121] A. P. Dowling, The dynamics of towed flexible cylinders. Part 2. negatively buoyant elements, J. Fluid Mech. 187 (1988) 533–571.

[122] G. S. Triantafyllou, C. Chryssostomidis, The dynamics of towed arrays, ASME J. Offshore Mech. Arct. Eng.g 111 (3) (1989) 208–213.

[123] M. Kheiri, M. P. Païdoussis, Linear dynamics and stability of a towed flexible cylinder, in: Proceedings of 23rd CANCAM, Vancouver, BC, Canada; IMECE2014-36691.

[124] M. Kheiri, M. P. Païdoussis, M. Amabili, A nonlinear model for a towed flexible cylinder, J. Sound Vib. 332 (7) (2013) 1789–1806.

[125] M. Kheiri, M. P. Païdoussis, M. Amabili, An experimental study of dynamics of towed flexible cylinders, J. Sound Vib. 348 (2015) 149–166.

[126] M. P. Païdoussis, E. Grinevich, D. Adamovic, C. Semler, Linear and nonlinear dynamics of cantilevered cylinders in axial flow. Part 1: physical dynamics, J. Fluids Struct. 16 (6) (2002) 691–713.

[127] J. L. Lopes, M. P. Païdoussis, C. Semler, Linear and nonlinear dynamics of cantilevered cylinders in axial flow. part 2: The equations of motion, J. Fluids Struct. 16 (6) (2002) 715–737.

[128] C. Semler, J. L. Lopes, N. Augu, M. P. Païdoussis, Linear and nonlinear dynamics of cantilevered cylinders in axial flow. part 3: Nonlinear dynamics, J. Fluids Struct. 16 (6) (2002) 739–759.

[129] Y. Modarres-Sadeghi, Nonlinear dynamics of a slender flexible cylinder subjected to axial flow, Ph.D. thesis, Department of Mechanical Engineering, McGill University (2006).

[130] Y. Modarres-Sadeghi, M. P. Païdoussis, C. Semler, P. Picot, Nonlinear dynamics of slender cylinders supported at both ends and subjected to axial flow, in: IUTAM Symposium on Integrated Modeling of Fully Coupled Fluid Structure Interactions Using Analysis, Computations and Experiments, Rutgers University, NJ, U.S.A., 2003, pp. 233–246.

[131] M. P. Païdoussis, Y. Modarres-Sadeghi, C. Semler, Nonlinear dynamics of pinned-pinned cylinders in axial flow, in: 21st International Congress of Theoretical and Applied Mechanics, Warsaw, Poland, 2004, pp. 15–21.

[132] Y. Modarres-Sadeghi, M. P. Païdoussis, C. Semler, A nonlinear model for an extensible slender flexible cylinder subjected to axial flow, J. Fluids Struct. 21 (5-7) (2005) 609–627.

[133] Y. Modarres-Sadeghi, M. P. Païdoussis, C. Semler, The nonlinear behaviour of a slender flexible cylinder pinned or clamped at both ends and subjected to axial flow, Comput. Struct. 85 (11-14) (2007) 1121–1133.

[134] M. Kheiri, M. P. Païdoussis, Dynamics and stability of a flexible pinned-free cylinder in axial flow, J. Fluids Struct. 55 (2015) 204–217.

[135] S. Rinaldi, M. P. Païdoussis, Theory and experiments on the dynamics of a free-clamped cylinder in confined axial air-flow, J. Fluids Struct. 28 (2012) 167–179.

[136] J. E. Sader, C. Huertas-Cerdeira, M. Gharib, Stability of slender inverted flags and rods in uniform steady flow, J. Fluid Mech. 809 (2016) 873–894.

[137] A. R. Abdelbaki, M. P. Païdoussis, A. K. Misra, A nonlinear model for a free-clamped cylinder subjected to confined axial flow, J. Fluids Struct. 80 (2018) 390–404.

[138] S. Rinaldi, M. P. Païdoussis, An improved theoretical model for the dynamics of a free–clamped cylinder in axial flow, J. Fluids Struct. 94 (2020) 102903.

[139] F. Cesari, S. Curioni, Buckling instability in tubes subject to internal and external axial fluid flow, in: Proceedings of the 4th Conference on Dimensioning, Hungarian Academy of Science Budapest, 1971, pp. 301–311.

[140] M. J. Hannoyer, M. P. Païdoussis, Dynamics of slender tapered beams with internal or external axial flow—part 1: Theory, J. Appl. Mech. 46 (1) (1979) 45–51.

[141] M. J. Hannoyer, M. P. Païdoussis, Dynamics of slender tapered beams with internal or external axial flow—part 2: Experiments, J. Appl. Mech. 46 (1) (1979) 52–57.

[142] M. P. Païdoussis, P. Besançon, Dynamics of arrays of cylinders with internal and external axial flow, J. Sound Vib. 76 (3) (1981) 361–379.

[143] J. J. Bailey, I. Finnie, An analytical study of drill-string vibration, ASME J. Eng. Ind. 82 (2) (1960) 122–127.

[144] I. Finnie, J. J. Bailey, An experimental study of drill-string vibration, ASME J. Eng. Ind. 82 (2) (1960) 129–135.

[145] J. V. Grigoriev, Stability of a drill tube column with an initial curvature in the axial stream, Journal of Bauman Moscow State Technical University: Mashinostronye 5 (1978) 23–28.

[146] T. P. Luu, On the dynamics of three systems involving tubular beams conveying fluid, Master's thesis, Department of Mechanical Engineering, McGill University, Canada (1983).

[147] X. Wang, F. Bloom, Dynamics of a submerged and inclined concentric pipe system with internal and external flows, J. Fluids Struct. 13 (4) (1999) 443–460.

[148] Q. Qian, L. Wang, Q. Ni, Vibration and stability of vertical upward-fluid-conveying pipe immersed in rigid cylindrical channel, Acta Mech. Solida Sin. 21 (5) (2008) 331–340.

[149] K. Fujita, A. Moriasa, Stability of cantilevered pipes subjected to internal flow and external annular axial flow simultaneously, in: ASME 2015 Pressure Vessels and Piping Conference, Boston, MA, USA; PVP2015-45141, 2015.

[150] K. Moditis, The dynamics of hanging tubular cantilevers in axial flow: An experimental and theoretical investigation, Master's thesis, Department of Mechanical Engineering, McGill University, Montreal, QC, Canada (2014).

[151] K. Kontzialis, K. Moditis, M. P. Païdoussis, Transient simulations of the fluid–structure interaction response of a partially confined pipe under axial flows in opposite directions, ASME J. Pressure Vessel Technol. 139 (3) (2017).

[152] S. Minas, M. P. Païdoussis, F. Daneshmand, Experimental and analytical investigation of hanging tubular cantilevers with discharging axial and radial flow, in: ASME 2017 International Mechanical Engineering Congress and Exposition, Tampa, FL, USA; IMECE2017-70466, 2017.

[153] M. P. Païdoussis, A. R. Abdelbaki, M. F. J. Butt, K. Moditis, A. K. Misra, M. Nahon, Dynamics of a pipe subjected to internal and confined external flow, in: ASME Pressure Vessels and Piping Conference, San Antonio, TX, USA; PVP2019-93227, 2019.

[154] A. R. Abdelbaki, A. K. Misra, M. P. Païdoussis, Dynamics of a tubular cantilever simultaneously subjected to internal and partially-confined external axial flows, in: ASME 2018 International Design Engineering Technical Conferences and Computers and Information in Engineering Conference, Québec City, QC, Canada; DETC2018-86176, 2018.

[155] A. R. Abdelbaki, M. P. Païdoussis, A. K. Misra, A nonlinear model for a hanging tubular cantilever simultaneously subjected to internal and confined external axial flows, J. Sound Vib. 449 (2019) 349–367.

[156] A. R. Abdelbaki, M. P. Païdoussis, A. K. Misra, A nonlinear model for a hanging cantilevered pipe discharging fluid with a partially-confined external flow, Int. J. Non-Linear Mech. 118 (2020) 103290.